ATLAS Note

ANA-HDBS-2019-04-INT1

15th August 2022

Draft version 0.1

Search for non-resonant di-Higgs production with multiple lepton final states using 139 fb^{-1} proton-proton collision data at $\sqrt{s}$ = 13 TeV recorded by the ATLAS detector

Babar Ali[a], Susan Bataju[b], Angela Maria Burger[c], Josefine Bjorndal Robl[d], Djamel Eddine Boumediene[c], Huirun Chen[e], Allison McCarn Deiana[b], Yaquan Fang[f], Thibault Mark Fleischmann[d], Yesenia Hernández Jiménez[g], Xiaozhong Huang[e], Aurelio Juste Rozas[h], Anna Kaczmarska[i], Katharine Leney[j], Chihao Li[k], Liang Li[l], Abdualazem Fadol Mohammed[f], Rohin Thampilali Narayan[b], Merve Nazlim Agaras[h], Santosh Parajuli[l], Océane Perrin[c], Arantxa Ruiz Martínez[m], Qiyu Sha[f], Varsha Senthilkumar[m], Andre Sopczak[a], Rui Wang[o], Yusheng Wu[k], Shuiting Xin[f], Wei-Ming Yao[p], Bartlomiej Henryk Zabinski[i], Bowen Zhang[e], Kaili Zhang[f], Lei Zhang[e], Yulei Zhang[l]

[a]*Czech Technical University in Prague*
[b]*Southern Methodist University, Department of Physics*
[c]*LPC Clermont-Ferrand*
[d]*European Laboratory for Particle Physics, CERN*
[e]*Nanjing University*
[f]*Beijing IHEP*
[g]*Stony Brook University*
[h]*IFAE, Barcelona Institute of Science and Technology*
[i]*Krakow IFJ PAN*
[j]*Dallas SMU*
[k]*University of Science and Technology of China*
[l]*Shanghai Jiao Tong University*
[m]*IFIC, Centro Mixto Universidad de Valencia - CSIC*
[n]*University of Manchester*
[o]*Argonne National Laboratory*
[p]*Berkeley LBNL*

A search is presented for non-resonant Higgs boson pair production, with multiple lepton final states using $139 fb^{-1}$ proton-proton collision data at $\sqrt{s} = 13$ TeV recorded by the ATLAS detector at the Large Hadron Collider. Several final state channels are defined depending on the number of light leptons (e,μ), hadronically decayed τs corresponding to $VVVV$ (W or Z boson), $VV\tau\tau$, $\tau\tau\tau\tau$, decay modes. In addition, final states with $\gamma\gamma + VV/\tau\tau$ are studied, as well as the $b\bar{b}4\ell$ channel targeting $b\bar{b}ZZ^*$ decay. The observed (expected) upper limits on non-resonant di-Higgs production with 95% CL are YYY(ZZZ) $\times$ SM predictions.

Contents

List of contributions

Babar Ali	$2\tau + 1/2\ell$: lepton optimization, analysis strategy, fake tau estimation
Susan Bataju	$2\ell SS + 1\tau$: light fake lepton uncertainty estimation
Angela Maria Burger	$2\ell SS$: definition of WZ and VVjj CRs
Josefine Bjorndal Robl	$2\ell SS + 1\tau$: light lepton fake estimation using fake factor method
Djamel Eddine Boumediene	$2\ell SS$: QMisID DD estimates. Supervisor of Merve and Oceane
Huirun Chen	$2\ell SS + 1\tau$: signal production, truth studies, fit result
Allison McCarn Deiana	3ℓ: Fake leptons, kinematic discriminants, supervision of Santosh
Yaquan Fang	Analysis contact. $yy + 1/2\ell$ and 2ℓSS: supervision of Kaili, Shuiting and Qiyu
Thibault Mark Fleischmann	$2\ell SS + 1\tau$: template fit uncertainties
Yesenia Hernández Jiménez	Analysis contact
Xiaozhong Huang	MC signal production, truth studies
Aurelio Juste Rozas	General discussion, supervision of Nazlim
Anna Kaczmarska	$2\ell SS + 1\tau$: tau optimisation, machine learning, fit, supervision of Bartek
Katharine Leney	MC signal production strategy
Chihao Li	$4\ell + bb$: MC generation, object definition, event selection
Liang Li	3ℓ: supervision of Yulei
Abdualazem Fadol Mohammed	4ℓ, object/event selection, BDT strategy
Rohin Thampilali Narayan	$2\ell SS$: Group analysis framework
Merve Nazlim Agaras	Int. note editor. Group framework developer and coordinator
Santosh Parajuli	3ℓ: analysis strategy, fake lepton estimation, fit results
Océane Perrin	$2\ell SS$: BDT strategy, fake estimation and uncertainty computation
Arantxa Ruiz Martínez	$2\ell + bb$: analysis strategy, BDT strategy, supervision of Varsha
Qiyu Sha	$\gamma\gamma + 1/2\ell$: object/event selection, analysis strategy
Varsha Senthilkumar	$2\ell + bb$: analysis strategy, BDT strategy, MC signal production
Andre Sopczak	$2\ell SS + 1\tau$: light lepton fake estimation, supervision of Josefine and Thibault
Rui Wang	Fit combination
Yusheng Wu	$4\ell + 2b$: supervision of Chihao
Shuiting Xin	2ℓSS: BDT strategy, fake estimation. MC signal production. Combination liason
Wei-Ming Yao	$2\tau + 1/2\ell$: tau selection, analysis strategy, tau fakes estimation
Bartlomiej Henryk Zabinski	HH -> taus + X: Tau optimisation, machine learning, fit, framework
Bowen Zhang	$1\ell + 3t\tau$: MC signal production
Kaili Zhang	$\gamma\gamma + 1/2\ell$: object/event selection, analysis strategy. Combination liason
Lei Zhang	$2\ell SS + 1\tau$: supervision of Huirun
Yulei Zhang	3ℓ: analysis strategy, fake lepton estimation

Executive Summary

0.1 Changelog

Version 0.0: for EB request

- Fist version Internal note.
- Nearly frozen object definition, event selection and analysis strategies are included. Posted the most updated results.

0.2 HDBS requirement

A checklist from PunCom to form an EB from twiki:
HDBS requirement

Physics overview

- Motivation
  - Done in Section 1.
  - This analysis targets the Stand Model (SM) Di-Higgs with a signature of multilepton final states, plus any other things, in which the SM backgrounds like QCD, are strongly suppressed in principle. Previous searches closing to this topic are the $\gamma\gamma WW^*$ analysis [1] and WW^*WW^* [2] analysis, done using luminosity of 36.1 fb^{-1}. There is no single "golden" channel in terms of the trade-offs between branching ratio and final stats in di-Higgs searches. Our multilepton analysis covers several di-Higgs decay modes with small branch ratios, about 5%. Instead of studying the dedicated channels in complex combinatorics signal, the analysis cares about the classification of final states. Final states channels are defined depending on the number of light leptons (e, μ), hadronically decaying taus τ_{had} and additionally final states with $\gamma\gamma$ plus something. In detail, the analysis considers 2ℓSS, 3ℓ, $b\bar{b}4\ell$, 1ℓ+$2\tau_{\text{had}}$, 2ℓSS+$1\tau_{\text{had}}$ sub-channel, named as *multilepton* channels for convenience, and a pair of photons plus $1\ell1\tau_{\text{had}}$, $2\ell0\tau_{\text{had}}$, $0\ell2\tau_{\text{had}}$, called $\gamma\gamma + ML$ channels.
- Signals and backgrounds
  - Both ggF and VBF decay mode signals are used. No specific optimization for VBF signals in our analysis.
  - Prompt backgrounds are simulated with MC, no-prompt backgrounds are estimated by Data-Driven or Simi Data-driven method, documented in A.
- Event selection & categorization (CRs, VRs, SRs).
  - Section 4 for general event section. Signal regions are formed after event selection. BDT cuts are further applied to determine signal regions in 2ℓSS, 3ℓ, 2ℓSS+$1\tau_{\text{had}}$ and $\gamma\gamma + ML$channels.
  - The VRs, and CRs are described in each channel section.
- Main systematics should be available, as well as demonstrations of "custom systematics" (i.e. not a recommendation from a CP group) even if these are not dominant.

  - Detailed in Section 10.

- Model testing - final variable, discussion of binning, systematic correlation model and treatment (pruning, smoothing, etc.)
  - Should be studied in Section 11.
- Final fit detailed, and expected limits (stat-only is acceptable, but with the main systematics included is preferred).
  - Section 11.
- Missing item.
  - See To do section.

Technical overview

- Analysis framework & derivation
  - DxAOD are produced using HIGG8D1 derivation framework. Documented in Section 2.1.
- Statistical and other packages
  - The statistical analysis is done with TrexFitter.

1 Introduction

With the discovery of a new scalar particle the Higgs boson [3, 4] at the LHC [5] by the ATLAS and CMS collaborations with a mass of 125 GeV [6–9], the whole content of the Standard Model (SM) of particle physics became complete. A priority of the ATLAS and CMS collaborations has been to better understand its properties and couplings. After the Electroweak Symmetry Breaking (EWSB) the Higgs field acquires the vacuum expectation value, the Higgs potential can be obtained as following,

$$V(\phi) \rightarrow V(\phi)_{\mathrm{EWSB}} = -\lambda v^2 h^2 - \lambda v h^3 - \frac{1}{4}\lambda h^4 + \mathrm{const.} \tag{1}$$

The first term of the above equation is the Higgs mass term, and the remaining are the trilinear and quadri-linear Higgs-self couplings,

$$\underbrace{m_h = \sqrt{-2\mu^2} = \sqrt{2\lambda v^2}}_{\text{Higgs boson mass}} \qquad \underbrace{\lambda_{hhh} \propto \frac{m_h^2}{v} \qquad \lambda_{hhhh} \propto \frac{m_h^2}{v^2}}_{\text{Trilinear and quadri-linear Higgs self-couplings}} \quad . \tag{2}$$

A measurements of this couplings would therefore give a hint about the actual structure of the potential, whose shape can have theoretical consequences. The quartic Higgs coupling, λ_{hhhh}, can not be measured at LHC since the cross-section of triple Higgs production is small [10] [11], while the trilinear coupling can be probed directly in Higgs pair production.

The trilinear coupling leads to non-resonant pair production of Higgs bosons, where an off-shell Higgs decays to a pair of Higgs bosons, the leading production mechanism being gluon-gluon fusion (ggF). Direct observation of Higgs pair production would lead to measurements directly sensitive to λ but in the SM there are competing diagrams, proceeding via quark (re: top quark) loops that are instead sensitive to the Yukawa coupling of the Higgs rather than the trilinear coupling λ. These HH production mechanisms are illustrated in the Feynman diagrams presented in Figure 1. Not only does the quark-loop induced process present itself as an irreducible background to the process sensitive to the Higgs self-coupling, but it interferences *destructively* with the latter, making the observation of this type of Higgs pair production more challenging.

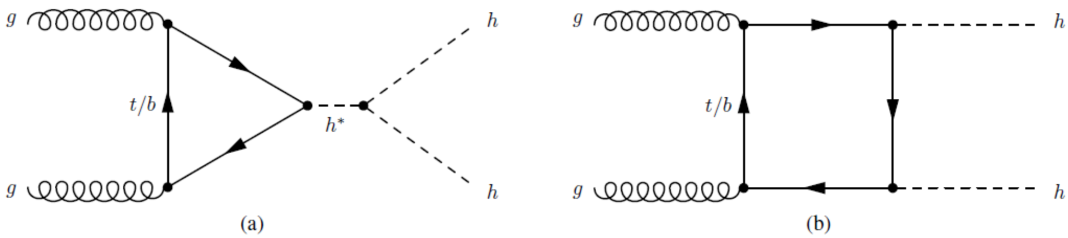

Figure 1: Representative diagrams that contribute to non-resonant hh production. *Left*: Diagram that is sensitive to the trilinear coupling, λ. *Right*: Box diagram that interferences destructively with the λ-sensitive process.

As a result of the destructive interference, and the already relatively large Higgs mass of 125 GeV, the SM HH production has a total cross-section of ~ 31.05 fb [12] at a pp center-of-mass collision energy of 13 TeV. The inclusive cross-section for the pair-production of top quarks, which will be one of the dominant

SM backgrounds in the present analysis, is nearly 100 0pb, or 1×10^6 fb [13, 14]. That of *single* Higgs production is $\sim$ 50 pb, or 5×10^4 fb [15].

Furthermore, enhancements to the di-Higgs production rate, either non-resonantly or through a resonance, may be observable with the full Run2 dataset and would point to new physics beyond the Standard Model, making such analyses interesting now. The wide class of two Higgs double models (2HDM) predict an altered and enlarged Higgs sector from which the currently Higgs is built. The Minimal Supersymmetric Standard Model (MSSM) is a class of 2HDM. For the latter set, one such model is a Randall-Sundrum type graviton or the lightest Kaluza-Klein excitation which have masses of at least 2× the mass of the SM Higgs boson. The presence of such BSM scenarios would act to alter the measured value of λ with respect to that of the SM, potentially enlarging it. As a result, early evidence for the pair-production of Higgs bosons within the current Run-2 dataset may indicate the presence of new physics without having to resort to precision measurements of λ. Examples of such decay scenarios are illustrated in example Feynman diagrams in Figure 2.

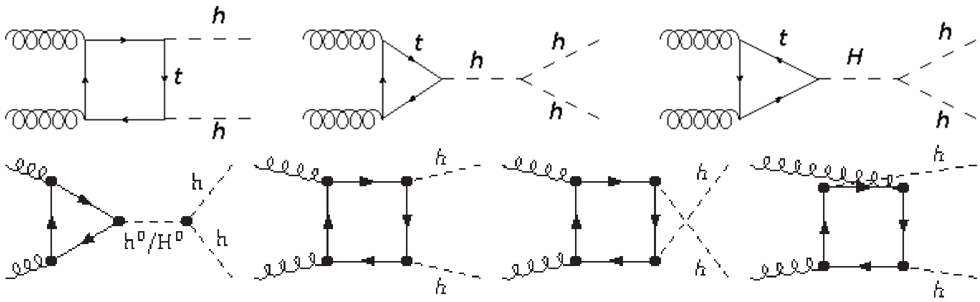

Figure 2: Diagrams contributing to enhanced hh production scenarios. *Top*: A heavy scalar, H, that couples to the Standard Model Higgs boson, h, contributes to the Standard Model processes (left two diagrams). *Bottom*: CP-even diagrams in 2HDM scenario that contribute to enhanced non-resonant production of Standard Model Higgs bosons as well as resonant channels with the heavy CP-even Higgs, H^0, decaying to the Standard Model low-mass CP-even Higgs, h.

Searches for non-resonant Higgs pair production have been performed in a number of final states, $b\bar{b}b\bar{b}$, $b\bar{b}\tau^{\pm}\tau^{\mp}$, $b\bar{b}\gamma\gamma$, $W^{\pm}W^{\mp *}\gamma\gamma$, $b\bar{b}VV$ (with V either Z or W) and $W^+W^-W^+W^-$ at $\sqrt{s}$ = 8 TeV and $\sqrt{s}$ = 13 TeV by ATLAS [16, 17] and CMS collaborations [18–20] including the combination of multiple final states.

In this note, the search for the non-resonant HH production in multilepton final states is described. Typically the decay modes of HH to $W^+W^-W^+W^-$, ZZ^*bb, $VV\tau_{\text{had}}\,\tau_{\text{had}}$, $\tau_{\text{had}}\,\tau_{\text{had}}\,\tau_{\text{had}}\,\tau_{\text{had}}$, $ZZZZ$ are the dominant ones which corresponds to $\sim$ 12% of all HH decay modes. The signal sensitivity are measured in 6 final states categorized by the number and flavour of leptons (mutilepton channels):

- final states of 4 light leptons (e or μ) originated from $H \to ZZ$ decay chain and 2 b-jet candidates decayed from the other Higgs ($b\bar{b}4\ell$). Channels other than $b\bar{b}4\ell$ require no b-jet in the final state;
- two same-sign light leptons and no hadronic τ lepton candidates (2ℓSS);
- three light leptons (3ℓ);
- two same-sign light leptons and one hadronical τ lepton candidate (2ℓSS+1τ_{had});
- two light leptons and two hadronical τ lepton candidates (2ℓ+2τ_{had});
- one light lepton and two hadronical τ lepton candidates (1ℓ+2τ_{had}).

Additionally, $\gamma\gamma + X$ final states are studied which corresponds to 0.14% of HH decays. The events are classified by the number of light leptons and τ_{had} into 3 sub-channels ($\gamma\gamma + ML$ channels):

- one light lepton ($\gamma\gamma$+ℓj);
- one τ_{had} ($\gamma\gamma$+$\tau_{\text{had}} j$);
- two leptons (light lepton or hadronic τ lepton) consist of $1\ell 1\tau_{\text{had}}$, $2\ell 0\tau_{\text{had}}$ and $0\ell 2\tau_{\text{had}}$ ($\gamma\gamma$+2L).

This note is organized as follows: Section 2 describes the Monte Carlo (MC) samples as well as the recorded dataset used in this analysis. The object definition are detailed in Section 3. The signal region definitions and the multivariate analysis discriminants are described in Section 4. From Section 5 to Section 9, detailed explanation of each analysis channels is described. Theoretical and experimental systematic uncertainties are described in Section 10. Finally the combination and results are given in Section 11.

2 Data and Monte Carlo samples

2.1 Derivation and analysis framework

The analysis uses data being prepared with `xAOD` format and further produced to `DxAOD` format using `HIGG8D1` derivation framework. This `xAOD` to `DxAOD` derivation named as GN1 framework, adapted from ttH multilepton analysis, provides a reduction specifically for the signal events with multileptons in the final states. The size reduction is the result of applying smart slimming (remove un-needed variables), thinning (remove entire objects from events) and additional skimming on both collision dataset and MC samples. The production framework is adapted for the $b\bar{b}4\ell$ channel which has lower threshold for leptons, which refers to the *baseline* lepton definition in Section 3.3. Other multilepton channels use the *Loose* leptons (see Tab. 4) at the level of the samples production. Finally, it has to be noted that $\gamma\gamma + ML$ channels use the HGam framework, for which the lepton and τ_{had} definitions are different from multilepton channels by construction.

2.2 Data

This analysis uses 139 fb^{-1} of data collected from proton-proton collision recorded by the ATLAS detector at $\sqrt{s}$ = 13 TeV during 2015-2018. The data set has been collected with a bunch crossing of 25 ns, IBL on, and verifying data quality cuts namely which must be in the recommended Good Run List.

- Year 2015: data15_1V3TeV.periodAllYear_DetStatus-v89-pro21-02_Unknown_PHYS_StandardGRL _All_Good_25ns.xml
- Year 2016: data16_13TeV.periodAllYear_DetStatus-v89-pro21-01_DQDefects-00-02-04_PHYS_ StandardGRL_All_Good_25ns.xml
- Year 2017: data17_13TeV.periodAllYear_DetStatus-v99-pro22-01_Unknown_PHYS_StandardGRL_ All_Good_25ns_Triggerno17e33prim.xml
- Year 2018: data18_13TeV.periodAllYear_DetStatus-v102-pro22-04_Unknown_PHYS_StandardGRL_ All_Good_25ns_Triggerno17e33prim.xml

2.3 Monte Carlo samples

There are three MC campaigns used for each simulated processes, mc16a, mc16d and mc16e, which correspond to different assumption on the distribution of the number of interactions per branching crossing in 2015-2016, 2017 and 2018 periods, respectively.
To match the number of interactions in data, the Monte Carlo samples are reweighed to the observed distribution using procedure provided by the `PileupReweightingTool` [21].

2.3.1 Background samples

Monte Carlo simulation samples were produced for the different signal and background processes using the configurations shown in Table 1, with the samples used to estimate the systematic uncertainties in parentheses. Pile up is modelled using events from minimum-bias interaction generated with Pythia 8.186 [38] using the NNPDF2.3LO set of PDFs and the A3 set of tuned parameters [39], and overlaid onto the simulated hard-scatter events according to the luminosity profile of the recorded data. The generated events were processed through a simulation [40] of the ATLAS detector geometry and response using Geant4 [41], and through the same reconstruction software as the data. Corrections were applied to the simulated events so that the particle candidates' selection efficiencies, energy scales and energy resolutions match those determined from data control samples. The simulated samples are normalised to their cross sections, computed to the highest order available in perturbation theory.

The nominal $t\bar{t}W$ sample is generated using Sherpa-2.2.10 [42] with a multi-leg configuration with `0,1j@NLO+2j@LO`. Both the factorization and renormalization scales are set to $H_T/2$, where the quantity H_T is defined as:

$$H_T = \Sigma_i m_T, i = \Sigma_i \sqrt{m_i^2 + p_T^2, i},$$

which is a sum over all outgoing partons in the matrix element calculation.

The sample is generated using NLO accuracy for matrix elements for up to one additional jet and LO accuracy for up to two additional jets. The additional partons are matched and merged with the Sherpa parton shower based on Catani-Seymour dipole factorization [30] using the MEPS@NLO prescription [31, 43–45] with CKKW merging scale of 30 GeV. The virtual QCD correction for matrix elements at NLO accuracy are provided by the OpenLoops 2 library. Samples are generated using the NNPDF3.0NNLO [35] PDF set. The LO electroweak contributions are obtained from a dedicated sample simulated with Sherpa-2.2.10 and stitched together with the NLO QCD sample described above.

The production of $t\bar{t}t\bar{t}$ events is modelled using the MadGraph5_aMC@NLO v2.6.2 generator which provides matrix elements at NLO in the strong coupling constant α_S with the NNPDF3.1 NLO parton distribution function. The functional form of the renormalization and factorization scales are set to $\mu_r = \mu_f = m_T/4$ where m_T is defined as the scalar sum of the transverse masses $\sqrt{m^2 + p_T^2}$ of the particles generated from the matrix element calculation. Top quarks are decayed at LO using MadSpin to preserve all spin correlations. The events are interfaced with Pythia 8.230 for the parton shower and hadronization, using the A14 set of tuned parameters and the NNPDF2.3 LO PDF set.

The $t\bar{t}H$ process samples are obtained from a generator setup of Powheg-Box generator at NLO. This sample uses `NNPDF3.0nlo` PDF set. The h_{damp} parameter [1] is set to $3/4 \times (m_t + m_{\bar{t}} + m_H) = 325$GeV.

The $t\bar{t}Z/\gamma^*$ sample generated using Sherpa-2.2.11 with a multi-leg configuration with `0j@NLO+1,2j@LO`. The invariant mass of the lepton pair (m_{ll}) is set to be greater than 1 GeV. For the theory systematics, the factorization and renormalization scale are varied by a factor of 0.5 and 2 and provided through the internal weighting scheme.

The $t\bar{t}$ events are generated with Powheg-Box v2.0 and interfaced with Pythia8 for the parton showering and fragmentation with A14 tune for showering. The single top events are simulated with Powheg-Box

[1] The h_{damp} parameter controls the transverse momentum (p_{T}) of the first additional emission beyond the leading-order Feynman diagram in the PS and therefore regulates the high-p_{T} emission against which the $t\bar{t}$ system recoils

and interfaced with Pythia8, where the interference between Wt ad $t\bar{t}$ production is handled with the DR overlap removal procedure.

A dedicated $t\bar{t}$ sample including rare $t \to Wb\gamma^*(\to l^+l^-)$ radiative decays, $t\bar{t} \to W^+bW^-\bar{b}l^+l^-$, is generated using a LO ME and requiring $m(l^+l^-) > 1$ GeV. In this sample the photon can be radiated from the top quark, the W boson, or the b-quark. Both the $t\bar{t}Z/\gamma^*$ and $t\bar{t} \to W^+bW^-\bar{b}l^+l^-$ samples are combined and together form the "$t\bar{t}Z$ (high mass)" sample.

The contribution from internal photon conversions ($\gamma^* \to l^+l^-$) with $m(l^+l^-) < 1$ GeV are modelled by QED multi-photon radiation via the PS in an inclusive $t\bar{t}$ sample and is referred to as "$t\bar{t}\gamma^*$ (low mass)".

Diboson backgrounds are normalised using the cross sections computed by Sherpa, and a 10% normalization uncertainty is assigned to WZ+light-jets, whereas WZ+≥1c and WZ+≥1b have a common free-floated normalization factor assigned in the fit.

Most of the rare background contributions (tZ, $ttWW$, $ttHH$, $ttWH$, $ttZZ$, WtZ, VVV) are normalized using their NLO theoretical cross sections, and assigned a 50% normalization uncertainty, with the exception of tZ where a 5% normalization uncertainty is used.

The cross-sections used to normalize the various background simulated processes can be found summarized in Table 2. Further information about the alternative Monte Carlo samples used as modelling systematic uncertainties can be found in Table 1.

The processes of W and Z associated with jets (V+jets) are simulated with Sherpa 2.2.1 using the NNPDF 3.0 NNLO PDF set and showered by the Sherpa built-in implementation which has matrix elements for up to 2 additional jets at NLO and up to 4 additional jets at LO. The cross section to normalize the simulations are calculated at NNLO accuracy in QCD and include EW corrections at NLO accuracy.

2.3.2 ggF signal samples

- Nominal ggF signal samples: The event generation is performed at the next leading-order (NLO) accuracy with Powheg-Box-V2 for matrix element calculation. Parton showering and hadronization are simulated using the Pythia8 generator with the A14 tune [46] and using the NNPDF 2.3 LO PDF set [35]. The EvtGen [32] programme is used for b- and c-hadron modelling. Detector effects are simulated using AltFastII(AF2) [47], with a fast simulation of the calorimeter response. A set of lepton filters are applied for multilepton channel targeting final states in different light lepton as well as the presence of τ, for instance, $2\ell 0\tau$, $2\ell 1\tau$, $3\ell 0\tau$ etc. In addition, a `MultiLeptonFilter` limits the lepton kinematic at $p_T > 7$ GeV and $|\eta| < 3$. No kinematic cut for photon is required in the generator level for $\gamma\gamma$ + multilepton samples.
  The same configurations of the job options are applied for $\kappa_\lambda = 10$ variation. [2]
- Alternative ggF signal samples: The alternative signal samples are produced by Powheg-Box-V2 interface to Herwig7, using PDF4LHC15 PDF set to study the parton shower uncertainties. The filter strategy are in line with Pythia8 sample cases.

[2] https://its.cern.ch/jira/browse/ATLMCPROD-9335

2.3.3 VBF signal samples

The Vector Boson Fusion (VBF) mode of Higgs boson pair production takes place through three channels as shown in Figure 3. When all three production modes are set to have the Higgs boson coupling constant set to 1 (C_{2V}, C_V, C_3), the Higgs boson pair production is said to be that predicted by the Standard Model [48].

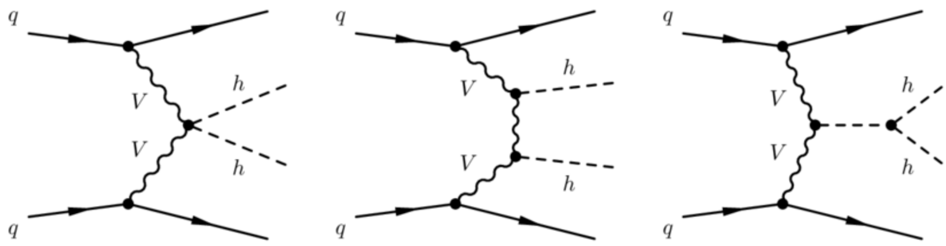

Figure 3: Feynman Diagrams for Higgs boson pair production by Vector Boson Fusion modes [48].

- Nominal VBF signal samples: The event generation is performed at the leading-order (LO) accuracy with MadGraph5_aMC@NLO 2.2.X or 2.3.X [22] for matrix element calculation. Parton showering and hadronization are simulated using the Pythia8 generator with the A14 tune [46] and using the NNPDF 2.3 LO PDF set [35]. The EvtGen [32] programme is used for b- and c-hadron modelling. Detector effects are simulated using AltFastII(AF2) [47], which is a fast simulation of the calorimeter response.

  - Final states targeting different light leptons and the presence of τ include the $2lep0\tau$, $2lep1\tau$, $3lep0\tau$, $3lep1\tau$, $4lep0\tau$ and $4lep1\tau$ channels. The branching ratios of the intermediate particles are set to $\mathrm{BR}(h^0 \rightarrow W^+W^-) = 0.706$, $\mathrm{BR}(h^0 \rightarrow Z^0Z^0) = 0.087$ and $\mathrm{BR}(h^0 \rightarrow \tau^+\tau^-) = 0.207$. In addition to a set of lepton filters, a `MultiLeptonFilter` limits the lepton kinematics at $p_\mathrm{T} > 7$ GeV and $|\eta| < 2.8$ and a `ElecMuTauThreeFilter` limits kinematics of the hadronic τ at $p_\mathrm{T} > 13$ GeV and $|\eta| < 2.8$.

  - In final states targeting $\gamma\gamma$ + multilepton, the branching ratios of the intermediate particles are set to to $\mathrm{BR}(h^0 \rightarrow W^+W^-) = 0.353$, $\mathrm{BR}(h^0 \rightarrow Z^0Z^0) = 0.043$ and $\mathrm{BR}(h^0 \rightarrow \tau^+\tau^-) = 0.104$. No kinematic cut for photon is required in the generator level and the branching ratio is set to $\mathrm{BR}(h^0 \rightarrow \gamma\gamma) = 0.5$.

  - The branching ratios of the intermediate Z bosons are set to $\mathrm{BR}(h^0 \rightarrow Z^0Z^0) = 0.5$ and no kinematic cuts are applied in the generator level.

- Alternative VBF signal samples: the alternative signal samples are produced by MadGraph5_aMC@NLO 2.2.X or 2.3.X [22] interface to Herwig7, using PDF4LHC15 PDF set to study the parton shower uncertainties. The filter strategy are in line with pythia8 sample cases.

Table 1: The configurations used for event generation of signal and background processes. The samples used to estimate the systematic uncertainties are indicated in between parentheses. V refers to production of an electroweak boson (W or Z/γ^*). The parton distribution function (PDF) shown in the table is the one used for the matrix element (ME). If only one parton distribution function (PDF) is shown, the same one is used for both the matrix element (ME) and parton shower generators; if two are shown, the first is used for the matrix element calculation and the second for the parton shower. Tune refers to the underlying-event tune of the parton shower generator. MG5_aMC refers to MadGraph5_aMC@NLO 2.2.X or 2.3.X [22]; Pythia 6 refers to version 6.427 [23]; Pythia 8 refers to version 8.2 [24]; Herwig++ refers to version 2.7 [25]; Herwig7 refers to version 7.0.4 [26]; MePs@Nlo refers to the method used in Sherpa [27–31] to match the matrix element to the parton shower. Samples using Pythia 6 or Pythia 8 have heavy flavour hadron decays modelled by EvtGen 1.2.0 [32]. All samples include leading-logarithm photon emission, either modelled by the parton shower generator or by PHOTOS [33]. The mass of the top quark and SM Higgs boson were set to 172.5 GeV and 125 GeV.

Process	Generator	ME order	Parton shower	PDF	Tune
$t\bar{t}W$	Sherpa 2.2.10	NLO	Sherpa	NNPDF3.0 NNLO	Sherpa default
	(MG5_aMC)	(NLO)	(Pythia 8)	(NNPDF3.0 NLO)	(A14)
$t\bar{t}t\bar{t}$	MG5_aMC	NLO	Pythia 8	NNPDF3.1 NLO	A14
	(Sherpa 2.2.10)	(NLO)	(Sherpa)	(NNPDF3.0 NNLO)	(Sherpa default)
$t\bar{t}H$	Powheg-BOX [34]	NLO	Pythia 8	NNPDF3.0 NLO [35]	A14
	(Powheg-BOX)	(NLO)	(Herwig7)	(NNPDF3.0 NLO)	(H7-UE-MMHT)
	(MG5_aMC)	(NLO)	(Pythia 8)	(NNPDF3.0 NLO)	(A14)
$t\bar{t}(Z/\gamma^* \to l^+l^-)$	Sherpa 2.2.11	NLO	Sherpa	NNPDF3.0 NNLO	Sherpa default
	(MG5_aMC)	(NLO)	(Pythia 8)	(NNPDF3.0 NLO)	(A14)
$t\bar{t} \to W^+bW^-\bar{b}l^+l^-$	MG5_aMC	LO	Pythia 8	NNPDF3.0 LO	A14
$t(Z/\gamma^*)$	MG5_aMC	NLO	Pythia 8	NNPDF2.3 LO	A14
$tW(Z/\gamma^*)$	MG5_aMC	NLO	Pythia 8	NNPDF2.3 LO	A14
$t\bar{t}W^+W^-$	MG5_aMC	LO	Pythia 8	NNPDF2.3 LO	A14
$t\bar{t}$	Powheg-BOX	NLO	Pythia 8	NNPDF3.0 NLO	A14
	(Powheg-BOX)	NLO	(Herwig7.1.3)	(NNPDF3.0 NLO)	(H7-UE-MMHT)
$t\bar{t}t$	MG5_aMC	LO	Pythia 8	NNPDF2.3 LO	A14
s-, t-channel, Wt single top	Powheg-BOX [36, 37]	NLO	Pythia 8	NNPDF3.0 NLO	A14
VV, $qqVV$, $lowm_{\ell\ell}$, VVV	Sherpa 2.2.2	NLO	Sherpa	NNPDF3.0 NNLO	Sherpa default
$Z \to l^+l^-$	Sherpa 2.2.1	NLO	Sherpa	NNPDF3.0 NLO	Sherpa default
$Z \to l^+l^-$ (matCO)	Powheg-BOX	NLO	Pythia 8	CTEQ6L1 NLO	A14
$Z \to l^+l^-+(\gamma*)$	Powheg-BOX	NLO	Pythia 8	CTEQ6L1 NLO	A14
W+jets	Sherpa 2.2.1	NLO	Sherpa	NNPDF3.0 NLO	Sherpa default
VH	Powheg-BOX	NLO	Pythia 8	NNPDF3.0 NLO	A14
$t\bar{t}ZZ$	Madgraph	LO	Pythia 8	NNPDF2.3 LO	A14
$t\bar{t}HH$	Madgraph	LO	Pythia 8	NNPDF2.3 LO	A14
$t\bar{t}WH$	Madgraph	LO	Pythia 8	NNPDF2.3 LO	A14

Table 2: The background sample normalizations and their uncertainties used in the analysis. The uncertainties on the inclusive cross sections are taken from the ATLAS Physics Modelling Group Twiki.

Process	Precision order	Cross section central value	Cross section uncertainty	Modelling uncertainty	Normalized to data
MC samples contributing to fake lepton templates					
$t\bar{t}$	NNLO+NNLL	832 pb	-	alternative MC	Yes
s-, t-channel single top	NLO	227 pb	-	-	Yes
Wt single top	NNLO approx	71.7 pb	-	-	Yes
$Z \to l^+l^-$	NNLO	0.9751×Sherpa	-	-	Yes
MC samples of irreducible background processes					
$t\bar{t}W$	NLO	601 fb	-	alternative MC scale variations	Yes
$t\bar{t}t\bar{t}$	NLO	12 fb	20%	alternative MC	No
$t\bar{t}(Z/\gamma^* \to l^+l^-)$	NLO	839 fb	-	alternative MC scale variations	Yes
$t\bar{t}H$	NLO	507 fb	11%	alternative MC scale variations	No
VV, $qqVV$	NLO	Sherpa	-	10% (+LF jets), scale variations	Yes (+HF jets)
$t(Z/\gamma^*)$	LO	240 fb	5%	-	No
$t\bar{t}t$	LO	1.6 fb	50%	-	No
$tW(Z/\gamma^*)$	NLO	16 fb	50%	-	No
$t\bar{t}W^+W^-$	NLO	9.9 fb	50%	-	No
VVV	NLO	Sherpa	50%	-	No

3 Object selection

This section describes the overall objection definition for multilepton channels and $\gamma\gamma + ML$ channels.

3.1 Primary vertices

The primary vertex in an event is chosen as the vertex with the highest $\sum p_{\mathrm{T}}^2$ of associated tracks [49]. Events with significant noise in the calorimeters or data corruption are removed.

3.2 Trigger

Triggers in multilepton channels: The single-lepton triggers and di-lepton triggers used in this analysis for 2015 - 2018 data are listed in Table 3. For channels have with at least 2 light leptons a logical OR between di-lepton and single-lepton triggers is applied. Events with 1 light lepton and 2 τ_{had} are required to pass un-prescaled single lepton triggers.
The trigger scale factors in order to apply the corrections to simulated samples are computed for each event, using the TrigGlobalEfficiencyCorrection package [50]. The scale factors associated to light leptons identification and isolation, which is introduced in Section 3.3 are suitably considered in the MC weight.

Triggers in $\gamma\gamma + ML$ channel: Di-photon trigger with two reconstructed photons with E_{T} larger than 35 and 25 GeV passing *loose* (2015/2016) and *medium* (2017/2018) requirements based on the energy leakage in the hadronic compartment and on the shower shape in the second layer of the electromagnetic calorimeter are used for the analysis.

- HLT_g35_loose_g25_loose (2015/2016)
- HLT_g35_loose_g25_medium_L12EM20VH (2017/2018)

3.3 Leptons

For multilepton channels, three sets of light lepton requirements are defined depending on the type and number of objects in the final state, namely as "Baseline" (B), "Loose" (L), "Tight" (T). The baseline lepton is only applied to $b\bar{b}4\ell$ channel to enhance the signal acceptance. A dedicated check of the overlap between $b\bar{b}4\ell$ and $b\bar{b} + 2\ell$ analysis is done and documented in Appendices H. Events except $b\bar{b}4\ell$ are splitted into different categories based on the light lepton and τ_{had} multiplicity, which are defined using the *Loose* definition, so that the orthogonality between each channel is guaranteed. In order to further maximize the signal sensitivity in the signal region, as well as suppress the background contribution, more tighter selections are used for those channels with up to 2 light leptons and 1 hadronic tau lepton. The lepton definition of 3 categories are presented in Sections 3.3.1, 3.3.2, 3.4 and summarized in Table 4.

The selection of leptons in $\gamma\gamma + ML$ channels follows the official working point of identification (ID) and isolation, which is the default setting in HGam framework and it is summarized below.

	Single lepton triggers (2015)
μ	HLT_mu20_iloose_L1MU15, HLT_mu50
e	HLT_e24_lhmedium_L1EM20VH, HLT_e60_lhmedium, HLT_e120_lhloose
	Dilepton triggers (2015)
$\mu\mu$ (asymm.)	HLT_mu18_mu8noL1
ee (symm.)	HLT_2e12_lhloose_L12EM10VH
$e\mu, \mu e$ (~symm.)	HLT_e17_lhloose_mu14
	Single lepton triggers (2016)
μ	HLT_mu26_ivarmedium, HLT_mu50
e	HLT_e26_lhtight_nod0_ivarloose, HLT_e60_lhmedium_nod0, HLT_e140_lhloose_nod0
	Dilepton triggers (2016)
$\mu\mu$ (asymm.)	HLT_mu22_mu8noL1
ee (symm.)	HLT_2e17_lhvloose_nod0
$e\mu, \mu e$ (~symm.)	HLT_e17_lhloose_nod0_mu14
	Single lepton triggers (2017 / 2018)
μ	HLT_mu26_ivarmedium, HLT_mu50
e	HLT_e26_lhtight_nod0_ivarloose, HLT_e60_lhmedium_nod0, HLT_e140_lhloose_nod0
	Dilepton triggers (2017 / 2018)
$\mu\mu$ (asymm.)	HLT_mu22_mu8noL1
ee (symm.)	HLT_2e24_lhvloose_nod0
$e\mu, \mu e$ (~symm.)	HLT_e17_lhloose_nod0_mu14

Table 3: List of lowest p_T-threshold, un-prescaled di-lepton triggers used for 2015-2018 data taking.

- Electrons: Electrons are reconstructed by matching the energy deposits from the EM calorimeter to the track in the inner detector. It requires $p_{\rm T} > 10$ GeV, $|\eta| < 1.37$ or $1.52 < |\eta| < 2.37$, Medium LH ID, $|d_0|/\sigma_{d_0} < 5$, $|\Delta z_0 \times \sin\theta| < 0.5$ mm. Isolation requirements: topoEtCone20 $< 0.02 \times p_{\rm T}$ and ptcone20 $< 0.15 \times p_{\rm T}$.
- Muons: Muons are reconstructed by using the information of Muon spectrometer and the Inner detector. The candidates should pass $p_{\rm T} > 10$ GeV, $|\eta| < 2.7$, Medium ID, $|d_0|/\sigma_{d_0} < 3$, $|\Delta z_0 \times \sin\theta| < 0.5$ mm. GradientLoose isolation criteria is required.

3.3.1 Muons

Muons are reconstructed by using the information of Muon spectrometer and the Inner detector. Muon candidates are selected with $p_T > 3$ GeV and $|\eta| < 2.5$. They are required to pass the Loose and Medium identification working point for baseline muons and muons tighter than baseline . The impact parameter

	e			μ		
	B	L	T	B	L	T
Isolation	No	PLVLoose	PLVTight	No	PLVLoose	PLVTight
Identification	LooseLH		TightLH	Loose		Medium
Charge MisID BDT	No		Yes	N/A		
Ambiguity type	No	Yes		N/A		
$\|d_0\|/\sigma_{d_0}$	< 5			< 3		
$\|z_0 \sin\theta\|$	< 0.5 mm					

Table 4: Baseline, Loose, Tight definitions in multilepton channels.

cut remain the same as electron but transverse parameter significance requires less than 3 .

Similarly as electrons, baseline muons are required to pass PLVLoose isolation. The Loose muons have to satisfy PLVLoose and Tight muons must be selected from PLVTight. The muon selection criteria is summarized in Table 5

Table 5: Muon selection criteria. For "identification" and "isolation", the first working point are the ones used for the inclusive *Loose* lepton definition , whereas the second working points are the ones used for *Tight* lepton definitions. The *baseline* lepton has no requirement on the isolation but the Loose identification is passed.

Feature	Criterion
Identification	`Loose` / `Medium`
Isolation	`PLVLoose` / `PLVTight`
$\|\eta\|$ cut	< 2.5
$\|d_0\|/\sigma_{d_0}$	< 3
z_0 cut	0.5 mm

3.3.2 Electrons

Electrons are reconstructed by matching the energy deposits from the EM calorimeter to the track in the inner detector. For the baseline electron candidates, they are required to have p_T>4.5 GeV and $|\eta| < 2.5$, the electron within the transition region between barrel and endcap electromagnetic calorimeter,$1.37 < |\eta| < 1.52$ are vetoed. To reduce the non-prompt electron contribution, cuts on the transverse parameter significance d_0 and longitudinal impact parameter z_0 are applied to ensure that the electron originates from a primary vertex. A likelihood-based selection at the "Loose" operation point is used.

The Loose electrons are used in multilepton channels except $b\bar{b}4\ell$, they are required to be isolated from other objects in the event by passing the PLVLoose working point. Loose electrons candidates should pass a charge misidentification BDT working point to reduce charge flip background contribution. Furthermore, the photon conversion background is not negligible, electrons are required to fulfill the ambiguity bit selection. For more tighter electron, a dedicated BDT, lepton isolation PromptLeptonVeto (PLV), recommended by the Isolation and Fake Forum group, is considered. The electron selection criteria is summarized in Table 6.

Table 6: Electron selection criteria. For "identification" and "isolation", the first working point is the one used for the inclusive loose lepton definition (*Loose*), whereas the second working points are the ones used for *Tight* lepton definitions. The *baseline* lepton has no requirement on the isolation but the Loose identification has to passed.

Feature	Criterion
Identification	`LooseLH` / `TightLH`
Isolation	`PLV Loose` / `PLV Tight`
Energy calibration	`es2018_R21_v0` (ESModel)
Object quality	Not from a bad calorimeter cluster Remove clusters from regions with EMEC bad HV (2016 data only)
$\lvert\eta\rvert$ cut	$(\lvert\eta\rvert < 1.37) \quad \lvert\lvert \quad (1.52 < \lvert\eta\rvert < 2.47)$
d_0 significance cut	5
z_0 cut	0.5 mm

3.4 Hadronically decaying taus

Hadronically decaying tau lepton candidates (τ_{had}) are reconstructed from clusters in the calorimeters and associated inner detector tracks. The candidates are required to have either one or three associated tracks, with a total charge of ±1. Candidates with $p_{\text{T}} > 20$ GeV and $|\eta| < 2.5$, excluding the electromagnetic calorimeter transition region, are considered. A RNN discriminant using calorimeter and tracking-based variables is used to identify τ_{had} candidates and reject generic jet backgrounds. The chosen working point has an efficiency of 75% (60%) for one- (three-) prong τ_{had} decays ["medium" tau ID working point]. In $\gamma\gamma + ML$ channels, the chosen working point has an efficiency of 85% (75%) for one- (three-) prong τ_{had} decays ["loose" tau ID working point], other definitions of hadronic tau are same as in τ channels. Considering the consistency across all the channels, we moved τ_{had} ID to medium in $\gamma\gamma + ML$ channels, its impact was relatively small. The definitions of hadronic tau in this analysis are summarized in Table 7.

3.5 Photon

The photon is reconstructed by using the supercluster method with the energy deposits in the EM calorimeter. Run-2 photon performance details could be found in Ref. [51]. The photon candidate is required to have $p_{\text{T}} > 25$ GeV and $|\eta| < 2.37$. Photon inside the crack region $1.37 < |\eta| < 1.52$ is rejected. The photon candidate is also required to pass the *Tight* cut-based photon identification selection which is based on the longitudinal and transverse shower profiles measured in the calorimeter. In addition, the photon candidate is required to be isolated and pass both calorimeter-based isolation topoEtCone20$< 0.065 \times p_{\text{T}}$ and track-based isolation ptcone20$< 0.05 \times p_{\text{T}}$. Candidate event is required to have at least two good isolated photons. To match the trigger threshold, the leading photon is required to have $p_{\text{T}} > 35$ GeV and subleading photon with $p_{\text{T}} > 25$ GeV.

!h

Table 7: τ_{had} selection criteria. For "identification" the `Loose` working point is used for $\gamma\gamma + ML$ channels , whereas the `Medium` working points are used for all τ_{had} channels.

Hadronic tau	
Identification	JetID RNN Loose / Medium
p_T [GeV]	> 20
$\|\eta\|$	< 2.5
Crack region $1.37 < \|\eta\| < 1.52$	vetoed
N_{track}	1 or 3
Charge	± 1
Electron veto	passEleBDT
Muon overlap removal	passMuonOLR

3.6 Jets and b-jets

The jets used in this analysis are reconstructed by the anti-k_{T} algorithm with radius parameter $R = 0.4$ from the particle-flow (PFlow) objects. The particle-flow algorithm provides a list of tracks and a list of topo-clusters containing both the unmodified topo-clusters and a set of new topo-clusters resulting from the energy subtraction procedure. The algorithm attempts to match each track to a single topo-cluster in the calorimeter. The expected energy deposited in the calorimeter (based on topo-cluster position and the track momentum) is subtracted cell by cell from the set of matched topo-clusters. If the remaining energy is consistent with the expected shower fluctuations of a single particle's signal, the topo-cluster remnants are removed [52].

The reconstructed jet collection is called `AntiKt4PFlowCustomVtxHggJets` [51] and is used as default in all analyses and across this document, unless stated differently. Technical details on the collection used are shown in Table 8.

Table 8: PFlow jet calibration recommendations. The `_Insitu` calibration is applied on data while the jet energy resolution `_Smear` is applied on MC.

Collection name:	`AntiKt4PFlowCustomVtxHggJets`, `AntiKt4EMPFlowJets`
Configuration file:	`JES_MC16Recommendation_Consolidated_PFlow_April2019_Rel21`
Calibration sequence:	`JetArea_Residual_EtaJES_GSC_Smear[_Insitu]`
Calibration area version:	00-04-82

The jet selection used for this analysis is:

- $p_{\text{T}} > 25$ GeV.
- anti-kt R = 0.4.
- $|\eta| < 2.5$ (for central jets).
- $|y| < 4.4$
- Jet-Vertex Tagger (JVT) WP: Tight

- Jet cleaning WP: LooseBad

The flavour tagging algorithm used to the determine the flavour of the jet is a high level algorithm based on a deep neural network that uses the output of "recurrent neural network impact parameter" (RNNIP) as input. DL1r outputs three different probabilities (p_{b}, p_{c} and p_{u}) that are combined to define a final discriminant. DL1r algorithm has been re-optimized in 2019 in order to maximize the performance on the jet collections recommended for use in ATLAS, PFlow jets and VR jets and to extend the algorithm performance to very high jet p_{T} [53],[54]. The b-tagging working point with a 77% efficiency is chosen, such efficiency is measured from $t\bar{t}$ MC samples and dedicated $t\bar{t}$ data. The associated SFs are taken into account.

3.7 Missing Energy

The $E_{\mathrm{T}}^{\mathrm{miss}}$ involves all the reconstructed and calibrated objects described above. Compared to the general definition, τ leptons are treated as normal hadronic jets here which does not change the performance [51]. The Track-based Soft Term (TST) is the chosen approach to compute the $E_{\mathrm{T}}^{\mathrm{miss}}$ soft term, and is therefore used here.

3.8 Overlap removal

Since objects are reconstructed with different algorithms in parallel, i.e. no check to see if a same set of clusters or tracks are used for reconstructing two different object, one needs to implement a set of rules to remove objects close to each other to avoid double counting.

Overlap removal in multilepton channels The chosen overlap removal procedure is commonly used in SUSY analysis, it is applied with ASG overlap removal tool in AnalysisTop [55]. The optimal overlap removal procedure is detailed below:

- Any calorimeter muon found to share a track with an electron is removed.
- Any electron found to share a track with a non-calorimeter muon is removed.
- Any jet found within a delta-R of 0.2 of an electron is removed.
- Any electron subsequently found within delta-R of of 0.4 of a jet is removed.
- Any jet with less than 3 tracks associated to it found within delta-R of 0.2 of a muon is removed.
- Any jet with less than 3 tracks associated to it which has a muon inner-detector track ghost-associated to it, is removed.
- Any muon subsequently found within delta-R of 0.4 of a jet is removed.
- Any tau found within a delta-R of 0.2 of a electron is removed.
- Any tau found within a delta-R of 0.2 of any type of muon with p_T greater than 2 GeV is removed, while noting that if the tau p_T is greater than 50 GeV, it will only be removed if it is found to overlap with a combined-type muon.
- Any jet found within a delta-R of 0.2 of a tau is removed.

- Any photon found within a delta-R of 0.4 of an electron or a muon is removed.
- Any jet found within delta-R of 0.4 of a photon is removed.

Overlap removal in $\gamma\gamma + ML$ channels This overlap removal is done after full object definitions and two loose photons. The rule is defined as below. More details can be found in Ref [56].

- The two leading photons are always kept.
- Electrons with $\Delta R(e, \gamma) < 0.4$ are removed.
- Jets with $\Delta R(jet, \gamma) < 0.4$ are removed.
- Jets with $\Delta R(jet, e) < 0.2$ are removed.
- Muons with $\Delta R(\mu, \gamma) < 0.4$ or $\Delta R(\mu, jet) < 0.4$ are removed
- Electrons with $\Delta R(e, jet) < 0.4$ are removed.

4 Signal region definition using multivariate analysis techniques

4.1 Introduction

The channels considered in this analysis include three light leptons final states: 2ℓSS, 3ℓ, $b\bar{b}4\ell$; and three τ_{had} related channels: 2ℓSS+$1\tau_{\text{had}}$, 1ℓ+$2\tau_{\text{had}}$, 2ℓ+$2\tau_{\text{had}}$. These six final states will be referred to as multilepton channels in the following. In addition, channels containing photons are also included: $\gamma\gamma + ML$ channels. An overall map is shown in Figure 4 to visualize final states for this HH-multilepton search. During the investigations of some specific channels low sensitivity is found so these are not considered in the combination. These channels include 4ℓ, 2ℓOS and $HH \to b\bar{b}ZZ \to b\bar{b} + 2\ell$ and they are documented in Appendices B, I, and E respectively. To-do: document removed channels

Multilepton and $\gamma\gamma + ML$ channels events are categorized by the number of light leptons satisfying the baseline selection detailed in Section 3.3, τ_{had} and photons after the overlap removal procedure is applied (see Section 3.8). Note that this guarantees orthogonality between channels as each category only selects events with the exact number of expected objects in the final state. The basic object requirements and analysis strategies of the individual channels are presented in Table 9.

All channels in this analysis make use of a multivariate technique in order to enhance the sensitivity of the search. Section 4.2 details the event pre-selection for each channel which is done prior training the Boost Decision Trees (BDT). After the event pre-selection each channel uses different kinematic variables, according to the objects in the final state, to train the BDT in order to separate HH signal from background processes. The description of the variables used for each channel is given in Section 4.3. Finally, the signal region is defined by using the BDT output. In the case of multilepton channels the full BDT output or the high BDT region is used in the statistical analysis to compute the upper limit as explained in Section 11. The $\gamma\gamma + ML$ channel uses the di-photon invariant mass ($m_{\gamma\gamma}$) shape in several BDT regions. An overall description of all the signal regions is summarized in Section 4.4.

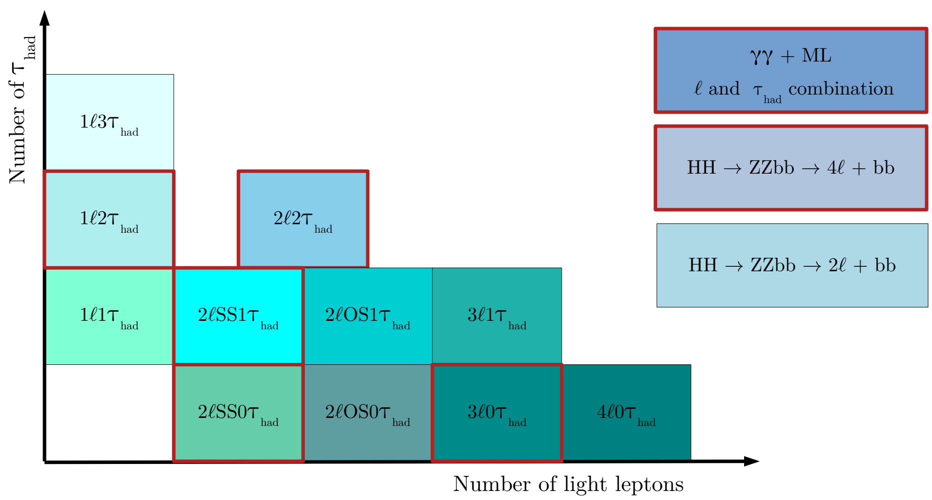

Figure 4: Channels of multiple lepton final states in this analysis.

	2ℓSS	2ℓSS+1τ_{had}	3ℓ	$b\bar{b}4\ell$	1ℓ+2τ_{had}	2ℓ+2τ_{had}	$\gamma\gamma$+ℓj	$\gamma\gamma$+$\tau_{\text{had}}j$	$\gamma\gamma$+2L
Light lepton	2T	2T	1L, 2T	2B, 2L	1L	2L	1	0	$n_\ell + n_{\tau h} = 2$
nτ_{had}	0	1	0	2	2	2	0	1	
N_{jets}	≥ 2	≥ 2	≥ 1	≥ 2	≥ 2	≥ 1	–	–	–
Non-prompt lepton strategy	TF,FF	TF	TF	TF	–	–	–	–	–
Fake tau strategy	–	FF	–	–	FF	FF	–	–	
BDT trained against	VV , $t\bar{t}$ and V+jets separately	VV	total background	total background	VV	VV	continuous background		
Discriminant	Combined BDT	BDT	BDT	BDT	BDT	BDT	$m_{\gamma\gamma}$ in BDT regions		
Control regions	5	3	4	4	-	-	-	-	-

Table 9: Summary of basic characteristics and strategies of the multilepton and $\gamma\gamma + ML$ channels. For the fake lepton and tau background estimates, from which *TF* is the template fit method and *FF* refers to the fake factor method.

4.2 Pre-MVA event selection

4.2.1 2ℓSS channel

In the 2ℓSS channel, events passing the following selections are required:

- **Trigger Selection**:
  - Global Trigger Decision
  - Trigger matching with Tight electrons or muons for Single lepton trigger or dilepton trigger
- **Leptons definition**:
  - Two leptons with same electric charge
  - The transverse momentum of each lepton has to be larger than 20 GeV
  - TightLH and MediumLH ID respectively for electrons and muons
  - Both leptons must satisfy tight prompt lepton veto isolation working point
  - The invariant mass of the two leptons has to be larger than 12 GeV
- **Hadronic tau veto**: All events with at least one hadronic tau are vetoed
- **Jet multiplicity**
  - A b-jet veto is required: events with b-jets are discarded
  - At least 2 jets are required

4.2.2 3ℓ channel

Events are required to pass the following common selection:

- **Trigger**:
  - Global Trigger Decision:
  - Single lepton triggers or Di-lepton triggers:
- **Lepton multiplicity**:
  - Exactly three leptons with a total electric charge of ±1.
  - Events are classified by their lepton flavour/charge composition as $l_1 l_2 l_3$, where the lepton with opposite charge with respect to the other two is noted as lepton index "1". The remaining lepton that is nearest to l_1 in ΔR is given the index "2" and the final lepton is noted as lepton "3".
  - $p_{\mathrm{T}}^{1} > 10$ GeV and $p_{\mathrm{T}}^{2,3} > 15$ GeV.
  - Lepton 1 is required to pass the loose selection while lepton 2 and 3 are required to pass the tight selection.
- **Hadronic tau veto**: Events with at least one hadronic tau are vetoed.
- **Jet multiplicity**: Events with at least one jet are selected: $N_{\mathrm{jet}} \geq 1$.
- **b-jet veto**: Veto events if they contain any b-tagged jets.
- **Low mass veto**: Events with at least one opposite-sign ame-flavour (OSSF) lepton pair with an invariant mass less than 12 GeV are vetoed.
- ***Z*-mass veto**:
  - Events with OSSF lepton pair with an invariant mass within a ±10 GeV window around m_Z are vetoed.
  - Invariant mass of the tri-lepton system is required to be ±10 GeV from the Z-mass pole: $|m_{lll} - m_Z| > 10$ GeV.

4.2.3 $b\bar{b}4\ell$ channel

After the object definition, only events containing exactly four leptons with zero total electric charge are selected as signal candidates. In addition the following requirements are applied to define the signal region.

- **Trigger**: Any of the standard single electron and single muon, or di-leptons.
- **Lepton multiplicity**: signal event candidates are selected by requiring exactly four leptons satisfying the Baseline selection described in Section 3.3.
  - Four leptons are sorted by p_T. Either of the third lepton and the forth lepton, which correspond to the second lowest and the lowest lepton p_T, is required to pass the $PflowLoose$ isolation working point. The isolation strategy is discussed in Appendix H.1 in detail.

  - p_T thresholds for the three leading leptons are 20, 15 and 10 GeV.
  - $\Delta R(l_i, l_j) = \sqrt{(\eta_i - \eta_j)^2 + (\phi_i - \phi_j)^2} > 0.02$ is required between any of lepton pairs.

- **Lepton pair definition** Two OSSF lepton pairs are required. The lepton pair with invariant mass closest to the nominal Z boson mass is selected as the leading lepton pair. Two remaining leptons are also required to be OSSF and form the sub-leading lepton pair.
- **Low Mass veto**: All OSSF lepton pairs are required to have invariant mass larger than 5 GeV to veto J/Ψ decays.
- **Z-mass window**: The invariant mass of the four leptons must satisfy $107 < m_{4l} < 133$ GeV to select an on-shell Higgs decay.
- **Jet multiplicity**: Only events with at least two jets are selected, $N_{\text{jet}} \geq 2$.
- ***b*-jet multiplicity**: Events should contain at least one b-jet, $N_{\text{b-jet}} \geq 1$.

4.2.4 1ℓ+$2\tau_{\text{had}}$ channel

Events are selected by requiring exactly one light lepton (electron or muon) and exactly two hadronically decaying τ leptons. The lepton is required to pass *minimal baseline* selection as summarized in Table 4. A single lepton trigger (Table 3) is used to select the events. The light lepton is required to be matched to the trigger signature. The τ_{had} candidates are required to pass the selection of Table 7 and must be of opposite charge. Events must have at least two reconstructed jets. A veto on events containing b jets, corresponds to working point with an average efficiency of 77%, is applied. In order to suppress the V+jets background, the angular distance between the two τ_{had} candidates is required to be less than 2. The event selection is summarized in Table 16.

4.2.5 2ℓ+$2\tau_{\text{had}}$ channel

Events are selected by requiring exactly two light leptons (electron or muon) with opposite-sign and exactly two hadronic τs. The leptons and τ_{had} candidates are required to pass selection exactly the same like in 1ℓ+$2\tau_{\text{had}}$ section (4.2.4) In this channel, a single lepton or dilepton triggers (Table 3) are used to select the events. The light leptons are required to be matched to the trigger signature. Events must have at least one reconstructed jets. A veto on events containing b jets at 77% working point is applied.

4.2.6 2ℓSS+$1\tau_{\text{had}}$ channel

Events are selected by requiring exactly two light leptons (electron or muon) and exactly one hadronically decaying τ lepton. The leptons and τ_{had} candidate are required to pass selection exactly the same like in 1ℓ+$2\tau_{\text{had}}$ section (4.2.4). The τ_{had} candidate and light leptons must be of opposite charge. In this channel, a single lepton or dilepton triggers (Table 3) are used to select the events. The light leptons are required to be matched to the trigger signature. Events must have at least two reconstructed jets. A veto on events containing b jets, corresponds to working point with an average efficiency of 77%, is applied. The event selection is based on the signal region optimization study presented in Section G.

4.2.7 $\gamma\gamma + ML$channels

The categorizations of $\gamma\gamma + ML$ channels are preformed by means of the number of light lepton and τ_{had} of event.

- **Classification of events**: Events are classified to be 3 different regions.
  - **1ℓ + jets**: Events with one light lepton.
  - **1τ_{had} +jets**: Events with one hadronic tau.
  - **2*L***: Events with two leptons including $1\ell 1\tau$, $2\ell 0\tau$ and $0\ell 2\tau$ combinations.
- **Trigger**: Di-photon trigger with two reconstructed photons with E_{T} larger than 35 and 25 GeV.
- **2 tight isolated photons**: At least two tight isolated photons with $E_{\text{T}} > 35$ GeV for leading photon and $E_{\text{T}} > 25$ GeV for subleading photon. A further p_{T} selection recommended by the $H \to \gamma\gamma$ analysis is applied to photon candidates with $p_{\text{T}}/m_{\gamma\gamma} > 0.35$ (0.25) for the leading (subleading) photon.
- **Mass window**: The diphoton invariant mass is initially required to fall within a broad mass window of 105 GeV < $m_{\gamma\gamma}$ < 160 GeV.
- **b-veto**: Veto events with the b-tagging efficiency of 77%.
- **p_{T} of di-photon**: $p_{\text{T}} > 50$ GeV for all channels.
- **MET**: $MET > 35$ GeV for all channels expect for $1\mu 0\tau$ channel.

4.3 MVA strategies

Multivariate analysis techniques have been developed using Boost Decision Tree (BDT) in all channels to separate numerous backgrounds from signal. The K-fold Cross Validation (CV) method are employed in limited statistic channels 3ℓ, $\gamma\gamma + ML$ channels. Training variables, MVA performance etc are documented in the following sub-section.

4.3.1 2ℓSS channel

In 2ℓSS channel, 3 specific BDTs have been trained to target the 3 leading background processes, which corresponding to VV , V+jets and $t\bar{t}$ productions. The final discriminate is derived by training a combined BDT using the 3 specific BDTs as input. The boost algorithm are chosen as GradientBoost. The background specific BDTs are used to defined background enriched regions (Validation Regions and potential Control Regions) targeting the VV , V+jets and $t\bar{t}$ background separately.

The 4 BDTs have been trained with the following variables:

- $M_{\ell\ell}$: the invariant mass of the di-leptonic system
- M_{all}: the invariant mass of all selected objects
- $M_{\ell 0 j}$: the invariant mass of the leading and its closest jet

- $M_{\ell 1 j}$: the invariant mass of the subleading and its closest jet
- M^T_{W0} and M^T_{W1}: the W transverse mass using the leading and the subleading leptons.
- MET : Missing transverse energy
- η_0 and η_1: η of the leading and the subleading leptons
- $\Delta\eta$: absolute value of η_0-η_1
- Number of jets
- HT: Scalar sum of transversal impulsion for all objects
- HT_{lep}: Scalar sum of transversal momentum for leptons
- Dilep_type: =1 if $\mu\mu$, =2 if $e\mu$ or μe, =3 if ee
- $\Delta R_{min\ell 0 jets}$: Minimum distance between the leading lepton and its closest jet
- $\Delta R_{min\ell 1 jets}$: Minimum distance between the subleading lepton and its closest jet
- $\Delta R_{\ell\ell}$: Distance between the leading and the subleading leptons
- Total_charge: Sum of the charge of the leading and the subleading lepton. The total charge is specific to the VV BDT. In the 2LSS, VV background is mainly due to WZ events. Unlike the HH final state, a charge asymmetry is therefore expected in the VV final state.

Figures 5, 6 and 7 show the overtraining test of each background-against BDT. The final discriminating variable is the output of the combined one training with the 3 main background MC.

Both $t\bar{t}$ and W+jets processes mainly produce events with fake lepton, the fake lepton origination of $t\bar{t}$ is dominated by bjet decay while in W+jets case the light jet plays an important role. Z+jets produces 2/3 charge flip events and 1/3 fake events, consequently the variation of the kinematics of those three background are expected. The difference on the training input variables between Z+jets and W+jets may misleading the minimizing direction during the training process so that the separation of the model would not be appreciated. The lepton origination motivates us to train the specific BDTs that are sensitive to the lepton type, corresponds to prompt, fake, and QMisID. The kinematics of top separated variable $\Delta R_{\ell\ell}$ suggest to consider using both $t\bar{t}$ and W+jets process to train a fake-BDT and using Z+jets events to train a QmisID-BDT. Details can be found in appendices C.

4.3.2 3ℓ channel

Two derivatives from BDT, Gradient BDT (BDTG) and XGBOOST BDT have been implemented in 3ℓ channel The statistics of MC training samples in 3ℓ channel are limited. In order to make the use of full samples, k-fold cross validation[57] (k-CV) is introduced. 2-CV a.k.a odd-even training is used, which gives the best and smoothest receiver operating characteristic (ROC) curve. In this mode, MC samples with odd event number are trained, then the training results are applied to the samples with even event number, and vice versa. Labelled signal and background samples are mixed together and split into 2 folds. The training background samples including all the prompt backgrounds ($t\bar{t}V$, VV, tV, VH, VVV and $t\bar{t}H$) and data-driven fakes.

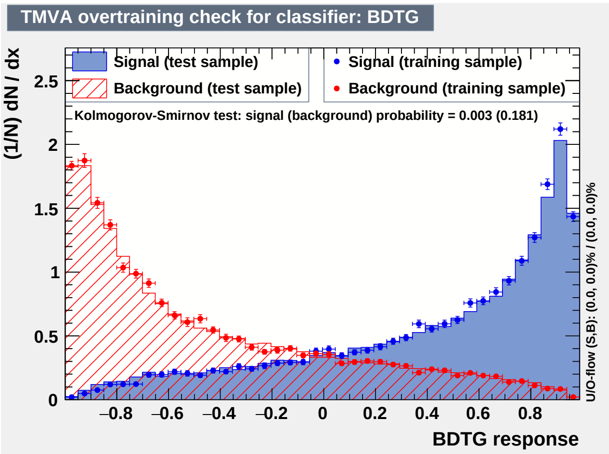

Figure 5: Discriminant output of VV VS HH training

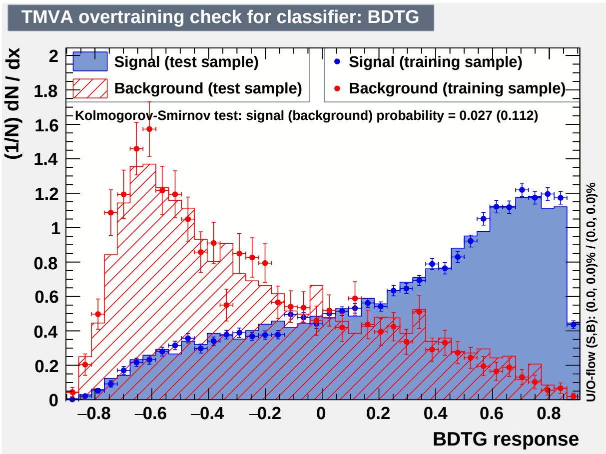

Figure 6: Discriminant output of $t\bar{t}$ VS HH training

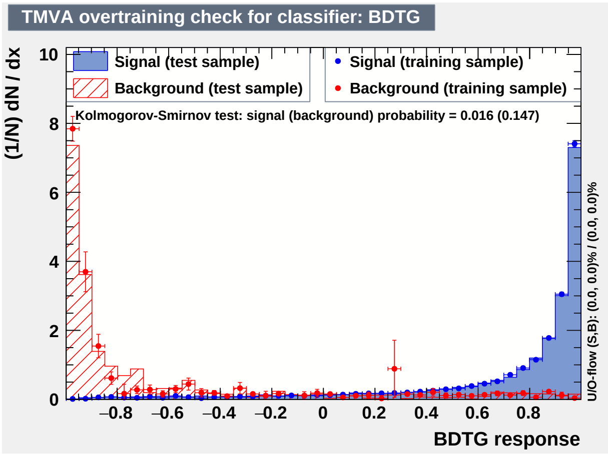

Figure 7: Discriminant output of V+jets VS HH training

The selected variables shown in FIGURE, are the most discriminant variables in the BDT training. [3]:

- $m_{ij} (i \neq j)$: invariant mass of any two of the trilepton system.
- ΔR_{ij}: distance between lepton i and lepton j.
- $\Delta R_{l_i j} (i = 1, 2, 3)$: distance between lepton i and the closest jet.
- $m_{l_i j} (i = 1, 2, 3)$: invariant mass of lepton i and the closest jet.
- m_{lll}: invariant mass of the three leptons.
- m_{llljj}: invariant mass of the three leptons and the leading and subleading jets.
- $m_{l_3 jj}$: invariant mass of lepton 3 and the leading and subleading jets.
- $\not{E}_T$: missing transverse energy.
- $p_T^{\ell(j)}$: transverse momentum of leptons and leading jet.

[3] Top 23 variables are selected by the rank of discriminant power in BDT training.

- $E^{\ell(j)}$: total energy of leptons and leading jet.
- N_{jets}: number of jets.
- FlavorCategory($l_1 l_2 l_3$): $\mu^{\mp}e^{\pm}e^{\pm}$, $e^{\mp}\mu^{\pm}\mu^{\pm}$, $e^{\mp}e^{\pm}\mu^{\pm}$, $\mu^{\mp}e^{\pm}\mu^{\pm}$, $e^{\mp}\mu^{\pm}e^{\pm}$, $\mu^{\mp}\mu^{\pm}e^{\pm}$, $e^{\mp}e^{\pm}e^{\pm}$, $\mu^{\mp}\mu^{\pm}\mu^{\pm}$.
- H_T: sum of transverse momentum of all visible objects.
- H_T^{ℓ}: sum of transverse momentum of all three leptons.
- $m_{ll}^{\text{Z-matched}}$: invariant mass of the OSSF lepton pair which is closer to the Z mass peak.

Their corresponding correlation matrix is presented in Figure 8.

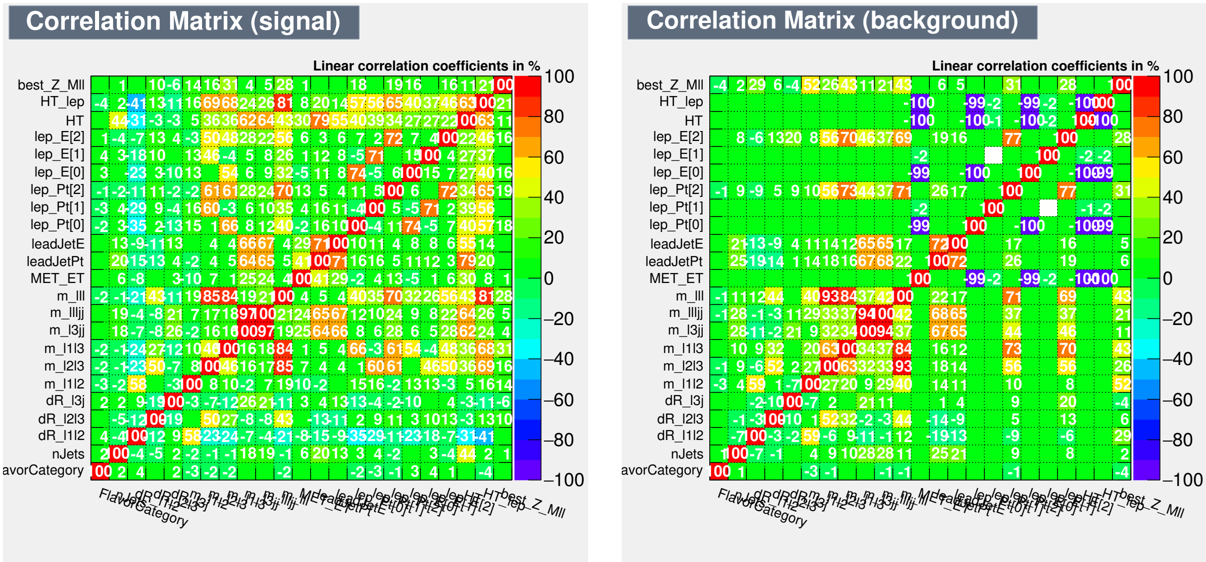

(a) (b)

Figure 8: The correlation matrix of MVA variables for signal and background samples.

[FIGURES to be added.]

For each fold, the training method stays the same (either BDTG or XGBOOST). For BDTG, the training parameters are listed as the following:

- Number of trees: 500
- Maximal depth of trees: 3
- Boost type: Gradient
- Bagged Boost is used. (Bagged sample fraction: 0.5)
- nCuts: 20

K-fold training results with BDTG method are summarized in Figure 9.

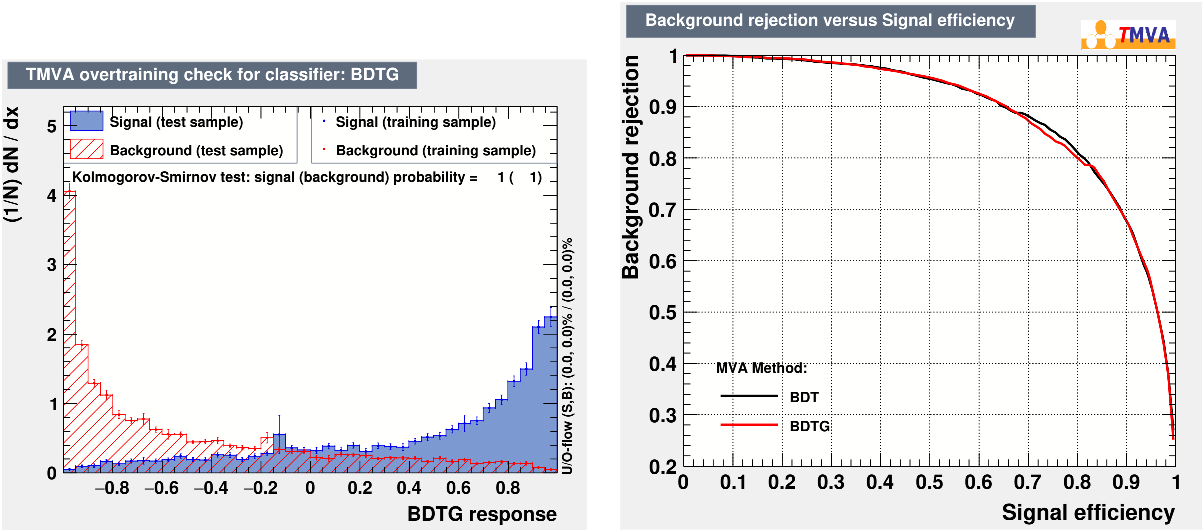

(a)

(b)

Figure 9: Training results of BDTG (*left*) in 3ℓ channel. BDT and BDTG methods show similar performances (*right*).

4.3.3 $b\bar{b}4\ell$ channel

The used variables for the BDT training are summarized in Table 10. The variables with the highest importance and separation power are listed in Table 11 and 12 respectively. Distributions of these input variables are shown in Figure 10.

Figure 10: Distributions of inputs for BDT training.

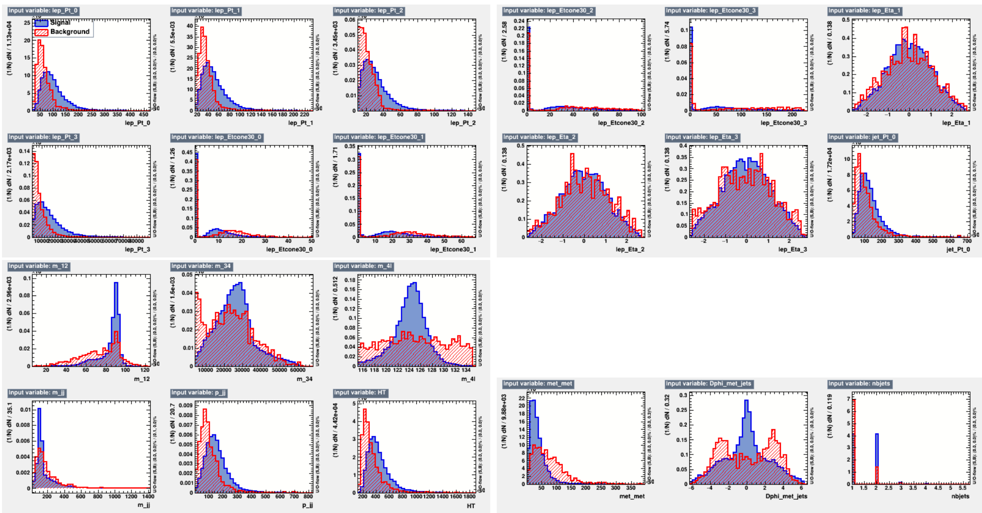

Events used for training is composed of randomly 90% of the total events from the signal and full backgrounds which pass the event selection. The rest of events are used for testing. The overtraining results is shown in Figure 164. More details about the setup of the training can be found in Appendix H. The overtraining result is shown in Figure 164 and the BDTG distribution of testing samples is well consistent

718 with the training samples, which indicates there is no obvious overtraining.

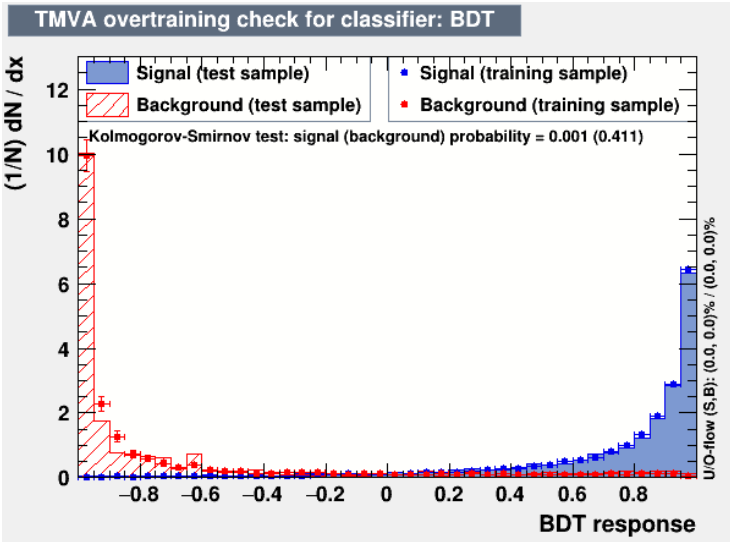

Figure 11: BDTG distributions from training and testing samples in $b\bar{b}4\ell$ channel.

Variables	Description
lep_Pt_*, lep_Etcone30_*, lep_Eta_*	p_T, $\sum_{\Delta R<0.3} E_T / E_T$, η of all the four leptons
jet_Pt_*	p_T of the two leading jets
m_12, m_34, m_4l, m_jj	Invariant mass of the leading lepton pair, sub-leading lepton pair, quadruplet and leading jet pair
p_jj	p_T of the leading jet pair
HT	Scalar sum of p_T of all the objects
met_met	Missing transverse energy
Dphi_met_jets	$\Delta\Phi$ of the MET and leading jets
nbjets	Number of b-jets

Table 10: Variables used as inputs for the BDT training in $b\bar{b}4\ell$.

4.3.4 τ channels

1ℓ+$2\tau_{\text{had}}$ The boosting algorithm employed is GradientBoost. A BDT discriminant is trained using nine variables, which are preselected from an initial pool of more than 30 variables. The variables are listed in Table 13 ranked according to their separation power to discriminate signal from background. Since the expected signal is too small as compared to the total background, several studies were performed to optimize the BDT as discussed in Appendix G.

The training is performed using VV and $t\bar{t}$ MC samples. The V+jets MC samples are not used in the training due to the large number of events with negative weights. Figure 12 shows the distributions of the input variables for signal and the background (sum of diboson and $t\bar{t}$). The selected events are split into two subsets with even and odd events based on their event number modulo 2. The BDTG is trained on odd events and tested on even events and vice-verse. The signal and background BDTG response distributions

Variables	Importance
m_41	5.996e-02
lep_Eta_1	5.602e-02
lep_Eta_2	5.585e-02
m_12	5.561e-02
met_met	5.213e-02
m_34	5.166e-02
lep_Eta_3	5.010e-02
Dphi_met_jets	4.987e-02
lep_Etcone30_3	4.773e-02
lep_Pt_3	4.697e-02
lep_Eta_0	4.671e-02
m_jj	4.603e-02
lep_Pt_0	4.417e-02
lep_Etcone30_0	4.361e-02
HT	4.203e-02
lep_Pt_2	3.954e-02
p_jj	3.948e-02
lep_Etcone30_2	3.918e-02
nbjets	3.861e-02
lep_Etcone30_1	3.504e-02
lep_Pt_1	3.410e-02
jet_Pt_0	2.559e-02

Table 11: Importance of the input variables in the BDT training.

for training and testing are shown in Figure 13. A good agreement between the training and test samples is observed, which indicates the absence of overtraining. Figure 13 also shows the background rejection versus signal efficiency so-called Receiver Operating Characteristic (ROC) curve for both even and odd events. The performance for both BDTs is same when training is performed on odd and even events. The correlation matrix between the input variables for both signal and background is shown in Figure 14. A high correlation of 73% is observed between $M(\ell_0,\ \text{jet})$ and min.$\Delta R(\ell_0,\ \text{jet})$ for signal, which is expected. For background, all the correlations are at 60% or lower.

TBD: The modeling of the BDT input variables will be checked in a dedicated control region to make sure they are well modeled by the MC simulation. Furthermore, a comparison of the input variable shapes for the fake τ_{had} between out-of-the-box MC simulation and data-driven estimation will also be checked. TODO: Results with training against VV background only. $t\bar{t}$ is not trained in the BDT as the impact on performance is negligible.

2ℓ+$2\tau_{\text{had}}$ channel The boosting algorithm employed is GradientBoost. A BDT discriminant is trained using eight variables The variables are listed in Table 14.
The BDTG is trained against VV and $t\bar{t}$ samples. Figure 15 shows the BDTG response distributions for training and testing with respect to signal and background, indicates the model is not over-trained. The ROC curves are shown for each of the fold and they are averaged to a red curve.

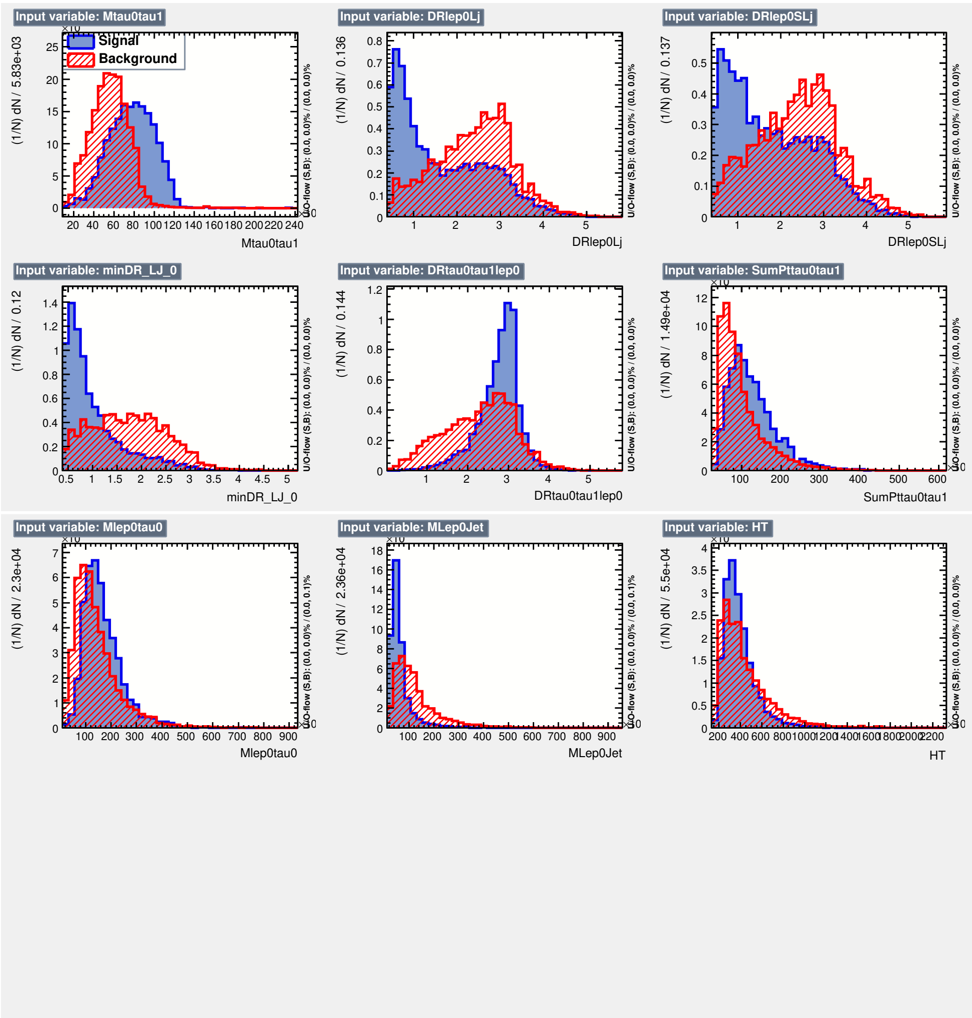

Figure 12: Signal (blue) and background (red) distributions of 9 input variables used in the BDTG training for $1\ell{+}2\tau_{\text{had}}$ Channels .

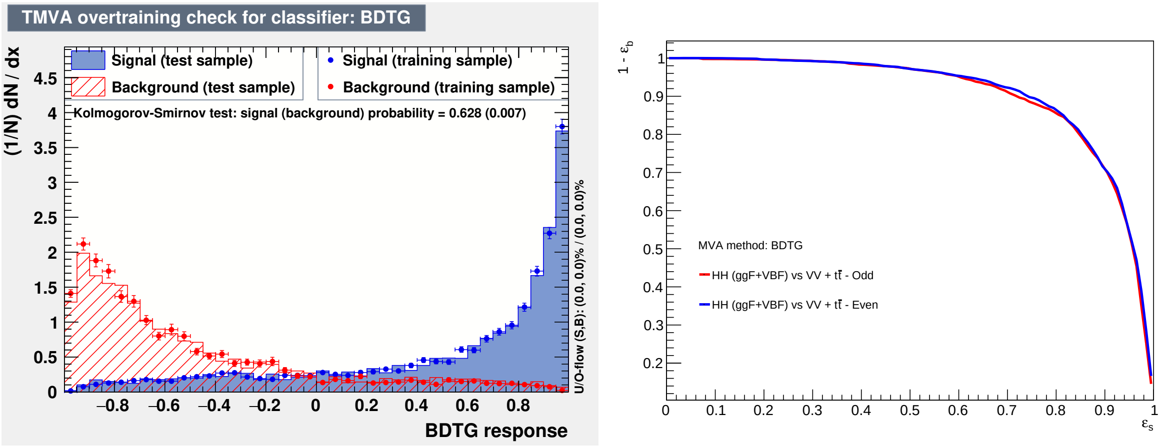

Figure 13: The BDTG distributions for the signal and background obtained during the training and testing (left) for 1ℓ+$2\tau_{\mathrm{had}}$ channel. The background rejection versus signal efficiency for both BDTs (right).

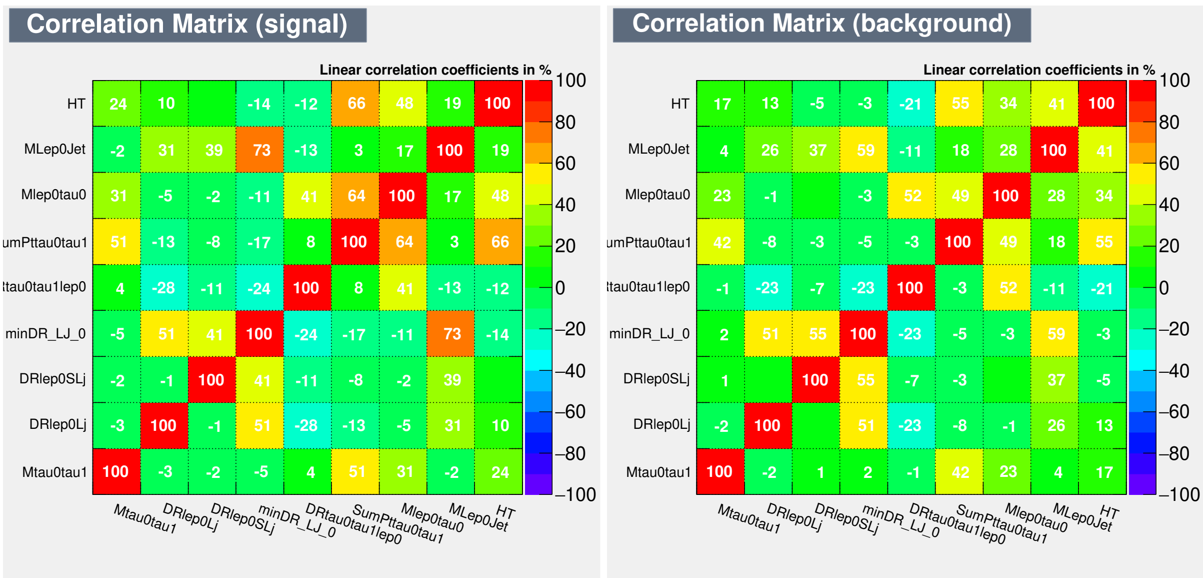

Figure 14: Correlation coefficients between the 9 BDTG input variables for signal (left) and background (right) for 1ℓ+$2\tau_{\mathrm{had}}$ channel.

Variables	Separation
lep_Pt_0	2.432e-01
lep_Pt_3	2.275e-01
m_41	2.235e-01
met met	2.131e-01
HT	1.941e-01
lep_Pt_1	1.924e-01
m_12	1.812e-01
lep_Pt_2	1.600e-01
p_jj	1.528e-01
lep_Etcone30_3	1.331e-01
nbjets	1.227e-01
lep_Etcone30_0	1.165e-01
Dphi_met_jets	1.062e-01
lep_Etcone30_1	9.586e-02
jet_Pt_0	9.547e-02
lep_Etcone30_2	7.792e-02
m_34	6.869e-02
m_jj	6.680e-02
lep_Eta_3	2.084e-02
lep_Eta_2	1.970e-02
lep_Eta 1	1.474e-02
lep_Eta_0	9.422e-03

Table 12: Separation power of the input variables in the BDT training in $b\bar{b}4\ell$ channel.

2ℓSS+1τ_{had} channel In this discussed channel the diboson background is dominant. To perform better separation boosted decision tree (BDT) methods are developed. The boosting algorithms employed are Adaptive Boost and Gradient Boost. A BDTs are trained on the selected events using the 14 variables, which are preselected from an initial pool of more than 144 variables. The variables are listed in Table 15 ranked according to their separation power to discriminate signal from background.

The training is performed using k-fold method with 6 folds over signal and dominant backgrounds sample. The distributions of the input variables for signal and background are shows in Figure 16.The signal and background BDT response distributions for training and testing are shown in Figure 17. A good agreement between the training and test samples indicating the absence of overtraining. Figure 18 shows the background rejection versus signal efficiency so-called Receiver Operating Characteristic (ROC) curve for two BDT methods. The performance for both BDTs is almost the same with a slight advantage on BDTG so BDT with Gradient Boost will be used for the studies. A high correlation of 66% is observed between $M(\ell_1,\ \mathrm{jet}_{\mathrm{leading}},\ \mathrm{jet}_{\mathrm{sub-leading}})$,$M(\ell_1,\ \mathrm{jet}_{\mathrm{leading}})$ and $M(\ell_0,\ \mathrm{closet-jet})$, $\Delta R(\ell_0,\ \mathrm{closet\ jet})$ for signal and background, which is expected. All correlations are shown on the correlation matrix Figure 19 between the input variables for both signal and background. The differences between the correlations are found to be consistent between signal and background.

Variable	Description	Rank	Separation power
min.$\Delta R(\ell_0,\ \text{jet})$	Minimum distance between lepton and it's closest jet	1	25.37%
$M(\tau_{\text{had}0},\ \tau_{\text{had}1})$	Ditau invariant mass	2	24.29%
$M(\ell_0,\ \text{jet})$	Invariant mass of lepton and it's closest jet	3	24.09%
$\Delta R(\ell_0,\ \text{lead jet})$	Distance between lepton and leading jet	4	15.82%
$\Delta R(\ell_0,\ \tau_{\text{had}0}\tau_{\text{had}1})$	Distance between lepton and ditaus	5	15.61%
$\Delta R(\ell_0,\ \text{Sublead jet})$	Distance between lepton and sub-leading jet	6	10.94%
Sum $p_T(\tau_{\text{had}0},\ \tau_{\text{had}1})$	Sum of ditau transverse momenta	7	10.50%
$M(\ell_0,\ \tau_{\text{had}0})$	Invariant mass of lepton and leading τ_{had}	8	7.98%
HT	Scalar sum of all jets p_T	9	5.02%

Table 13: Variables used in the multivariate analysis for 1ℓ+$2\tau_{\text{had}}$ channel.

Variable	Description
$M(\tau_{\text{had}0},\ \tau_{\text{had}1})$	Ditau invariant mass
$M(\ell_0,\ \ell_1)$	Di-lepton invariant mass
$\Delta R(\ell_0,\ \ell_1)$	Distance between two leptons
$p_T(\tau_{\text{had}0})$	Leading tau p_T
$\Delta R(\ell_1,\ \tau_{\text{had}1})$	Distance between subleading lepton and subleading tau
$p_T(\tau_{\text{had}1})$	Subleading tau p_T
HT	Scalar sum of all jets p_T
MET	Missing transverse momentum

Table 14: Variables used in the multivariate analysis for 2ℓ+$2\tau_{\text{had}}$ channel.

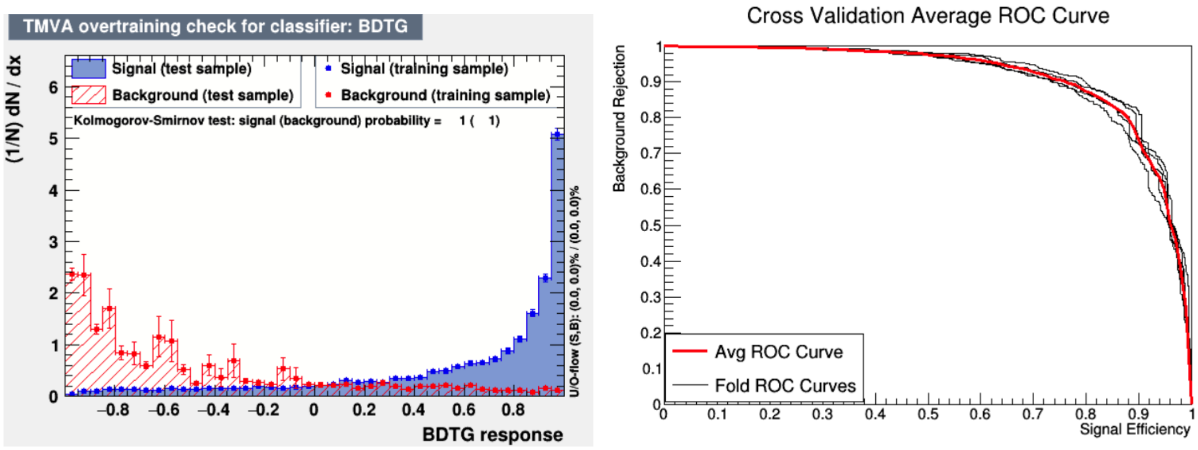

Figure 15: The BDTG distributions for the signal and background obtained during the training and testing (left). The background rejection versus signal efficiency for BDTs of each folds and the averaged one (right) ROC integration of each folds: 0.92, 0.90, 0.92, 0.91, 0.91, average: 0.914.

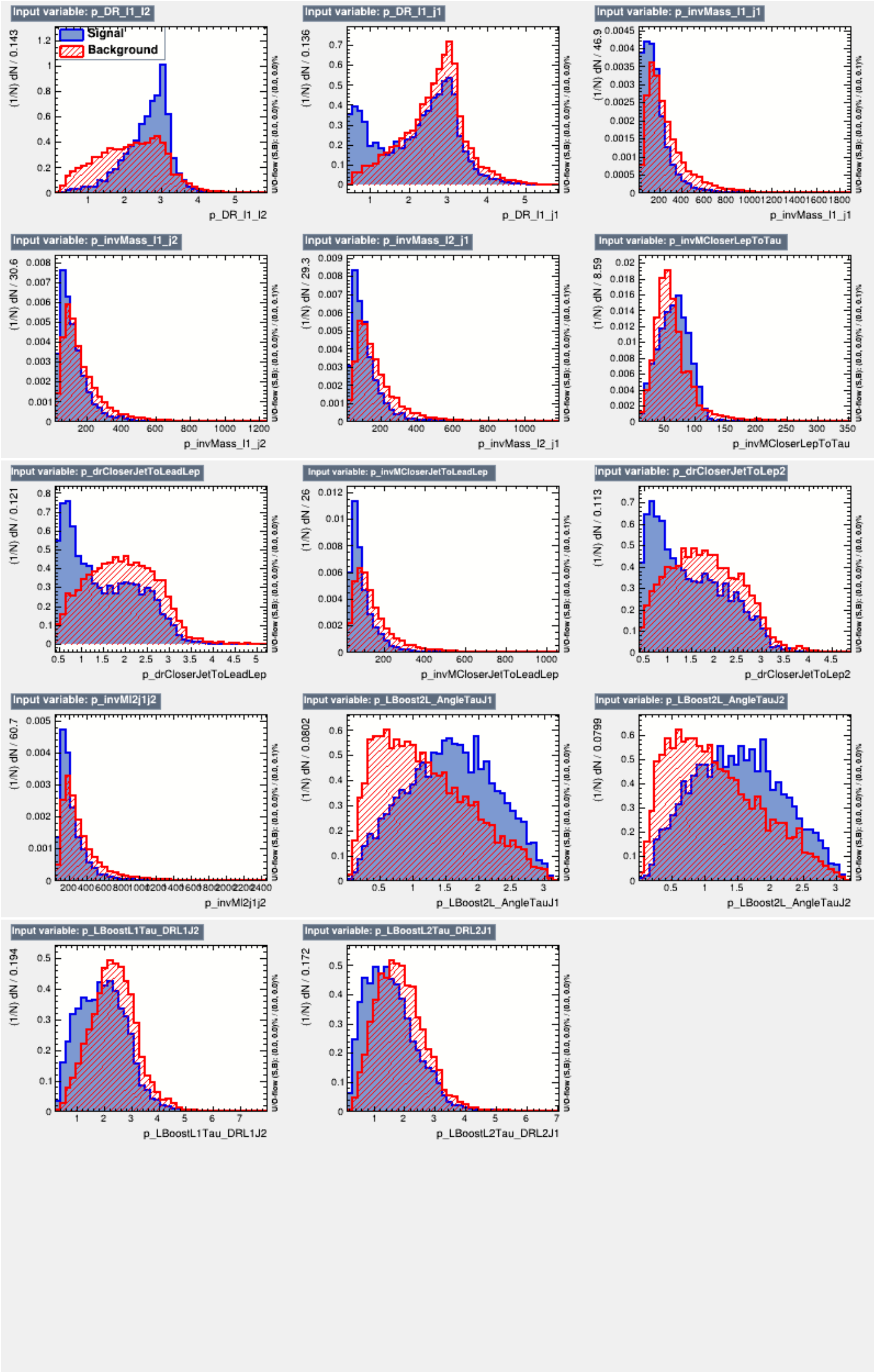

Figure 16: Signal (blue) and background (red) distributions of 14 input variables used in the BDT training for $2\ell SS{+}1\tau_{\text{had}}$ channel.

Variable	Description	Rank	Separation power
$\Delta R(\ell_0,\ \ell_1)$	Distance between leading and sub-leading leptons	1	12.77%
$M(\ell_0,\ \text{jet}_{\text{leading}})$	Invariant mass of leading lepton and leading jet	2	11.23%
$M(\ell_0,\ \text{closet}-\text{jet})$	Invariant mass of leading lepton and it's closet jet	3	11.16%
$\Delta R(\ell_0,\ \text{closet jet})$	Distance between leading lepton and it's closet jet	4	10.14%
$\Delta R(\ell_0,\ \text{jet}_{\text{leading}})$	Distance between leading lepton and leading jet	5	8.98%
$M(\ell_1,\ \text{jet}_{\text{leading}})$	Invariant mass of sub-leading lepton and leading jet	6	8.95%
$\Theta(boost\ell_0, \ell_1,\ \tau_{\text{had}}, \text{jet}_{\text{leading}})$	Angle between tau and leading jet after lorentz boost to two leading leptons system	7	8.65%
$M(\ell_1,\ \text{jet}_{\text{leading}},\ \text{jet}_{\text{sub-leading}})$	Invariant mass of sub-leading lepton, leading and sub-leading jets	8	7.55%
$\Theta(boost\ell_0, \ell_1,\ \tau_{\text{had}}, \text{jet}_{\text{sub-leading}})$	Angle between tau and sub-leading jet after lorentz boost to two leading leptons system	9	7.05%
$\Delta R(\ell_1,\ \text{closet jet})$	Distance between sub-leading lepton and it's closet jet	10	6.7%
$\Delta R(boost\ell_0,\ \tau_{\text{had}}, \ell 0, \text{jet}_{\text{sub-leading}})$	Distance between leading lepton and sub-leading jet after lorentz boost to tau and leading leptons system	11	6.25%
$M(\ \tau_{\text{had}}, \ell closet)$	Invariant mass of tau and it's closet lep	12	5.84%
$M(\ell_0,\ \text{jet}_{\text{sub-leading}})$	Invariant mass of leading lepton and sub-leading jet	13	5.83%
$\Delta R(boost\ell_1,\ \tau_{\text{had}}, \ell 1, \text{jet}_{\text{leading}})$	Distance betwee sub-leading lepton and leading jet after lorentz boost to tau and sub-leading leptons system	14	5.7%

Table 15: Variables used in the multivariate analysis for 2ℓSS+$1\tau_{\text{had}}$ channel.

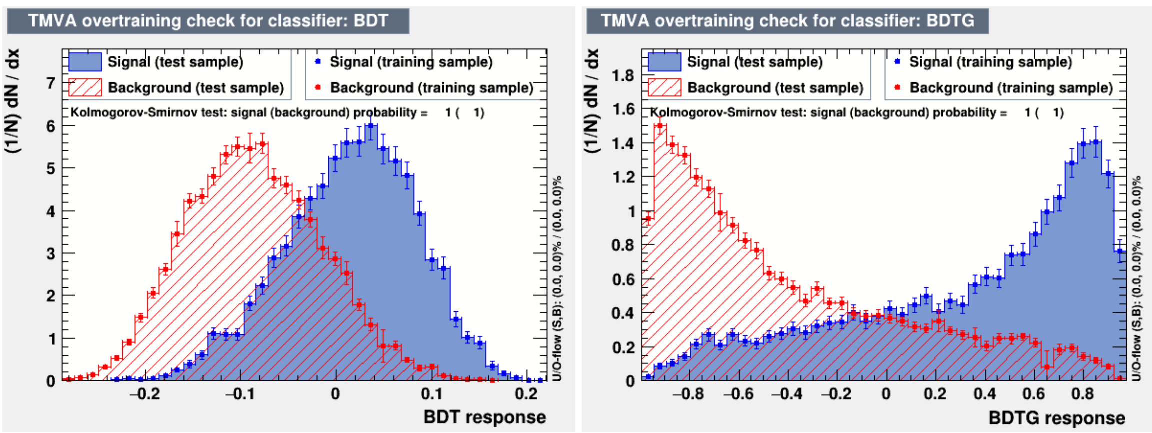

Figure 17: The BDT distributions for the signal and background obtained during the training and testing for 2ℓSS+$1\tau_{\text{had}}$ channel.

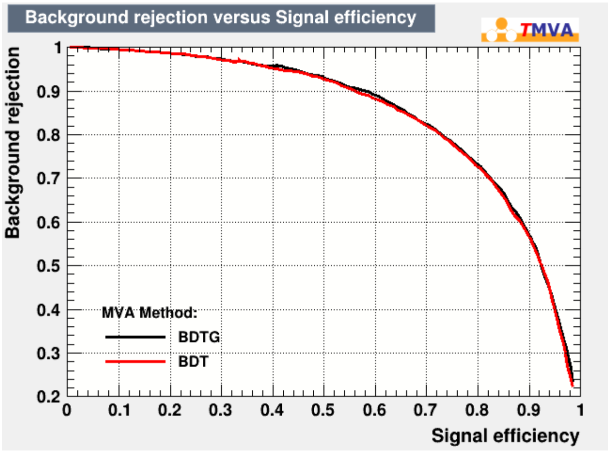

Figure 18: The background rejection versus signal efficiency for both BDTs for 2ℓSS+$1\tau_{\mathrm{had}}$ channel.

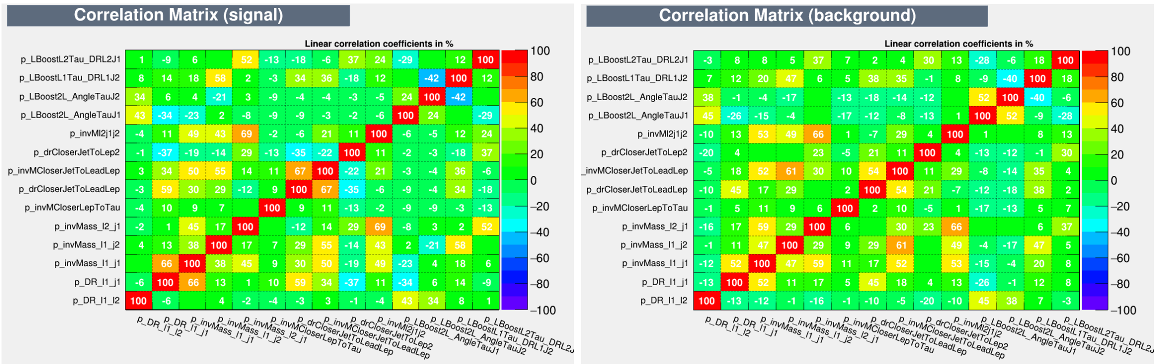

Figure 19: Correlation coefficients between the 14 BDT input variables for signal (left) and background (right) for 2ℓSS+$1\tau_{\mathrm{had}}$ channel.

4.3.5 $\gamma\gamma + ML$ channels

Multiple discriminating variables separating signal and background are chosen as inputs for the BDT training. The BDT output, which reflects an optimal combination of these input, is used to define the signal regions to have a good significance.

In order to improve this sensitivity with limited MC statistics, 4-CV training is used, which gives a better and smoother receiver operating characteristic (ROC) curve. The training sample and test sample are separated by the event number which is reproducible for each simulation events. As MC samples are splitter by event number, it is possible to trace back the source fold of the training. Variables regarding different objects of the physics topology of $H \to \gamma\gamma$ and $H \to WW/ZZ/\tau\tau$, are constructed and listed below.

Following variables are used for $\gamma\gamma$+ℓj BDTG training:

- $p_{\mathrm{T}}(H)$: transverse momentum of H.
- $\phi(\ell)$: ϕ of lepton.

- $p_{\mathrm{T}}(\ell)$: transverse momentum of lepton.
- E_T^{miss}: missing transverse momentum.
- $\phi(\gamma_1)$: ϕ of the leading γ.
- N_{jcen}: number of central jets.
- $\min\Delta\Phi(E_T^{\mathrm{miss}}, j, \ell)$: minimum polar angle difference between E_T^{miss}, jets and the lepton.
- $\Delta\Phi(E_T^{\mathrm{miss}}, \gamma\gamma)$: polar angle difference between E_T^{miss} and di-photon system.
- $\Delta R(\ell\nu)$: angle difference between ℓ and E_T^{miss} system.
- $\Delta R(\gamma\gamma, W)$: angle difference between $\gamma\gamma$ and W system.
- $\eta(W)$: η of W.

Following variables are used for $\gamma\gamma$+$\tau_{\mathrm{had}}j$ BDTG training:

- $p_{\mathrm{T}}(H)$: transverse momentum of H.
- $\phi(\ell)$: ϕ of lepton.
- $p_{\mathrm{T}}(\ell)$: transverse momentum of lepton.
- E_T^{miss}: missing transverse momentum.
- N_{jcen}: number of central jets.
- $\phi(\gamma_1)$: ϕ of the leading γ.
- $\eta(\gamma_1)$: η of the leading γ.
- $\Delta\Phi(E_T^{\mathrm{miss}}, \gamma\gamma)$: polar angle difference between E_T^{miss} and di-photon system.

Following variables are used for $\gamma\gamma$+2L (include $1\ell1\tau_{\mathrm{had}}$, $2\ell0\tau_{\mathrm{had}}$ and $0\ell2\tau_{\mathrm{had}}$) BDTG training:

- $p_{\mathrm{T}}(H)$: transverse momentum of H
- $\phi(H)$: ϕ of H.
- $\phi(\ell_1)$: ϕ of leading lepton.
- $p_{\mathrm{T}}(\ell_1)$: transverse momentum of the leading lepton.
- $p_{\mathrm{T}}(\ell_2)$: transverse momentum of the subleading lepton.
- E_T^{miss}: missing transverse momentum.
- N_{jcen}: number of central jets.
- $\Delta\Phi(E_T^{\mathrm{miss}}, \gamma\gamma)$: polar angle difference between E_T^{miss} and di-photon system.
- $\Delta\Phi(E_T^{\mathrm{miss}}, \ell\ell)$: polar angle difference between E_T^{miss} and di-lepton system.
- $\Delta m(\ell, \ell)$: mass of di-lepton system.
- $\Delta R(\ell, \ell)$: angular difference between two leptons.
- $\Delta\phi(\ell, \ell)$: polar angle difference between two leptons.

- $\Delta R(\ell\ell, \gamma\gamma)$: angular difference between di-lepton system and di-photon system.
- $\Delta R(\ell\nu)$: angle difference between ℓ and E_T^{miss} system.
- $\min\Delta\Phi(E_T^{\text{miss}}, j, \ell)$: minimum polar angle difference between E_T^{miss}, jets and the lepton.
- $pt(j_1)$: transverse momentum of leading jet.

For each fold, the training method stays the same and for BDTG, the training parameters are listed as the following:

- Number of trees: 1000
- Maximal depth of trees: 2
- Boost type: Gradient
- Bagged Boost is used. (Bagged sample fraction: 0.5)
- nCuts: 20

The 4-fold training results for $\gamma\gamma$+2L with BDTG method is summarized in Figure 20. Other 2 channels can be found in Appendix F, 152, 153.

4.4 Signal regions

After filtering out events using the selections described in Section 4.2 and training the multivariate models (Section 4.3), the signal region of each channel is optimized based on its analysis strategy accordingly. The definition of signal region used in the final fit are presented in this section, the summary table of all signal region selections can be seen in Table 16.

In 2ℓSS channel the signal region is defined by means of cutting on the combined BDT. The boundary value is determined by maximizing the medium significance of the BDT distribution. Other three dimensional BDT_{VV} , $BDT_{t\bar{t}}$ and BDT_{V+jets} are primarily proposed to design dedicated validation region (VR) in order to validate MC prediction, which should be an orthogonal region contains a negligible amount of signal events and is not used in the final fit. The

The signal region in 3ℓ channel uses the high BDT and the low BDT region is treated as VR. In $b\bar{b}4\ell$ and τ channels the region of BDTG output after pre-MVA selection is defined as signal region.

TODO: In τ channel ...

In $\gamma\gamma + ML$ channel, three optimal value of the BDT cut can be obtained by maximizing the expected significance, using the equation as below,

$$Z = \sqrt{2 \times \left[(B + S) \times \left(ln \frac{S + B}{B} - S \right) \right]} \tag{3}$$

Consequently three regions are defined, where the lowest one is used as background control region, other two are signal regions. As in $\gamma\gamma$+ℓj channel the interval of BDTG ≤ 0 is regarded as control region, and $0 <$ BDTG ≤ 0.6, $0.6 <$ BDTG are signal regions.

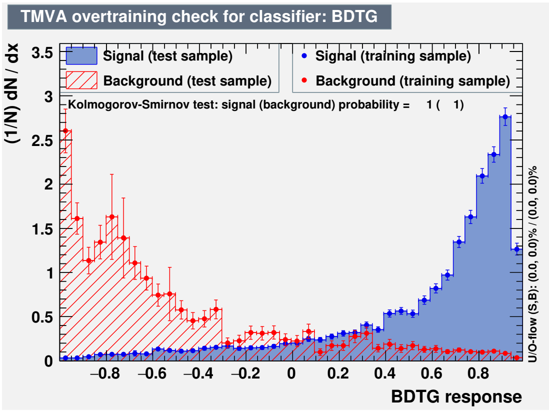

(a)

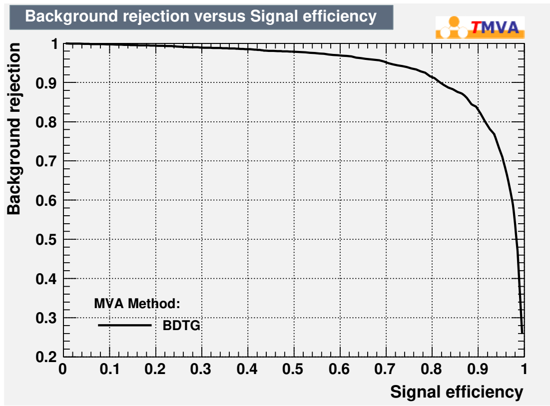

(b)

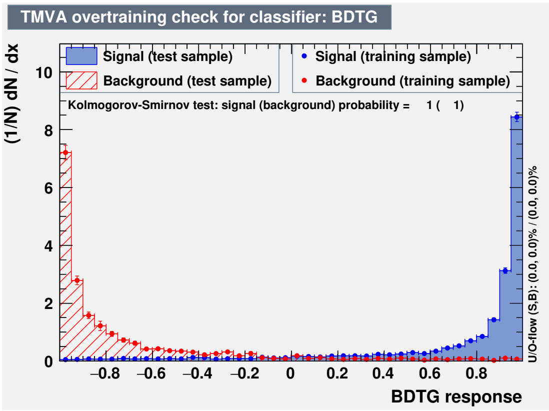

(c)

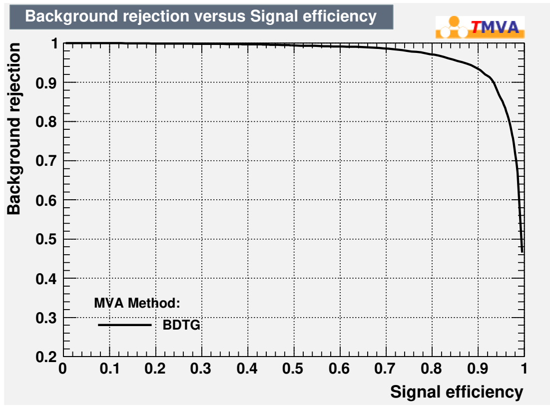

(d)

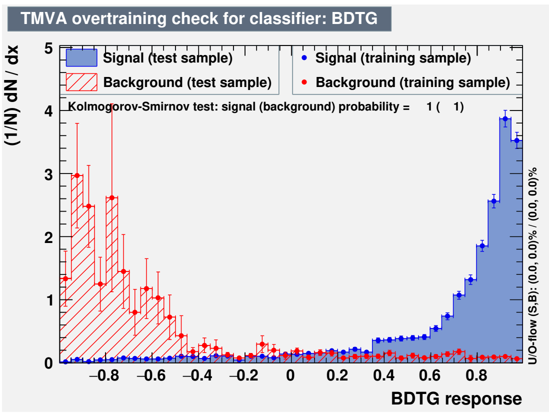

(e)

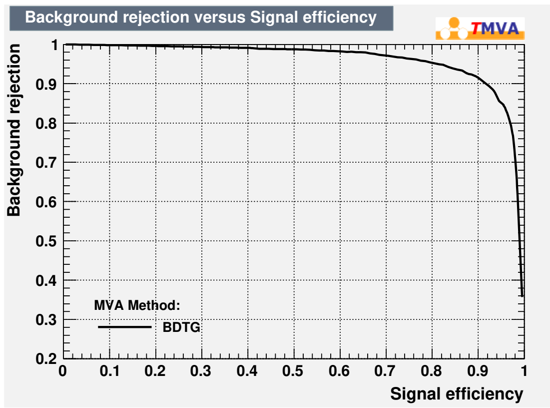

(f)

Figure 20: Training results for $\gamma\gamma$+2L channel (Include $1\ell 1\tau$, $2\ell 0\tau$ and $0\ell 2\tau$). Plot(a)(c)(e) shows the overtraining plots with ks test values in fold1 for $1\ell 1\tau$, $2\ell 0\tau$ and $0\ell 2\tau$ channel respectively. Plot(b)(d)(f) presents the background rejection as a function of the signal efficiency when requiring various BDT output thresholds for $1\ell 1\tau$, $2\ell 0\tau$ and $0\ell 2\tau$ separately.

Channels	Selections
2ℓSS	Two same-sign T leptons, $p_{\mathrm{T}} \geq 20$ GeV $N_{\mathrm{jets}} \geq 2$ and $N_{b-\mathrm{jets}} == 0$ $m_{\ell\ell} > 12$ GeV
3ℓ	One L lepton with leading $p_{\mathrm{T}} \geq 10$ GeVand two T leptons with $p_{\mathrm{T}} > 15$ GeV total electric charge of ±1. $N_{\mathrm{jets}} \geq 1$ and $N_{b-\mathrm{jets}} == 0$ $m_{\ell\ell} > 12$GeVand $\|m_{\ell\ell} > 91.2$GeV$\| > 10$GeV for all SFOS pairs $m_{\ell\ell\ell} > 12$GeV
$b\bar{b}4\ell$	Two leading B leptons and two subleading T leptons, $p_T^1 \geq 20$ GeV, $p_T^2 \geq 15$ GeV, $p_T^3 \geq 10$ GeV $\Delta R < 0.1$ to any lepton pairs $m_{\ell\ell} > 5$ GeVfor OSSF pairs. $N_{\mathrm{jets}} \geq 2$ and $N_{b-\mathrm{jets}} \geq 1$ 107 GeV< $M_{4\ell} < 133$ GeV
1ℓ+$2\tau_{\mathrm{had}}$	exactly one L lepton exactly two RNN medium τ_{had} with opposite-sign $\Delta_{R(\tau_0,\tau_1)} \leq 2$ $N_{\mathrm{jets}} \geq 2$ and $N_{b-\mathrm{jets}} == 0$
2ℓ+$2\tau_{\mathrm{had}}$	exactly two L leptons with opposite-sign exactly two RNN medium τ_{had} of opposite charge Z-veto $\Delta_{R(\tau_0,\tau_1)} \leq 2$ $N_{\mathrm{jets}} \geq 1$ and $N_{b-\mathrm{jets}} == 0$
2ℓSS+$1\tau_{\mathrm{had}}$	Two same-sign T leptons, $p_{\mathrm{T}} \geq 20$ GeV $N_{\mathrm{jets}} \geq 2$ and $N_{b-\mathrm{jets}} == 0$ exactly one RNN medium τ_{had} with $p_{\mathrm{T}} \geq$25 GeV opposite tau charge to leptons
$\gamma\gamma + ML$common selections	2 tight isolated photons with $p_{\mathrm{T}} > 35$ GeV and $p_{\mathrm{T}} > 25$ GeV for leading and sub-leading $p_{\mathrm{T}}/m_{\gamma\gamma} > 0.35$ (0.25) for the leading (subleading) photon 105 GeV < $m_{\gamma\gamma}$ < 160 GeV b-veto $MET > 35$ GeV except $1\mu + 0\tau_{\mathrm{had}}$ channel $p_{\mathrm{T}} > 50$ GeV

Table 16: Selection criteria applied to each channel to form the signal regions.

5 The analysis of two Same Signed Lepton

5.1 Overview

This section presents the analysis of non-resonant di-Higgs with a signature of two same-sign leptons and absence of b-jet, which strongly suppresses the SM, such as QCD and $t\bar{t}$ backgrounds, etc. In this signature only light leptons, e, μ are considered. Previous di-Higgs search in ATLAS using this signature forces two Higgs from pair production decay to $W^{\pm}W^{\mp}$. In this analysis using 139 fb^{-1} of pp collision data, as well as $W^{\pm}W^{\mp}$, decay modes $Z^{\pm}Z^{\mp}$ and $\tau\tau$ of Higgs are also taken into account, which brings 30% more signal yields at the same luminosity level.

To improve the significance of the channel with such a low branch ratio, a multivariate discriminant analysis is performed to optimize the separation of signal and background. The main backgrounds, dominated by diboson due to the absence of b-jet, and non-prompt leptons, usually happened in a two sign-same leptons final state, are modeled in dedicated control regions.

5.2 Signal region

For the 2ℓSS channel, the pre-selection defined in Section 4.2.1 are used to determine the signal region. To ensure a good sensitivity to the di-Higgs signals, the SR is optimized by mean of multivariate techniques. 3 specific BDTs are trained respectively against VV, $t\bar{t}$ and V+jets samples. Therefore a BDT combining the 3 individual BDTs is purposed as the final discriminant. The relative process of multivariate analysis is given in Section 4.3.1. The final signal region is determined using the high BDT region of the combined BDT, thus the low BDT region is used to design the validation region. The boundary is obtained by maximizing the expected significance.

5.3 Background estimation

After pre-selection the background source for 2LSS channel can be classified into two categories, irreducible background and reducible background. The irreducible background includes events where all lepton candidates are prompt leptons or are decayed from τ. The reducible background contains events where at least one of the candidate leptons is not prompt (including charge misidentified (QmisID) leptons and fake leptons). In the irreducible background category, the prompt leptons are mainly from VV process, $tV, ttV, t\bar{t}H$ and VH, where V stands for W or Z bosons. They are predicted by MC simulation only. Those ingredient are illustrated in Figure 21,corresponding to low BDT bins after pre-selection, by cutting on $BDT_{All} < -0.4$. Plots of more variables can be found in Appendices C.1. The discrepancy between data and pure MC simulation indicates that QmisID and fakes leptons are not well modeled by MC simulation, so data-driven estimations are needed to describe these two background types.

The control regions defined in this channel are to model the fake backgrounds from different origins: QED conversions, material conversion electrons, and heavy flavour leptons. In template fit method, 5 control regions are created especially to highlight these backgrounds. Additionally, two CRs for diboson background, checking the modeling of WZ process and $W^{\pm}W^{\pm}$ are being developed.

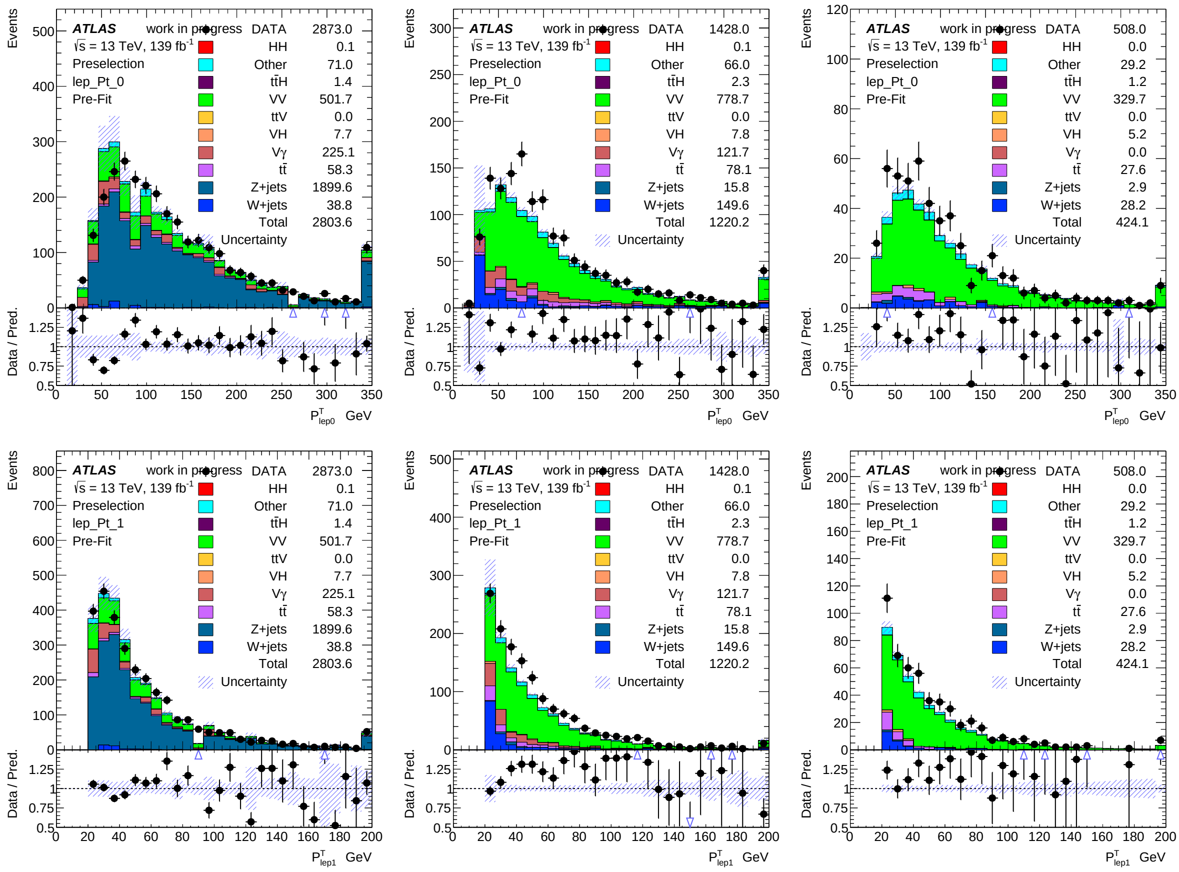

Figure 21: The distribution of leading lepton p_T and sub-leading lepton p_T for N_{jets} = 2 at pre-selection level. Left: $e^{\pm}e^{\pm}$, middle $e^{\pm}\mu^{\pm}$ OR $\mu^{\pm}e^{\pm}$, right $\mu^{\pm}\mu^{\pm}$.

5.3.1 QmisID background estimation

Charge-flip events originate mainly from Z+jets, di-boson and $t\bar{t}$ processes. These events pollute ee and $e\mu$ regions because of one electron having hard bremsstrahlung plus asymmetric conversion ($e^{\pm} \to e^{\pm}\gamma^{*} \to e^{\pm}e^{+}e^{-}$) or a wrongly measured track curve. Muon charge-flip is negligible in in the p_{T} range relevant to this analysis. A dedicated tool to reduce electron charge flip is used (ref to ECID cut).

The rate of electron charge flips is measured from the data, based on the measured ratio of $Z \to e^{+}e^{-}$ that are reconstructed as a same-sign electron pair ($e^{+}e^{+}$ or $e^{-}e^{-}$). For this, a likelihood-based method has been developed to provide the charge flip rates, $\epsilon_{\text{mis id}}$, as a function of the electron $|\eta|$ and p_{T}, as shown in Fig. 22. Sources of systematical uncertainties on $\epsilon_{\text{mis id}}$ are summarized as follows:

- The statistical uncertainty from the likelihood method $\sigma_{\epsilon}^{\text{likelihood}}(|\eta|, p_{\mathrm{T}})$.
- The difference between rates measured with the likelihood method and truth-matching with simulated $Z \to e^{+}e^{-}$ events.
- The variation of the rates with the definition of the di-lepton invariant mass region, defining the Z-peak, and its sidebands which are used to subtract the contamination from non-prompt leptons.

The values of the total systematic uncertainties are shown in Fig. 23 for tight and anti-tight electrons.

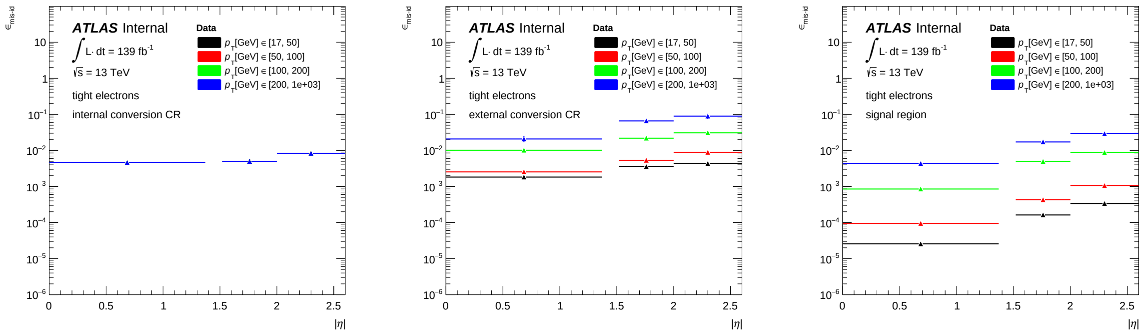

Figure 22: Electron charge-flip rates derived from the data with the likelihood method. The rates are presented as a function of $|\eta|$, parameterized in p_T for (a) internal-conversion (b) external-conversion and (c) prompt candidates.

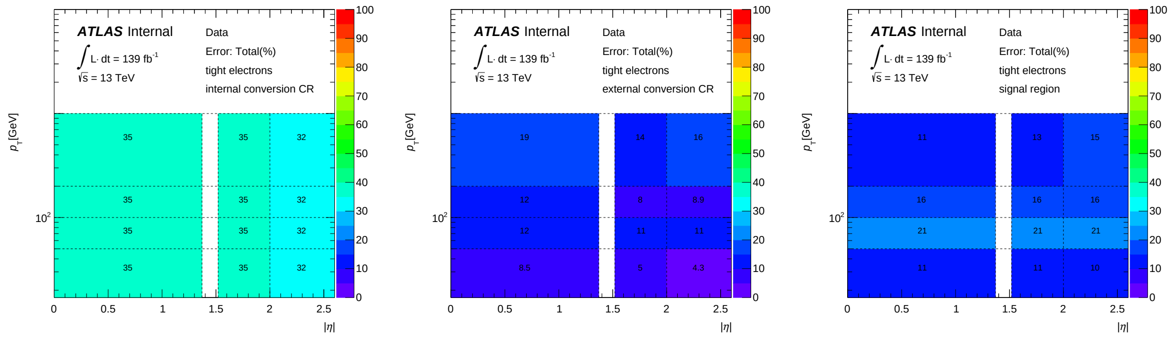

Figure 23: Total relative systematic uncertainty (in %) on the cha rge-flip rate in bins of $|\eta|$ and p_T for (a) internal-conversion (b) external-conversion and (c) prompt electron candidates.

Event yields with charge flip electrons are obtained by weighing pre-selected events but asking for opposite-sign lepton instead of same-sign. The event weights (w_{QmisID}) are defined as: with the expression:

$$w_{QmisID} = \frac{\epsilon_{\text{mis id},1} + \epsilon_{\text{mis id},2} - 2\epsilon_{\text{mis id},1}\epsilon_{\text{mis id},2}}{1 - (\epsilon_{\text{mis id},1} + \epsilon_{\text{mis id},2} - 2\epsilon_{\text{mis id},1}\epsilon_{\text{mis id},2})} \tag{4}$$

where $\epsilon_{\text{mis id},1}(1-\epsilon_{\text{mis id},2}) + \epsilon_{\text{mis id},2}(1-\epsilon_{\text{mis id},1}) = \epsilon_{\text{mis id},1} + \epsilon_{\text{mis id},2} - 2\epsilon_{\text{mis id},1}\epsilon_{\text{mis id},2}$ is the rate of events in which exactly one electron is reconstructed with charge flip. In order to account for the strong dependence of the rates to the p_T and to improve the modeling of the kinematical observables, p_T continuous rates are used. Details can be found in appendices C.

5.3.2 Fake light lepton background estimation

The fake leptons represent an important background in 2LSS channel in spite of a very tight lepton definition. Events originate from non-prompt and fake backgrounds can also contribute to same-sign lepton final state. In this document non-prompt and fake leptons form the fake background.
Non-prompt leptons arise mainly from heavy-flavor hadron decays (b or c hadrons), they are real leptons but not from primary interaction point. In addition, it may originate from photon conversion or hadronic jet misidentified as prompt charged leptons, making the fake leptons consisting of multiple components. Simulating each process which leads to a fake lepton is not reliable and precise in MC samples, leading to a challenging estimation on fake background. For this reason, data-driven method is necessary to make a reasonable fake estimation. In this analysis, $t\bar{t}$ and $W + jets$ are main processes providing fake leptons. A semi-data-driven method, template fit method and a data-driven method fake factor method are studied to estimate the fake backgrounds. They are presented in the following section.

Template fit method The template fit method is a semi-data-driven method based on a simultaneous fit using all processes contributing to background and Data. In this part, all backgrounds except charge miss-assignments events are extracted from MC simulation. QmiID candidates are extracted from data driven method as introduced in section A.1.1. Five control regions have been defined in order to estimate the four following normalization factors left as free-floating in the fit:

- NF^{Conv}: Normalization factor applied to events from material conversions
- NF^{QED}: Normalization factor applied to events from QED processes
- NF$_e^{HF}$: Normalization factor applied to non-prompt electrons from heavy flavour decays
- NF$_\mu^{HF}$: Normalization factor applied to non-prompt muons from heavy flavour decays

The method is more detailed in the appendix A.1.1. The following distributions are exploited to best discriminate among the NFs in the simultaneous template fit:

- ΔR_{ll} in $\mu e + ee$ channel with exactly 1 b-jet, to estimate NF_e^{HF}
- HT_{lep} in $e\mu + \mu\mu$ channel, to estimate NF_μ^{HF}
- HT_{lep} in μe + ee channel with at least 2 b-jets, to estimate NF_e^{HF}

The five Control Regions are shown on Figures 24 and 25 prior and after the fit to data while the measured NFs are shown on Figure 26.

This results has been calculated with the charge mis-assignment uncertainty (details are given in the appendix A.1.7).

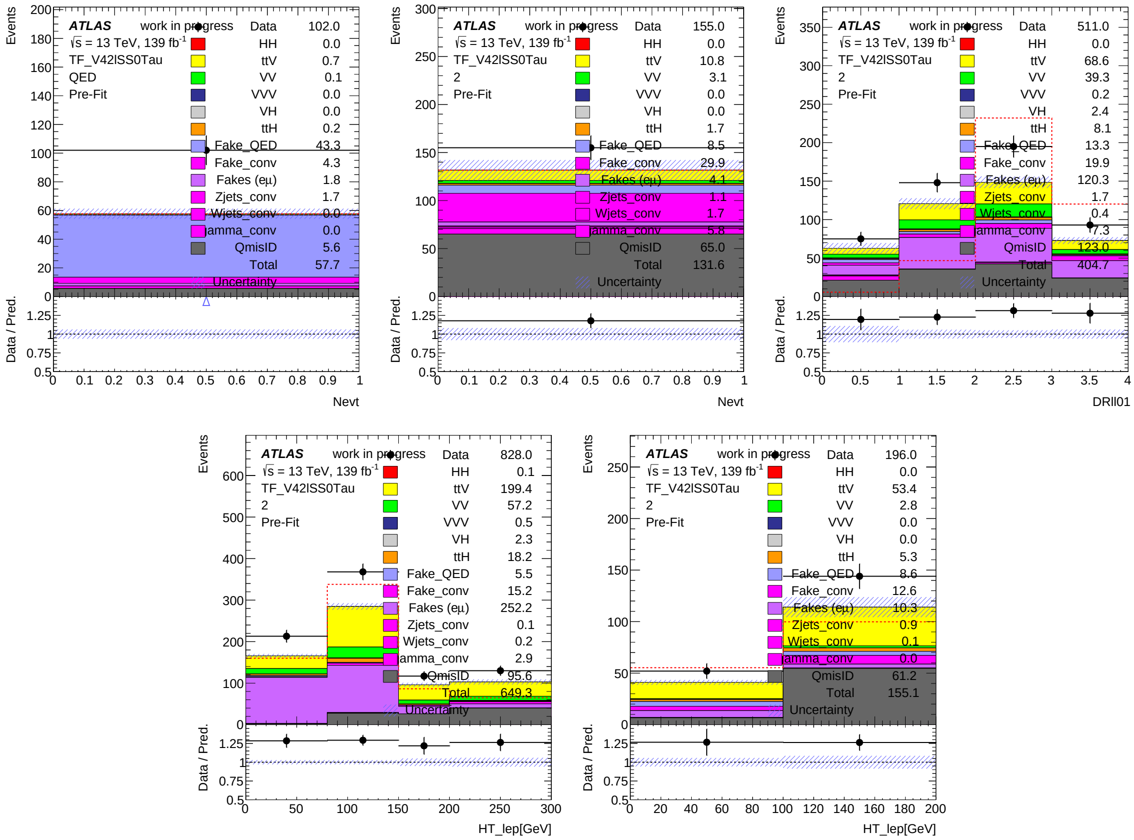

Figure 24: Pre-fit plots of the control regions.

5.4 Background validation

A region enriched in the VV background could be defined through a selection at low combined BDT (lower than 0.5). In addition, a Z-veto is applied in order to reject events from charge miss-assignment events. A selection on the BDT specific to V+jets background (higher than -0.8) rejects events from charge miss-assignment and from material conversions. In this section the charge miss-assignment events and the fake light lepton background have been estimated by the data-driven method (Template-Fit + QmisID estimation) introduced in the previous section. The distribution of the impulsion (HT, leading and sub-leading lepton p_t) can be found in figure 27.

A second region enriched in non-prompt leptons from heavy flavour decays can be defined. As in the previous regions a Z-veto and a selection on the BDT specific to V+jets are applied in order to reject the QmisID events and events from material conversion. Then, the number of jets and b-jet are respectively set at 4 jets and 1 b-jet. The distribution of the leading and subleading lepton p_T can be found in Figure 27 in $e^{\pm}e^{\pm}$, $e^{\pm}\mu^{\pm}$ and $\mu^{\pm}\mu^{\pm}$ channel.

The plots corresponding to this region can be find in figure 28.

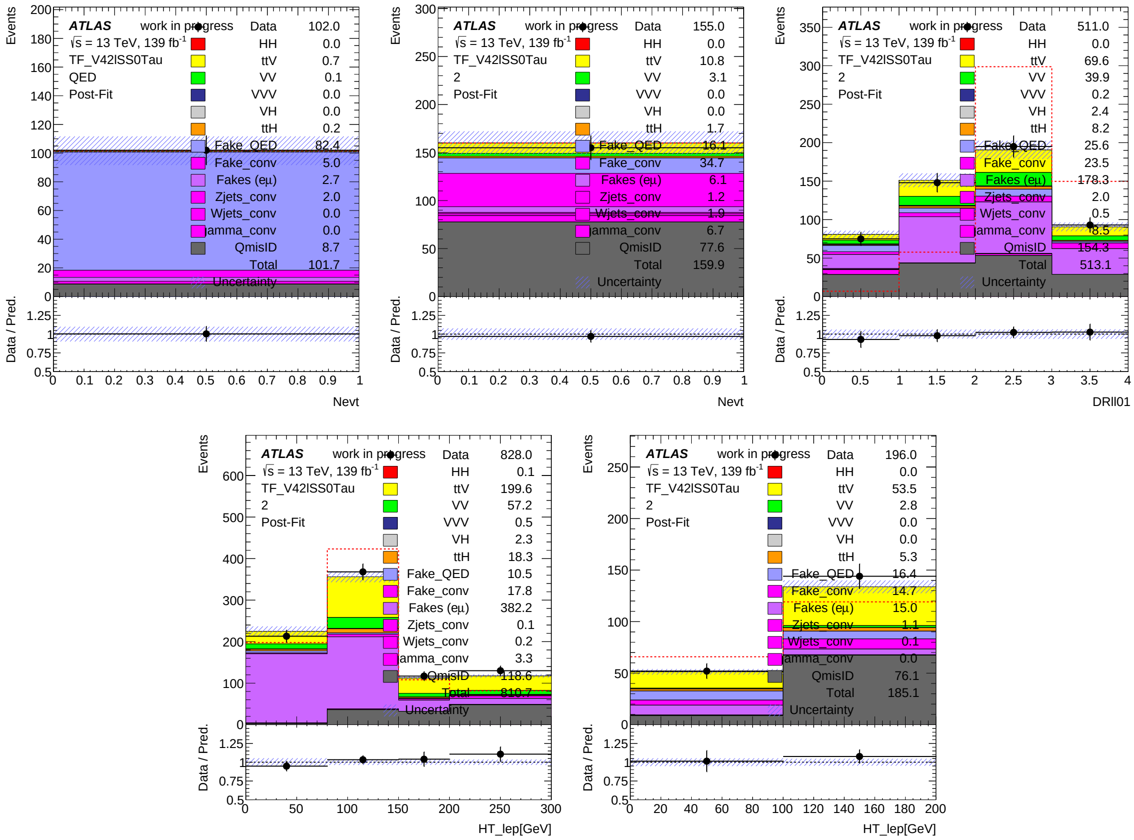

Figure 25: Post-fit plots of the control regions.

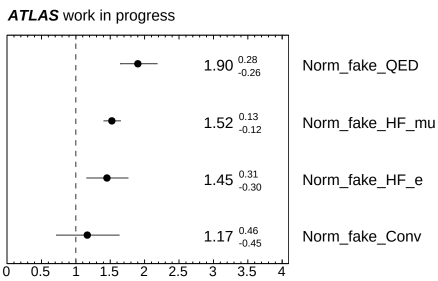

Figure 26: Normalization factors obtained after the fit to data using the CR.

5.5 Statistical analysis

A signal+background fit is preformed to determine the expected upper limits of di-Higgs production cross section using Asimov data. The detector systematic are assigned to prompt MC, VV , $t\bar{t}H$, $t\bar{t}W$, $t\bar{t}Z$ etc and signal. The total events yields of signal are the sum of ggF and VBF production mode of di-Higgs. Partial data driven uncertainties are included in the fit: The QmisID uncertainties are considered as shape validation, the detailed results can be found in A.1.7.

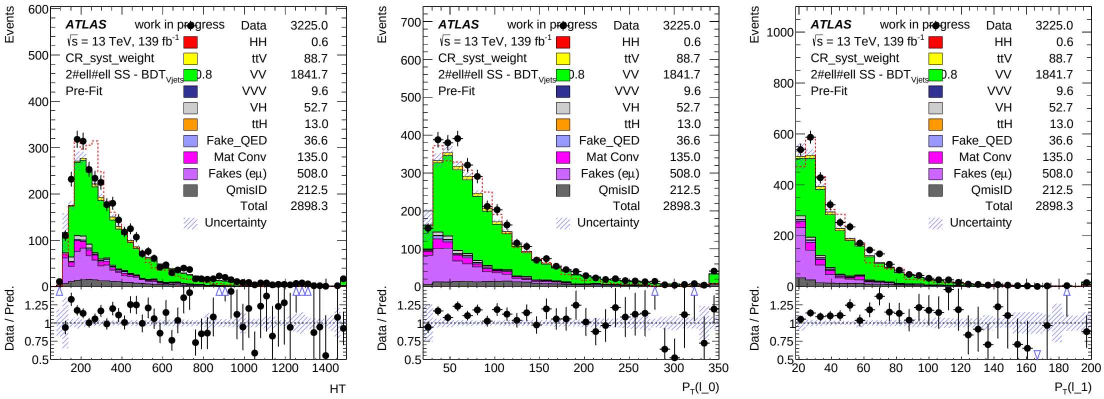

Figure 27: The distribution of HT (left), leading lepton p_T (center) and sub-leading lepton p_T (right) all flavours included with data-driven backgrounds.

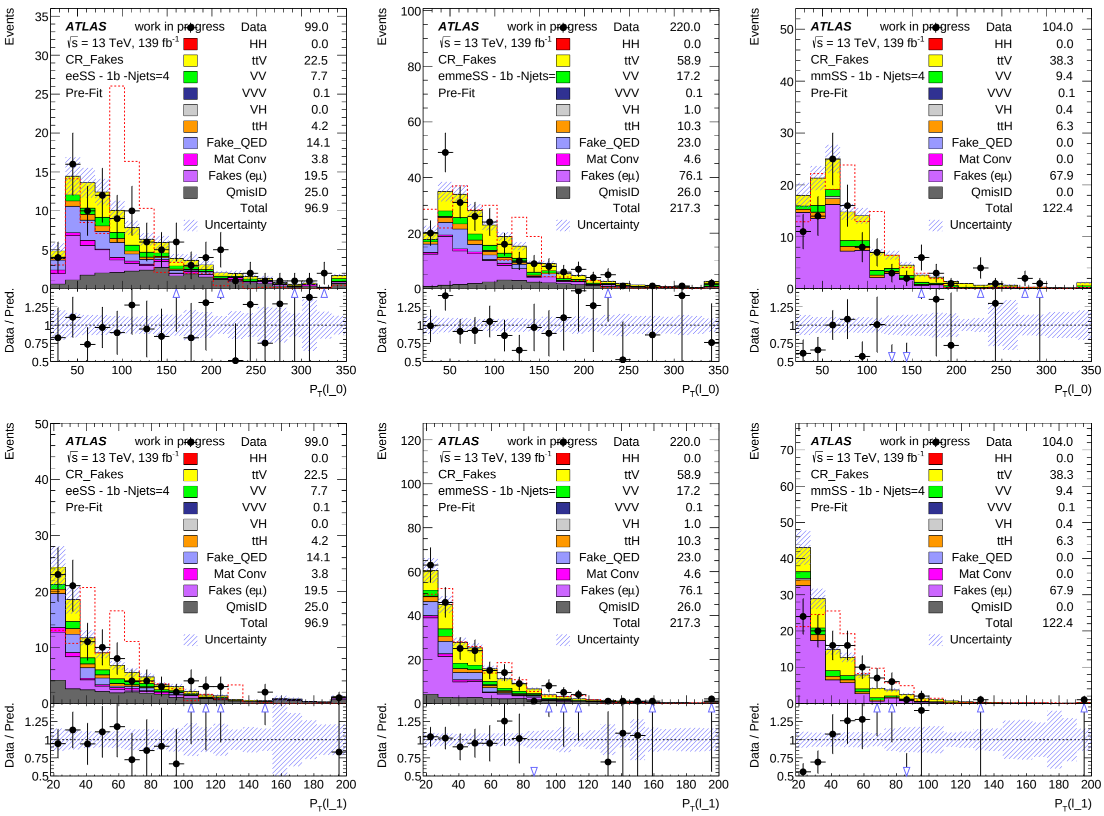

Figure 28: The distribution of leading lepton p_T (top) and sub-leading lepton p_T (bottom) all flavour included with data-driven backgrounds. Left: $e^{\pm}e^{\pm}$, middle $e^{\pm}\mu^{\pm}$, right $\mu^{\pm}\mu^{\pm}$.

Figure 29 and Figure 30 show the correlation matrix of nuisance parameters and the pull of nuisance parameters, respectively. The QmisID uncertainty looks like a kind of over-constraint.

Figure 31 gives the ranking of the nuisance parameters 1% threshold on shape and 0.5% threshold on

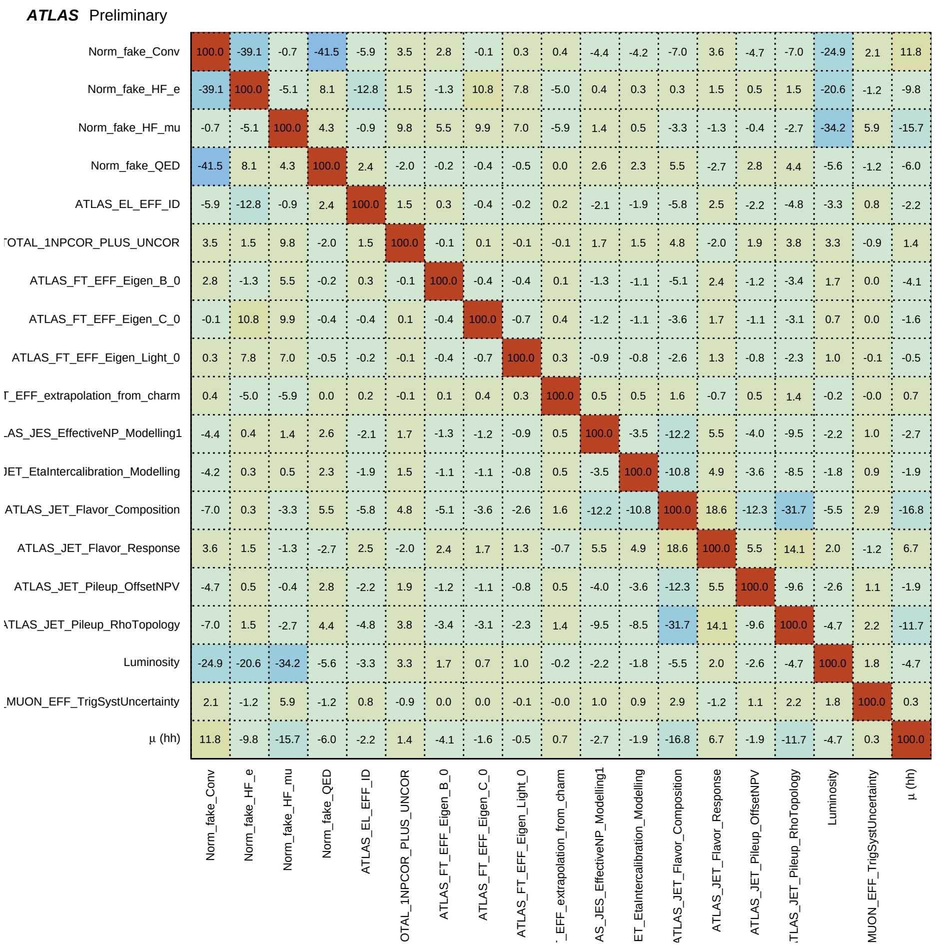

Figure 29: The correlation matrix in 2ℓSS channel. Detector systematic on prompt background and data driven nuisance parameters included.

normalization in the pruning process. Except MC statistical uncertainty, the systematic uncertainty are dominated by fake background and QmisID background estimation. It has been found that the JER/JES impacts are problematic, the bug of deriving those quantities is the framework results in one-slide behavior. It has to be fixed in the next production. The expected upper limits in 2ℓSS channel is presented in Table 17.

	-2σ	-1σ	Expected	$+1\sigma$	$+2\sigma$	Observed
$\sigma_{HH}/\sigma_{HH}^{SM}$ Stats.	17.35	23.30	32.34	45.67	62.67	blinded
$\sigma_{HH}/\sigma_{HH}^{SM}$ Sys.	19.22	25.80	35.81	50.79	70.20	blinded

Table 17: Expected Upper limits in 2ℓSS channel. First row: Limits with stats only; Second row: Limits with systematics.

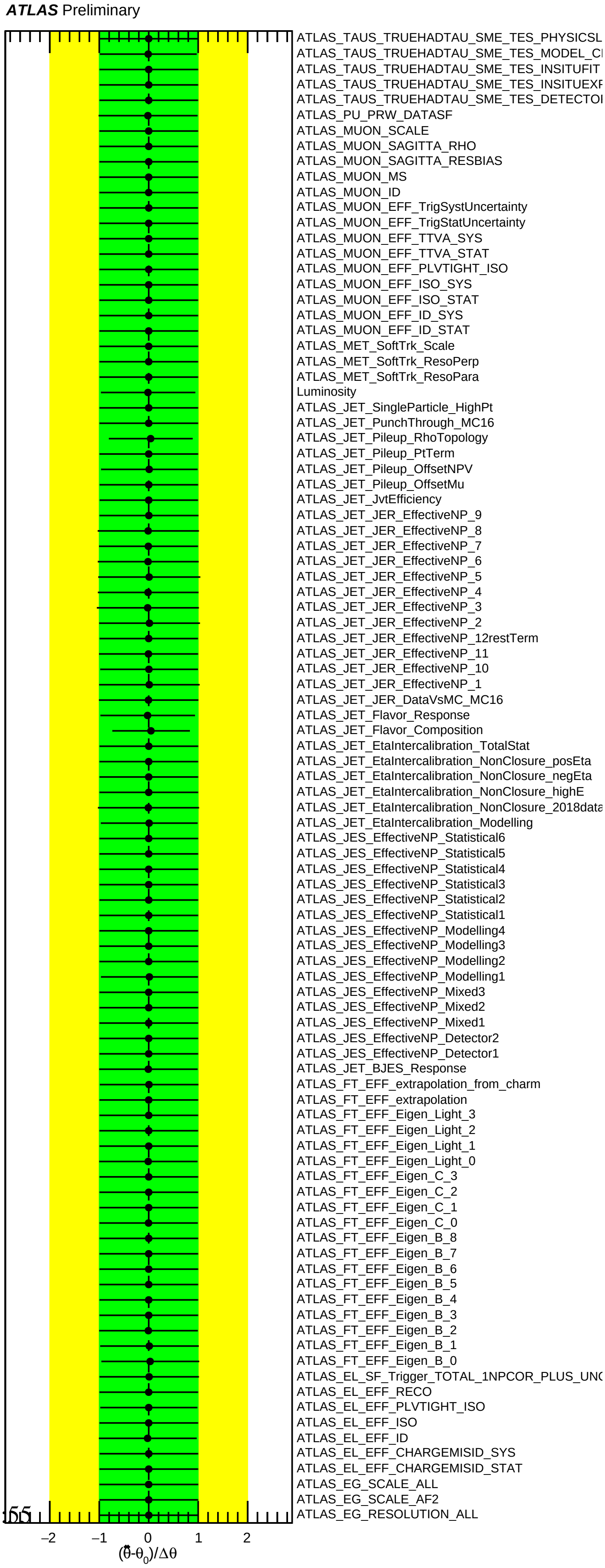

Figure 30: The pull of all nuisance parameters in 2ℓSS channel. Detector systematic on prompt background and data driven nuisance parameters included.

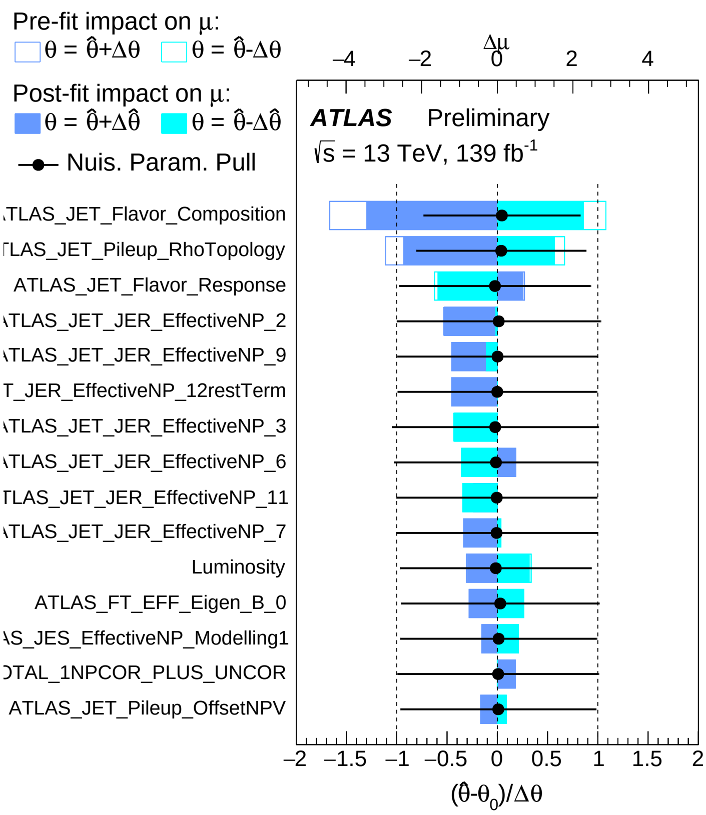

Figure 31: The ranking of top 15 nuisance parameters in 2ℓSS channel. Detector systematic on prompt background and data driven nuisance parameters included.

6 The Analysis of Three-lepton Channel

6.1 Overview

This section describes the search of Higgs pair production in the decay channel of $hh \to 3\ell0\tau_h$ + jets. In this channel, the signal is clean with relatively low branching ratio. Multi-lepton requirement in the final state strongly suppresses the multi-jet background. Background coming from faking leptons which is dominant in the previous analysis [58] can also be significantly suppressed with a more advanced lepton ID and isolation working point (PLV) [59]. The dominant background comes from $WZ \to 3\ell0\tau_h$ process.

6.2 Signal region

Events are required to pass the basic event selection criteria as described in Section 3. Table 18 shows the Monte Carlo and data samples yields after each pre-selection.

Selection Criteria	signal	prompt bkg	MC jet fakes	total bkg	data
three leptons with a total charge of ±1	6.94	73754.50	715726.08	789480.59	1213079.00
Triggers	6.46	68044.74	609585.72	677630.46	913339.00
Lepton loose quality	4.34	49949.86	89759.85	139709.71	147952.00
Hadronic tau veto	3.82	49173.91	89146.99	138320.90	146597.00
$p_T^{1,2,3} > 10, 15, 15$ GeV	3.57	46337.00	52967.58	99304.57	110888.00
Electron quality	2.87	38972.05	14958.10	53930.15	60166.00
b-jet veto	2.61	36080.07	12953.46	49033.53	54689.00
Low mass veto	2.58	35480.95	12330.87	47811.82	52759.00
$N_{\text{jet}} \geq 1$	2.20	18800.96	4374.60	23175.56	23641.00
Z-mass veto	1.60	3029.54	1073.11	4102.65	4141.00
Lepton tight quality	1.20	2362.96	345.08	2708.04	2566.00

Table 18: The raw yields with pre-selection cut-flow for the 3-lepton analysis.

6.2.1 Signal topology

The searched three-lepton signal contains three mainly di-Higgs decay channels: $WWWW$, $WWZZ$ and $WW\tau\tau$, which gives the combined final state of $3\ell0\tau_h$+jets. $WWWW$ accounts for over 60% in branching ratios among these three channels, therefore it is the dominating channel in the signal topology analysis. Most of the Higgs bosons are moderately boosted. In particular, the two leptons from the Higgs leptonically decaying W-bosons tend to be close in spatial distance due to the spin correlation of W-bosons from the Higgs bosons decay. For the 3-lepton channel, a significant background arises from the diboson production. In particular, WZ background, where both bosons decay to leptons, can mimic signal features in absence of b-jets.

The following points summarize the sub-channels of 3ℓ channel:

- **SFOS-0** no same-flavour opposite-sign pair: $\mu^\mp e^\pm e^\pm$, $e^\mp \mu^\pm \mu^\pm$
- **SFOS-1,2** one or two same-flavour opposite-sign pair(s): $e^\mp e^\pm \mu^\pm$, $\mu^\mp e^\pm \mu^\pm$, $e^\mp e^\pm e^\pm$, $\mu^\mp \mu^\pm \mu^\pm$

The variables used to enhance signal sensitivity can be found in Sec. 4.3.2. After the MVA training, the background validation region is defined as BDTG ≤ 0.2 and the signal region is defined as BDTG > 0.2.

6.3 Background Estimation

There are two major backgrounds in this analysis: events containing three prompt leptons dominated by diboson background and events in which one or more jets (photons) are misidentified as leptons, which are called fakes. The prompt backgrounds are modelled with Monte Carlo simulation and the jet fakes background is estimated using template fit method, which is introduced in Section 6.3.1, and more detailed in Appendix A.1.1.

The prompt background with a final state of three prompt leptons with a total charge of ± 1 is estimated using simulation samples. In this analysis. the prompt background consists of $t\bar{t}V, VV, tV, VH, VVV$ and $t\bar{t}H$ processes. WZ processes accounts for over 85% of all the prompt backgrounds.

6.3.1 Control regions and background estimation Using template fit method

Four dedicated control regions have been chosen for template fit. All four control regions are required to pass the following basic selections:

- Global Trigger Decision
- Single lepton triggers or Di-lepton triggers
- Exact 3 leptons with a total electric charge of ± 1
- $p_{\mathrm{T}}^{l1} > 10$ GeV and $p_{\mathrm{T}}^{l2,l3} > 15$ GeV
- Events with at least one hadronic tau are vetoed
- Loose ID cut for l_1 and Tight ID cut for l_2/l_3
- Events with at least one same-flavour opposite-sign (SFOS) lepton pair with an invariant mass less than 12 GeV are vetoed.

Each CR is orthogonal to SR, their definition are as follows,

- WZ Control Region: WZ control region is defined as follows;
  - Loose Isolation for l_1 and Tight Isolation for l_2/l_3
  - Veto events if they contain any b-tagged jets
  - $N_{\mathrm{jet}} \geq 0$
  - Events with at least one same-flavour opposite-sign (SFOS) lepton pair with an invariant mass within a ± 10 GeV window around m_Z are vetoed.
  - $|m_{lll} - m_Z| > 10$ GeV
- Electron/Muon coming from Heavy Flavor Decay Control Regions: HF-E/HF-MU control regions are defined as follows;

  - $N_{\text{jet}} \geq 1$
  - $N_{\text{bjet}} \geq 1$
  - Events with at least one same-flavour opposite-sign (SFOS) lepton pair with an invariant mass within a ±10 GeV window around m_Z are vetoed.
  - $|m_{lll} - m_Z| > 10$ GeV
  - L1 and L2 must be electron for HF-E control region
  - L1 and L2 must be muon for HF-MU control region
- Electron coming from Material Conversion Control Regions: Material Conversion control region is defined as follows;
  - Loose Isolation for L0 and Tight Isolation for L1/L2
  - Veto events if they contain any b-tagged jets
  - $|m_{l0l1l2} - 91.2| < 10$ GeV
  - For L1 and L2: a conversion vertex is found with radius $r > 20$mm, and the mass of the vertex is 0<m(trk-trk)$atCV$ <100MeV

The following distributions are exploited to best discriminate among the NFs in the simultaneous template fit:

- ΔR_{ll01} in lee channel, to estimate NF_e^{HF}
- N_{Jets} in $l\mu\mu$ channel, to estimate NF_μ^{HF}
- N_{Jets} to estimate NF_{VV}

The four Control Regions are shown on Figures 32 and 33 prior and after the fit to data while the measured NFs are shown on Figure 34.

The Uncertainties of the template fit method are presented in Appendices A.1.2.

6.4 Statistical analysis

The distribution of the final discriminant variable (BDTG score) is shown in Figure.TRExFitter[60] software framework is used to perform profile likelihood fitting and statistical analysis. The discriminant distribution is used to obtain the best fit of signal and background distributions to the data distribution. The parameter of interest during fitting is the ratio of the signal cross-section over the SM prediction. The fitting results are shown in FIGURE. The signal distributions are blinded in the signal region. Figure 35 shows the final discriminant distributions after fitting in both signal and background regions.

After the statistical analysis, the maximum significance of the signal is calculated to be 0.086 and the $HH \rightarrow 3l$ cross-section upper limit over the SM prediction is $26.25^{+11.56}_{-7.34}$

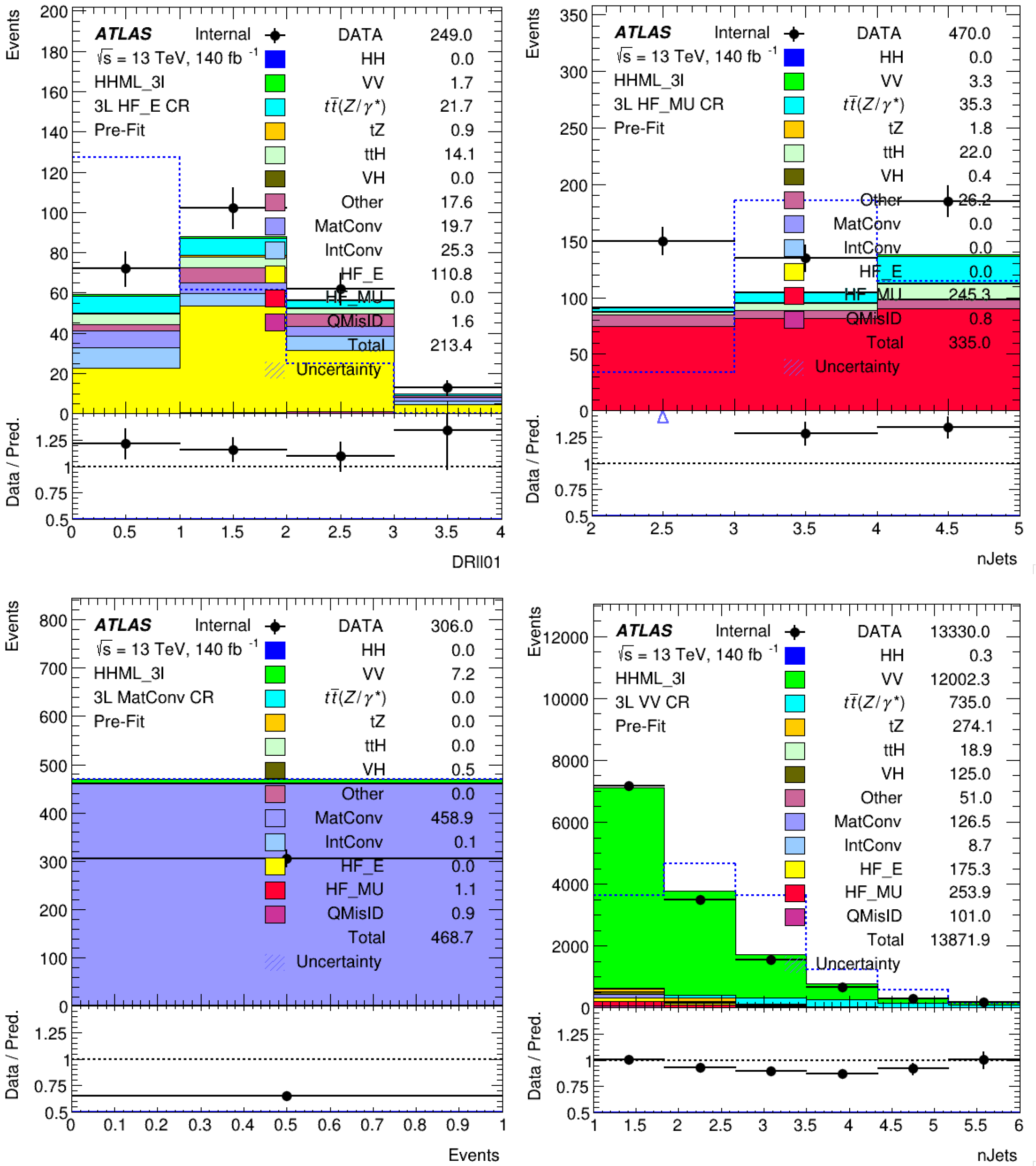

Figure 32: Pre-fit plots of the control regions.

6.4.1 Limit estimation

The search for SM Higgs pair production with the decay channel of three charged leptons (no hadronic taus) and at least two hadronic jets and missing transverse energy, is performed using 140fb^{-1} of $p-p$ collision data at a centre-of-mass of $\sqrt{13}$ TeV collected at the ATLAS experiment from 2015 to 2018. The main Standard Model background processes which result in three prompt leptons and $V\gamma$ production are modelled using MC. Other backgrounds containing jet faking leptons are estimated by a data-driven method. The main prompt background WZ is re-normalized due to the overestimation of MC in the high

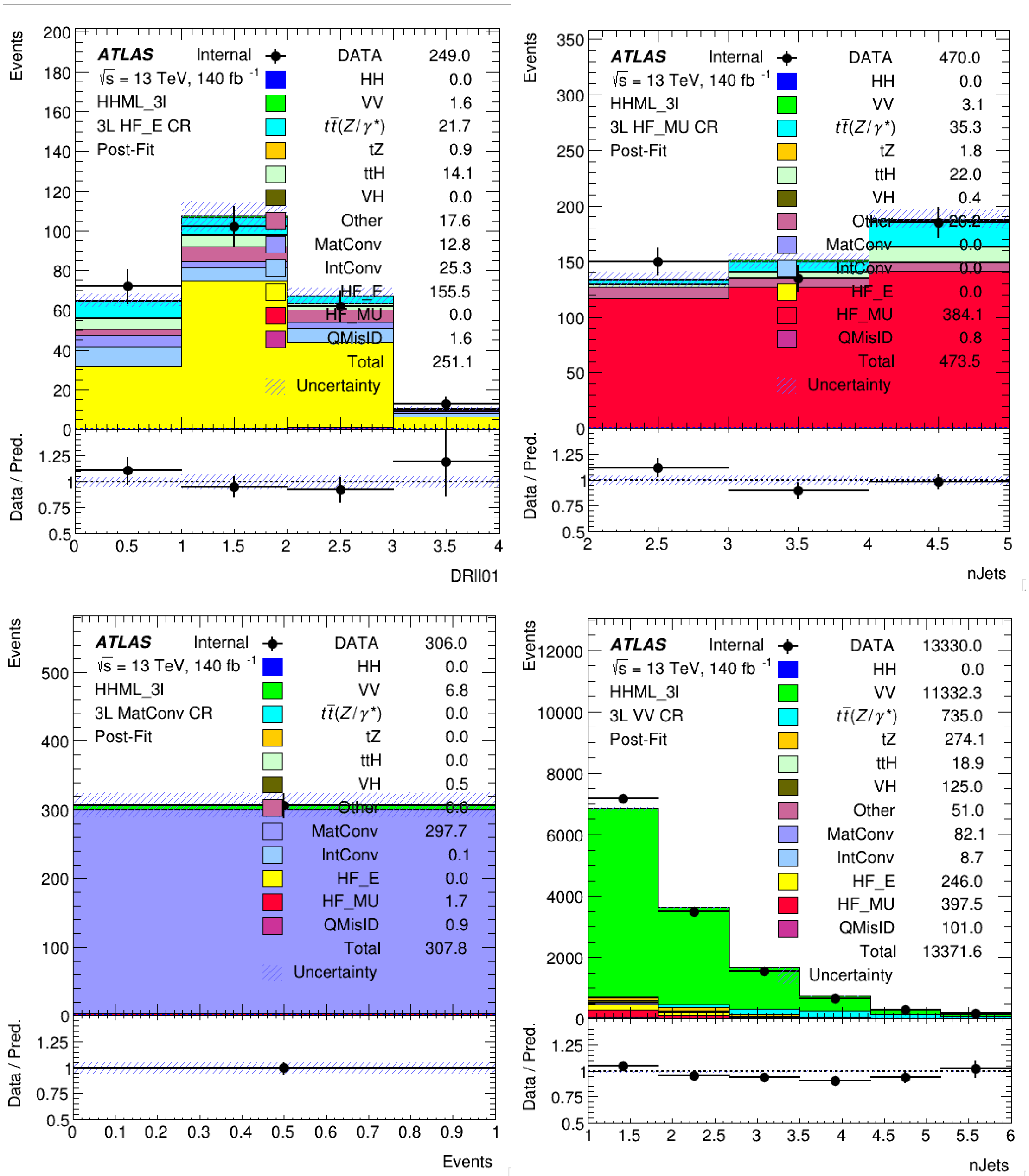

Figure 33: Post-fit plots of the control regions.

jet multiplicities region. The multi-variate analysis is applied as the final selection to explore the sensitivity of this channel. The data are found to be consistent with the background expectation and an upper limit is set at 95% C.L. on the production cross section. An expected upper limit of 10.23 fb is set on Standard Model non-resonant Higgs pair production with the decay channel of $hh \to 3\ell 0\tau_h +$ jets.

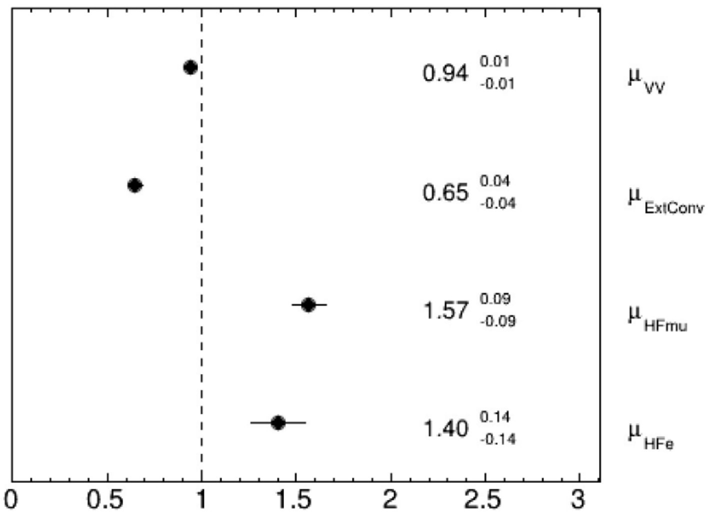

Figure 34: Normalization factors obtained after the fit to data using the CR.

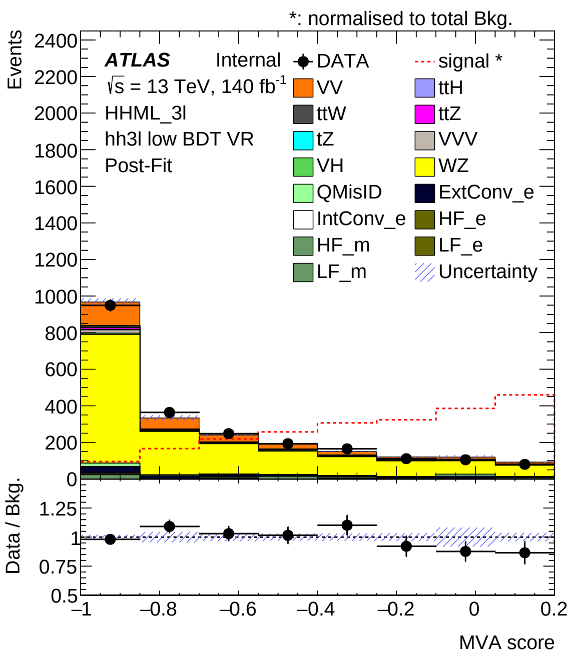

(a)

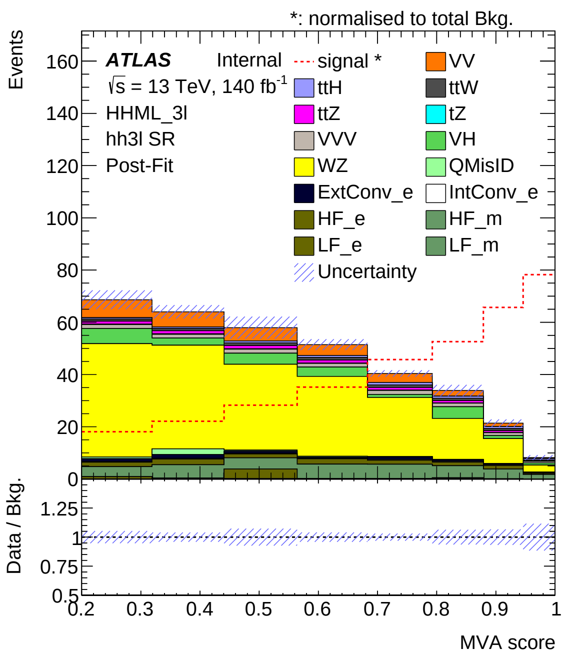

(b)

Figure 35: The post-fit result of BDTG score in the 3ℓ channel. In the signal region (*right*), data is blinded.

7 The Analysis of $\gamma\gamma$+Lepton Channel

7.1 Overview

This section describes the search of Higgs pair production with the final states of mutilepton and $\gamma\gamma$. The events are categorized by the number of light leptons and τ_{had} as one light lepton ($\gamma\gamma$+ℓj), one τ_{had} ($\gamma\gamma$+$\tau_{\text{had}}j$), and two leptons(light lepton or hadronical τ lepton), namely $1\ell 1\tau_{\text{had}}$, $2\ell 0\tau_{\text{had}}$ and $0\ell 2\tau_{\text{had}}$ ($\gamma\gamma$+2L).

The section is organized as the following. Section 7.2 describes the signal region. Section 7.3.1 introduces the composition of the background. In Section 7.3.2, the background reweighting is considered. Section 7.4 describes the systematic uncertainties. The statistical analysis results are shown in the Section 7.5.

7.2 Signal region

Events are required to pass the basic event selection criteria as described in Section 3. Table 19 shows the Monte Carlo and data samples yields after each pre-selection which is shown in 16.

Selection Criteria	signal	Single Higgs	Vyy	Sherpa	Continuum bkg	Data
Total	6.38	8611.58	7922.06	2880000.00	2887922.06	58900000
Two tight photons	2.57	6255.87	1485.70	943180.00	944665.70	1180000
b-jet veto	2.25	6047.06	1278.58	912849.00	914127.58	1150000
pass all pre-selections	1.38	495.00	457.21	49895.00	50352.21	64923
pass $\gamma\gamma$+ℓj	0.39	18.05	167.58	62.91	230.48	420
pass $\gamma\gamma$+$\tau_{\text{had}}j$	0.18	7.70	32.23	810.22	842.45	881
pass $1\ell 1\tau_{\text{had}}$	0.05	0.28	2.57	0.23	2.81	7
pass $0\ell 2\tau_{\text{had}}$	0.04	0.15	1.09	3.58	4.67	3
pass $2\ell 0\tau_{\text{had}}$	0.05	0.66	6.11	0.06	6.17	12

Table 19: The event yields at pre-selection level cut-flow for the $\gamma\gamma + ML$analysis.

The signal regions are further optimized by using the BDTG shape. The BDTG distribution applied to divide regions is shown in Figure 36. By maximizing expected significance, three regions divided by the BDTG value are used in each channel. The background control region is defined as BDTG ≤ 0 and the signal regions are defined as $0 <$ BDTG ≤ 0.6 and $0.6 <$ BDTG.

7.3 Background estimation

7.3.1 Background components

This analysis is affected both by backgrounds from single-Higgs production and non-resonant backgrounds with continuum $m_{\gamma\gamma}$ spectra. The single-Higgs production contributing to the background are associated production with five modes: VH, ggH, VBF, ttH and tH. As for continuum backgrounds, the major contributions are vector boson production associated with photons ($V\gamma\gamma$) and multi-jets processes associated with photons ($\gamma\gamma$+jets, also known as "Sherpa").

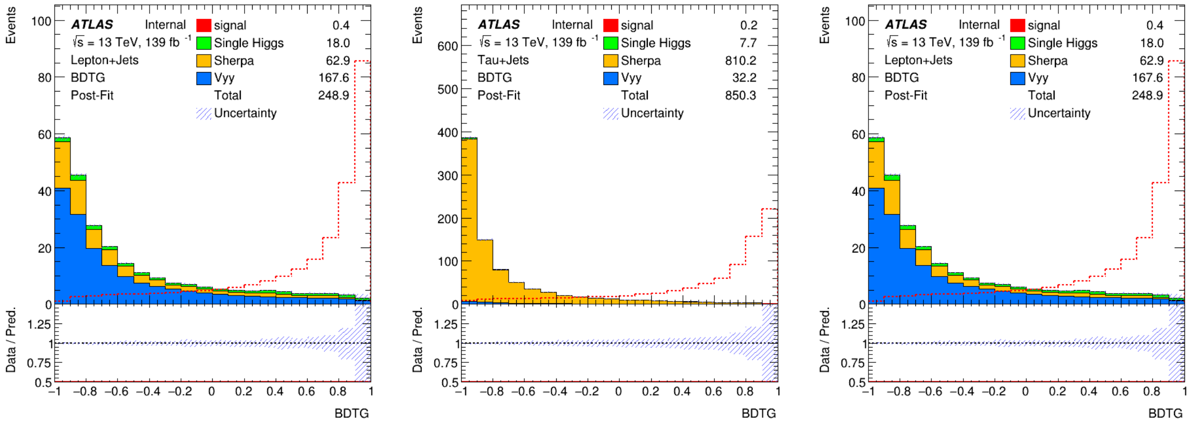

(a) (b) (c)

Figure 36: The post-fit result of BDTG score in different channels: (a) $\gamma\gamma$+ℓjchannel; (b) $\gamma\gamma$+$\tau_{\text{had}}j$channel; (c) $\gamma\gamma$+2L (include $1\ell 1\tau_{\text{had}}$, $2\ell 0\tau_{\text{had}}$ and $0\ell 2\tau_{\text{had}}$) channel.

7.3.2 Background modeling by reweighting

The background reweighting is performed to ensure the consistency of MC continuum background samples (include $\gamma\gamma + jets$, $V\gamma\gamma$, $tt\gamma\gamma$) and sideband data. The distributions of the final discriminant variable(m_{yy} shape) after reweighting are shown in Figure 37.

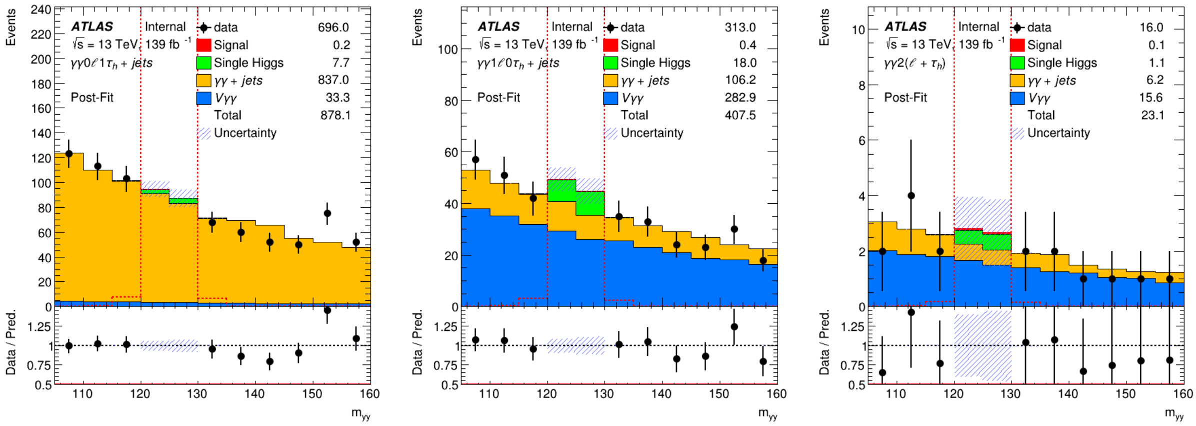

(a) (b) (c)

Figure 37: The post-fit result of m_{yy} shape in different channels: (a) $\gamma\gamma$+ℓjchannel; (b) $\gamma\gamma$+$\tau_{\text{had}}j$channel; (c) $\gamma\gamma$+2L (include $1\ell 1\tau_{\text{had}}$, $2\ell 0\tau_{\text{had}}$ and $0\ell 2\tau_{\text{had}}$) channel.

7.4 Systematic uncertainties

7.4.1 Theoretical uncertainties

In progress...

7.4.2 Experimental uncertainties

The experimental uncertainties due to the reconstruction of physics objects, which known as detector systematic, composed of light leptons, taus, jets, flavour tagging, and MET which are described in sub-section 10.1.

Each value of the systematics is computed as the relative difference from nominal signal MC samples with $\pm 1\sigma$ variation:

$$\delta n_{\mathrm{c}}^{\pm 1\sigma} = \frac{n_{\mathrm{c}}^{\pm 1\sigma}}{n_{\mathrm{c}}^{\mathrm{nom}}} - 1. \tag{5}$$

Systematic uncertainties are computed for each individual category c. All the systematic sources are implemented in the fit with asymmetric constraints since up and down variations can have different values.

The uncertainties in the combined 2015-2018 integrated luminosity is 1.7%. This uncertainty is applied to the signal and SM signal-Higgs samples.

7.5 Statistical Analysis

A signal + background binned fit is performed to determine the expected upper limit of di-Higgs production cross-section by using Asimov data. The detector systematic are assigned to signal and the total events yields are the sum of ggF and VBF production mode of di-Higgs.

The distributions of $m_{\gamma\gamma}$ shape of the $\gamma\gamma$+ℓjchannel in control region and signal regions are shown in Figure 38. Where the small mass window of $m_{\gamma\gamma}$ is always blinded.

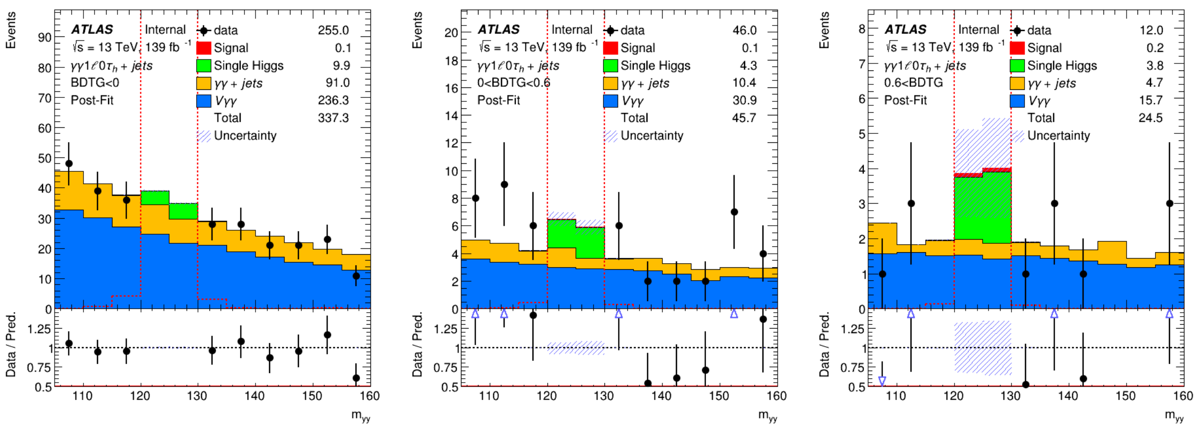

(a) (b) (c)

Figure 38: The post-fit result of $m_{\gamma\gamma}$ shape in control region and signal regions: (a) BDTG ≤ 0; (b) $0 <$ BDTG ≤ 0.6; (c) $0.6 <$ BDTG.

Figure 39 gives the ranking of the nuisance parameters(NPs) 1% threshold on shape and 0.5% threshold on normalization in thr pruning process. The expected upper limit in different channels are presented in Table 20.

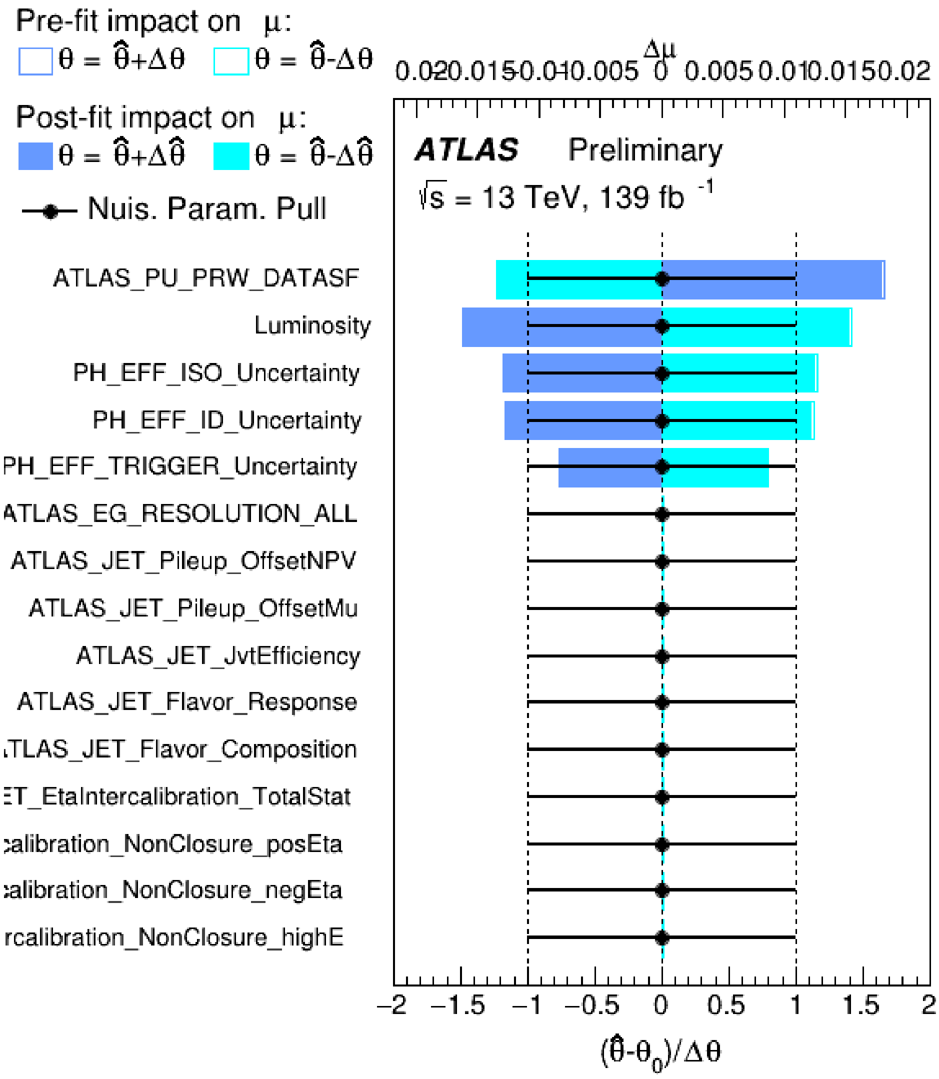

Figure 39: Nuisance parameters ranking and pull distributions in $\gamma\gamma + mutilepton$ combined fit.

	-2σ	-1σ	Expected	$+1\sigma$	$+2\sigma$	Observed
$\gamma\gamma$+ℓjchannel Sys.	13.57	18.22	25.28	36.90	53.69	blinded
$\gamma\gamma$+$\tau_{\text{had}} j$channel Sys.	26.54	35.64	49.46	72.65	106.41	blinded
$\gamma\gamma$+2L channel Sys.	14.35	19.27	26.74	40.76	64.32	blinded
Combined Sys.	8.05	10.81	15.00	21.92	32.03	blinded

Table 20: Expected Upper limits in $\gamma\gamma + mutilepton$ final states with systematic. First row: Limits in $\gamma\gamma$+ℓjchannel; Second row: Limits in $\gamma\gamma$+$\tau_{\text{had}} j$channel; Third row: Limits in $\gamma\gamma$+2L channel; Last row: Combined limits in $\gamma\gamma + mutilepton$ final states.

8 The Analysis of τ Channels

This section describes the analyses of channels with hadronically decaying τ leptons, including 1ℓ+$2\tau_{\text{had}}$,2ℓSS+$1\tau_{\text{had}}$ and 2ℓSS+$1\tau_{\text{had}}$.

8.1 1ℓ+$2\tau_{\text{had}}$ channel

8.1.1 Overview

The 1ℓ+$2\tau_{\text{had}}$ channel is primarily sensitive to $HH \rightarrow W^+W^-\ \tau^+\tau^-$ decay mode and about 82% of signal events come from this mode, as shown in Figure 40. In such decay mode, one of the W boson decays into a lepton and neutrino while other to hadrons. The tau leptons decay hadronically. A signal event is expected to be characterized by the presence of one light lepton, two hadronically decaying τ leptons, missing energy from neutrinos and lower jet multiplicity. At least two jets are expected in the event primarily from W or Z boson decays, not taking into account the additional jets from initial and final state radiation.

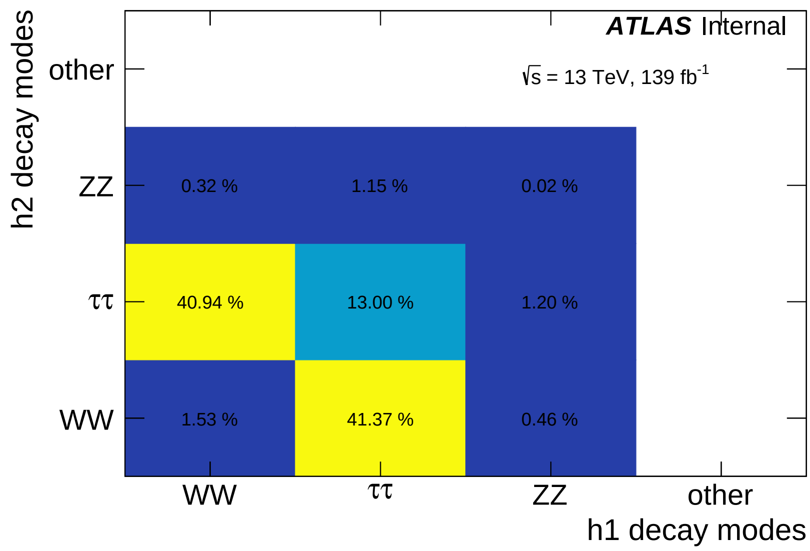

Figure 40: DiHiggs decay modes in the 1ℓ+$2\tau_{\text{had}}$ channel.

8.1.2 Signal region optimization

The signal region optimization study can be found in Appendix G. Several studies were carried out to determine the best definition for physics objects. The event selection was also optimized to increase the event acceptance in the 1ℓ+$2\tau_{\text{had}}$ channel. The figure of merit for the optimization studies is the z_0 significance. The current object and event selection provide the maximum significance. The event selection is given in in Table 16. The event yields in the 1ℓ+$2\tau_{\text{had}}$ signal region are given in Table 21 for all the MC samples. The dominant backgrounds are VV and V+jets .

Process	Event yields
Diboson	162.85 ± 1.54
V + Jets	158.34 ± 27.12
$t\bar{t}$+stop	71.28 ± 3.14
$v\gamma$	36.33 ± 9.48
$t\bar{t}$H+VH	9.96 ± 2.14
Other	7.39 ± 0.29
Total Background	446.14 ± 29.02
hh (signal)	0.51 ± 0.01
z_0	0.02397

Table 21: Event yields for all the MC samples in 1ℓ+$2\tau_{\rm had}$ signal region. z_0 significance is also given. The uncertainties are only statistical. Background processes $t\bar{t}$W, $t\bar{t}$Z, tZ, tWZ, $t\bar{t}$WW, $t\bar{t}$t, $t\bar{t}t\bar{t}$, rare top decay, and triboson production are labeled as “Other.”

8.1.3 Background estimation

Fake taus are estimated using the data-driven fake factor method. The tau fake factor is parametrized in 12 bins depending on three $p_{\rm T}$ bins (25-35, 35-50, 50- GeV), two bins for 1- and 3- prong taus, and two bins for $|\eta| < 1.37$ and $1.52 < |\eta| < 2.47$, separately. The FFs obtained from the Z+jets and the di-lepton $t\bar{t}$ samples are compared as shown in Figure 41. They are consistent each other and the differences between them are treated as systematic uncertainties due to possible different jet composition.

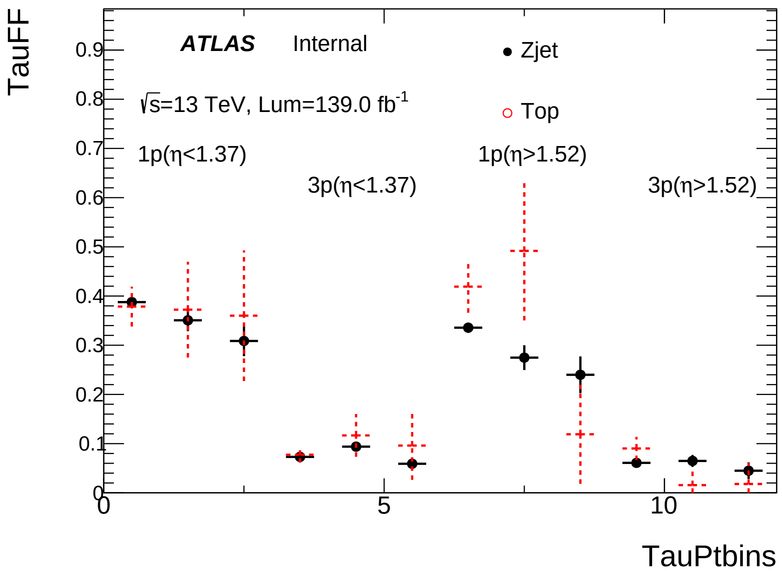

Figure 41: The FFs obtained from the Z+jets and the di-lepton $t\bar{t}$ samples are compared as function of $\tau_{\rm had}$ $p_{\rm T}$ bins in 1- and 3-prong and η regions.

The fakes and other irreducible contributions in SRs are summarized in Table 22 where the uncertainties are statistical only. The difference between the predicted fakes using two different FFs is small (< %). The comparison of kinematic distributions between the data and background predictions in the SRs and the same-sign taus VRs are shown in Figure 42 and 43, which are in a good agreement between data and background modelling.

Process	Event yields in SR	Event yields in VR
tth	2.72 ± 0.06	0.25 ± 0.02
$t\bar{t}$	3.2 ± 0.7	0.95 ± 0.38
ttV	3.6 ± 0.2	0.33 ± 0.05
Diboson	150.3 ± 1.2	5.4 ± 0.2
Vjets	11.9 ± 1.8	0.14 ± 0.07
Others	14.9 ± 2.5	0.53 ± 0.17
Fakes	386.6 ± 16.6	345.0 ± 16.0
Total Background	573 ± 17	352.6 ± 16.0
hh (signal)	0.510 ± 0.006	0.030 ± 0.001
Data		349
z_0	0.0213	0.002

Table 22: Event yields for all the MC samples with real taus and data-driven fakes in 1ℓ+$2\tau_{\text{had}}$ signal region and the same-sign taus validation region. z_0 significance is also given. The uncertainties are only statistical.

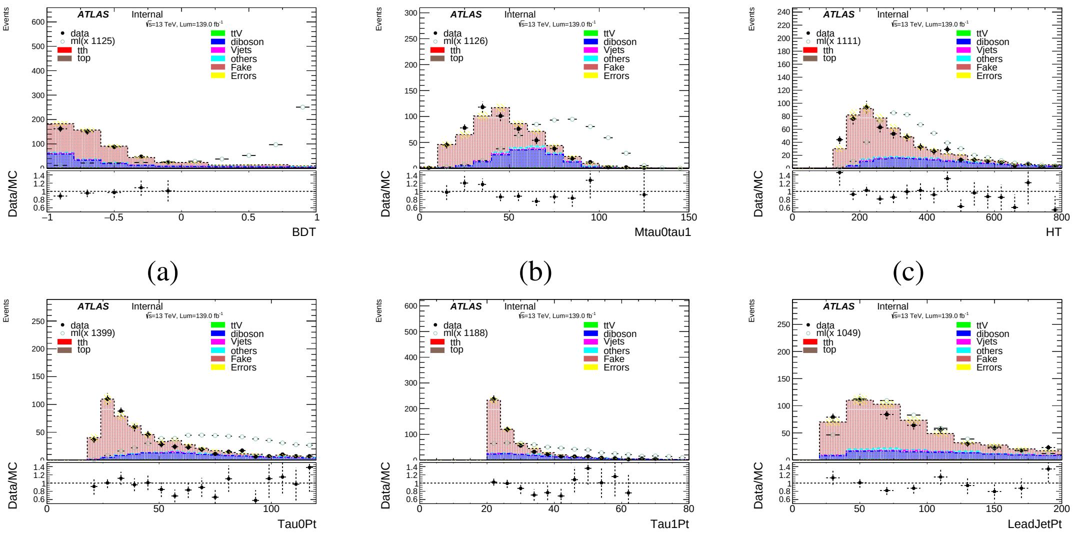

(a) (b) (c)

(d) (e) (f)

Figure 42: Kinematic distributions are compared between the data and background predictions with data-driven fakes in SRs: BDT (a), $M_{\tau\tau}$ (b), HT (c), Leading tau p_{T} (d), Sub-leading tau p_{T} (e), Leading Jet p_{T} (f). The error is statistical only. The lower panels show the data to prediction ratio.

8.1.4 Systematic uncertainties

TBD..

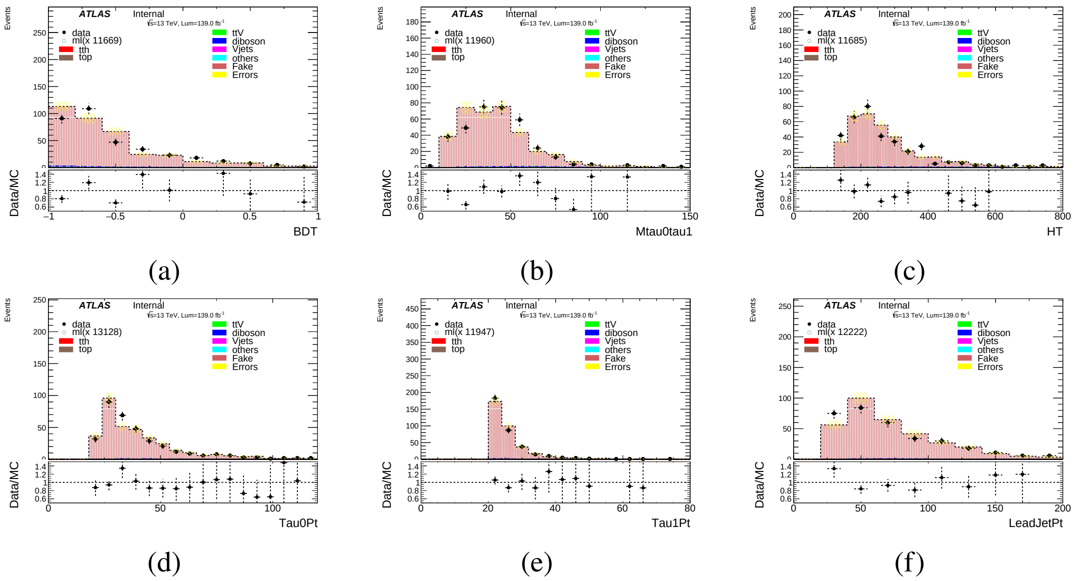

Figure 43: Kinematic distributions are compared between the data and background predictions with data-driven fakes in the same-sign VRs: BDT (a), $M_{\tau\tau}$ (b), HT (c), Leading tau p_{T} (d), Sub-leading tau p_{T} (e), Leading Jet p_{T} (f). The error is statistical only. The lower panels show the data to prediction ratio.

	Expected limit on signal strength				
	Median	$+2\sigma$	$+1\sigma$	-1σ	-2σ
1ℓ+$2\tau_{\mathrm{had}}$	32.67	75.03	49.58	23.53	17.53

Table 23: Preliminary expected 95% CL exclusion limit on the signal strength.

8.1.5 Preliminary results

Figure 44 shows the pre-fit distribution of the BDT output. A statistical analysis using a profile-likelihood-ratio test statistic is performed using BDT output as a final discriminant. The signal strength of non-resonant Standard Model (SM) HH production is defined as the ratio of the signal cross-section to the SM prediction. A preliminary expected limit on the production cross-section for non-resonant hh production is calculated and is shown in Table 23. No systematic uncertainties are included in the profile-likelihood fit.

8.2 2ℓ+$2\tau_{\mathrm{had}}$ channel

8.2.1 Overview

This section describes the analysis on 2ℓ+$2\tau_{\mathrm{had}}$ channel for the di-higgs search.

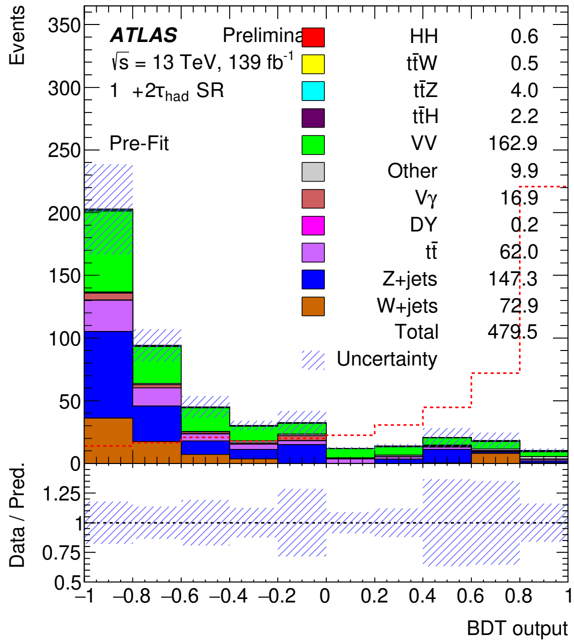

Figure 44: The BDT distributions expected in the $1\ell+2\tau_{\text{had}}$ channel. The background pre-fit contributions are shown as filled histograms. The hh signal contribution is scaled and superimposed on the backgrounds.

8.2.2 Signal region

8.2.3 Background estimation

The contribution of fake taus is also estimated using the data-driven fake factor method as discussed in the $1\ell+2\tau_{\text{had}}$ channel in Section 8.1. The same FFs ana analysis strategies are used to estimate the fakes in SRs, except the $\mathcal{K}$ is not needed in the di-lepton final states. The events with two opposite-sign (OS) leptons, and two same-sign (SS) τ_{had} , are also selected, providing a validation region (VR) for the background estimation.

The fakes and other irreducible contributions in SRs are summarized in Table 24 where the uncertainties are statistical only. The comparison of kinematic distributions between the data and background predictions in the SRs and the same-sign taus VRs are shown in Figure 45 and 46, which are in a good agreement between data and background modelling.

8.2.4 Systematic uncertainties

TBD..

8.2.5 Preliminary results

TBD..

Process	Event yields in SR	Event yields in VR
tth	0.58 ± 0.02	0.007 ± 0.002
$t\bar{t}$	-	-
ttV	0.72 ± 0.08	0.026 ± 0.011
Diboson	13.00 ± 0.35	0.20 ± 0.04
V-jets	0.04 ± 0.04	-
Others	2.52 ± 0.68	0.019 ± 0.004
Fakes	39.40 ± 5.65	33.9 ± 5.3
Total Background	56.2 ± 5.7	34.1 ± 5.3
hh (signal)	0.214 ± 0.002	0.0041 ± 0.0004
Data		30
z_0	0.0286	0.0007

Table 24: Event yields for all the MC samples with real taus and data-driven fakes in 2ℓ+$2\tau_{\mathrm{had}}$ signal region and the same-sign taus validation region. z_0 significance is also given. The uncertainties are only statistical.

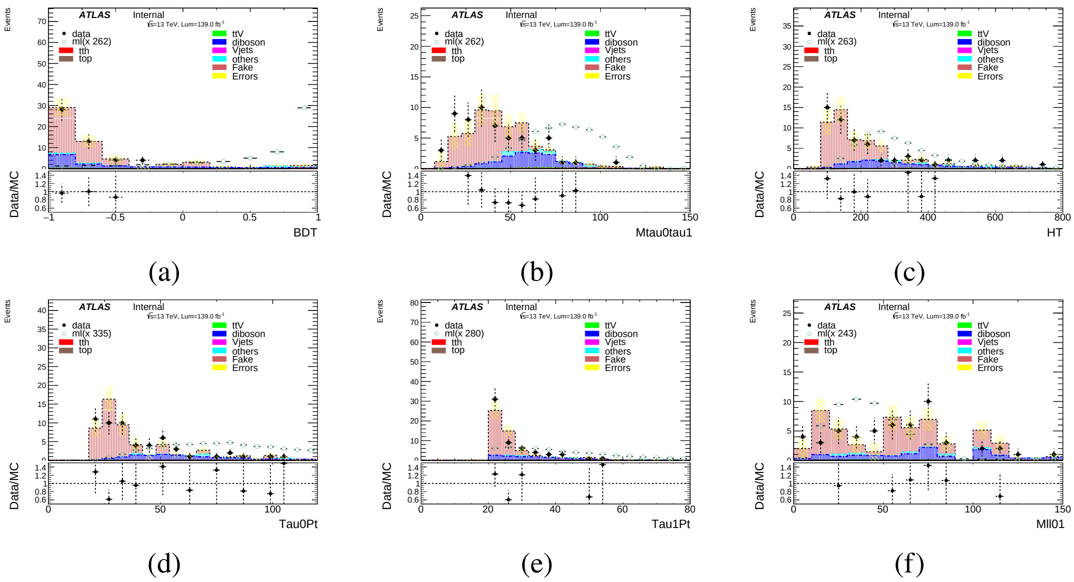

Figure 45: Kinematic distributions are compared between the data and background predictions with data-driven fakes in SRs: BDT (a), $M_{\tau\tau}$ (b), HT (c), Leading tau p_{T} (d), Sub-leading tau p_{T} (e), $M_{\ell\ell}$ (f). The error is statistical only. The lower panels show the data to prediction ratio.

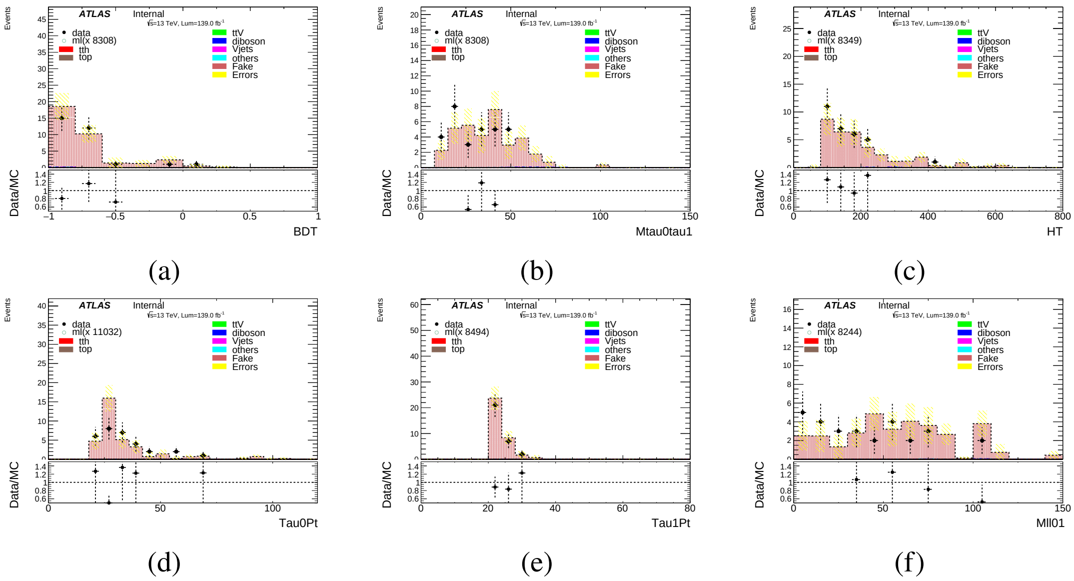

Figure 46: Kinematic distributions are compared between the data and background predictions with data-driven fakes in the same-sign VRs: BDT (a), $M_{\tau\tau}$ (b), HT (c), Leading tau p_{T} (d), Sub-leading tau p_{T} (e), $M_{\ell\ell}$ (f). The error is statistical only. The lower panels show the data to prediction ratio.

8.3 2ℓSS+$1\tau_{\mathrm{had}}$ channel

The 2ℓSS+$1\tau_{\mathrm{had}}$ channel is sensitive to $HH \rightarrow W^+W^- \tau^+\tau^-$, $HH \rightarrow W^+W^- W^+W^-$ and $HH \rightarrow \tau^+\tau^- \tau^+\tau^-$ decay modes. The signal events came mostly from $HH \rightarrow W^+W^- \tau^+\tau^-$ decay mode and posse of 70% of all decay modes. The rest of decay modes are dominate by two decay modes $HH \rightarrow W^+W^- W^+W^-$ and $HH \rightarrow \tau^+\tau^- \tau^+\tau^-$ as shown in Figure 47. In such decay modes, leptons came from W boson decays into a lepton and neutrino and tau decays to a light lepton and neutrino or hadronically. A signal event is expected to be characterized by the presence of two light leptons with same sign and one hadronically decaying τ leptons, missing energy from neutrinos and lower jet multiplicity. At lest two reconstructed jets are expected in such events, not taking into account the additional jets from initial and final state radiation.

8.3.1 Signal region

The signal region is defined as the BDTG output 4.3.4 after applying selections 4.2.6. The event yields for all the MC samples after passing the selection are given in Table 25. The diboson and $t\bar{t}$ backgrounds are dominant in the 2ℓSS+$1\tau_{\mathrm{had}}$ channel.

8.3.2 Background estimation

TBD...

8.3.3 Systematic uncertainties

TBD..

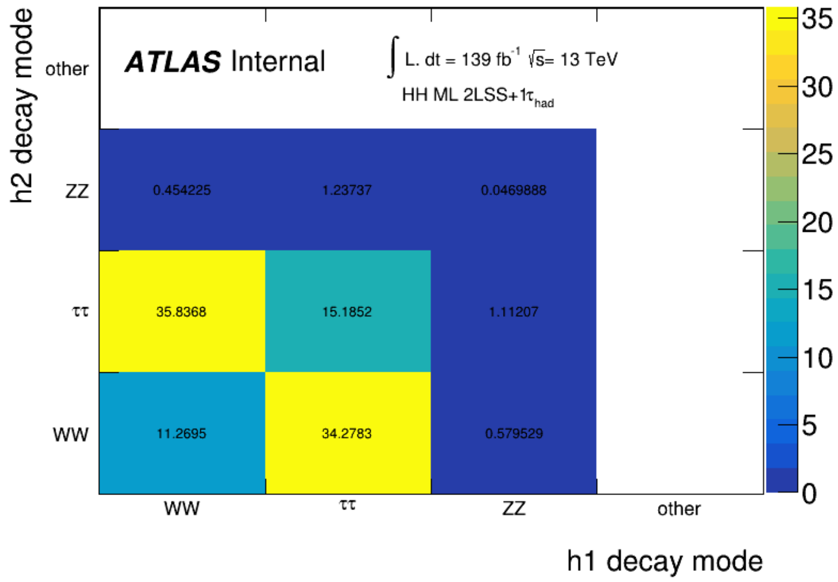

Figure 47: DiHiggs decay modes in the 2ℓSS+1τ_{had} channel.

Process	Event yields
ttV	10.735 ± 0.308
$t\bar{t}$	314.566 ± 6.906
ttH	4.6020 ± 0.4536
tZ	1.3940 ± 0.1192
Diboson	195.9820 ± 3.6769
Triboson	5.1280 ± 0.0146
vγ	3.543 ± 1.794
vH	7.353 ± 1.981
Z + Jets	67.388 ± 8.115
W + Jets	67.298 ± 16.184
DY/low mass Z	0.2350 ± 0.2350
Total Background	678.224 ± 19.913
hh (signal)	0.493 ± 0.070
z_0	0.0189

Table 25: Event yields for all the MC samples in 2ℓSS+1τ_{had} signal region. z_0 significance is also given. The uncertainties are only statistical.

	Expected limit on signal strength				
	Median	$+2\sigma$	$+1\sigma$	-1σ	-2σ
$2\ell SS+1\tau_{had}$	55.96	111.8	79.81	40.33	30.04

Table 26: Preliminary expected 95% CL exclusion limit on the signal strength.

8.3.4 Preliminary results

Figure 48 shows the pre-fit distribution of the BDT output. A statistical analysis using a profile-likelihood-ratio test statistic is performed using BDT output as a final discriminant. The signal strength of non-resonant Standard Model (SM) HH production is defined as the ratio of the signal cross-section to the SM prediction. A preliminary expected limit on the production cross-section for non-resonant hh production is calculated and is shown in Table 26. No systematic uncertainties are included in the profile-likelihood fit.

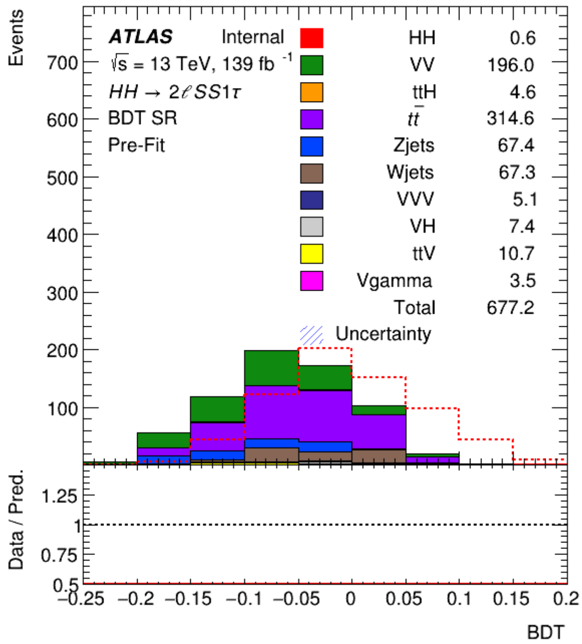

Figure 48: The BDT distributions expected in the $2\ell SS+1\tau_{had}$ channel. The background pre-fit contributions are shown as filled histograms. The hh signal contribution is scaled and superimposed on the backgrounds.

s

9 The Analysis of $b\bar{b}4\ell$ Channels

9.1 Overview

This section presents the analysis work done in $HH \to ZZ + b\bar{b} \to 4l + b\bar{b}$ channel. This analysis is to search for non-resonant HH production on LHC with 139 fb^{-1} of pp collision data at $\sqrt{s} = 13$ TeV. Both the gluon-gluon-fusion process (ggF), which accounts for more than 90% of the HH production cross section, and the vector-boson-fusion (VBF) process are considered here.

In this channel, the final state consists of two b-jets from a Higgs boson decay and two Z bosons decay signatures from the other Higgs boson decay: two opposite-sign same-flavor (OSSF) lepton pairs from the Z bosons decay. The branching fraction of this final state represents 0.0031% of the full HH decay, which would be a challenge of a search in the $4l + b\bar{b}$ channel with so small cross section. In this case, the signal efficiency would be a priority in the following analysis. A multivariate discriminant is used to optimize the separation between signal and background.

9.2 Signal region

The signal criteria of events containing exactly 4 leptons are introduced in 4.2.3, a comprehensive summary of the preselction is shown in Table 27. The summary of the expected yields of signal and the SM background are listed in Table 28.

Event Selection	
Trigger Matching	One of the lepton passes the single-lepton trigger or di-lepton trigger
Isolation	Either of the third lepton or the forth lepton passes the $PLVLoose$ isolation working point
p_T requirement	p_T > 20, 15, 10 GeV for the three leading leptons
Separation	$\Delta R(l_i, l_j) = \sqrt{(\eta_i - \eta_j)^2 + (\phi_i - \phi_j)^2} > 0.02$
Pair Selection	Exactly two OSSF lepton pairs
J/Ψ veto	The mass of all OSSF lepton pairs is above 5 GeV
Quadruplet Mass	115 GeV < M_{4l} < 135 GeV
Jets requirement	$N_{\text{jets}} \geq 2$
b-Jets requirement	$N_{\text{bjets}} \geq 1$

Table 27: The event selection used to define the signal criteria.

The multi-variable analysis (MVA) with Boosted Decision Tree (BDT) training approach is introduced in this channel to better distinguish the signal process from the SM backgrounds. The MVA implementation is referred to 4.3.3.

The classifier extracted from this training is then applied to all the signal and background samples and produces the outputs, i.e. BDTG, of which the values vary between -1.0 to 1.0. The distribution of BDTG in SR is shown in Figure 49.

	tt	VV	ttV	Higgs	Zjets	ggF HH	VBF HH
Exactly 4 leptons	19015.59±27.91	12962.92±31.63	620.71±2.20	576.82±10.47	80192.04±885.74	0.29±0.00	0.014±0.000
Trigger Matching	16655.97±26.13	11306.38±31.25	590.71±2.11	540.95±10.11	70129.88±824.88	0.28±0.00	0.013±0.000
Isolation	5243.36±14.61	10504.62±31.00	478.74±1.76	480.23±9.08	23842.50±439.29	0.26±0.00	0.013±0.000
Separation	4817.95±13.98	10349.94±30.91	470.92±1.71	474.47±8.94	18654.99±353.54	0.26±0.00	0.012±0.000
p_T requirement	2787.19±10.56	8221.37±30.47	434.91±1.61	437.90±8.54	3405.91±127.60	0.25±0.00	0.012±0.000
Pair Selection	527.48±4.60	7179.27±9.53	165.39±0.97	347.16±6.44	962.03±63.78	0.23±0.00	0.011±0.000
J/ψ Veto	2345.58±9.70	8165.18±30.47	432.52±1.60	434.79±8.53	3155.83±123.51	0.24±0.00	0.012±0.000
Jets requirement	221.26±2.98	1007.32±1.99	141.39±0.91	62.88±2.75	135.10±10.22	0.19±0.00	0.008±0.000
b-Jets requirement	127.75±2.26	109.18±0.61	119.26±0.83	16.51±1.07	23.06±3.30	0.18±0.00	0.007±0.000
Quadruplet Mass	19.02±0.87	4.84±0.13	4.45±0.17	4.62±0.81	5.00±1.83	0.16±0.00	0.007±0.000

Table 28: Expected yields of signal and SM background in SR.

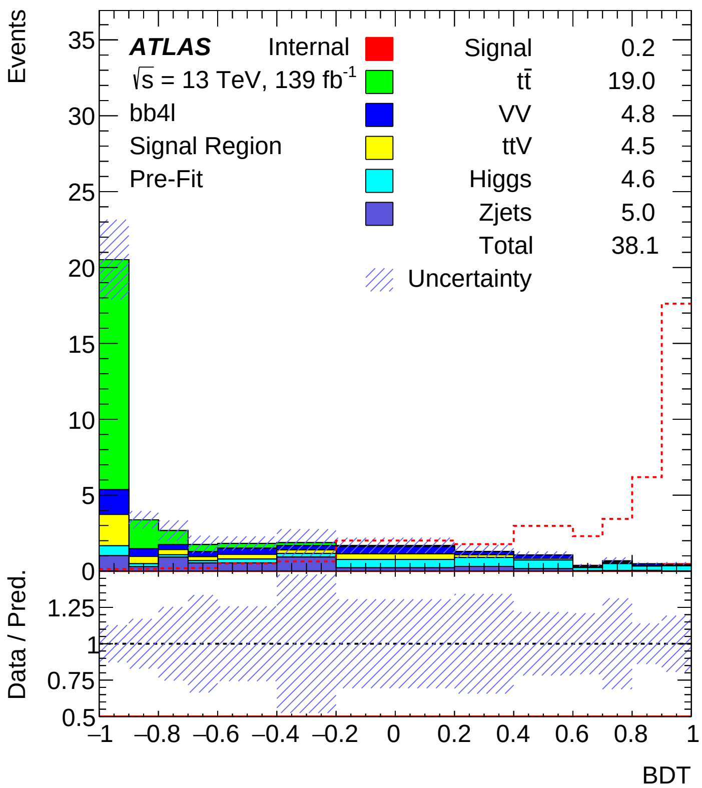

Figure 49: BDTG distribution in SR. Dashed line represents signal normalized to total background

9.3 Background estimation

As mentioned in Section 2, the dominant background in $4l + b\bar{b}$ channel includes the $t\bar{t}$, $t\bar{t}Z$, diboson, single Higgs and Z+jets processes. Since the event selection in SR is relatively loose, there would be a lot of fake events contributed by the non-prompt background, i.e. the $t\bar{t}$ and Z+jets process. Some other processes with exactly the same topology as the signal, i.e. the $t\bar{t}Z$, diboson and single Higgs process, also have some contribution. To estimate these dominant backgrounds, several dedicated control regions are defined to perform the template fit and derive normalization corrections for the MC results in SR: $t\bar{t}$ CR for $t\bar{t}$, $t\bar{t}Z$ CR for $t\bar{t}Z$, VV+Higgs CR for the combination of diboson with single Higgs, and Z+jets CR for Z+jets. These normalization corrections have a uniform prior and are validated in a validation region.

9.3.1 Control regions

To well define the CRs, their phase space should be kinematically close to SR in order to minimize the theoretical uncertainties related to this extrapolation and satisfy that each CR is orthogonal to SR. This ensures that the normalization correction determined in the fit for the background results in an accurate estimate of the dominant backgrounds process in CRs. Besides, CRs also need to be optimized to be enriched in SM events from the background process of interest and have a high purity with negligible contribution from the signal process. This helps to reduce the statistical uncertainty.

In this channel, the selected events in each CR are required to pass the selection of SR except the requirements below:

- $t\bar{t}$ CR: The sub-leading lepton pair is required not to be OSSF (anti-OSSF), which is ensured to be orthogonal to SR. The invariant mass of the leading lepton pair should be below 75 GeV or above 100 GeV to suppress the processes with Z decay.
- $t\bar{t}Z$ CR: The sub-leading lepton pair is required to be anti-OSSF. All the four leptons must pass the isolation to suppress the contribution from fake leptons. The invariant mass of the leading lepton pair should be above 75 GeV and below 100 GeV to suppress the processes without Z decay. The requirement on the invariant mass of the quadruplet is removed to enhance $t\bar{t}Z$ process.
- VV+Higgs CR: Events are required to contain no b jets to be orthogonal to SR. All the four leptons are required to pass the isolation.
- Z+jets CR: The p_T of the third and fourth leptons should be below 10 GeV to be orthogonal to SR. The invariant mass of the leading lepton pair should be above 75 GeV and below 100 GeV.

The differences between the above CRs with SR are summarized in Table 29. The BDT classifier introduced in Section H.2 is also applied to data and MC samples in CRs to obtain the BDTG distributions. The results are shown in Figure 50.

$t\bar{t}$ CR	Sub-leading pair anti-OSSF $M_{\text{leading pair}} < 75$ GeV or $M_{\text{leading pair}} > 100$ GeV
$t\bar{t}V$ CR	Sub-leading pair anti-OSSF All four leptons pass the isolation 75 GeV $< M_{\text{leading pair}} <$ 100 GeV No requirement on M_{4l}
VV+Higgs CR	$N_{\text{bjets}} = 0$ All four leptons pass the isolation
Z+jets CR	$p_{T,l_3(l_4)} < 10$ GeV 75 GeV $< M_{\text{leading pair}} <$ 100 GeV

Table 29: Definition of CRs. Only the differences with SR are listed.

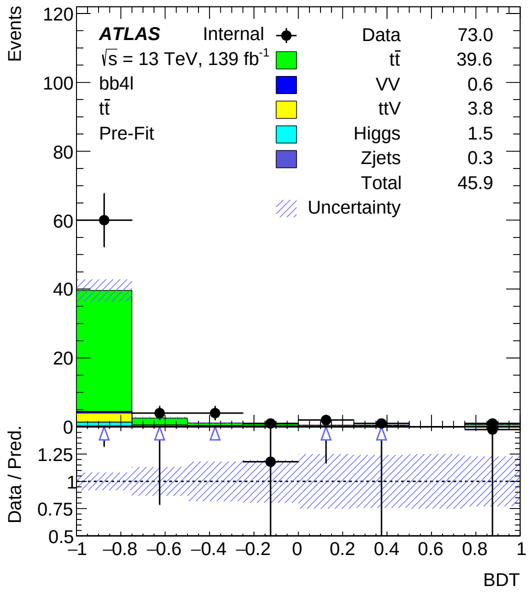

(a) $t\bar{t}$ CR

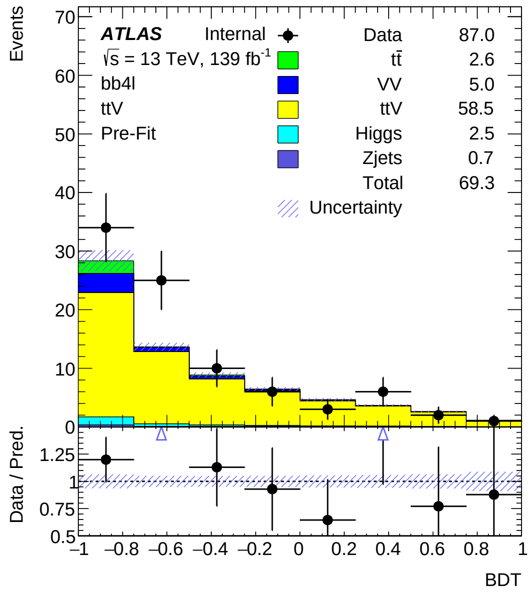

(b) $t\bar{t}$V CR

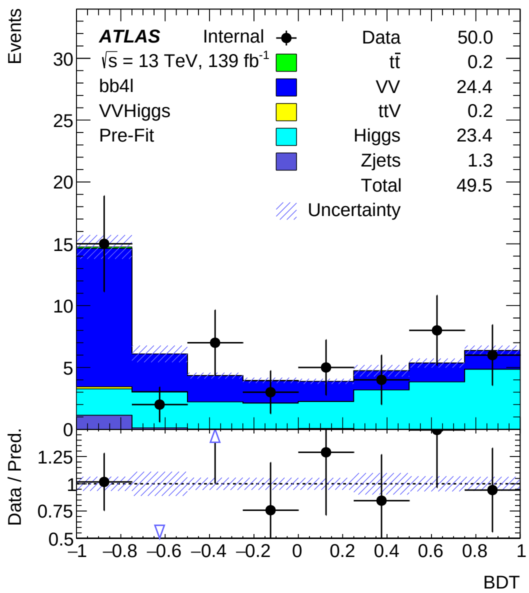

(c) VV+Higgs CR

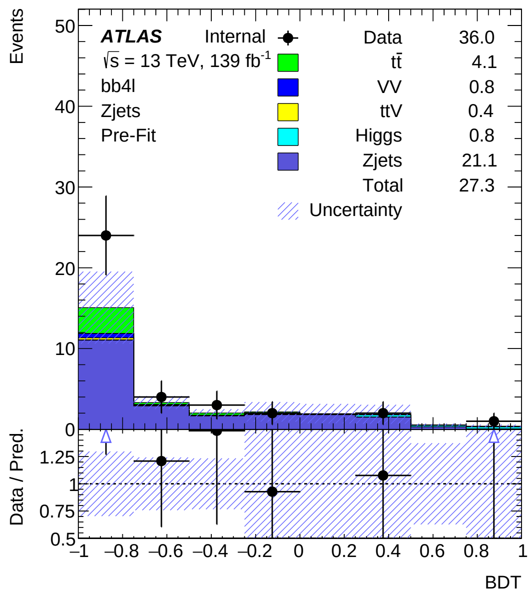

(d) Z+jets CR

Figure 50: Pre-fit results in each CR, (a) is $t\bar{t}$ CR, (b) is $t\bar{t}$V CR, (c) is VV+Higgs CR, (d) is Z+jets CR.

9.3.2 Fitting and validation

The normalization corrections on MC samples are derived from the background-only fit with the real data in CRs. This fit is performed with the distributions of BDTG as in order to avoid severe correlation on some specific variables between CRs with SR or VR, which ensures no bias on the extrapolation.

Table 30 shows the background yields in each CR before the correction and compares the expected yields with the observed yields. After the background-only fit performed in CRs simultaneously, the normalization factors (NFs) are extracted, respectively $\mu_{t\bar{t}} = 1.64 \pm 0.23$, $\mu_{t\bar{t}Z} = 1.28 \pm 0.17$, $\mu_{VV} = 0.89 \pm 0.35$, $\mu_{\text{Higgs}} = 1.13 \pm 0.35$, and $\mu_{Z\text{+jets}} = 1.16 \pm 0.37$, which are also listed in Table 30.

Event Yields						
	$t\bar{t}$ CR	$t\bar{t}Z$ CR	VV+Higgs CR	Z+jets CR	VR	SR
$t\bar{t}$	39.56±1.13	2.63±0.33	0.17±0.08	4.13±0.41	108.73±2.08	19.02±0.87
$t\bar{t}Z$	3.81±0.16	58.54±2.40	0.23±0.04	0.41±0.05	114.81±0.82	4.45±0.17
VV	0.61±0.07	5.05±0.34	24.37±1.31	0.82±0.05	104.34±0.59	4.84±0.13
Higgs	1.54±0.03	2.47±0.11	23.39±1.39	0.79±0.68	10.90±0.71	4.62±0.81
Z+jets	0.35±0.78	0.66±1.36	1.33±0.52	21.09±4.81	18.06±2.74	5.00±1.83
Total Bkg.	45.87±1.38	69.35±3.21	49.48±2.67	27.24±4.88	356.84±3.65	37.93±2.19
Data	73±9	87±9	50±7	36±6	457±21	-
Post-fit Normalization						
$\mu_{t\bar{t}} = 1.64 \pm 0.23$ | $\mu_{t\bar{t}Z} = 1.28 \pm 0.17$ | $\mu_{VV} = 0.89 \pm 0.35$ | $\mu_{\text{Higgs}} = 1.13 \pm 0.35$ | $\mu_{Z\text{+jets}} = 1.16 \pm 0.37$						

Table 30: The expected yields of the SM background in SR, CRs and VR compared to the observed yields. The NFs extracted from the background-only fit are listed in the bottom row. Only the statistical uncertainties are included.

.

With the background-only fit performed, distributions of BDTG in CRs are shown in Figure 51 after the MC simulated backgrounds corrected by the NFs. To validate these normalization corrections, a VR enriched with events from the dominant backgrounds is built. The definition of this VR is almost the same as SR except requiring the quadruplet satisfying $M_{4l} < 115$ GeV or $M_{4l} > 135$ GeV to be orthogonal to SR.

The above NFs are also extrapolated to the VR. The BDTG distributions in VR are shown in Figure 52 before and after the correction. Good agreement between the data and SM prediction provided by the post-fit is observed, which validates the correction.

9.3.3 Template fit uncertainties

The uncertainties from the template fit include the statistical uncertainties and the systematic uncertainties. The statistical uncertainties are derived from the CRs fit directly and listed in Table 30. The systematic uncertainties cover the potential bias on the extraction of normalization factors. Several sources of systemtic uncertainties are desribed below.

- NF evolution with p_T: Since the fake rate should be dependent on the lepton p_T, the uncertainty associated to the evolution of NFs with p_T is considered for the non-prompt background, i.e. the $t\bar{t}$ and Z+jets process. By varying the p_T range in the corresponding CRs and performing the CRs only fitting separately, the variation of NFs represents the systematic uncertainty.

  For the $t\bar{t}$ CR, there is extra requirement on the p_T of the fourth lepton, so a threshold of 6 GeV is selected on p_{T,l_4} to divided the $t\bar{t}$ CR into two part with similar statistics as shown in Table 31. Table 31 also shows the NFs extracted from $t\bar{t}$ CR with different p_T range.

  For the Z+jets CR, the p_T of the fourth lepton is required below 10 GeV. This threshold is varied to 8 GeV to extract the NF. The comparison between different p_T threshold is shown in Table.

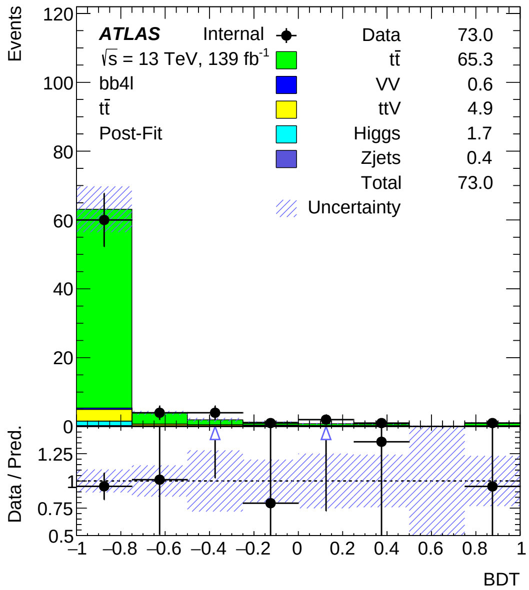

(a) $t\bar{t}$ CR

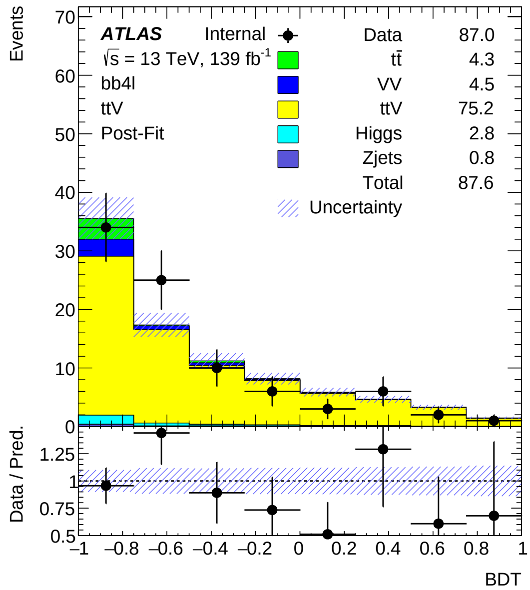

(b) $t\bar{t}$V CR

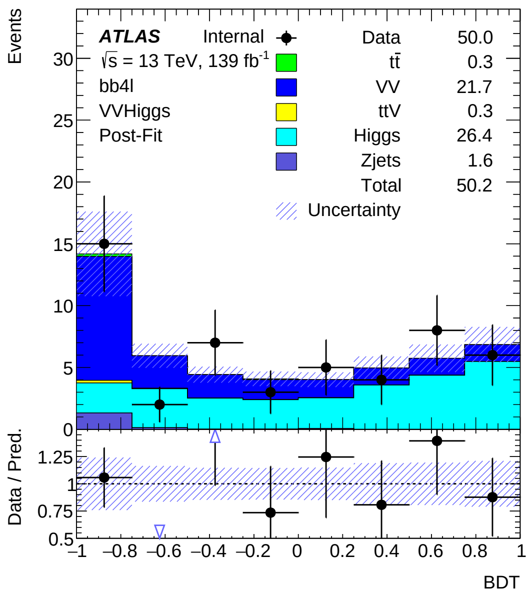

(c) VV+Higgs CR

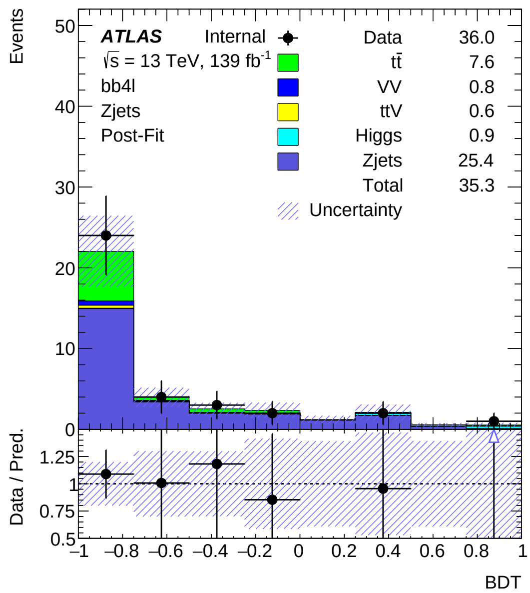

(d) Z+jets CR

Figure 51: Post-fit results in each CR, (a) is $t\bar{t}$ CR, (b) is $t\bar{t}$V CR, (c) is VV+Higgs CR, (d) is Z+jets CR.

- Non-closure: To validate the normalization correction, a VR is built and the post-fit results are shown in Section 9.3.2. The differences between data and MC is assigned as systematic uncertainties bin by bin.

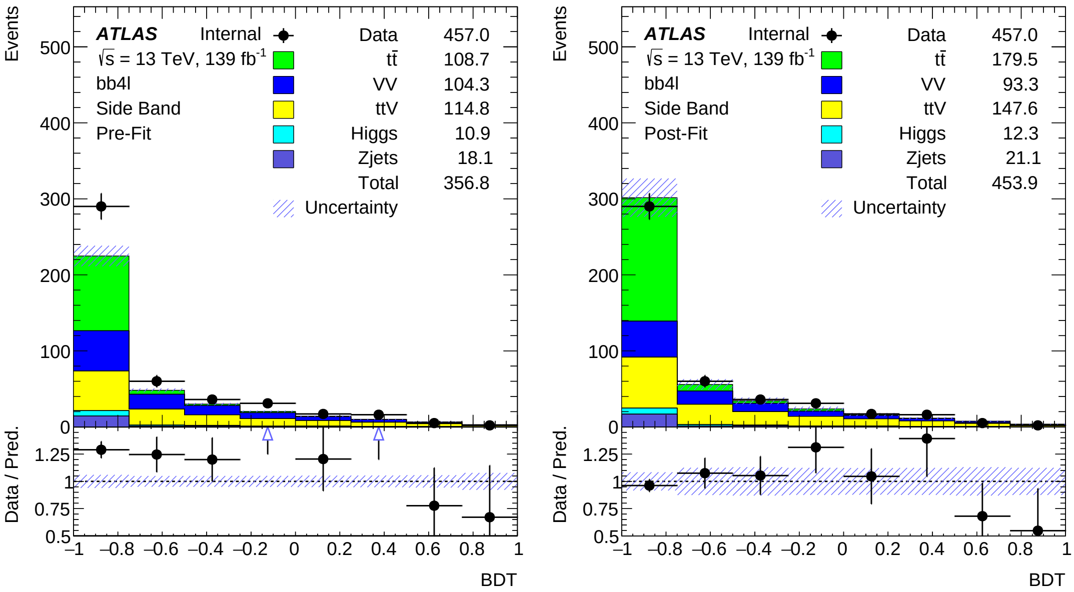

(a) Pre-fit (b) Post-fit

Figure 52: Pre-fit and post-fit results in VR, (a) is the pre-fit one, (b) is the post-fit one.

Event Yields			
$t\bar{t}$ CR	No requirement on p_{T,l_4}	p_{T,l_4} >5.5 GeV	p_{T,l_4} <5.5 GeV
$t\bar{t}$	39.56±1.13	20.29±0.90	19.31±0.87
$t\bar{t}Z$	3.81±0.16	2.65±0.13	1.17±0.10
VV	0.61±0.07	0.31±0.04	0.30±0.05
Higgs	1.54±0.03	1.21±0.02	0.32±0.01
Z+jets	0.35±0.78	0.66±0.39	-0.31±0.67
Total Bkg.	45.87±1.38	25.12±0.99	20.79±1.11
Data	73±9	32±6	41±6
Post-fit Normalization			
$\mu_{t\bar{t}}(p_{T,l_4} > 6\text{GeV}) = 1.24 \pm 0.23$ | $\mu_{t\bar{t}}(p_{T,l_4} < 6\text{GeV}) = 1.77 \pm 0.24$			

Table 31: The expected yields of the SM background in the $t\bar{t}$ CR compared to the observed yields. The NFs extracted from the background-only fit are listed in the bottom row. Only the statistical uncertainties are included.

.

9.4 Systematic uncertainties

The experimental and theoretical uncertainties, for both signal and background MC samples, are included in this analysis. The experimental uncertainties are described in Section 9.4.1, which are associated with objects reconstruction in the detector, pileup effects and luminosity. The theoretical uncertainties are described in Section 9.4.2, which are associated with parton density functions (PDF) sets, QCD scales, strong coupling constant α_S and parton shower models used in the MC simulation. The above uncertainties are combined and estimated from a simultaneous signal+background fit in SR and CRs. The results are presented in Section **??** in detail.

Event Yields		
Z+jets CR	p_{T,l_4} <10 GeV	p_{T,l_4} <8 GeV
$t\bar{t}$	4.13±0.41	3.14±0.36
$t\bar{t}Z$	0.41±0.05	0.22±0.04
VV	0.82±0.05	0.42±0.03
Higgs	0.79±0.68	0.04±0.01
Z+jets	21.09±4.81	19.18±3.38
Total Bkg.	27.24±4.88	22.99±3.4
Data	36±6	26±5
Post-fit Normalization		
$\mu_{t\bar{t}}(p_{T,l_4} < 10\text{GeV}) = 1.16 \pm 0.37$ | $\mu_{t\bar{t}}(p_{T,l_4} < 8\text{GeV}) = 1.10 \pm 0.32$		

Table 32: The expected yields of the SM background in the Z+jets CR compared to the observed yields. The NFs extracted from the background-only fit are listed in the bottom row. Only the statistical uncertainties are included.

.

9.4.1 Experimental uncertainties

The experimental uncertainties attributed to the muons come from reconstruction efficiency, transverse momentum resolution and energy scale. The uncertainties due to the reconstruction efficiency come from the statistical and systematic uncertainties of determining the scale factors, which are related to muon identification, isolation and track-to-vertex-association. The correction of p_T of the muon is affected by both scale and resolution uncertainties, for which the effect from ID and MS are considered respectively.

Similar to muons, the experimental uncertainties attributed to the electrons also come from transverse reconstruction efficiency, momentum resolution and energy scale. The uncertainties due to the reconstruction efficiency are combined in the "TOTAL" model and categorized into four items: reconstruction, identification, isolation and trigger. The correction of p_T of electrons is varied to get the corresponding uncertainties. In this analysis, a very simplified model "1NP_v1" is used to combine and categorized these variations into two items EG RESOLUTION ALL and EG SCALE ALL, where all the physical effects are summed in quadrature and considered fully correlated in eta.

Uncertainties of jet energy scale affects the E_T^{missing} reconstruction in this analysis. The systematic variation is applied through the tool "JetUncertaintiesTool" with a release using Moriond2016 calibration version. A "category reduction" model is used to evaluate the total uncertainty. The 75 in-situ parameters are combined based on their source (statistical, modelling, detector, mixed) with resulting 16 reduced nuisance parameters (NPs), and the remaining 13 original NPs round out this configuration for a total of 29 NPs.

The MC jets are smeared by JERSmearingTool to correct the jet energy resolution. This tool is also used to evaluate the JER systematic uncertainties. The "Full" configuration is applied and it contains 12 NPs in total.

The systematic uncertainties associated to the b-tagging are considered. They are evaluated as uncertainties on the scaling factor to take account for possible disagreement of the b-tag efficiency between data and MC. Separated scale factors and corresponding systematic uncertainties are provided for b-jets based on several measurements. Three separate nuisance parameters for each are included in the fitting procedure.

Missing transverse momentum is calculated using the preselected leptons and jets. The uncertainties of those objects are then passed into the uncertainties of missing E_T reconstruction. Besides those uncertainties, the uncertainties due to soft terms scale and resolution are also considered using METSystematicsTool. The uncertainties on the soft track component are derived from the agreement between data and MC of the p_T balance between the hard and soft MET components. The uncertainties are categorized in SoftTrk_Scale, SoftTrk_ResoPara and SoftTrk_ResoPerp, corresponding to offset along the p_T-Hard axis.

The systematic uncertainty of pile-up reweighting comes from the DataScaleFactor, which scales the μ to improve the data/MC agreement. The nominal value of DataScaleFactor is set to 1.0/1.09. It is then varied to 1.0 and 1/1.18 to represent the systematic uncertainty.

The uncertainty in the combined 2015-2018 integrated luminosity is 1.7%, obtained by using the LUCID-2 detector for the primary luminosity measurements.

9.4.2 Theoretical uncertainties

TBD

9.5 Statistical analysis

A signal+background fit is applied with Asimov data in SR and real data in CRs. The ranking plot for top 20 systematic uncertainties is shown in Figure 53. The pull and constraints of the NPs in this fit are shown in Figure 54. The correlation matrix between the NPs is shown in Figure 55.

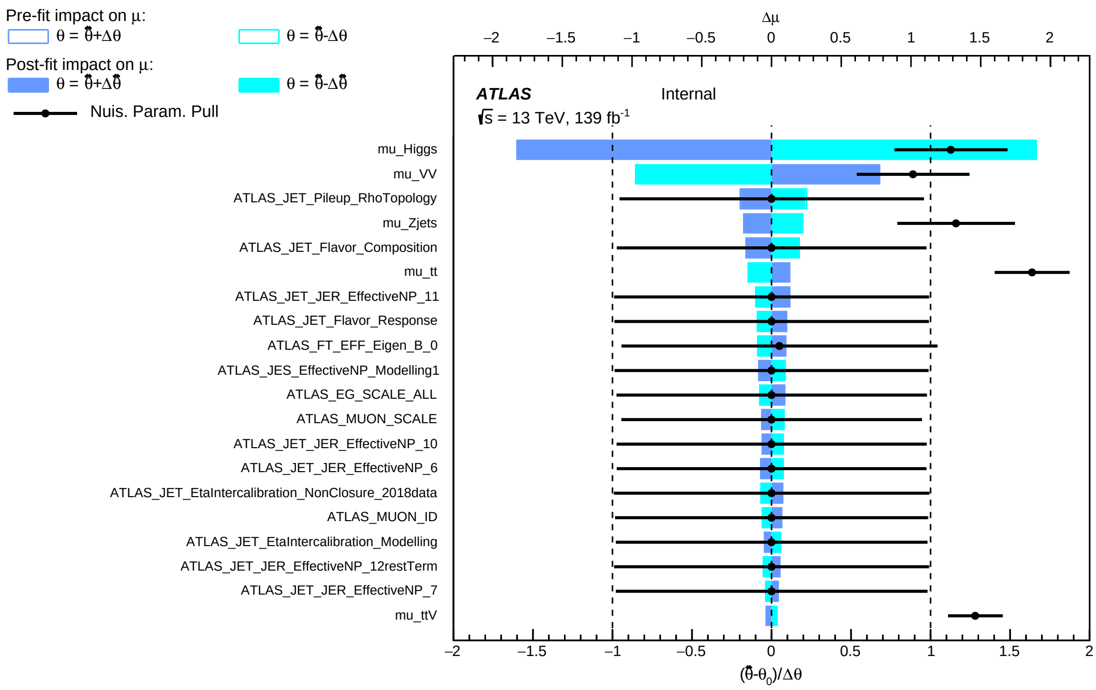

Figure 53: Ranking of the 20 NPs with the largest post-fit impact on μ in the fit for case SM signal. The empty blue rectangles correspond to the pre-fit impact on μ and the filled blue ones to the post-fit impact on μ, both referring to the upper scale. The impact of each NP, $\Delta\mu$, is computed by comparing the nominal best-fit value of μ with the result of the fit when fixing the considered NP to its best-fit value, $\hat{\theta}$ shifted by its pre-fit (post-fit) uncertainties $\pm\Delta\theta$ ($\pm\Delta\hat{\theta}$). The black points show the pulls of the NPs relative to their nominal values, θ_0.

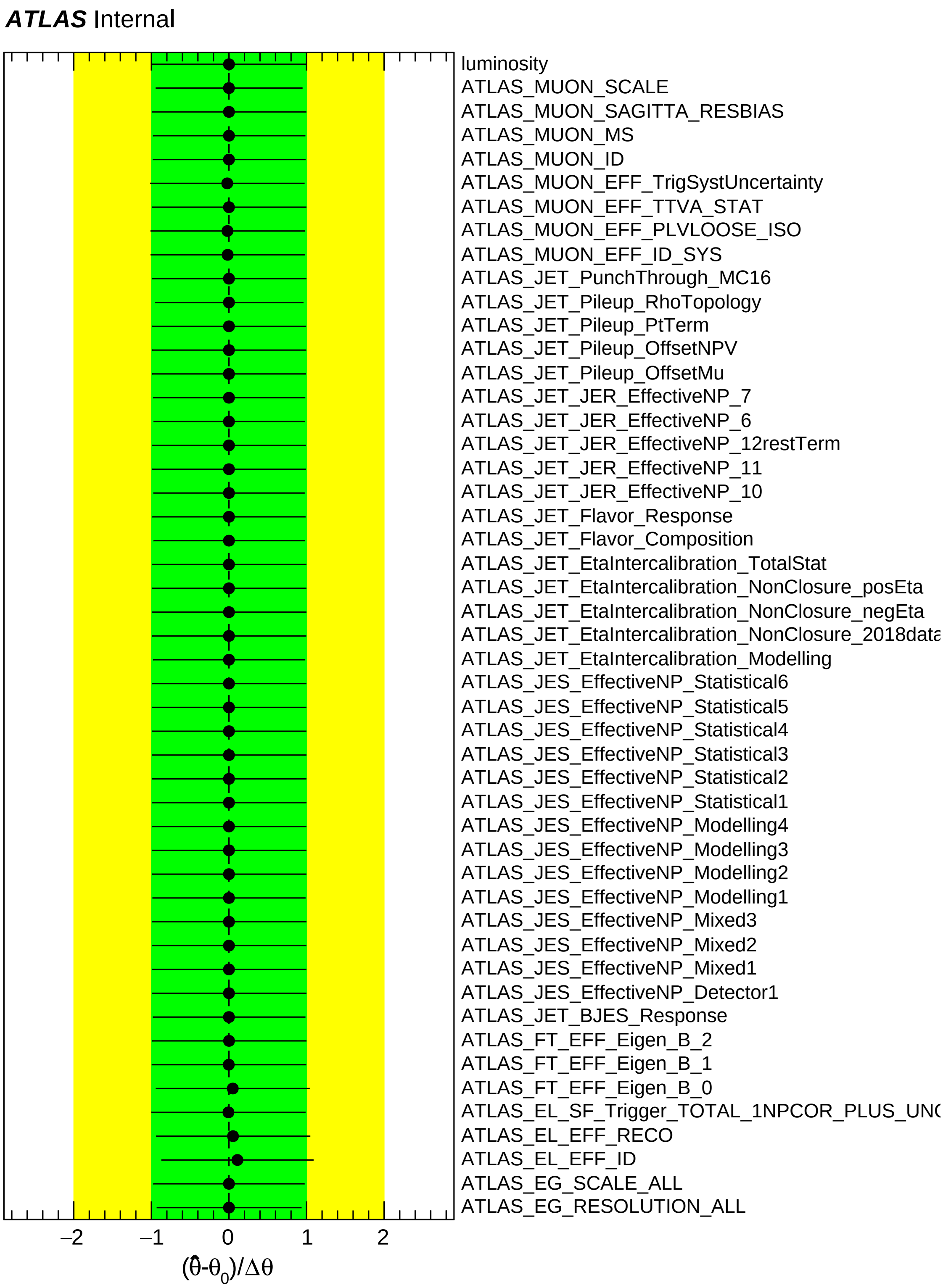

Figure 54: Plots of the pulls and constraints of the NPs in the fit with Asimov data in SR and real data in CRs.

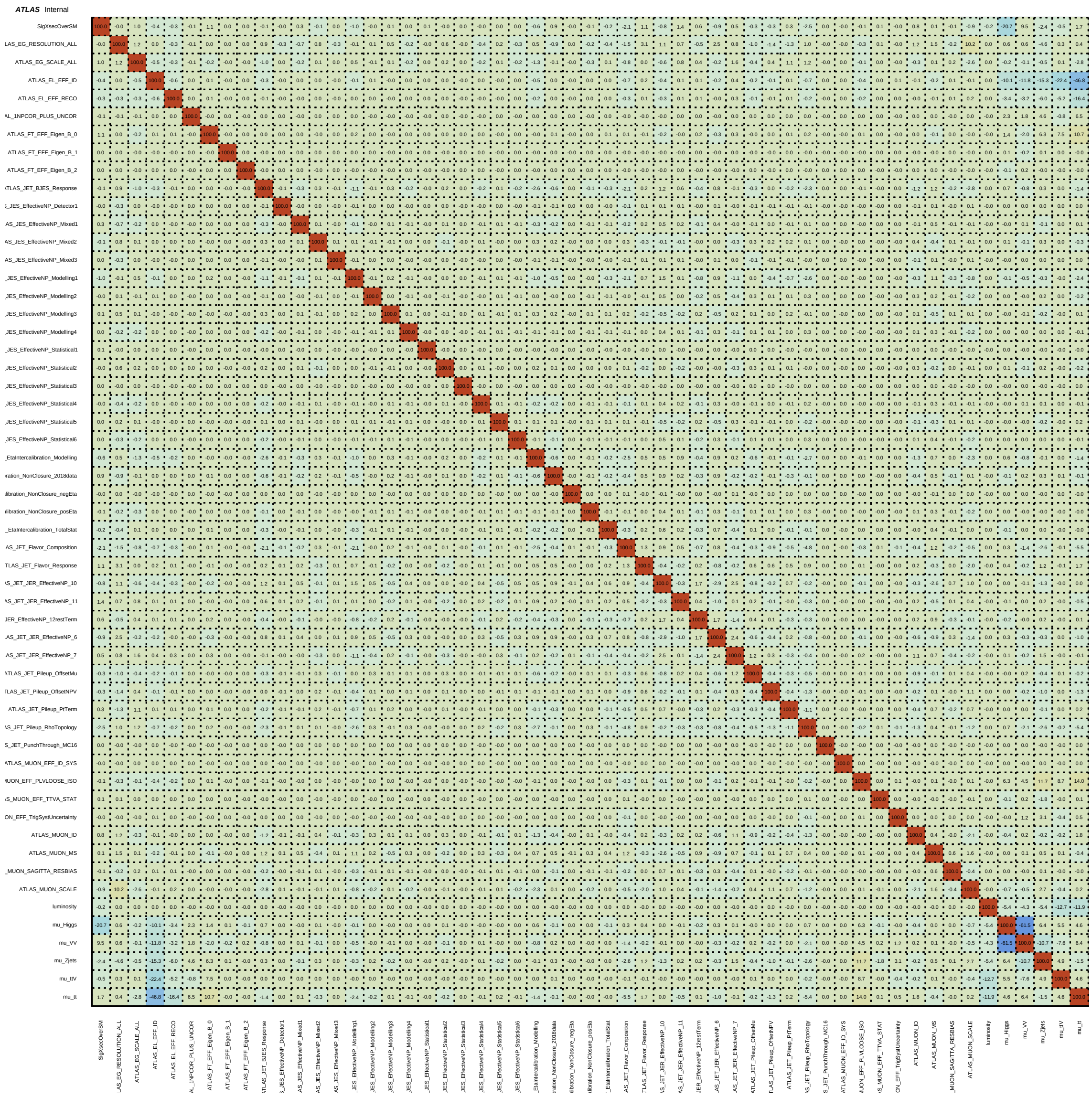

Figure 55: Correlation matrix between the fit parameters.

9.5.1 Upper limits on SM HH production

Following the procedure described in Section 11.1 we proceed to set upper-limits on the parameter of interest, i.e. the signal strength parameter for SM HH production, by using the CLs method. Table 33 shows upper limits with only statistical uncertainties included. Table 34 shows upper limits with systematic uncertainties included.

	-2σ	-1σ	Expected	$+1\sigma$	$+2\sigma$	Observed
$\sigma_{HH}/\sigma_{HH}^{SM}$	15.92	21.37	29.66	45.30	72.28	blinded

Table 33: Observed and expected upper limits on the SM non-resonant HH production cross-section at 95% CL and their ratios to the SM prediction. The $\pm 1\sigma$ and $\pm 2\sigma$ variations about the expected limit are also shown. Only statistical uncertainties are included.

	-2σ	-1σ	Expected	$+1\sigma$	$+2\sigma$	Observed
$\sigma_{HH}/\sigma_{HH}^{SM}$	15.93	21.39	29.68	45.43	73.28	blinded

Table 34: Observed and expected upper limits on the SM non-resonant HH production cross-section at 95% CL and their ratios to the SM prediction. The $\pm 1\sigma$ and $\pm 2\sigma$ variations about the expected limit are also shown. Both statistical and systemtic uncertainties are included.

10 Systematic uncertainties

This section is devoted to the systematic implementation in this analysis. Both experimental uncertainties and theoretical uncertainties are considered. Experimental systematics are described in sub-section 10.1 and the signal and background modelling theoretical systematics in sub-section 10.2.

10.1 Experimental uncertainties

Experimental uncertainties due to the reconstruction of physics objects, composed of light leptons, taus, jets, MET as well as the uncertainty on the integrated luminosity of the dataset are involved. The detector uncertainly terms are given by the recommendations from the SUSYTools getSystInfoList interface [61].

- **luminosity:** The uncertainly of the combined Run-2 dataset is 1.7%. It is derived, following a methodology similar to that detailed in [62], from a preliminary calibration of the luminosity scale using x-y beam-separation scans performed from 2015 to 2018. This uncertainty applied to all the MC samples but not for data and fake continuum background.
- **Pileup:** The pileup reweighing procedure is based on the comparing the average number of interactions per pp collision ($< \mu >$) in data to the corresponding simulated samples. The uncertainly on this method is obtained by varying the scaling factor in data.
- **Trigger:** Uncertainly on the efficiency of the electron and muon trigger selection are taken into account by using the related trigger scale factor as described in a general page [63]. For leptonic channels SLT or DLT strategy is used and the corresponded scale factor is applied.
- **Muons:** As described by Muon CP group [64], the uncertainties on efficiency, energy scale, resolution, object reconstruction, identification and isolation are taken into account. Table 35 list the details of the systematics included in this analysis. The efficiency uncertainly contains the statistical and systematic evaluations separately for the bad muon, isolation, reconstruction respect to low pt ($<$ 15 GeV) muon and above and the track-to-vertex association (TTVA).

MUON_ID
MUON_MS
MUON_SAGITTA_RESBIAS
MUON_SAGITTA_RHO
MUON_SCALE
MUON_EFF_BADMUON_STAT
MUON_EFF_BADMUON_SYS
MUON_EFF_ISO_STAT
MUON_EFF_ISO_SYS
MUON_EFF_RECO_STAT_LOWPT
MUON_EFF_RECO_STAT
MUON_EFF_RECO_SYS_LOWPT
MUON_EFF_RECO_SYS
MUON_EFF_TTVA_STAT
MUON_EFF_TTVA_SYS

Table 35: Systematic uncertainties associated to the muon

- **Electrons:** similarly to muons, We consider the resolution, scale, efficiency uncertainties provided by Egamma CP group [65]. The default correction model (TOTAL) uncertainties in the resolutions identification and isolated is not implemented, as the working point are different in terms of channels. This term is noted as EL_EFF_ISO_* .

EG_RESOLUTION_ALL
EG_SCALE_ALL
EG_SCALE_AF2, only for AF2
EL_EFF_ISO_*
EL_CHARGEID_STAT
EL_CHARGEID_SYStotal
EL_EFF_ChargeIDSel_TOTAL_1NPCOR_PLUS_UNCOR

Table 36: Systematic uncertainties associated to the electron.

- **Jets:** Jets are reconstructed from energy deposits forming topological clusters of calorimeter cells, using the anti-kt algorithm with radius parameter R=0.4. The jet energy scale (JES) calibration consists of several consecutive stages derived from a combination of MC-based methods and in situ techniques. The Jet energy resolution (JER) uncertainties is also considered [66].

JET_BJES_Response
JET_EffectiveNP_Detector1
JET_EffectiveNP_Detector2
JET_EffectiveNP_Mixed1
JET_EffectiveNP_Mixed2
JET_EffectiveNP_Mixed3
JET_EffectiveNP_Modelling1
JET_EffectiveNP_Modelling2
JET_EffectiveNP_Modelling3
JET_EffectiveNP_Modelling4
JET_EffectiveNP_Statistical1
JET_EffectiveNP_Statistical2
JET_EffectiveNP_Statistical3
JET_EffectiveNP_Statistical4
JET_EffectiveNP_Statistical5
JET_EffectiveNP_Statistical6
JET_EtaIntercalibration_Modelling
JET_EtaIntercalibration_NonClosure_2018data
JET_EtaIntercalibration_NonClosure_highE
JET_EtaIntercalibration_NonClosure_negEta
JET_EtaIntercalibration_NonClosure_posEta
JET_EtaIntercalibration_TotalStat
JET_Flavor_Composition
JET_Flavor_Response
JET_Pileup_OffsetMu
JET_Pileup_OffsetNPV
JET_Pileup_PtTerm
JET_Pileup_RhoTopology
JET_PunchThrough (AFII/MC16)
JET_RelativeNonClosure (AFII only)
JET_SingleParticle_HighPt
JER_DataVsMC (AFII/MC16)
JER_Effective_NP_1
JER_Effective_NP_2
JER_Effective_NP_3
JER_Effective_NP_4
JER_Effective_NP_5
JER_Effective_NP_6
JER_Effective_NP_7_RestTerm

Table 37: Systematic uncertainties associated to JES and JER

- **Flavour Tagging:** In most of the signal regions, expect for $bbZZ$ 4l channel, a b-jet veto is applied at 77% tagging efficiency to be orthogonal with other di-Higgs analysis. The uncertainties arise from the efficiency of the tagger to select jets containing a true b-hardon, charmed hadron, light hardons or coming from hadronically-decaying taus. The corresponded scale factors can be retrieved by the BtaggingEfficiencyTool and its getScaleFactor method [67].

FT_EFF_B_systematics
FT_EFF_C_systematics
FT_EFF_Light_systematics
FT_EFF_extrapolation
FT_EFF_extrapolation_from_charm

Table 38: Systematic uncertainties associated to the missing transverse momentum.

- **Missing Transverse Momentum:** The systematic variations is respect to the scale, parallel resolution, and perpendicular resolution of the soft term E_T^{miss}.

MET_SoftTrk_ResoPara
MET_SoftTrk_ResoPerp
MET_SoftTrk_Scale

Table 39: Systematic uncertainties associated to the missing transverse momentum.

10.2 Theory uncertainties

The sources of theory uncertainties is summarized in this sub-section, for both signal and background. The list of uncertainties can be found in Table 40.

ggF HH: Inclusive ggF cross sections for Higgs boson pair production are reported in [68] for $m_H = 125$ GeVwith the central scale $\mu_0 = \mu_R = \mu_F = M_{HH}/2$. The uncertainties scheme to be considered are PDF, α_S (combined "PDF + α_S unc"), scale and m_{top} (combined "Scale + mtop unc"), as recommended by LHC-HH group [69].

ttH: Cross sections are calculated at NLO QCD and NLO EW accuracies, the corresponded uncertainties in QCD scale and PDF are taken from CERN Report4 [70].

ttV: [71]

Other prompt backgrounds: For other multiboson processes (VV, VVV), V + γ, and rare decay (tZ, WtZ, ttWW ...) processes, their cross section uncertainties are not determined yet at this moment.

10.3 Uncertainties on data-driven background estimation

Global description of the data driven uncertainties will be documented here.

Process	X-section [%]
HH signal	QCD Scale:$^{+2.2}_{-5}$, PDF(+α_S): $^{+3}_{-3}$, m_{top} :$^{+2.6}_{-2.6}$
$t\bar{t}H$	QCD Scale:$^{+5.8}_{-9.2}$, PDF(+α_S): $^{+3.6}_{-3.6}$
$t\bar{t}Z$	QCD Scale:$^{+9.6}_{-11.3}$, PDF:$^{+4}_{-4}$
$t\bar{t}W$	QCD Scale:$^{+12.9}_{-11.5}$, PDF:$^{+3.4}_{-3.4}$
$t\bar{t}$	± -
$V\gamma$	± -
$DrellYan$	± -
VV	± -
VVV	± -
$raretop$	± -

Table 40: Summary of theoretical uncertainties for the MC predictions of different processes.

11 The Combined results of different channels

11.1 Statistical model

The statistical model is built up with a binned likelihood function. In order to obtain the cross section of $pp \to hh$ production, this likelihood fit is performed for the number of events in the signal regions and the control regions of all sub-channels simultaneously. For a blinded analysis, the number of observed data events in the signal regions is taken from the sum of the expected MC for SM processes. The likelihood is constructed as follows

$$\mathcal{L} = \prod_{c \in \text{channels}} \prod_{b \in \text{bins}} \text{Poisson}(n^{\text{obs}}_{c,b} | n^S_{c,b}, n^B_{c,b}) \times \prod_{s \in \mathbb{S}} \mathcal{G}(0|\theta_s, 1), \tag{6}$$

where c stands for the channel index, b is the bin index for each channel. The Poisson terms Poisson are given by

$$\text{Poisson}(n^{\text{obs}}_{c,b} | n^S_{c,b}, n^B_{c,b}) = \frac{1}{n^{\text{obs}}_{c,b}!} \left(\mu * S_{c,b} + n^B_{c,b}\right)^{n^{\text{obs}}_{c,b}} \exp^{-\left(\mu * S_{c,b} + n^B_{c,b}\right)} \tag{7}$$

where number of events observed in each bin is marked as $n^{\text{obs}}_{c,b}$, and the expected numbers of signal and background is the corresponded bin is $n^S_{c,b}$ and $n^B_{c,b}$, respectively. The Parameter-of-interest (POI) μ is the signal strength, which is shared among different bins and channels. To represent the nuisance parameter (NP) constraint terms, a Gaussian function, $\mathcal{G}(0|\theta_s, 1)$ is considered, where θ_s is the NP term.

11.2 Test statistic

The procedure of statistical computation uses the profile likelihood ratio test statistic $\tilde{q}_\mu$,

$$\tilde{\lambda}(\mu) = \begin{cases} \frac{\mathcal{L}(\mu, \hat{\hat{\theta}}(\mu))}{\mathcal{L}(\hat{\mu}, \hat{\hat{\theta}}(\hat{\theta}))} & \hat{\mu} \geq 0, \\ \frac{\mathcal{L}(\mu, \hat{\hat{\theta}}(\mu))}{\mathcal{L}(0, \hat{\hat{\theta}}(0))} & \hat{\mu} < 0. \end{cases} \tag{8}$$

Where $\hat{\hat{\boldsymbol{\theta}}}(0)$ and $\hat{\hat{\boldsymbol{\theta}}}(\mu)$ is the conditional maximum likelihood (ML) estimators of $\boldsymbol{\theta}$ for a given strength 0 and μ, respectively. The test statistic $\tilde{q}_\mu$ is given by

$$\tilde{q}_\mu = \begin{cases} -2 \ln \frac{\mathcal{L}(\mu, \hat{\hat{\theta}}(\mu))}{\mathcal{L}(0, \hat{\hat{\theta}}(0))} & \hat{\mu} < 0, \\ -2 \ln \frac{\mathcal{L}(\mu, \hat{\hat{\theta}}(\mu))}{\mathcal{L}(\hat{\mu}, \hat{\hat{\theta}})} & 0 \leq \hat{\mu} \leq \mu, \\ 0 & \hat{\mu} > \mu. \end{cases} \tag{9}$$

The upper limit on the cross section of di-Higgs production is derived at 95% confidence level by means of the CL_s method, with the asymptotic approximation, the procedure is described in [72].

11.3 Overview of the statistical procedure

The setup of signal regions and control regions, as well as the discriminating variables can be found in the corresponding section. The statistical analysis is performed with TrexFitter package [73, 74]. The asimov datasets for the signal regions is used to determine the expected upper limits, the contribution of MC statistical uncertainties are added during the fit with an extra poisson term (γ) for each bin. Regions of all channels are summarized in the Table 41. The bin width of the signal region is not yet optimized.

Table 41: Regions and POI used for each channel. The POI in the TRexFitter configuration is "mu_XS_hh".

Channels	Signal Regions	Control Regions	Norm Factors
2ℓSS	1	5	4
3ℓ	1	4	4
$b\bar{b}4\ell$	1	5	5
1ℓ+$2\tau_{\text{had}}$	1	-	-
2ℓ+$2\tau_{\text{had}}$	1	-	-
2ℓSS+$1\tau_{\text{had}}$	1	5	4
$\gamma\gamma$+ℓj	1	-	-
$\gamma\gamma$+$\tau_{\text{had}} j$	1	-	-
$\gamma\gamma$+2L	1	-	-

11.4 Preliminary results

The results shown in this sub section are obtained by preforming signal + background fit with part of systematic MC in the multilepton signal regions. The theoretical uncertainties on signal and background MC are not derived yet. Asimov datasets are assumed in all signal regions for the upper limit setting. Prepared individual workspaces for combination are:

- 2ℓSS: detector systematic on prompt backgrounds, partial data driven uncertainties included.
- 3ℓ: detector systematic included.
- $b\bar{b}4\ell$: detector systematic included.
- $\gamma\gamma + ML$: detector systematic included .
- τ channels with MC simulation background.

Figure 56 presents the pulls and constrains on the nuisance parameters listed by channels. No obvious constraint are observed in the fit. Those no-overlap terms, especially the JER/JES related uncertainties, indicate that they are not yet correlated in the combined fit. Improving that is a task in the future.

The norm factors in the combined fit are fail to float due to the intermediate datasets in which the real data are involved in the CRs are not able to propagate to final fit. The fitted values are hold at 1.

The results of signal upper limits and strength from this combined fit are displayed in Figure 57.

for the next fit.

Table 42: Upper limits on the signal strength shown as $\texttt{Median}^{+\sigma}_{-\sigma}$. Asimov data is used to derive the limit in statistic only and detector systematic included case.

Channels	Stats. Only (Asimov)	Systematics (Asimov)
2ℓSS	$32.34^{51.69}_{26.25}$	$35.8^{50.77}_{28.85}$
3ℓ	$34.9^{51.69}_{26.25}$	$35.5^{50.31}_{25.59}$
$b\bar{b}4\ell$	$28.85^{44.01}_{20.79}$	$28.97^{44.28}_{20.87}$
1ℓ+$2\tau_{\text{had}}$	$32.7^{49.60}_{23.56}$	-
2ℓSS+$1\tau_{\text{had}}$	$46.15^{66.60}_{24.77}$	-
$\gamma\gamma + ML$	$14.98^{21.86}_{10.79}$	$15.00^{21.11}_{10.81}$
Combined	$9.98^{14.33}_{7.19}$	$10.12^{14.54}_{7.29}$

TODO: On going work: Previously the combination is preformed by Trexfitter with "multifit". It is found that there are a couple of inconvenience: the mixed dataset can not be passed to combined workspace; the post Fit plots are not available. It is suggested to move the workflow to standard fit. Works are on going to intergate all steerings to one configuration file.

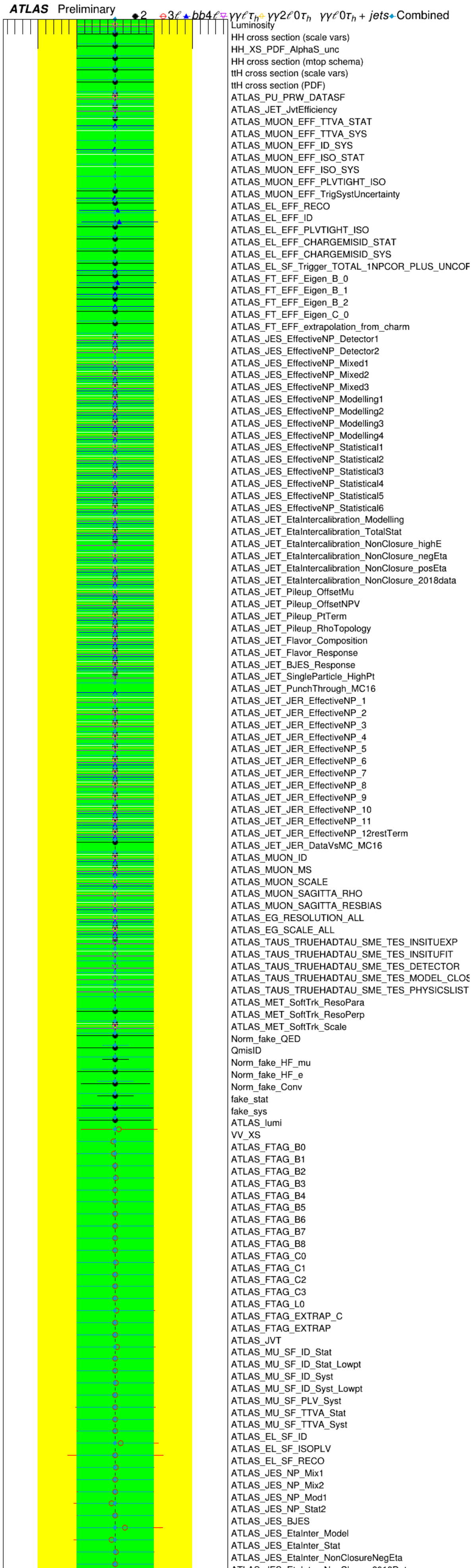
ATLAS Preliminary
2ℓ
3ℓ
bb4ℓ
γγℓτh
γγ2ℓ0τh
γγℓ0τh + jets
Combined
Luminosity
HH cross section (scale vars)
HH_XS_PDF_AlphaS_unc
HH cross section (mtop schema)
ttH cross section (scale vars)
ttH cross section (PDF)
ATLAS_PU_PRW_DATASF
ATLAS_JET_JvtEfficiency
ATLAS_MUON_EFF_TTVA_STAT
ATLAS_MUON_EFF_TTVA_SYS
ATLAS_MUON_EFF_ID_SYS
ATLAS_MUON_EFF_ISO_STAT
ATLAS_MUON_EFF_ISO_SYS
ATLAS_MUON_EFF_PLVTIGHT_ISO
ATLAS_MUON_EFF_TrigSystUncertainty
ATLAS_EL_EFF_RECO
ATLAS_EL_EFF_ID
ATLAS_EL_EFF_PLVTIGHT_ISO
ATLAS_EL_EFF_CHARGEMISID_STAT
ATLAS_EL_EFF_CHARGEMISID_SYS
ATLAS_EL_SF_Trigger_TOTAL_1NPCOR_PLUS_UNCOR
ATLAS_FT_EFF_Eigen_B_0
ATLAS_FT_EFF_Eigen_B_1
ATLAS_FT_EFF_Eigen_B_2
ATLAS_FT_EFF_Eigen_C_0
ATLAS_FT_EFF_extrapolation_from_charm
ATLAS_JES_EffectiveNP_Detector1
ATLAS_JES_EffectiveNP_Detector2
ATLAS_JES_EffectiveNP_Mixed1
ATLAS_JES_EffectiveNP_Mixed2
ATLAS_JES_EffectiveNP_Mixed3
ATLAS_JES_EffectiveNP_Modelling1
ATLAS_JES_EffectiveNP_Modelling2
ATLAS_JES_EffectiveNP_Modelling3
ATLAS_JES_EffectiveNP_Modelling4
ATLAS_JES_EffectiveNP_Statistical1
ATLAS_JES_EffectiveNP_Statistical2
ATLAS_JES_EffectiveNP_Statistical3
ATLAS_JES_EffectiveNP_Statistical4
ATLAS_JES_EffectiveNP_Statistical5
ATLAS_JES_EffectiveNP_Statistical6
ATLAS_JET_EtaIntercalibration_Modelling
ATLAS_JET_EtaIntercalibration_TotalStat
ATLAS_JET_EtaIntercalibration_NonClosure_highE
ATLAS_JET_EtaIntercalibration_NonClosure_negEta
ATLAS_JET_EtaIntercalibration_NonClosure_posEta
ATLAS_JET_EtaIntercalibration_NonClosure_2018data
ATLAS_JET_Pileup_OffsetMu
ATLAS_JET_Pileup_OffsetNPV
ATLAS_JET_Pileup_PtTerm
ATLAS_JET_Pileup_RhoTopology
ATLAS_JET_Flavor_Composition
ATLAS_JET_Flavor_Response
ATLAS_JET_BJES_Response
ATLAS_JET_SingleParticle_HighPt
ATLAS_JET_PunchThrough_MC16
ATLAS_JET_JER_EffectiveNP_1
ATLAS_JET_JER_EffectiveNP_2
ATLAS_JET_JER_EffectiveNP_3
ATLAS_JET_JER_EffectiveNP_4
ATLAS_JET_JER_EffectiveNP_5
ATLAS_JET_JER_EffectiveNP_6
ATLAS_JET_JER_EffectiveNP_7
ATLAS_JET_JER_EffectiveNP_8
ATLAS_JET_JER_EffectiveNP_9
ATLAS_JET_JER_EffectiveNP_10
ATLAS_JET_JER_EffectiveNP_11
ATLAS_JET_JER_EffectiveNP_12restTerm
ATLAS_JET_JER_DataVsMC_MC16
ATLAS_MUON_ID
ATLAS_MUON_MS
ATLAS_MUON_SCALE
ATLAS_MUON_SAGITTA_RHO
ATLAS_MUON_SAGITTA_RESBIAS
ATLAS_EG_RESOLUTION_ALL
ATLAS_EG_SCALE_ALL
ATLAS_TAUS_TRUEHADTAU_SME_TES_INSITUEXP
ATLAS_TAUS_TRUEHADTAU_SME_TES_INSITUFIT
ATLAS_TAUS_TRUEHADTAU_SME_TES_DETECTOR
ATLAS_TAUS_TRUEHADTAU_SME_TES_MODEL_CLOS
ATLAS_TAUS_TRUEHADTAU_SME_TES_PHYSICSLIST
ATLAS_MET_SoftTrk_ResoPara
ATLAS_MET_SoftTrk_ResoPerp
ATLAS_MET_SoftTrk_Scale
Norm_fake_QED
QmisID
Norm_fake_HF_mu
Norm_fake_HF_e
Norm_fake_Conv
fake_stat
fake_sys
ATLAS_lumi
VV_XS
ATLAS_FTAG_B0
ATLAS_FTAG_B1
ATLAS_FTAG_B2
ATLAS_FTAG_B3
ATLAS_FTAG_B4
ATLAS_FTAG_B5
ATLAS_FTAG_B6
ATLAS_FTAG_B7
ATLAS_FTAG_B8
ATLAS_FTAG_C0
ATLAS_FTAG_C1
ATLAS_FTAG_C2
ATLAS_FTAG_C3
ATLAS_FTAG_L0
ATLAS_FTAG_EXTRAP_C
ATLAS_FTAG_EXTRAP
ATLAS_JVT
ATLAS_MU_SF_ID_Stat
ATLAS_MU_SF_ID_Stat_Lowpt
ATLAS_MU_SF_ID_Syst
ATLAS_MU_SF_ID_Syst_Lowpt
ATLAS_MU_SF_PLV_Syst
ATLAS_MU_SF_TTVA_Stat
ATLAS_MU_SF_TTVA_Syst
ATLAS_EL_SF_ID
ATLAS_EL_SF_ISOPLV
ATLAS_EL_SF_RECO
ATLAS_JES_NP_Mix1
ATLAS_JES_NP_Mix2
ATLAS_JES_NP_Mod1
ATLAS_JES_NP_Stat2
ATLAS_JES_BJES
ATLAS_JES_EtaInter_Model
ATLAS_JES_EtaInter_Stat
ATLAS_JES_EtaInter_NonClosureNegEta

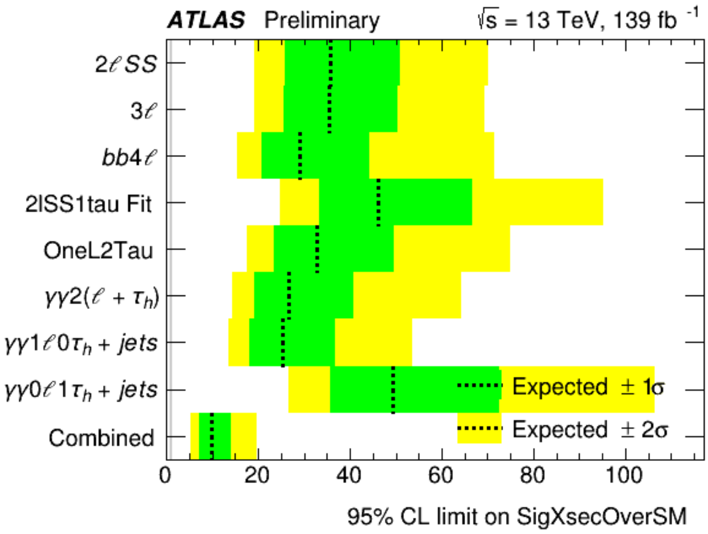

Figure 57: Combined upper limits.

References

[1] ATLAS Collaboration, *Search for Higgs boson pair production in the $\gamma\gamma WW^*$ channel using pp collision data recorded at $\sqrt{s} = 13$ TeV with the ATLAS detector*, Eur. Phys. J. C **78** (2018) 1007, arXiv: 1807.08567 [hep-ex] (cit. on p. 7).

[2] ATLAS Collaboration, *Search for Higgs boson pair production in the $WW^{(*)}WW^{(*)}$ decay channel using ATLAS data recorded at $\sqrt{s} = 13$ TeV*, JHEP **05** (2019) 124, arXiv: 1811.11028 [hep-ex] (cit. on p. 7).

[3] ATLAS Collaboration, *Observation of a new particle in the search for the Standard Model Higgs boson with the ATLAS detector at the LHC*, Phys. Lett. B **716** (2012) 1, arXiv: 1207.7214 [hep-ex] (cit. on p. 9).

[4] CMS Collaboration, *Observation of a new boson at a mass of 125 GeV with the CMS experiment at the LHC*, Phys. Lett. B **716** (2012) 30, arXiv: 1207.7235 [hep-ex] (cit. on p. 9).

[5] L. Evans and P. Bryant, *LHC Machine*, JINST **3** (2008) S08001 (cit. on p. 9).

[6] ATLAS Collaboration, *Measurement of the Higgs boson mass in the $H \to ZZ^* \to 4\ell$ and $H \to \gamma\gamma$ channels with $\sqrt{s} = 13$ TeV pp collisions using the ATLAS detector*, Phys. Lett. B **784** (2018) 345, arXiv: 1806.00242 [hep-ex] (cit. on p. 9).

[7] ATLAS Collaboration, *Measurement of the Higgs boson mass from the $H \to \gamma\gamma$ and $H \to ZZ^* \to 4\ell$ channels in pp collisions at center-of-mass energies of 7 and 8 TeV with the ATLAS detector*, Phys. Rev. D **90** (2014) 052004, arXiv: 1406.3827 [hep-ex] (cit. on p. 9).

[8] ATLAS and CMS Collaborations, *Combined Measurement of the Higgs Boson Mass in pp Collisions at $\sqrt{s} = 7$ and 8 TeV with the ATLAS and CMS Experiments*, Phys. Rev. Lett. **114** (2015) 191803, arXiv: 1503.07589 [hep-ex] (cit. on p. 9).

[9] CMS Collaboration, *Precise determination of the mass of the Higgs boson and tests of compatibility of its couplings with the standard model predictions using proton collisions at 7 and 8 TeV*, Eur. Phys. J. C **75** (2015) 212, arXiv: 1412.8662 [hep-ex] (cit. on p. 9).

[10] T. Binoth, S. Karg, N. Kauer and R. Rückl, *Multi-Higgs boson production in the standard model and beyond*, Phys. Rev. D **74** (11 2006) 113008, URL: https://link.aps.org/doi/10.1103/PhysRevD.74.113008 (cit. on p. 9).

[11] B. Fuks, J. H. Kim and S. J. Lee, *Probing Higgs boson self-interactions in proton-proton collisions at a center-of-mass energy of 100 TeV*, Phys. Rev. D **93** (3 2016) 035026, URL: https://link.aps.org/doi/10.1103/PhysRevD.93.035026 (cit. on p. 9).

[12] *Higgs cross sections for HL-LHC and HE-LHC*, URL: https://twiki.cern.ch/twiki/bin/view/LHCPhysics/HiggsEuropeanStrategy#SM_Higgs_production_cross_se_AN2 (visited on 27/08/2021) (cit. on p. 9).

[13] ATLAS Collaboration, *Measurement of the $t\bar{t}$ production cross-section using $e\mu$ events with b-tagged jets in pp collisions at $\sqrt{s} = 13$ TeV with the ATLAS detector*, Phys. Lett. B **761** (2016) 136, arXiv: 1606.02699 [hep-ex] (cit. on p. 10), Erratum: Phys. Lett. B **772** (2017) 879.

[14] ATLAS Collaboration, *Measurements of the $t\bar{t}$ production cross-section in the dilepton and lepton-plus-jets channels and of the ratio of the $t\bar{t}$ and Z boson cross-sections in pp collisions at $\sqrt{s} = 13$ TeV with the ATLAS detector*, ATLAS-CONF-2015-049, 2015, URL: https://cds.cern.ch/record/2052605 (cit. on p. 10).

[15] ATLAS Collaboration, *Measurement of the Higgs boson production cross section at* 7, 8 *and* 13 *TeV center-of-mass energies in the* $H \rightarrow \gamma\gamma$ *channel with the ATLAS detector*, ATLAS-CONF-2015-060, 2015, URL: https://cds.cern.ch/record/2114826 (cit. on p. 10).

[16] ATLAS Collaboration, *Searches for Higgs boson pair production in the* $hh \rightarrow bb\tau\tau, \gamma\gamma WW^{*}, \gamma\gamma bb, bbbb$ *channels with the ATLAS detector*, Phys. Rev. D **92** (2015) 092004, arXiv: 1509.04670 [hep-ex] (cit. on p. 10).

[17] G. Aad et al., *Combination of searches for Higgs boson pairs in* pp *collisions at* $\sqrt{s}$ *=13 TeV with the ATLAS detector*, Phys. Lett. B **800** (2020) 135103, arXiv: 1906.02025 [hep-ex] (cit. on p. 10).

[18] CMS Collaboration, *Search for two Higgs bosons in final states containing two photons and two bottom quarks in proton–proton collisions at* 8 *TeV*, Phys. Rev. D **94** (2016) 052012, arXiv: 1603.06896 [hep-ex] (cit. on p. 10).

[19] CMS Collaboration, *Search for Higgs boson pair production in the* $bb\tau\tau$ *final state in proton–proton collisions at* $\sqrt{(s)} = 8$ *TeV*, Phys. Rev. D **96** (2017) 072004, arXiv: 1707.00350 [hep-ex] (cit. on p. 10).

[20] *Combination of searches for Higgs boson pair production in proton-proton collisions at* $\sqrt{s} = 13$ TeV, tech. rep., CERN, 2018, URL: https://cds.cern.ch/record/2628486 (cit. on p. 10).

[21] *PileupReweighting*, URL: https://twiki.cern.ch/twiki/bin/viewauth/AtlasProtected/ExtendedPileupReweighting (cit. on p. 12).

[22] J. Alwall et al., *The automated computation of tree-level and next-to-leading order differential cross sections, and their matching to parton shower simulations*, JHEP **07** (2014) 079, arXiv: 1405.0301 [hep-ph] (cit. on pp. 15, 16).

[23] T. Sjöstrand et al., *High-energy-physics event generation with Pythia 6.1*, Comput. Phys. Commun. **135** (2001) 238, arXiv: hep-ph/0010017 [hep-ph] (cit. on p. 16).

[24] T. Sjöstrand, S. Mrenna and P. Skands, *A brief introduction to PYTHIA 8.1*, Comput. Phys. Commun. **178** (2008) 852, arXiv: 0710.3820 [hep-ph] (cit. on p. 16).

[25] M. Bahr et al., *Herwig++ physics and manual*, Eur. Phys. J. C **58** (2008) 639, arXiv: 0803.0883 [hep-ph] (cit. on p. 16).

[26] J. Bellm et al., *Herwig 7.0/Herwig++ 3.0 release note*, Eur. Phys. J. C **76** (2016) 196, arXiv: 1512.01178 [hep-ph] (cit. on p. 16).

[27] T. Gleisberg et al., *Event generation with SHERPA 1.1*, JHEP **02** (2009) 007, arXiv: 0811.4622 [hep-ph] (cit. on p. 16).

[28] F. Cascioli, P. Maierhofer and S. Pozzorini, *Scattering Amplitudes with Open Loops*, Phys. Rev. Lett. **108** (2012) 111601, arXiv: 1111.5206 [hep-ph] (cit. on p. 16).

[29] T. Gleisberg and S. Höche, *Comix, a new matrix element generator*, JHEP **12** (2008) 039, arXiv: 0808.3674 [hep-ph] (cit. on p. 16).

[30] S. Schumann and F. Krauss, *A parton shower algorithm based on Catani–Seymour dipole factorisation*, JHEP **03** (2008) 038, arXiv: 0709.1027 [hep-ph] (cit. on pp. 13, 16).

[31] S. Höche, F. Krauss, M. Schönherr and F. Siegert, *QCD matrix elements + parton showers: The NLO case*, JHEP **04** (2013) 027, arXiv: 1207.5030 [hep-ph] (cit. on pp. 13, 16).

[32] D. J. Lange, *The EvtGen particle decay simulation package*, Nucl. Instrum. Meth. A **462** (2001) 152 (cit. on pp. 14–16).

[33] P. Golonka and Z. Was, *PHOTOS Monte Carlo: A Precision tool for QED corrections in Z and W decays*, Eur. Phys. J. **C45** (2006) 97, arXiv: hep-ph/0506026 [hep-ph] (cit. on p. 16).

[34] S. Frixione, G. Ridolfi and P. Nason, *A positive-weight next-to-leading-order Monte Carlo for heavy flavour hadroproduction*, JHEP **09** (2007) 126, arXiv: 0707.3088 [hep-ph] (cit. on p. 16).

[35] R. D. Ball et al., *Parton distributions for the LHC Run II*, JHEP **04** (2015) 040, arXiv: 1410.8849 [hep-ph] (cit. on pp. 13–16).

[36] E. Re, *Single-top Wt-channel production matched with parton showers using the POWHEG method*, Eur. Phys. J. C **71** (2011) 1547, arXiv: 1009.2450 [hep-ph] (cit. on p. 16).

[37] S. Alioli, P. Nason, C. Oleari and E. Re, *NLO single-top production matched with shower in POWHEG: $s-$ and $t-$channel contributions*, JHEP **09** (2009) 111, arXiv: 0907.4076 [hep-ph] (cit. on p. 16).

[38] T. Sjöstrand, S. Mrenna and P. Z. Skands, *A brief introduction to PYTHIA 8.1*, Comput. Phys. Commun. **178** (2008) 852, arXiv: 0710.3820 [hep-ph] (cit. on p. 13).

[39] ATLAS Collaboration, *The Pythia 8 A3 tune description of ATLAS minimum bias and inelastic measurements incorporating the Donnachie–Landshoff diffractive model*, ATL-PHYS-PUB-2016-017, 2016, URL: https://cds.cern.ch/record/2206965 (cit. on p. 13).

[40] ATLAS Collaboration, *The ATLAS Simulation Infrastructure*, Eur. Phys. J. C **70** (2010) 823, arXiv: 1005.4568 [physics.ins-det] (cit. on p. 13).

[41] S. Agostinelli et al., *GEANT4 – a simulation toolkit*, Nucl. Instrum. Meth. A **506** (2003) 250 (cit. on p. 13).

[42] E. Bothmann et al., *Event generation with Sherpa 2.2*, SciPost Phys. **7** (2019) 034, arXiv: 1905.09127 [hep-ph] (cit. on p. 13).

[43] S. Höche, F. Krauss, M. Schönherr and F. Siegert, *A critical appraisal of NLO+PS matching methods*, JHEP **09** (2012) 049, arXiv: 1111.1220 [hep-ph] (cit. on p. 13).

[44] S. Catani, F. Krauss, R. Kuhn and B. R. Webber, *QCD Matrix Elements + Parton Showers*, JHEP **11** (2001) 063, arXiv: hep-ph/0109231 (cit. on p. 13).

[45] S. Höche, F. Krauss, S. Schumann and F. Siegert, *QCD matrix elements and truncated showers*, JHEP **05** (2009) 053, arXiv: 0903.1219 [hep-ph] (cit. on p. 13).

[46] ATLAS Collaboration, *ATLAS Pythia 8 tunes to 7 TeV data*, ATL-PHYS-PUB-2014-021, 2014, URL: https://cds.cern.ch/record/1966419 (cit. on pp. 14, 15).

[47] ATLAS Collaboration, *The simulation principle and performance of the ATLAS fast calorimeter simulation FastCaloSim*, ATL-PHYS-PUB-2010-013, 2010, URL: https://cds.cern.ch/record/1300517 (cit. on pp. 14, 15).

[48] F. A. Dreyer and A. Karlberg, *Vector-boson fusion Higgs pair production at* N^3LO, Phys. Rev. D **98** (11 2018) 114016, URL: https://link.aps.org/doi/10.1103/PhysRevD.98.114016 (cit. on p. 15).

[49] ATLAS Collaboration, *Vertex Reconstruction Performance of the ATLAS Detector at $\sqrt{s}$ = 13 TeV*, ATL-PHYS-PUB-2015-026, 2015, URL: https://cds.cern.ch/record/2037717 (cit. on p. 18).

[50] *TriggerEfficiency*, URL: https://twiki.cern.ch/twiki/bin/viewauth/Atlas/TrigGlobalEfficiencyC (cit. on p. 18).

[51] I. Nomidis, *Event selection, performance and background estimation in the $H \to \gamma\gamma$ channel with Run-2 data*, tech. rep. ATL-COM-PHYS-2020-378, CERN, 2020, URL: https://cds.cern.ch/record/2718255 (cit. on pp. 21–23).

[52] ATLAS Collaboration, *Jet reconstruction and performance using particle flow with the ATLAS Detector*, Eur. Phys. J. C **77** (2017) 466, arXiv: 1703.10485 [hep-ex] (cit. on p. 22).

[53] A. Collaboration, *ATLAS Flavor-Tagging Calibration Results with 139 ifb*, 2019, URL: http://atlas.web.cern.ch/Atlas/GROUPS/PHYSICS/PLOTS/FTAG-2019-004/ (cit. on p. 23).

[54] A. Collaboration, *Expected performance of the 2019 ATLAS b-taggers*, 2019, URL: http://atlas.web.cern.ch/Atlas/GROUPS/PHYSICS/PLOTS/FTAG-2019-005/ (cit. on p. 23).

[55] *Overlap Removal*, URL: https://twiki.cern.ch/twiki/bin/view/AtlasProtected/TopRecoObjTwikiModel#Overlap_Removal (cit. on p. 23).

[56] ATLAS Collaboration, *Supporting Note: Selection and performance for the $H \to \gamma\gamma$ and $H \to Z\gamma$ analyses*, (2015), URL: https://cds.cern.ch/record/2196102 (cit. on p. 24).

[57] P. Refaeilzadeh, L. Tang and H. Liu, 'Cross-Validation', *Encyclopedia of Database Systems*, ed. by L. LIU and M. T. ÖZSU, Springer US, 2009 532, ISBN: 978-0-387-39940-9, URL: https://doi.org/10.1007/978-0-387-39940-9_565 (cit. on p. 30).

[58] S. Lai, X. Li, L. Li, J. Veatch and M. Zhou, *Search for Higgs pair production decaying to WWWW with the final state of three leptons, missing energy and at least two jets in 36.1 fb^{-1} proton-proton data at $\sqrt{s}$ = 13 TeV*, tech. rep., CERN, 2016, URL: https://cds.cern.ch/record/2229725 (cit. on p. 57).

[59] R. Ospanov, R. T. Roberts and T. R. Wyatt, *Tagging non-prompt electrons and muons*, tech. rep., CERN, 2016, URL: https://cds.cern.ch/record/2220954 (cit. on p. 57).

[60] K. Cranmer, G. Lewis, L. Moneta, A. Shibata and W. Verkerke, *HistFactory: A tool for creating statistical models for use with RooFit and RooStats*, tech. rep., New York U., 2012, URL: https://cds.cern.ch/record/1456844 (cit. on p. 59).

[61] *SUSYTools*, URL: https://twiki.cern.ch/twiki/bin/viewauth/AtlasProtected/SUSYSystematicUncertaintiesRun2 (cit. on p. 89).

[62] ATLAS Collaboration, *Luminosity determination in pp collisions at $\sqrt{s}$ = 13 TeV using the ATLAS detector at the LHC*, ATLAS-CONF-2019-021, 2019, URL: https://cds.cern.ch/record/2677054 (cit. on p. 89).

[63] *trigger recommendations*, URL: https://twiki.cern.ch/twiki/bin/view/Atlas/TriggerRecommendationsForAnalysisGroupsFullRun2 (cit. on p. 89).

[64] *Muon CP group*, URL: https://twiki.cern.ch/twiki/bin/view/AtlasProtected/MCPAnalysisWinterMC16 (cit. on p. 89).

[65] *Egamma-CP*, URL: https://twiki.cern.ch/twiki/bin/view/AtlasProtected/LatestRecommendatio (cit. on p. 90).

[66] ATLAS Collaboration, *Jet energy scale measurements and their systematic uncertainties in proton–proton collisions at $\sqrt{s}$ = 13 TeV with the ATLAS detector*, Phys. Rev. D **96** (2017) 072002, arXiv: 1703.09665 [hep-ex] (cit. on p. 90).

[67] *Btagging Calibration*, URL: https://twiki.cern.ch/twiki/bin/view/AtlasProtected/BTagging_Calibration_December2020CDI (cit. on p. 92).

[68] M. Grazzini et al., *Higgs boson pair production at NNLO with top quark mass effects*, Journal of High Energy Physics **2018** (2018) 59, ISSN: 1029-8479, URL: https://doi.org/10.1007/JHEP05(2018)059 (cit. on p. 92).

[69] *LHCHXSWGHH*, URL: https://twiki.cern.ch/twiki/bin/view/LHCPhysics/LHCHWGHH?redirectedfrom=LHCPhysics.LHCHXSWGHH (cit. on p. 92).

[70] *ttH cross section*, URL: https://twiki.cern.ch/twiki/bin/view/LHCPhysics/CERNYellowReportPageA ttH_Process (cit. on p. 92).

[71] *CrossSectionYR4*, URL: https://twiki.cern.ch/twiki/bin/view/LHCPhysics/CrossSectionYR4 (cit. on p. 92).

[72] G. Cowan, K. Cranmer, E. Gross and O. Vitells, *Asymptotic formulae for likelihood-based tests of new physics*, Eur. Phys. J. C **71** (2011) 1554, arXiv: 1007.1727 [physics.data-an] (cit. on pp. 94, 183), Erratum: Eur. Phys. J. C **73** (2013) 2501.

[73] *TRexFitter framework documentatio*, URL: https://trexfitter-docs.web.cern.ch/trexfitter-docs/ (cit. on p. 95).

[74] *TRexFitter framework gitlab project* (cit. on p. 95).

[75] *FakeLeptonBackgrounds*, URL: https://twiki.cern.ch/twiki/bin/viewauth/AtlasProtected/FakeLeptonBackgrounds (visited on 27/08/2021) (cit. on p. 116).

[76] J. B. Robl and A. Sopczak, *Light Non-prompt (Fake) Lepton Background Estimation with the Matrix Method for HH Production with a Signature of Two Same Electric Charge Light Leptons Associated with a Tau - Summer Student Project*, tech. rep., ATL-COM-PHYS-2021-974: CERN, 2021, URL: https://cds.cern.ch/record/2789839 (cit. on p. 148).

[77] ATLAS Collaboration, *Measurement of the tau lepton reconstruction and identification performance in the ATLAS experiment using pp collisions at $\sqrt{s}$ = 13 TeV*, ATLAS-CONF-2017-029, 2017, URL: https://cds.cern.ch/record/2261772 (cit. on p. 155).

[78] ATLAS Collaboration, *Measurement of the $W^{\pm}Z$ boson pair-production cross section in pp collisions at $\sqrt{s}$ = 13 TeV with the ATLAS Detector*, Phys. Lett. B **762** (2016) 1, arXiv: 1606.04017 [hep-ex] (cit. on p. 171).

[79] ATLAS Collaboration, *Observation of electroweak $W^{\pm}Z$ boson pair production in association with two jets in pp collisions at $\sqrt{s}$ = 13 TeV with the ATLAS detector*, Phys. Lett. B **793** (2019) 469, arXiv: 1812.09740 [hep-ex] (cit. on p. 171).

[80] ATLAS Collaboration, *Observation of electroweak production of a same-sign W boson pair in association with two jets in pp collisions at $\sqrt{s}$ = 13 TeV with the ATLAS detector*, (2019), arXiv: 1906.03203 [hep-ex] (cit. on pp. 171, 174, 176).

[81] ATLAS Collaboration, *Multi-Boson Simulation for 13 TeV ATLAS Analyses*, ATL-PHYS-PUB-2017-005, 2017, URL: https://cds.cern.ch/record/2261933 (cit. on pp. 172, 176).

[82] The ATLAS Collaboration, *Modelling of rare top quark processes at $\sqrt{s}$ = 13 TeV in ATLAS*, tech. rep., All figures including auxiliary figures are available at https://atlas.web.cern.ch/Atlas/GROUPS/PHYSICS/PUBNOTE PHYS-PUB-2020-024: CERN, 2020, URL: http://cds.cern.ch/record/2730584 (cit. on p. 172).

[83] S. von Buddenbrock et al., *Phenomenological signatures of additional scalar bosons at the LHC*, Eur. Phys. J. **C76** (2016) 580, arXiv: 1606.01674 [hep-ph] (cit. on p. 180).

Appendices

A Fake lepton and tau, photon background estimation methods

The SM background processes contributing to each signal region are very diverse, although some of them are common, and can therefore be estimated jointly in a given control region. In some cases, alternative regions are studied for the background estimates and systematic uncertainties or corrections can be derived from them. Different estimation methods are studied depending on the channel and its fake sources. In this section, reducible background estimations within each channel will be described.

A.1 Fake light-lepton estimations

There are two methods are used to estimate light lepton fakes. Template fit method, described in Section A.1.1 used to estimate electron fake background since in this method, different sources of backgrounds can be estimated from dedicated CRs, and a data-driven factor method method, described in Section A.1.4 is used for muon fake background estimations. For 3ℓ channel, fake factor method also has been studied as described in Section A.1.5. For 2ℓSS+1τ_{had} channel, matrix method for estimation of fake light lepton has been used (Section A.1.6).

A.1.1 Template fit in 2ℓSS and 3ℓ channels

Since the non-prompt light lepton background in the 2ℓSS and 3ℓ channels is a mixture of leptons from semi-leptonic heavy-flavour (HF) decays and photon conversions, a template method has been developed to estimate these backgrounds.

Within the template fit method, the normalisation of the different "fakes" contribution templates, as given by the Monte Carlo of all processes contributing to non-prompt lepton background, are left free-floating in a fit to data, and these normalisation factors are used to correct the fakes Monte Carlo estimates. The template fit method is a semi-data-driven method, i.e. it relies on the truth information from $t\bar{t}$, $Z + jets$, $W + jets$, and single top Monte Carlo simulation to define different types of fake/non-prompt leptons, and on the general description of fakes kinematics by Monte Carlo.

The main contribution to non-prompt lepton background comes from $t\bar{t}$, and $V + jets$. Based on the truth classification of events containing a non-prompt lepton, following main contributions are distinguished, and free-floating normalization factors (NF) is assigned to each of them:

- NF_e^{HF}: normalization factor applied to events with one non-prompt electron from B decay, C decay or light hadron (dominated by B decay).
- NF_μ^{HF}: normalization factor applied to events with one non-prompt muon from B decay, C decay or light hadron (dominated by B decay).
- $NF^{internalCO}$: normalization factor applied to photon conversion ($\gamma* \to \ell\ell$). It arrives mainly from $t\bar{t}\gamma$ and $V\gamma$ events.

- $NF_e^{externalCO}$: normalization factor applied to events with one fake electron from photon conversion due to interactions with detector material.

In this iteration, light-flavor leptons are combined with heavy flavor ones. The classification of Monte Carlo samples in the aforementioned categories is based on their truth origin (based on the MCTruthClassifier) as follows:

- Prompt leptons: leptons (truth origin = 10), Bremsstrahlung radiation (truth origin = 5, parent truth is the same particle and truth type = 2) or rare Top decay (muon truth origin = 0).
- Conversion: Conversion photon fakes to electron (truth origin = 5, except Bremsstrahlung radiation)
  - Internal Conversion: electron with decay radius below 20mm
  - External Conversion: electron with decay radius larger than 20mm
- B decay: non-prompt leptons from B decay (truth origin = 26, 29, 33);
- C decay: non-prompt leptons from C decay (truth origin = 25, 27, 28, 32)
- Other decay: leptons from light quarks or other processes.

Monte Carlo events containing a charge-flip electron are vetoed, since they are estimated with data-driven methods. The vetoed events are those containing either a charge flipped isolated electron, or a background electron with opposite charge compared to the prompt mother electron.

While the analysis is blinded, the templates are fitted to the data using control regions only. At this stage, the NFs extracted from the blinded fit and inserted into the full fit model in order to obtain the expected analysis sensitivity from Asimov data set. After unblinding the normalization factors are derived in one simultaneous fit including the signal region.

Four dedicated control regions have been developed in order to improve the constraint on the NFs of the internal and external conversions, and decrease the correlation between these two mainly in the electron channels. Events with same-sign di-leptons and at least one b-tagged jets are used to define control regions regions that are orthogonal to the signal region and that contain all the variety of non-prompt leptons. These regions are used to constraints the modeling of the various non-prompt leptons in the Monte Carlo.

The internal conversion and external conversion control regions are defined based on three electron variables. The variables are: the conversion radius, the invariant mass of the track associated to the electron and its closest track (originating from the conversion) calculated at conversion vertex ($m_{trk-trk,CV}$), and the same invariant mass calculated at the primary vertex ($m_{trk-trk,PV}$).

The following definitions are also considered:

- External conversion candidate: a conversion vertex is found with radius $r > 20$mm, and the mass of the vertex is $0<\text{m(trk-trk)}atCV <100$MeV
- Internal conversion candidate: not an External conversion candidate and $0<\text{m(trk-trk)}atPV <100$MeV

The following distributions are exploited to best discriminate among the NFs in the simultaneous template fit:

- ΔR_{ll} in $\mu e + ee$ channel with exactly 1 b-jet, to estimate NF_e^{HF}

- H_T in $e\mu + \mu\mu$ channel, to estimate NF_{μ}^{HF}

The main uncertainty corresponds to the statistical uncertainty on the NFs that varies from 10% to 30%. Since the Template Fit is relying on MC, modelling uncertainties on heavy flavour and conversion fakes should be included. The systematic uncertainty on the fake (non-prompt) lepton background can be estimated as the shape difference between MC-based fake template and fakes in data, which can be defined as residual from selected data events minus all non-fake background events estimated from MC. The region definition to derive the uncertainties are provided by relaxing isolation criteria for one of leptons passing selection, while mis-charge (QMisID) and electron definition selections are remain the same. The ratio of data fakes (after subtracting all non-fake MC background) to TF fakes will be used to derive the HF systematic uncertainties.

- $t\bar{t}$ modelling systematics
- HF systematics binned in BDT
- Internal/External conversion systematics

A.1.2 Template fit systematic uncertainties in 2ℓSS channel

Heavy flavour systematic uncertainties: The strategy to estimate the systematic uncertainty on heavy flavour lepton is to enriched the contribution of the fake by relaxing isolation criteria for one of the lepton passing the selection. The template fit systematics for Heavy flavour is assessed by the study of this selection on the TF method, therefore the template fit regions. The low N$_{jets}$ CR with relaxed isolation criteria are presented on the Figure 58, respectively for electrons (on top) and muons (on bottom). The uncertainty is extracted through the distribution of the final discriminant variable, considering the ratio $\frac{Data-NonFakes}{Fakes_{HF}}$. The distibution and the discrepancy is presented on the figure 59. Because the ratio is not steady over the distribution, the uncertainty has been estimated bin per bin and implemented as a branch.

Conversion uncertainty estimation: The strategy to estimate the systematic uncertainty on conversion is to enriched the contribution of the conversion by relaxing isolation criteria (as done in the previous section) and inverse the ambiguity criteria. This ambiguity type requirement is now above to zero for one lepton passing the selection. A study of the effect of this selection on the TF region. The low N$_{jets}$ CR with relaxed isolation criteria and inverted ambiguity type are presented on the Figure 60. Then, the uncertainty is measured by considering the distribution of the final discriminant variable and the ratio $\frac{Data-NonFakes}{Fakes_{Conv}}$. The distribution and the discrepancy is presented on the figure 61. As done previously, the uncertainty is estimated bin per bin and implemented as a branch.

t$\bar{\text{t}}$ MC modelling uncertainties: The template fit method is dependent on our knowledge of the standard model and therefore on the MC modelling. The Modelling uncertainties of t$\bar{\text{t}}$ background can be estimated by considering various sources: the choice of the matrix element generator (ME), the Parton Shower modelling (PS), and the hdamp parameter value (Initial or Final state radiation, ISR/FSR).
All MC samples in HIGG8D1 derivations are listed in the Table 43. The analysis is performed by selecting one tight non-prompt lepton in the dedicated signature 2LSS (or 3L). The method is detailled below, adapted for the 2LSS signature, the jobs for getting these uncertainties are running. Each uncertainties are treated as one-sided variations, and symmetrised around nominal value.

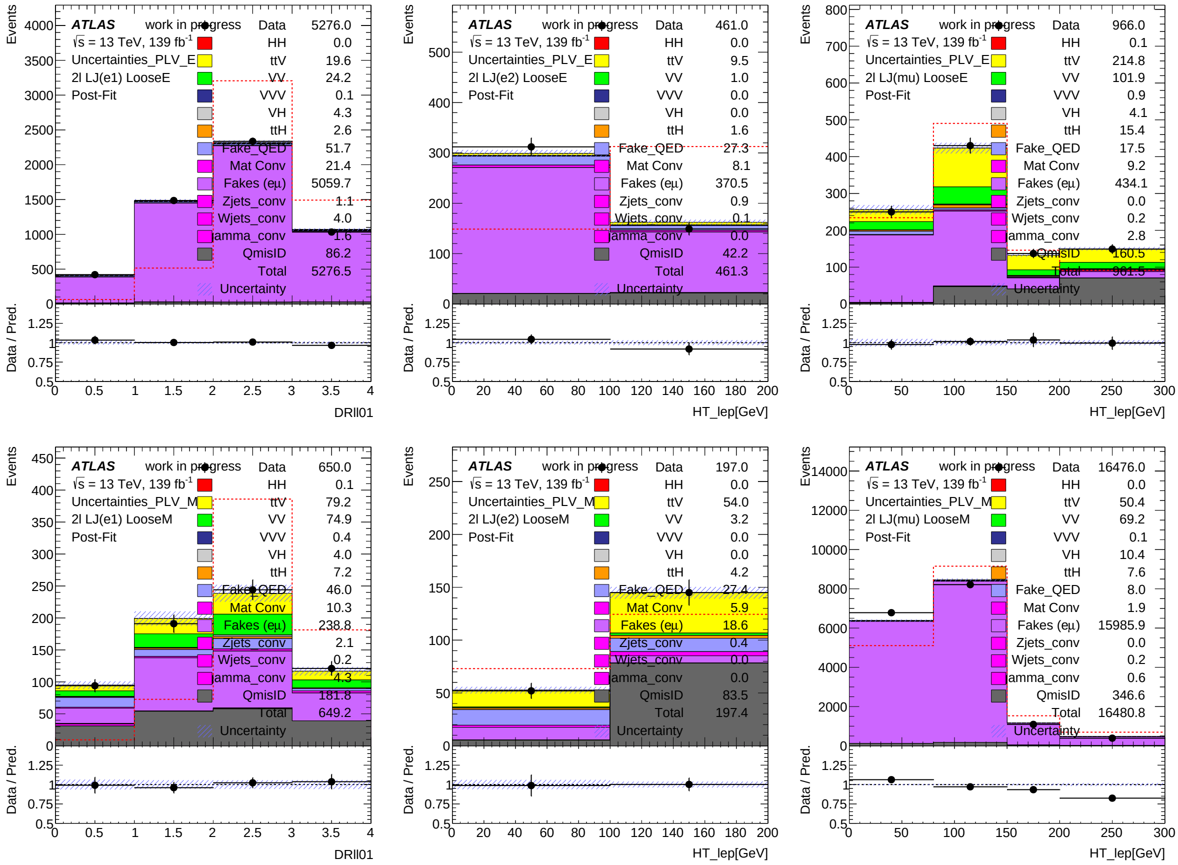

Figure 58: The low-N$_{jets}$ Control regions for relaxed isolation criteria for one leptons passing the selection, respectivelly for electrons (top) and muons (bottom): DRll01 (on left),HT$_{lep}$ μe or ee (center) and HT$_{lep}$ eμ or $\mu\mu$ (right)

The Fragmentation and Hadronization modelling: Alternative samples produced with the same Powheg parameters as the nominal $t\bar{t}$ (410470) sample in term of PDF choice, renormalisation and factorisation scales or hdamps parameters. These sample are interfaced by Herwig7 alternative generator instead of Pythia8. The Uncertainty is estimated by comparing the distribution of kinematic or thruth origin variables for fake leptons 2ℓSS with 1 non-prompt lepton candidates.

Initial-State and Final-State Radiation: This uncertainty in the modelling of the Initial-State radiation is estimated using Powheg+Pythia8 samples, comparing nominal sample having $hdamp = 1.5m_t$ with an alternative samples having $hdamp = 3.0m_t$ and the varying the showering (Var3c up). The distribution of truth origin or kinematic variables for 2ℓSS with one non-prompt leptons selections is compared for nominal Powheg+Pythia8 non-allhadronic sample (410470) and radiation up Powheg+Pythia8 sample (410480-410482). The ratio between the two distribution will be the uncertainty.

NLO matching uncertainty: This uncertainty can be estimated by comparing the Powheg generator (410470) nominal sample with alternative generator aMcAtNlo samples (410465-410464). These samples compare NLO matching and Matrix Element Correction (MEC) at the same time.

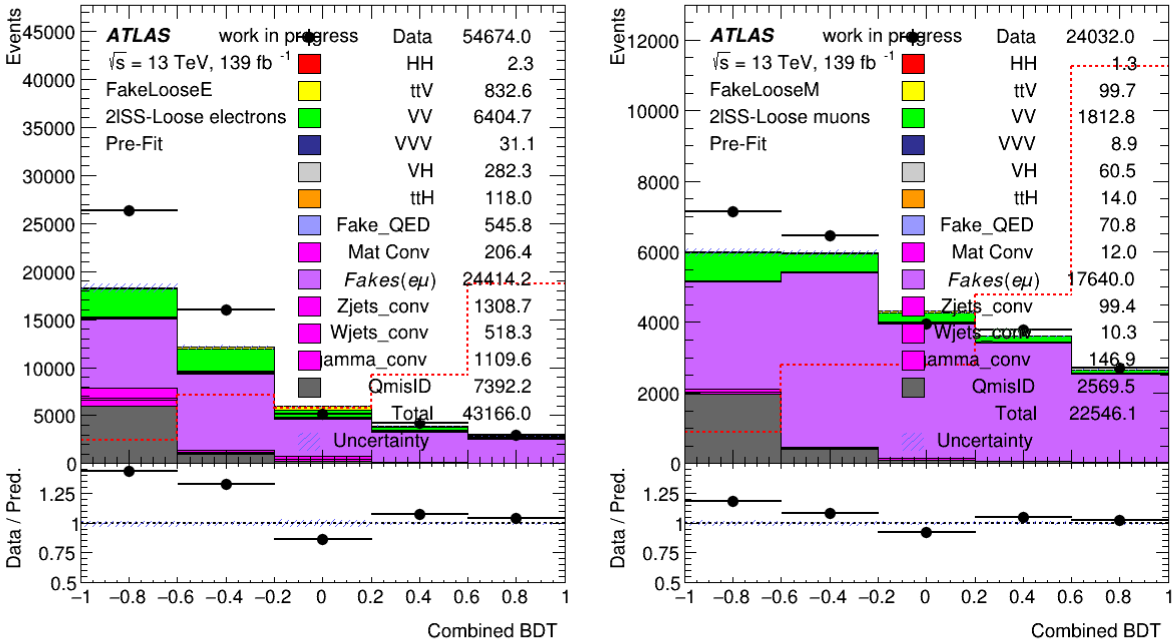

Figure 59: BDT$_{2LSS}$ shape for electrons (on left) and muons (on right) with relaxed isolation criteria, passing the selection.

Process	Generator	DSID	Additional comments
tt̄	Powheg+Pythia8	410470	nonallhad (nominal)
tt̄	Powheg+Pythia8	410471	allhad (nominal)
tt̄	aMCAtNLO+Pythia8	410464-410465	single-lep, di-lep (alternative ME)
tt̄	Powheg+Herwig7	410557-41055	single-lep, di-lep (alternative PS)
tt̄	Powheg+Pythia8	410480-410482	single-lep, di-lep (alt. hdamp = 3.0mt)

Table 43: List of MC Samples used for the MC modelling uncertainties study

As previously, the uncertainty is estimated by comparing the distribution of the truth origin or kinematic variables for 2ℓSS candidates with one non-prompt lepton.

A.1.3 Template fit systematic uncertainties in 3ℓ channel

Since the Template Fit is relying on MC, there are three main types of systematics associated:

- $t\bar{t}$ modelling systematics
- fakes template systematics

The $t\bar{t}$ modelling systematics follows standard top group recipes and uses samples with varied amount of radiation and scale choices. This set of systematics have a very small impact on the final results.

The shape systematics on the fakes templates is derived as follows. The complex tight lepton definition is split into parts which are targeting different components of the fakes – the conversions (ambiguity bin)

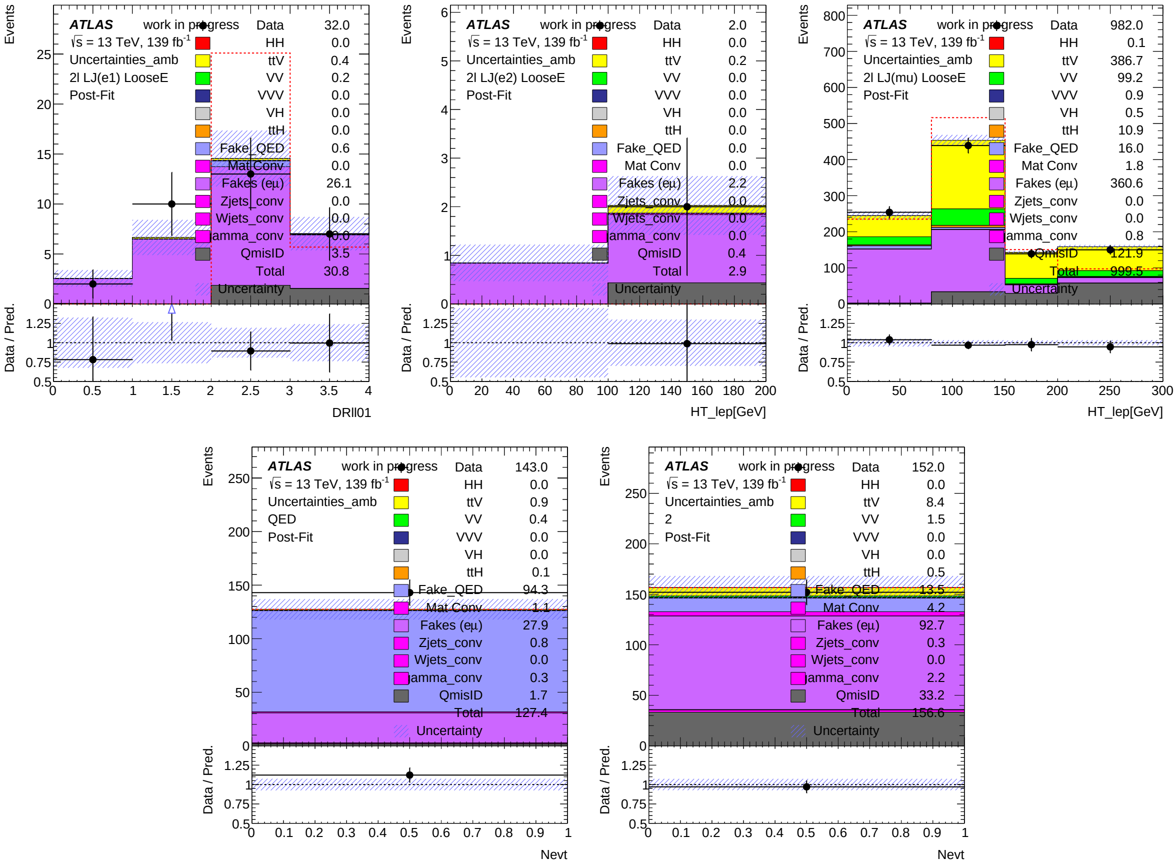

Figure 60: The TF Control regions for relaxed isolation criteria for one leptons passing the selection and inverted ambiguity bit: DRll01 (top left),HT$_{lep}$ μe or ee (top center), HT$_{lep}$ eμ or $\mu\mu$ (top right), QED (bottom left), Conversions (bottom right)

vs heavy flavours (relaxing the cut on the Tight ID Selection on $l1andl2$). In this way, selections with dominating fake fractions are obtained and after subtraction of remaining backgrounds compared to data. In this way, a systematics for each of the heavy flavour template component (electron/muon) is derived as re-weighting in all bins of the final fit used as one nuisance parameter in a correlated way. These shape systematics are not ranked among the most important uncertainties.

The shapes in control regions with relaxed cuts (relaxed ID cut for heavy flavor and relaxed ambiguity cut for conversion) criteria for electron (muon) template are presented on Figures 62. The values from the ratio($(Data - NonFakeBG)/FakeBG$) are added to the fit as an additional systematic uncertainty for the HF fakes and Conversion fakes in particular control or signal region.

A.1.4 Fake factor method in 2ℓSS channel

The number of prompt leptons is estimated using both data and MC simulation on a fake enriched control region. The control region is constructed by same-sign events in which one lepton pass the tight selection and another lepton so-called anti-tight lepton fails the tight selection. In this method, two fake factors

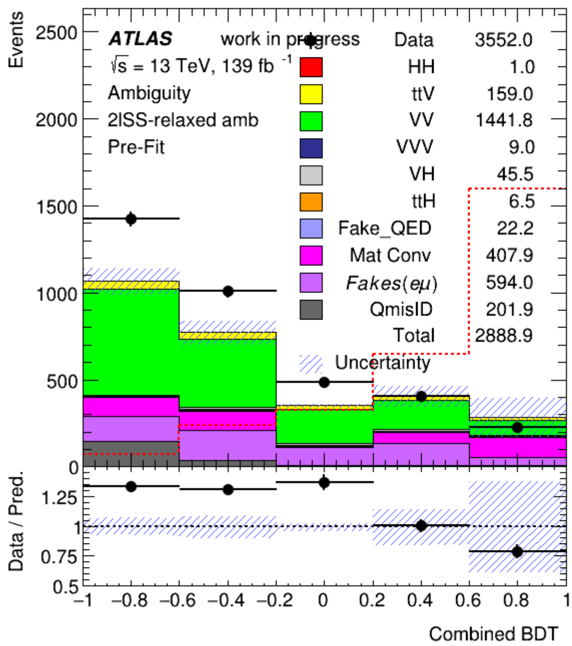

Figure 61: BDT_{2LSS} shape with relaxed isolation criteria and inverted ambiguity type.

related the events from fake enriched region to the background in signal region are derived. The method assumes that the fake factor is independent of the parameter chosen for extrapolation. The fake factor is defined as the ratio of number of same-sign events with two tight leptons between same-sign events with one tight lepton and one anti-tight lepton, as below

$$\theta_\ell = \frac{N_{\ell\ell}}{N_{\ell\not\ell}} \tag{10}$$

where ℓ the tight lepton e or μ and $\not\ell$ the anti-tight lepton e or μ. The tight and anti-tight lepton definitions used for fake measurement are presented in Table 44. In the signal region, the fake electrons are dominated by jets misidentified as electrons, following the photon conversions and non-prompt heavy flavour decay products. A check on fake lepton composition is preformed in low jet multiplicity and high jet multiplicity region. The fake composition, consist of external Conversion, internal conversion, b decay, c or other decay, and rest unknown, are classified by TruthClassifier Tool. A non QmisID origination selection is required to avoid the contamination from charge flipped electrons. The fake composition of electron looks similar for low jet multiplicity control region and high jet multiplicity signal region. While in muon case, the regions with b-jet are chosen as the fake muon measurement control region, as fake muons are mainly from heavy flavor decays. The fake composition check of $t\bar{t}$ can be found in Figure 63.

Fake factor measurements The fake factors for e and μ can be written as

$$\theta_e\left(N_{\mathrm{jet}} == 1\right) = \frac{N_{ee}^{\mathrm{data}} - N_{ee}^{\mathrm{prompt}} - N_{ee}^{V\gamma} - N_{ee}^{\mathrm{QmisID}}}{N_{e\not e}^{\mathrm{data}} - N_{e\not e}^{\mathrm{prompt}} - N_{e\not e}^{V\gamma} - N_{e\not e}^{\mathrm{QmisID\ MC}}} \tag{11}$$

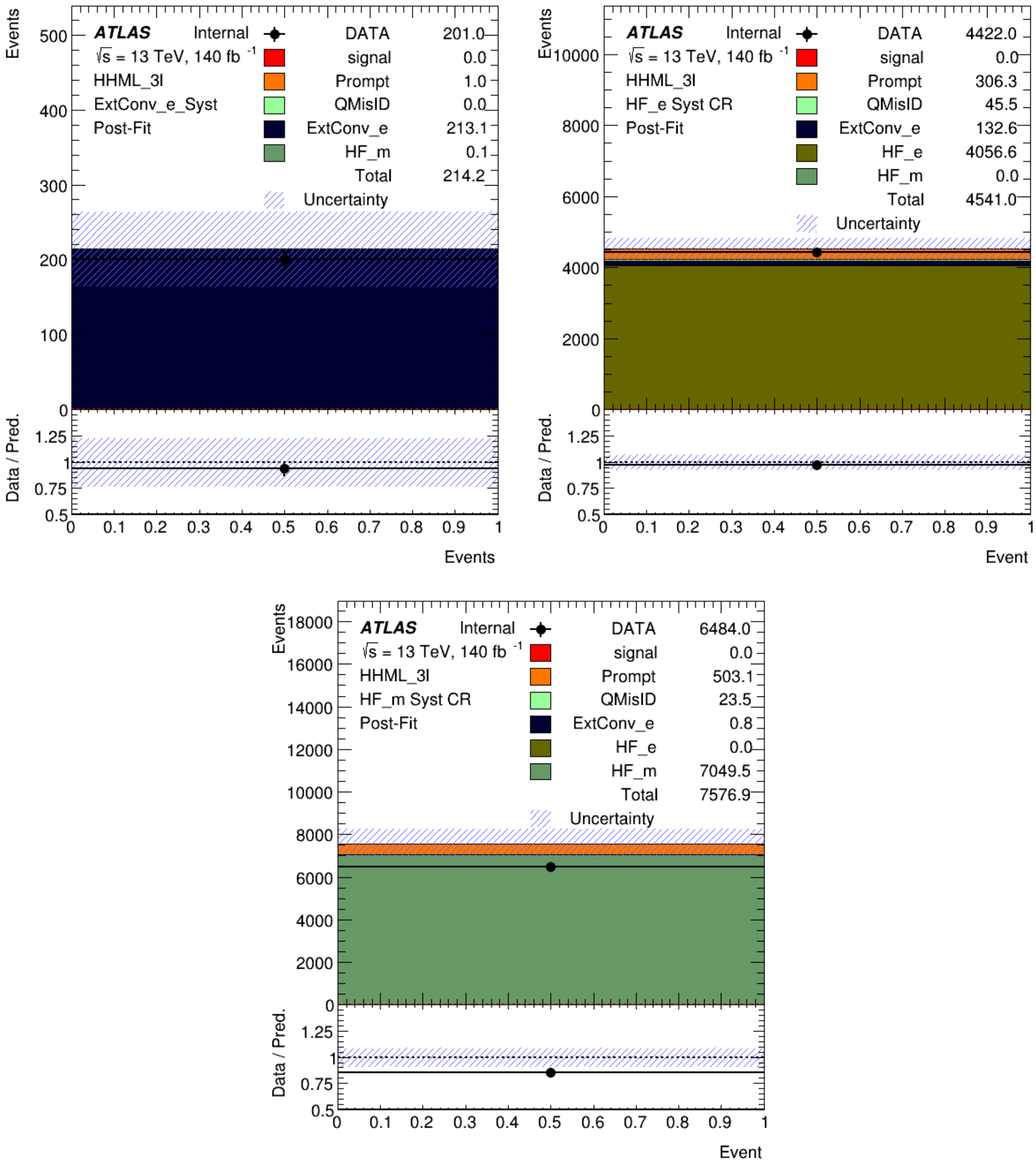

Figure 62: The shapes in HF_E, HF_MU and Material Conversion control regions and with relaxed cut criteria for electron and muon templates.

$$\theta_\mu \left(N_{\text{b-jet}} \geq 1\right) = \frac{N^{\text{data}}_{\mu\mu} - N^{\text{prompt}}_{\mu\mu} - N^{V\gamma}_{\mu\mu}}{N^{\text{data}}_{\mu\not\mu} - N^{\text{prompt}}_{\mu\not\mu} - N^{V\gamma}_{\mu\not\mu}} \qquad (12)$$

In both denominator and numerator region, the contributions from other background, composed of prompt same-sign leptons from VV,VH,tV,ttV and ttH processes, Vγ process and QmisID process, are subtracted. N^{prompt} the background from prompt sames-sign lepton pair and Vγ background are estimated using

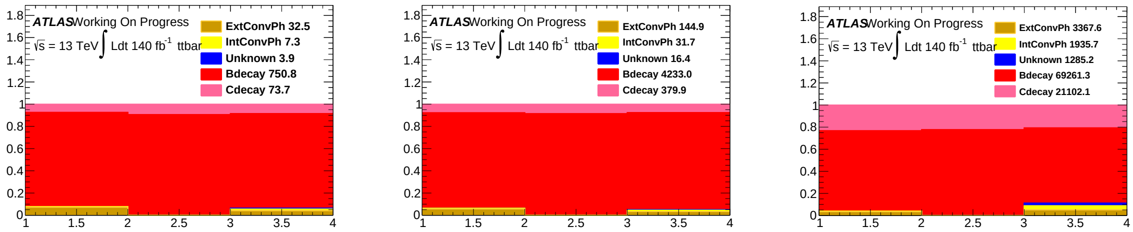

Figure 63: The fake lepton origination of $t\bar{t}$ process. Events are divided into 5 categories, external conversion, interval conversion, B decay , C decay and rest unknown by the TruthClassifier tool. X-axis are different lepton pair flavor, $e^{\pm}e^{\pm}$, $e^{\pm}\mu^{\pm}$ and $\mu^{\pm}\mu^{\pm}$, respectively.Left: Signal region ($N_{\text{jets}} \geq 3$, to be reversed); Middle: Low N_{jets} multiplicity region; Right: Low N_{jets} multiplicity with at least one b-jet region.

MC simulation. For fake factor of electron, N^{QmisID} in the numerator is estimated from opposite-sign events computing with corresponding QmisID rates as discussed in section. In the denominator, N^{QmisID} is computed from MC events in which one electron is required to be a real electron.

Due to the fact the sub-leading lepton is an anti-tight lepton in most cases, thus for numerator events, the sub-leading lepton is chosen to be the fake candidate. While for one tight lepton and one anti-tight lepton in denominator, no subleading lepton should match to anti-tight selection. The numerator leptons follow the same trigger strategy applied in signal region.

Lepton	electron		muon	
	Loose	Tight	Loose	Tight
PLVTight	No	Yes	No	Yes
ID	LooseLH	TightLH	Loose	Medium
QmisID BDT	Yes	Yes		
Ambiguity bit	Yes	Yes		
$\|d_0\|/\sigma_{d_0}/mm$	<5	<5	<3	<3
$\|z_0 sin\theta\|/mm$	<0.5	<0.5	<0.5	<0.5

Table 44: The tight and anti-tight lepton used in the fake factor calculation.

It was found that an inclusive fake factor can't describe the distribution of lepton kinematics, η, p_{T} very well. A p_T dependence fake factor therefore is raised to be implemented in each p_T bins. The p_T are divided into 4 bins, [20,40],[40,60],[60,100],[100,1000]. The η and p_T dependent fake factor is presented in Figure 65.

Each kinds of subtracted background and observed data in low jet multiplicity region is listed in Table and Table for electrons and muons. To measure the number of fakes in signal region, following equations are

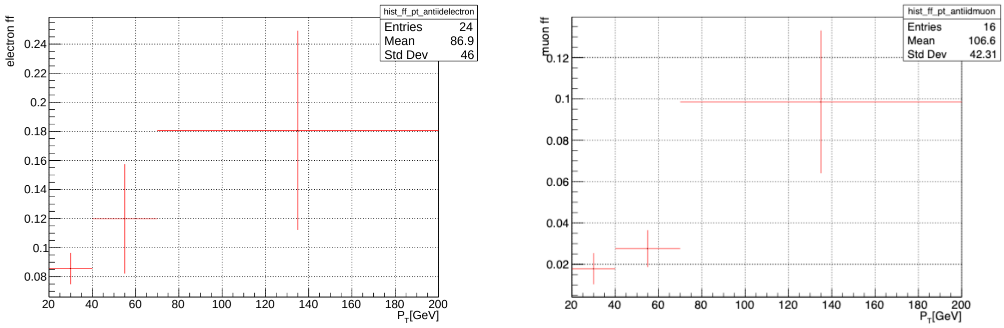

Figure 64: The fake factor of electron and muon as a function of p_T.

used,

$$N^{\text{fakes}}_{ee}\left(N_{\text{jet}} \geq 2\right) = \left(N^{\text{data}}_{e\not{\ell}} - N^{\text{promptSS}}_{e\not{\ell}} - N^{V\gamma}_{e\not{\ell}} - N^{\text{QmisID MC}}_{e\not{\ell}}\right)\left(N_{\text{jet}} \geq 2\right) \times \theta_e \tag{13}$$

$$N^{\text{fakes}}_{\mu\mu}\left(N_{\text{jet}} \geq 2\right) = \left(N^{\text{data}}_{\mu\not{\mu}} - N^{\text{promptSS}}_{\mu\not{\mu}} - N^{V\gamma}_{\mu\not{\mu}}\right)\left(N_{\text{b-jet}} \geq 1\right) \times \theta_\mu \tag{14}$$

$$\begin{aligned} N^{\text{fakes}}_{e\mu}\left(N_{\text{jet}} \geq 2\right) = &\left(N_{e\mu} - N^{\text{promptSS}}_{e\mu} - N^{V\gamma}_{e\mu^{\mu}} - N^{\text{QmisID}}_{e\mu}\right)\left(N_{\text{b-jet}} \geq 1\right) \times \theta_\mu \\ &+ \left(N_{\not{\ell}\mu} - N^{\text{promptSS}}_{\not{\ell}\mu} - N^{V\gamma}_{\not{\ell}\mu} - N^{\text{QmisID MC}}_{\not{\ell}\mu}\right)\left(N_{\text{jet}} \geq 2\right) \times \theta_e \end{aligned} \tag{15}$$

Fake factor estimation and results The fake factor are measured separately for electron and muon. Events in which the number of jet requirement is inversed from signal region are used for electron fake calculation. And in the case of muon the b-veto is inversed. It was found that an inclusive fake factor can't describe the distribution of lepton kinematics, p_{T} very well. A p_T dependence fake factor therefore is raised to be implemented in each p_T bins. The p_T are divided into 4 bins, [20,40],[40,60],[60,100],[100,1000]. The p_T dependent fake factor is presented in Figure 65.

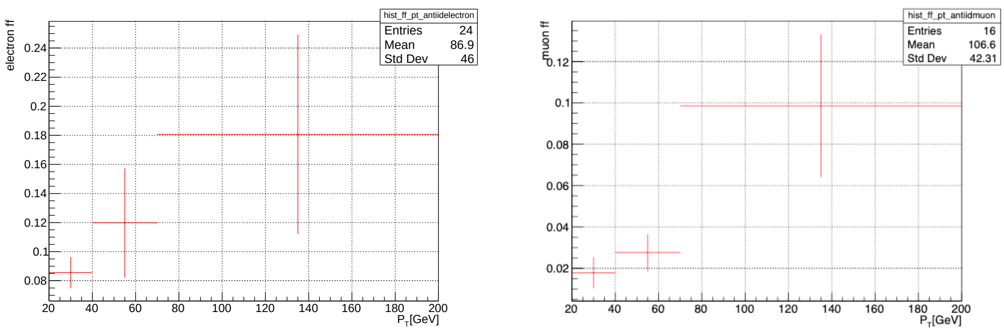

Figure 65: The fake factor of electron and muon as a function of p_T.

The fake factor method uncertainties are studied with the recommendation from IFF group, they are detailed in appendices A.1.4. The main source is the differences of the fake factors in the control regions and the signal regions. A closure test is done by applied factor factor method on fake MC ($t\bar{t}$, W+jets) in control region and pre-selection region. The fake composition and yields are displayed in Figure 66 for this two regions, the expected distribution is obtained from fake factor method and is compared to MC counting classified into type heavy, light, conversion and others from MC truth information. For the total yields in the signal region, a 17.6% uncertainty is found from the MC/exp ratio. In addition, the composition difference of type heavy is changed from 75.5% $\rightarrow$ 61.4%.

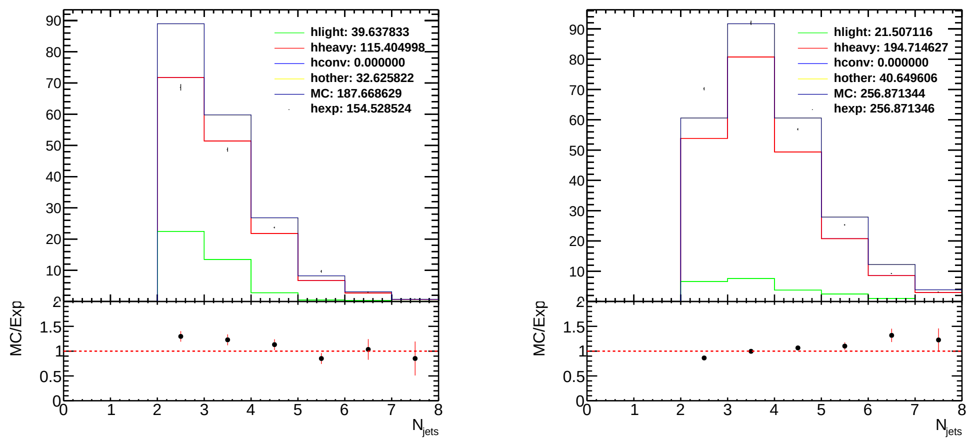

Figure 66: The predicted MC and MC count fake events in control region and signal region for muon.

Fake background systematics uncertainties with fake factor method in 2ℓSS channel Following sources of systematic uncertainties on estimated fake factors are considered. These are mostly related to fake factor measurement. The estimation follows the guideline provided by IFF group [**FakeObjectBgEstimation twiki.**]

- **Fake-factors statistics:** The statistical uncertainty on fake factors θ_e and θ_μ.
- **QmisID subtraction:** The uncertainty of QmisID estimation in the measurement regions: the full uncertainty on this background is propagated to the fake factor measurement.
- **Prompt subtraction:** The systematics on prompt MC modeling in the measurement regions. The uncertainties raise from the prompt background cross section and CP systematic uncertainties.
- **CR to SR extrapolation:** The composition difference between CR and SR. The differences of the fake factors in the control regions and the signal regions are taken into account as the systematic uncertainty (symmetrize).
- **Trigger:** Accounts for a potential bias at trigger level. Under investigation. Plan to apply the trigger match to "tag" lepton in anti-tight control region and to both two leptons in tight control region.

A.1.5 Fake factor method in 3ℓ channel

The fake factor method is the similar to what has been given on Section A.1.4 for 2ℓSS channel. The jet fakes enhanced control region is obtained after applying preselection and reversing the tight lepton ID or isolation requirement. The workflow for doing fake factor method is shown in Fig. 67.

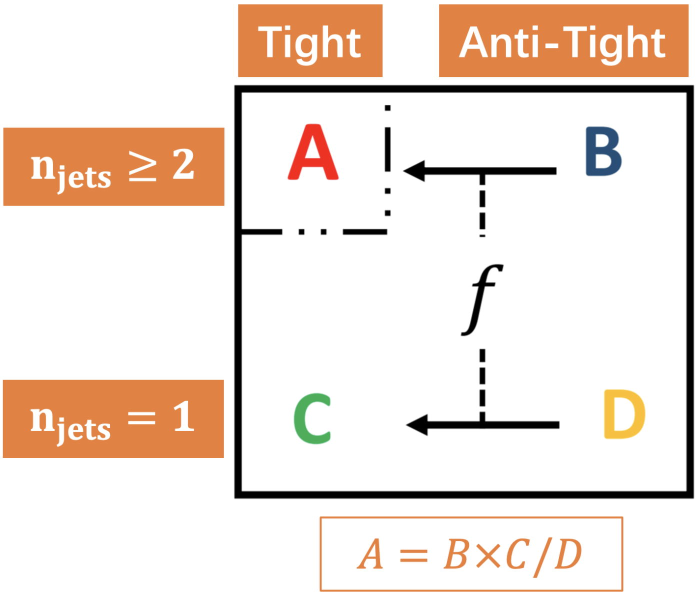

Figure 67: The workflow of fake factor method for 3ℓ channel. *Region A*: Signal region ($N_{\text{jets}} \geq 2$). *Region B*: Jet fakes enhanced control region for calculating fakes in signal region ($N_{\text{jets}} \geq 2$). *Region C*: Tight control region with $N_{\text{jets}} = 1$. *Region D*: Jet fakes enhanced control region with $N_{\text{jets}} = 1$.

The dependence of the fake factor on jet multiplicity has been checked to ensure that the fake factor method is valid in the kinematics region of interest. Also, it is desirable not only estimate the event yields of the jet fakes background, but also to model the shapes of various kinematic variables, the fake factor is further parameterized in terms of the transverse momentum (p_T) of leptons. The lepton p_T is categorized into four bins: $(0, 30], (30, 50], (50, 80], (80, \infty)$. In each p_T bin, a p_T dependent fake factor is calculated and applied to the signal region corresponding accordingly. The fake factor, denoted as θ_e for electrons and θ_μ for muons, can be calculated using the following formula:

$$\theta_e(p_T, N_{\text{jets}} = 1) = \frac{(N^{\text{data}}_{\ell ee} - N^{\text{prompt}}_{\ell ee} - N^{V\gamma}_{\ell ee})(p_T, N_{\text{jets}} = 1)}{(N^{\text{data}}_{\ell e\not{e}} - N^{\text{prompt}}_{\ell e\not{e}} - N^{V\gamma}_{\ell e\not{e}})(p_T, N_{\text{jets}} = 1)} \tag{16}$$

$$\theta_\mu(p_T, N_{\text{jets}} = 1) = \frac{(N^{\text{data}}_{\ell\mu\mu} - N^{\text{prompt}}_{\ell\mu\mu} - N^{V\gamma}_{\ell\mu\mu})(p_T, N_{\text{jets}} = 1)}{(N^{\text{data}}_{\ell\mu\not{\mu}} - N^{\text{prompt}}_{\ell\mu\not{\mu}} - N^{V\gamma}_{\ell\mu\not{\mu}})(p_T, N_{\text{jets}} = 1)} \tag{17}$$

where ℓ represents for "loose" electrons or muons, e/μ are "tight" electrons or muons as described in Section ?? and ??. $\not{e}/\not{\mu}$ are the "anti-tight" leptons, also known as the fake leptons. We estimate prompt and $V\gamma$ backgrounds by MC. Two fake factors can be calculated for each p_T bin, namely $\theta_{e/\mu}(p_T^{\ell_1})$ and $\theta_{e/\mu}(p_T^{\ell_2})$.

The jet fakes background in the signal region can be calculated as:

$$N^{\text{fake}}_{\ell ee}(p_T, N_{\text{jets}} \geq 2) = (N^{\text{data}}_{\ell e\not{e}} - N^{\text{prompt}}_{\ell e\not{e}} - N^{V\gamma}_{\ell e\not{e}})(p_T, N_{\text{jets}} \geq 2) \times \theta_e(p_T, N_{\text{jets}} = 1) \tag{18}$$

$$N^{\text{fake}}_{\ell\mu\mu}(p_T, N_{\text{jets}} \geq 2) = (N^{\text{data}}_{\ell\mu\not{\mu}} - N^{\text{prompt}}_{\ell\mu\not{\mu}} - N^{V\gamma}_{\ell\mu\not{\mu}})(p_T, N_{\text{jets}} \geq 2) \times \theta_\mu(p_T, N_{\text{jets}} = 1) \tag{19}$$

1851
$$N^{\text{fake}}_{\ell e\mu}(p_T, N_{\text{jets}} \geq 2) = (N^{\text{data}}_{\ell\mu\not{e}} - N^{\text{prompt}}_{\ell\mu\not{e}} - N^{V\gamma}_{\ell\mu\not{e}}) \times \theta_e + (N^{\text{data}}_{\ell e\not{\mu}} - N^{\text{prompt}}_{\ell e\not{\mu}} - N^{V\gamma}_{\ell e\not{\mu}}) \times \theta_\mu \quad (20)$$

1852 Total yields of MC and data sample are summarized in Table 45.

	hh	VV	other prompt bkg	DD fakes	total backgrounds	Data
yields	1.0	938.2	147.1	231.6	1316.9	1341
entries	20783	372234	64470	139309	-	-

Table 45: Total yields of MC and data samples after the preselection and WZ re-normalization.

1853 A.1.6 Matrix Method estimation in the 2ℓSS+$1\tau_{\text{had}}$ channel

1854 Two same-sign electrically charged light leptons and one hadronically decaying tau (2ℓSS+$1\tau_{\text{had}}$ channel),
1855 the $t\bar{t}$ background is dominant and the estimation of this background by a data-driven method is studied.
1856 For the data-driven $t\bar{t}$ background determination, the Matrix Method is used with the implementation of
1857 ATLAS Isolation and Fake Forum (IFF) tools. The IFF tools are used both for the real and fake efficiency
1858 determination of light leptons, and the Matrix Method event weight determination. For the display of
1859 signal, background and data the TRexFitter package is used. The study shows that the Matrix Method
1860 is well suited for the data-driven background determination of expected $t\bar{t}$ events, and closure tests are
1861 successfully completed. They indicate the expected systematic uncertainty of the method to be below 10%.
1862 The data-driven efficiencies are applied in the Matrix Method for a test in the control region and in the
1863 signal region.

1864 The Fake Efficiency Tool is an IFF standalone package to derive lepton fake/non-prompt (and real)
1865 efficiencies for common usage [75].

1866 A brief description of the Matrix Method (MM) estimation of the light non-prompt lepton background
1867 (also referred to as fakes) is given.

1868 The matrix method is a data driven technique used to estimate the contamination of fake physics objects
1869 (electrons and muons in the context of this analysis) which pass a given selection corresponding to the one
1870 used for objects in the signal region definition, referred to in the following as "tight" selection. The basic
1871 idea underlying the matrix method can be outlined first in a simplified scenario where only one lepton
1872 is taken into account. The number of events with a tight lepton (denoted with T) and that with a lepton
1873 which fails the tight selection (referred to as anti-tight, $\overline{T}$) can be expressed in terms of efficiencies and
1874 inefficiencies for "loose" (denoted L such that $L \equiv T \cup \overline{T}$) real[4] (prompt) or fake leptons to pass the tight
1875 selection via a system of two equations:

$$\begin{aligned} N^T &= \epsilon_r N^r + \epsilon_f N^f \\ N^{\overline{T}} &= \bar{\epsilon}_r N^r + \bar{\epsilon}_f N^f \end{aligned} \quad (21)$$

1876 or, in a matrix form:

$$\begin{pmatrix} N^T \\ N^{\overline{T}} \end{pmatrix} = \begin{pmatrix} \epsilon_r & \epsilon_f \\ \bar{\epsilon}_r & \bar{\epsilon}_f \end{pmatrix} \begin{pmatrix} N^r \\ N^f \end{pmatrix}, \quad (22)$$

[4] In the context of this analysis, "real" denotes prompt and isolated leptons coming from the primary interaction vertex

where ϵ_r (ϵ_f) represents the efficiency for a real (fake) lepton to pass tight selection, and $\overline{\epsilon}_r \equiv (1 - \epsilon_r)$ ($\overline{\epsilon}_f \equiv (1 - \epsilon_f)$) represents the probability for a real (fake) lepton to fail tight but still pass the loose selection.

Inverting the equation above allows us to access the unknown number of events with real and fake leptons in a region of interest, through observable quantities, i.e. the number of events with tight and anti-tight leptons and the efficiencies of passing the tight selection. The real and fake lepton efficiencies can be measured directly in dedicated control regions using data as discussed later on.

In this analysis case, the dilepton case of the matrix method formalism is employed. Depending on whether or not each lepton passes the tight selection, each i-th event populates only one of the following four orthogonal (side-bands) regions:

- TT_i: an event where both lepton candidates pass the tight selection. The total number of events in this region is labeled N^{TT}.
- $T\overline{T}_i$: an event where the leading (most energetic) lepton passes the tight selection whereas the subleading (second most energetic) lepton fails it. The total number of events in this region is labeled $N^{T\overline{T}}$
- $\overline{T}T_i$: an event where the leading lepton fails the tight selection while the subleading lepton passes it. $N^{\overline{T}T}$ denotes the total number of events in this region.
- $\overline{TT}_i$: an event where both lepton candidates fail the tight selection. $N^{\overline{TT}}$ denotes the total number of events in this region.

As for the “single lepton” simplified scenario, one can define an efficiency matrix of dimension 4 for the dilepton case, mapping the observed total number of events above to that in four orthogonal regions with different real and fake lepton composition, as follows:

- rr_i: corresponds to an event where both leptons are real (prompt). N^{rr} denotes the total number of events in this region.
- rf_i: an event where the leading lepton is real while the subleading lepton is fake. The total number of events in this region is labeled N^{rf}.
- fr_i: an event where the leading lepton is fake and the subleading lepton is real. N^{fr} corresponds to the total number of events in this region.
- ff_i: an event where both leptons are fake. The total number of such events is labeled N^{ff}

The corresponding 4×4 matrix equation can be written as:

$$\begin{pmatrix} N^{TT} \\ N^{T\bar{T}} \\ N^{\bar{T}T} \\ N^{\bar{T}\bar{T}} \end{pmatrix} = \begin{pmatrix} \epsilon_{r,1}\epsilon_{r,2} & \epsilon_{r,1}\epsilon_{f,2} & \epsilon_{f,1}\epsilon_{r,2} & \epsilon_{f,1}\epsilon_{f,2} \\ \epsilon_{r,1}\bar{\epsilon}_{r,2} & \epsilon_{r,1}\bar{\epsilon}_{f,2} & \epsilon_{f,1}\bar{\epsilon}_{r,2} & \epsilon_{f,1}\bar{\epsilon}_{f,2} \\ \bar{\epsilon}_{r,1}\epsilon_{r,2} & \bar{\epsilon}_{r,1}\epsilon_{f,2} & \bar{\epsilon}_{f,1}\epsilon_{r,2} & \bar{\epsilon}_{f,1}\epsilon_{f,2} \\ \bar{\epsilon}_{r,1}\bar{\epsilon}_{r,2} & \bar{\epsilon}_{r,1}\bar{\epsilon}_{f,2} & \bar{\epsilon}_{f,1}\bar{\epsilon}_{r,2} & \bar{\epsilon}_{f,1}\bar{\epsilon}_{f,2} \end{pmatrix} \begin{pmatrix} N^{rr} \\ N^{rf} \\ N^{fr} \\ N^{ff} \end{pmatrix}, \tag{23}$$

where the indices of ϵ_r and ϵ_f correspond to the p_T order of the lepton.

The number of fake events in the signal region can be accessed through observable quantities, by inverting the above equation:

$$\begin{pmatrix} N^{rr} \\ N^{rf} \\ N^{fr} \\ N^{ff} \end{pmatrix} = \begin{pmatrix} \epsilon_{r,1}\epsilon_{r,2} & \epsilon_{r,1}\epsilon_{f,2} & \epsilon_{f,1}\epsilon_{r,2} & \epsilon_{f,1}\epsilon_{f,2} \\ \epsilon_{r,1}\bar{\epsilon}_{r,2} & \epsilon_{r,1}\bar{\epsilon}_{f,2} & \epsilon_{f,1}\bar{\epsilon}_{r,2} & \epsilon_{f,1}\bar{\epsilon}_{f,2} \\ \bar{\epsilon}_{r,1}\epsilon_{r,2} & \bar{\epsilon}_{r,1}\epsilon_{f,2} & \bar{\epsilon}_{f,1}\epsilon_{r,2} & \bar{\epsilon}_{f,1}\epsilon_{f,2} \\ \bar{\epsilon}_{r,1}\bar{\epsilon}_{r,2} & \bar{\epsilon}_{r,1}\bar{\epsilon}_{f,2} & \bar{\epsilon}_{f,1}\bar{\epsilon}_{r,2} & \bar{\epsilon}_{f,1}\bar{\epsilon}_{f,2} \end{pmatrix}^{-1} \begin{pmatrix} N^{TT} \\ N^{T\bar{T}} \\ N^{\bar{T}T} \\ N^{\bar{T}\bar{T}} \end{pmatrix} \tag{24}$$

The total number of fake events (where at least one of the leptons is fake) in the signal region i.e where both leptons pass the tight selection, N^{f}_{TT}, can then be derived as follows:

$$N^{f}_{TT} = N^{rf}_{TT} + N^{fr}_{TT} + N^{ff}_{TT} = \epsilon_{r,1}\epsilon_{f,2}N^{rf} + \epsilon_{r,2}\epsilon_{f,1}N^{fr} + \epsilon_{f,1}\epsilon_{f,2}N^{ff} \tag{25}$$

When combining the matrix equation (24) with the above formula and making the weighted sum over the events explicit, we finally obtain:

$$\begin{aligned} N^{f}_{TT} &= \sum_{i}(\epsilon_{r,1}\epsilon_{f,2}rf)_i + (\epsilon_{r,2}\epsilon_{f,1}fr)_i + (\epsilon_{f,1}\epsilon_{f,2}ff)_i \\ &= \sum_{i}^{\{TT\}}(w^{MM}_{TT}TT)_i + \sum_{i}^{\{T\overline{T}\}}(w^{MM}_{T\overline{T}}T\overline{T})_i + \sum_{i}^{\{\overline{T}T\}}(w^{MM}_{\overline{T}T}\overline{T}T)_i + \sum_{i}^{\{\overline{TT}\}}(w^{MM}_{\overline{TT}}\overline{TT})_i \end{aligned} \tag{26}$$

Where the matrix method weights, w^{MM}, are defined as follows:

$$\begin{aligned} w^{MM}_{TT\ i} &= (1 - \beta\epsilon_{r,1}\epsilon_{r,2}\bar{\epsilon}_{f,1}\bar{\epsilon}_{f,2})_i \\ w^{MM}_{T\overline{T}\ i} &= (\beta\epsilon_{r,1}\epsilon_{r,2}\epsilon_{f,2}\bar{\epsilon}_{f,1})_i \\ w^{MM}_{\overline{T}T\ i} &= (\beta\epsilon_{r,1}\epsilon_{r,2}\epsilon_{f,1}\bar{\epsilon}_{f,2})_i \\ w^{MM}_{\overline{TT}\ i} &= -(\beta\epsilon_{r,1}\epsilon_{r,2}\epsilon_{f,1}\epsilon_{f,2})_i \\ \beta &= \frac{1}{(\epsilon_{r,1_i} - \epsilon_{f,1_i})(\epsilon_{r,2_i} - \epsilon_{f,2_i})} \end{aligned} \tag{27}$$

Evidently, each i-th event will contribute to only one of the four sums on the right side of equation (26).

The measurement of the efficiency for real and fake leptons to pass the tight selection, which are key ingredients for the MM formalism, is performed in dedicated control regions referred to as CR. This control region is designed to be representative of the signal region in terms of kinematics and background composition while being completely orthogonal to the SR and retaining sufficiently large statistics.

In order to provide a fake prediction dependent on the lepton kinematics, the efficiencies have been parametrized in bins of p_T.

Type of fakes In this study the truth information from the simulation is used to understand the type of the events with fake light leptons.

- Fake electron: UnknownElectron = 1, NonIsoElectron = 3, BkgElectron = 4
- Real prompt electron: IsoElectron = 2
- Fake muon: UnknownMuon = 5, NonIsoMuon = 7, BkgMuon = 8
- Real prompt muon: IsoMuon = 6
- Fakes from Hadron = 17

ee Figure 68 shows the truth type of fakes for the ee selection. Leading and subleading leptons are defined by being most energetic and second most energetic, respectively. Also, the data number of events are given in bin zero, as for data no truth information exists.

$\mu\mu$ Figure 69 shows the truth type of fakes for the $\mu\mu$ selection.

eμ Figure 70 shows the truth type of fakes for the eμ selection.

Combined flavours Figure 71 shows the truth type of fakes for selection with the flavours combined.

The result of this study is the demonstration that events with a fake light lepton arises predominantly from the $t\bar{t}$ process. Mostly, the subleading lepton is the fake lepton for both electrons and muons.

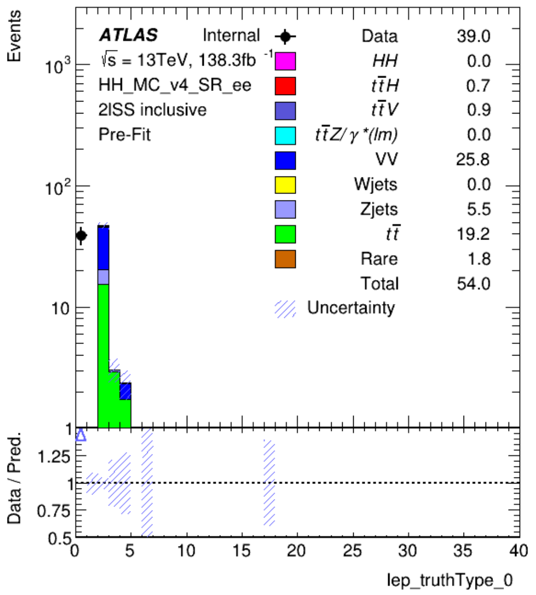

(a) Truth type for leading lepton in signal region with ee selection.

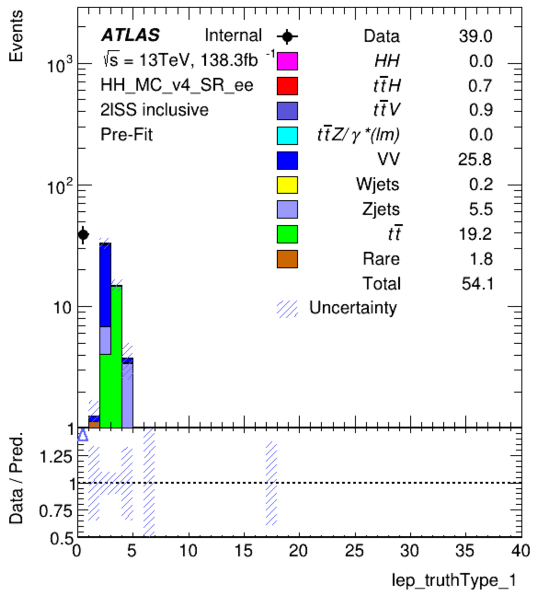

(b) Truth type for sub-leading lepton in signal region with ee selection.

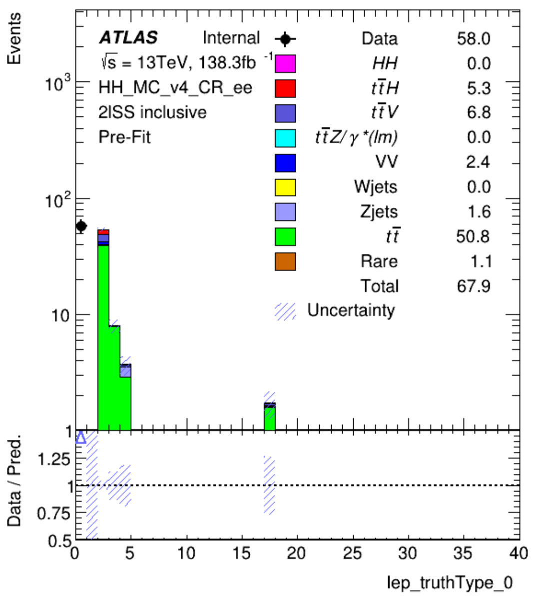

(c) Truth type for leading lepton in control region with ee selection.

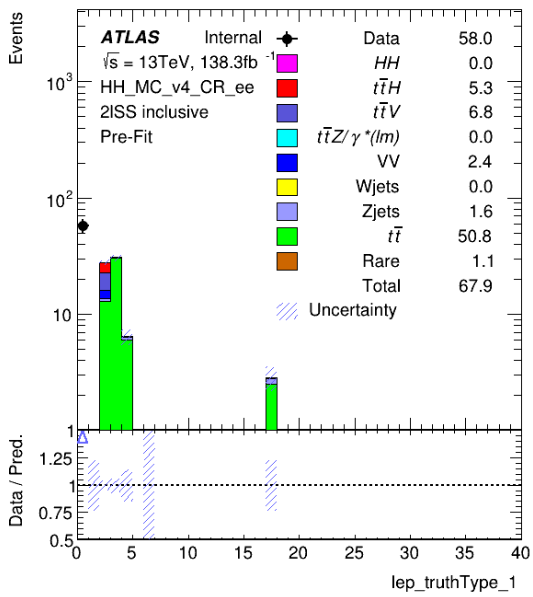

(d) Truth type for sub-leading lepton in control region with ee selection.

Figure 68: Truth types for leading lepton and sub-leading lepton in both signal and control region with ee selection.

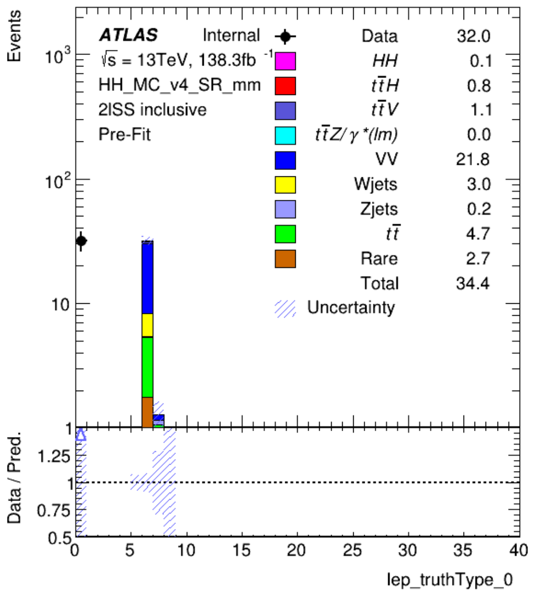

(a) Truth type for leading lepton in signal region with $\mu\mu$ selection.

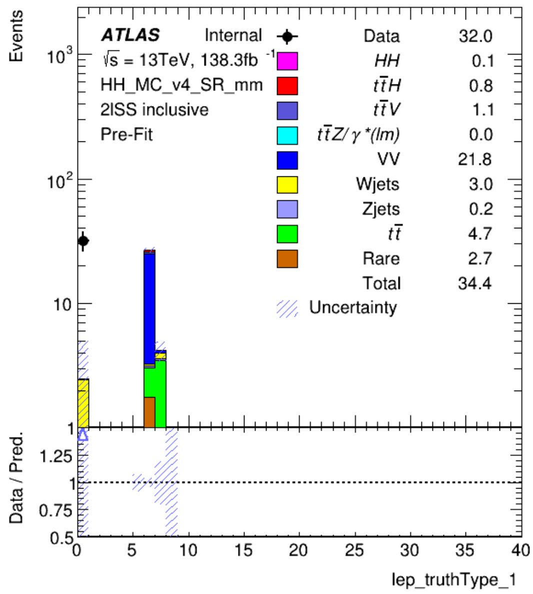

(b) Truth type for sub-leading lepton in signal region with $\mu\mu$ selection.

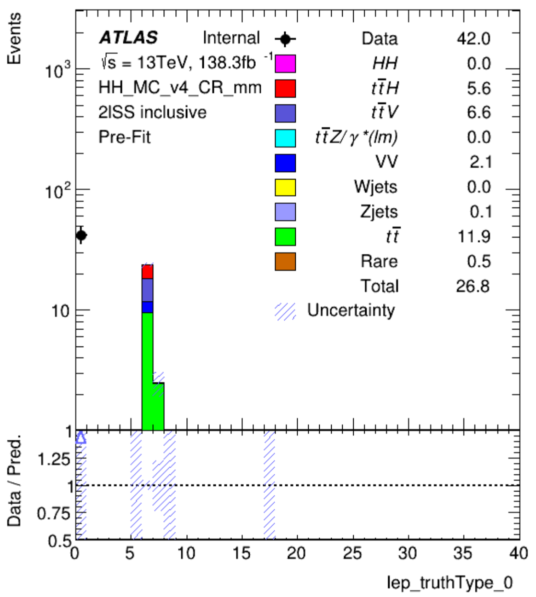

(c) Truth type for leading lepton in control region with $\mu\mu$ selection.

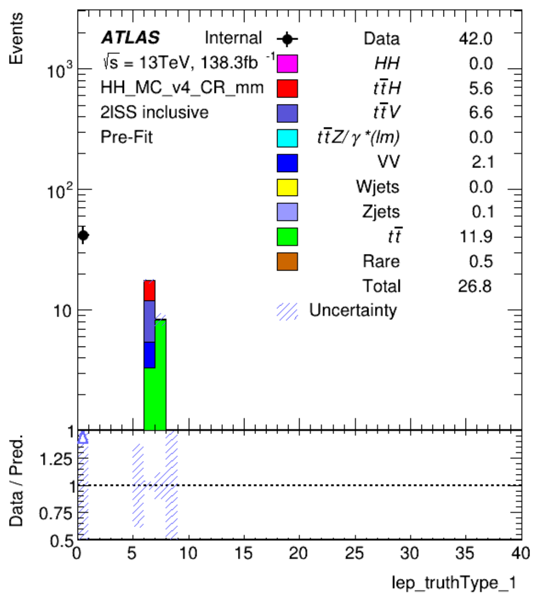

(d) Truth type for sub-leading lepton in control region with $\mu\mu$ selection.

Figure 69: Truth types for leading lepton and sub-leading lepton in both signal and control region with $\mu\mu$ selection.

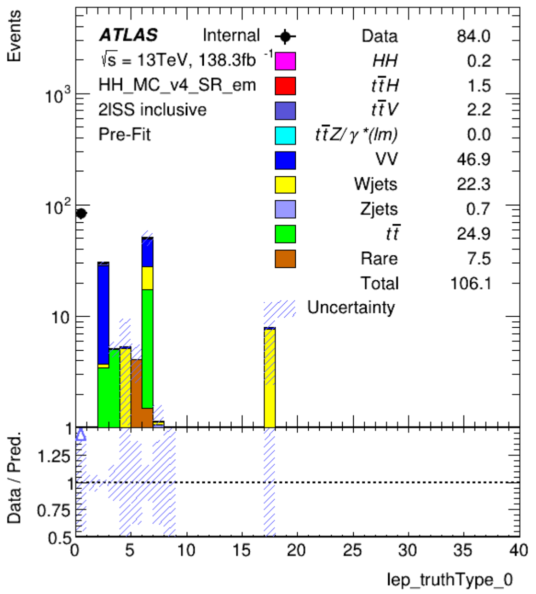

(a) Truth type for leading lepton in signal region with eμ selection.

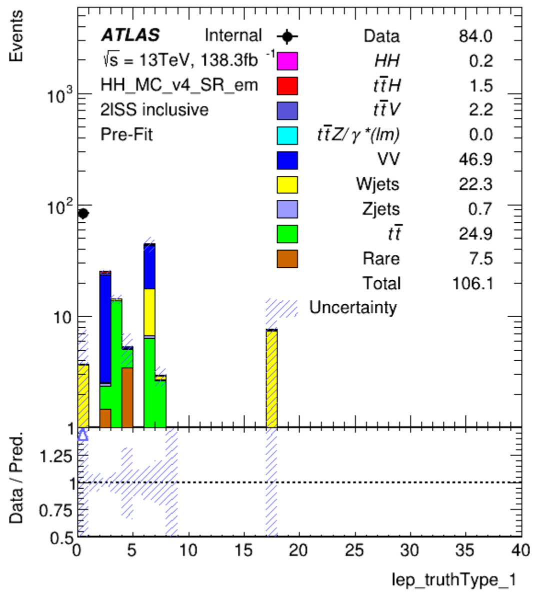

(b) Truth type for sub-leading lepton in signal region with eμ selection.

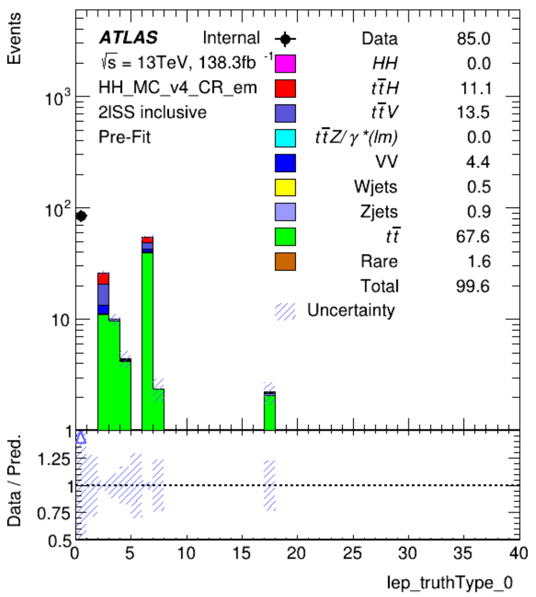

(c) Truth type for leading lepton in control region with eμ selection.

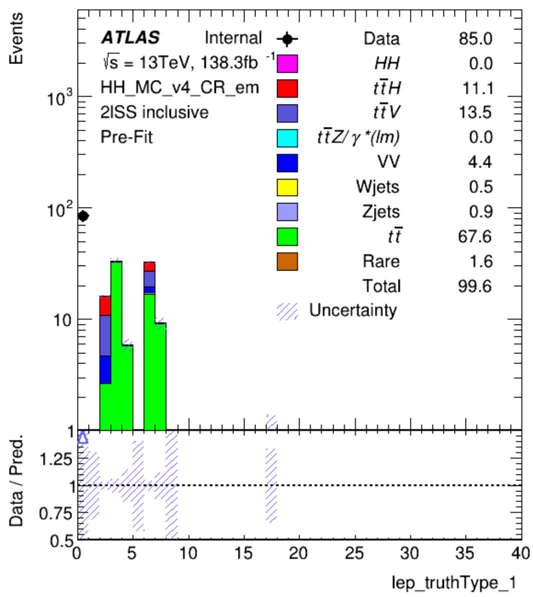

(d) Truth type for sub-leading lepton in control region with eμ selection.

Figure 70: Truth types for leading lepton and sub-leading lepton in both signal and control region with eμ selection.

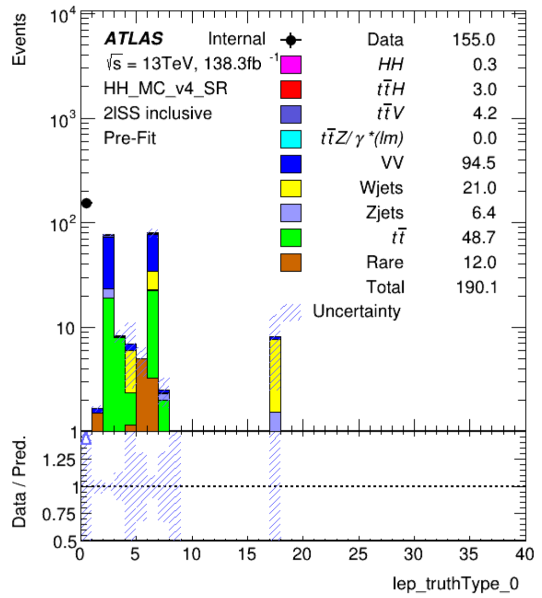

(a) Truth type for leading lepton in signal region with combined flavour selection.

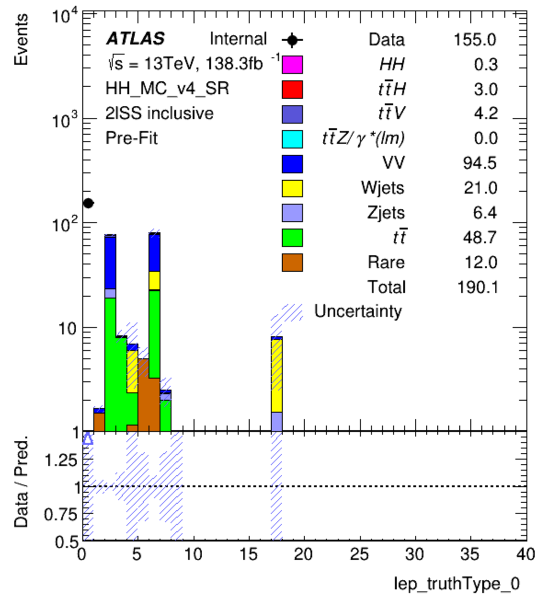

(b) Truth type for sub-leading lepton in signal region with combined flavour selection.

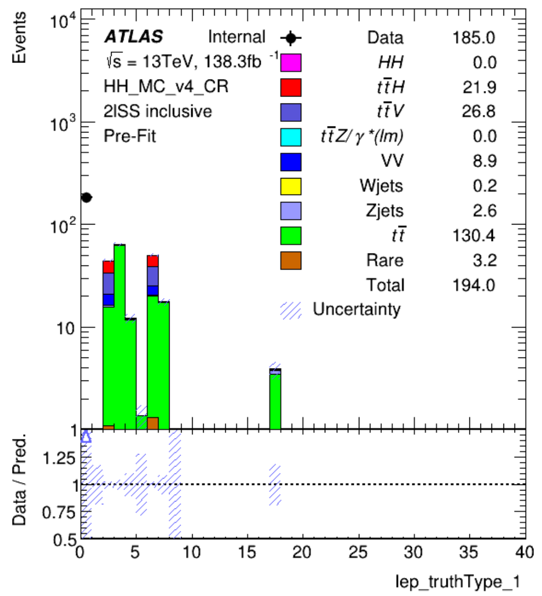

(c) Truth type for leading lepton in control region with combined flavour selection.

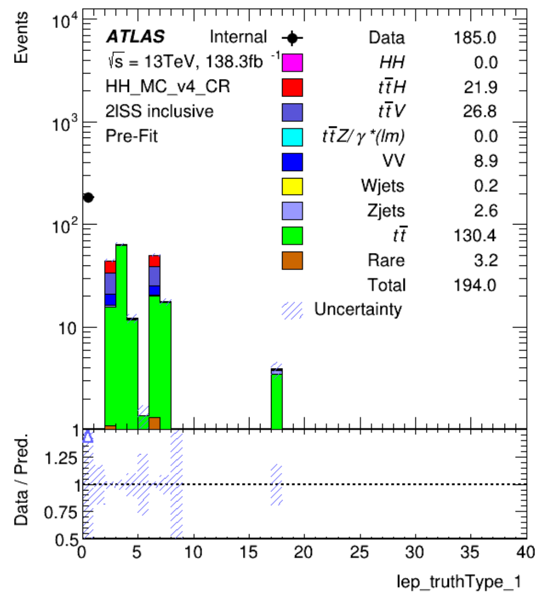

(d) Truth type for sub-leading lepton in control region with combined flavour selection.

Figure 71: Truth types for leading lepton and sub-leading lepton in both signal and control region with combined flavour selection.

Origin of fakes In this study the truth information from the simulation is used to understand the the origin of the events with fake light leptons.

Particle origin:

- Not defined = 0
- Photon conversion = 5
- Dalitz = 6
- top = 10
- W boson = 12
- Z boson = 13
- Higgs = 14
- Charmed meson = 25
- Bottom meson = 26
- Bottom baryon = 33
- Kaon decay = 35,
- Di-boson = 43

ee Figure 72 shows the truth type of fakes for the ee selection.

$\mu\mu$ Figure 73 shows the truth type of fakes for the $\mu\mu$ selection.

eμ Figure 74 shows the truth type of fakes for the eμ selection.

Combined flavours Figure 75 shows the truth type of fakes for the combined flavours selection.

The result of this study is the demonstration that the light fake leptons originate mostly from semileptonic B-meson decays in the $t\bar{t}$ process, both in the CR and SR.

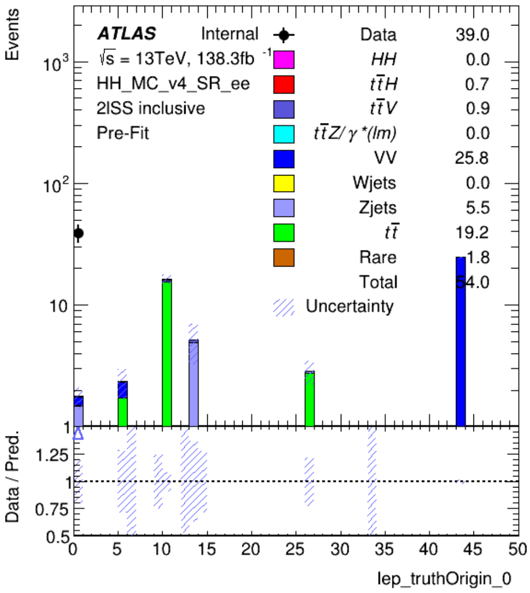

(a) Origin of the fakes for the leading lepton in signal region with ee selection.

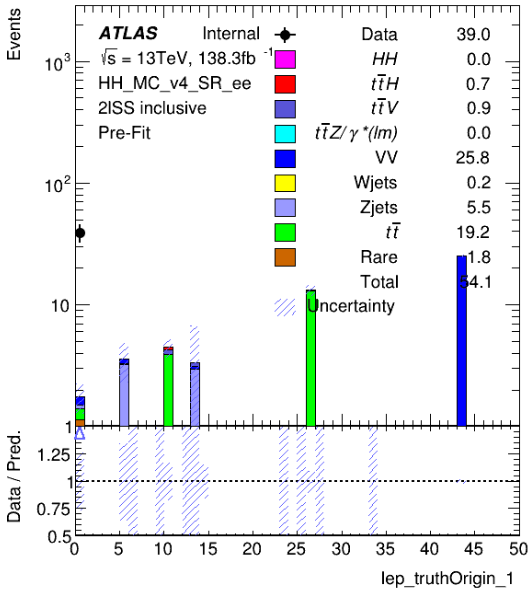

(b) Origin of the fakes for the sub-leading lepton in signal region with ee selection.

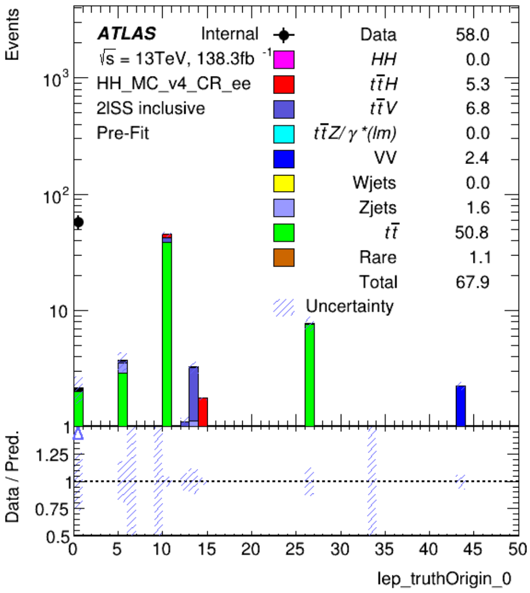

(c) Origin of the fakes for the leading lepton in control region with ee selection.

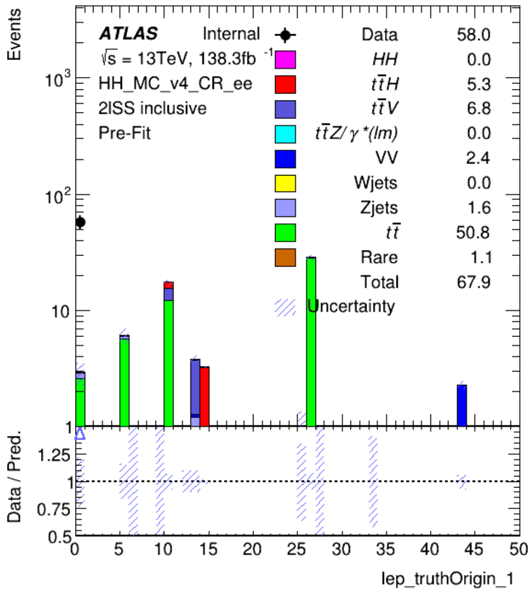

(d) Origin of the fakes for the sub-leading lepton in control region with ee selection.

Figure 72: Origins of the fakes for the leading lepton and sub-leading lepton in both signal and control region with ee selection.

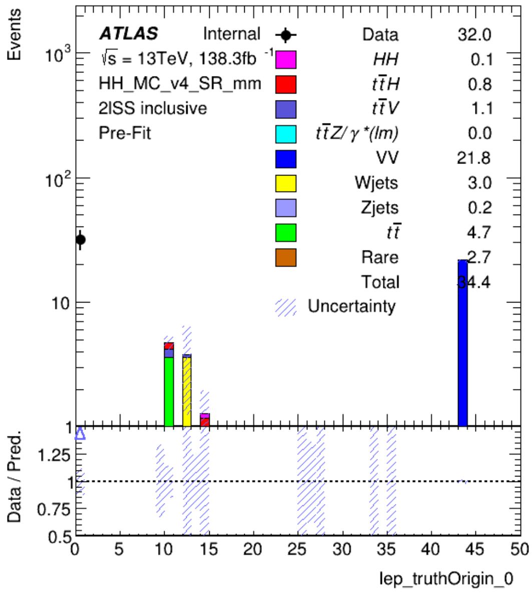

(a) Origin of the fakes for the leading lepton in signal region with $\mu\mu$ selection.

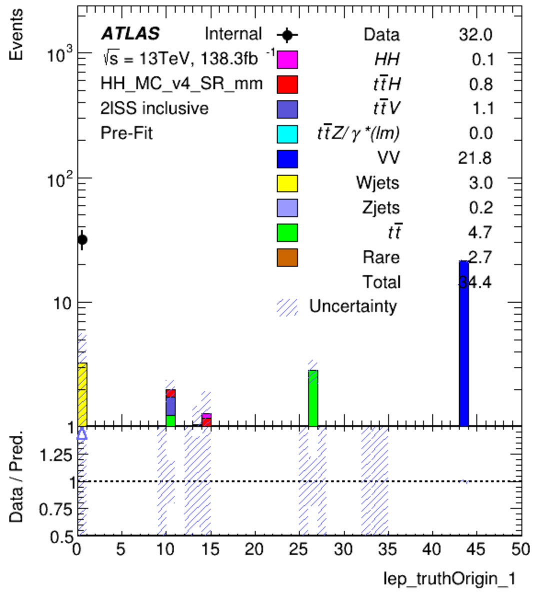

(b) Origin of the fakes for the sub-leading lepton in signal region with $\mu\mu$ selection.

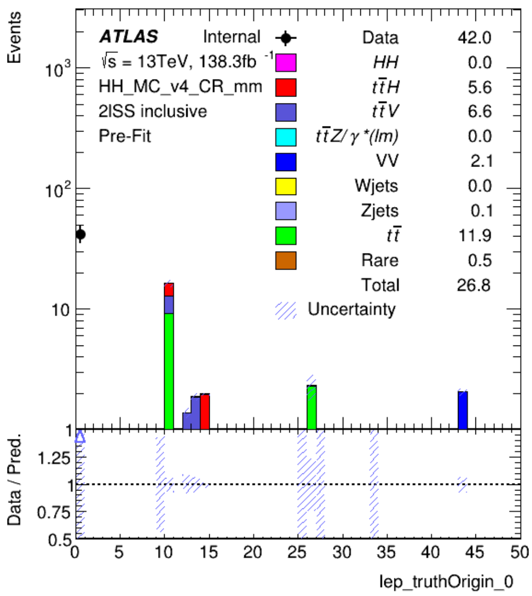

(c) Origin of the fakes for the leading lepton in control region with $\mu\mu$ selection.

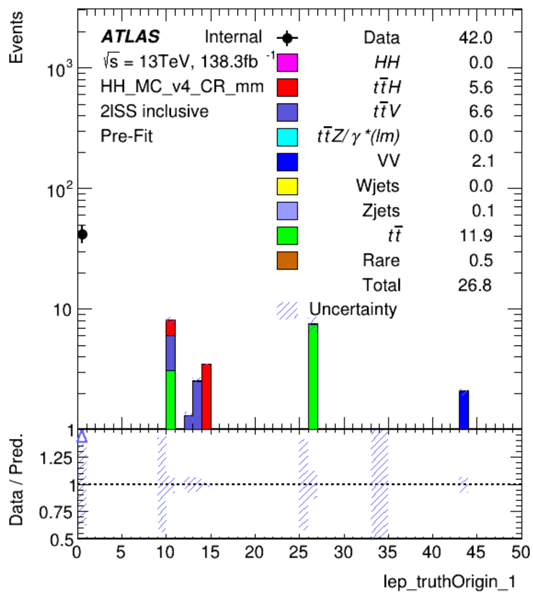

(d) Origin of the fakes for the sub-leading lepton in control region with $\mu\mu$ selection.

Figure 73: Origins of the fakes for the leading lepton and sub-leading lepton in both signal and control region with $\mu\mu$ selection.

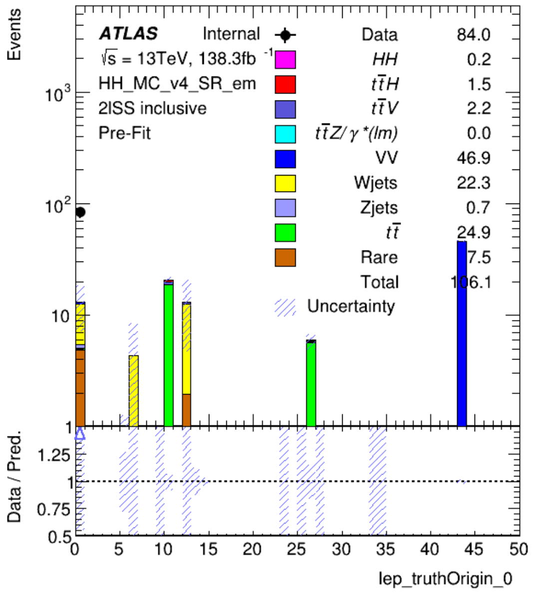

(a) Origin of the fakes for the leading lepton in signal region with $e\mu$ selection.

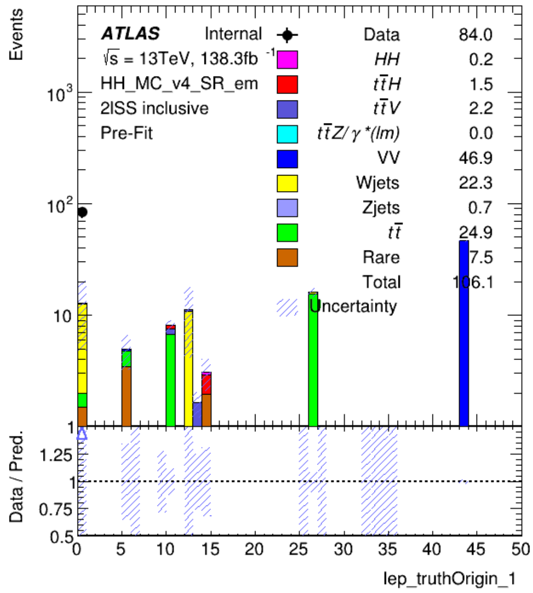

(b) Origin of the fakes for the sub-leading lepton in signal region with $e\mu$ selection.

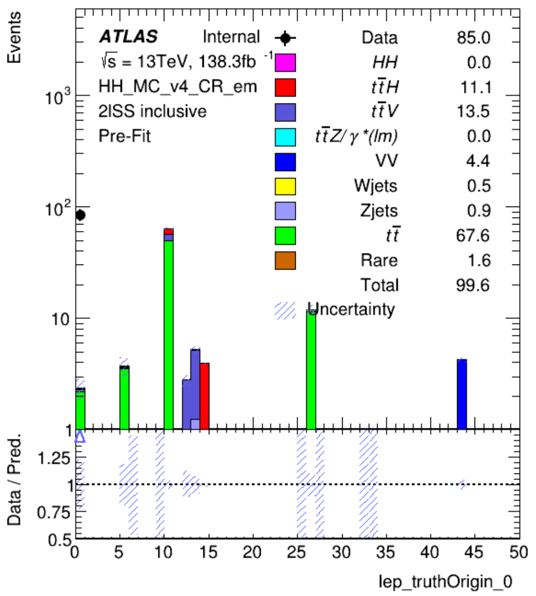

(c) Origin of the fakes for the leading lepton in control region with $e\mu$ selection.

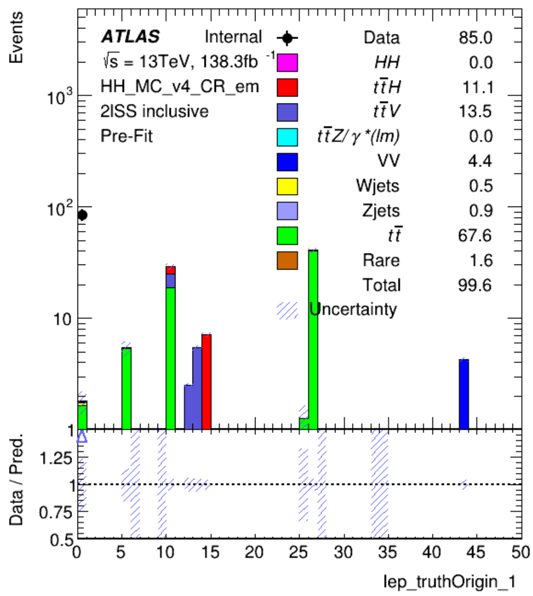

(d) Origin of the fakes for the sub-leading lepton in control region with $e\mu$ selection.

Figure 74: Origins of the fakes for the leading lepton and sub-leading lepton in both signal and control region with $e\mu$ selection.

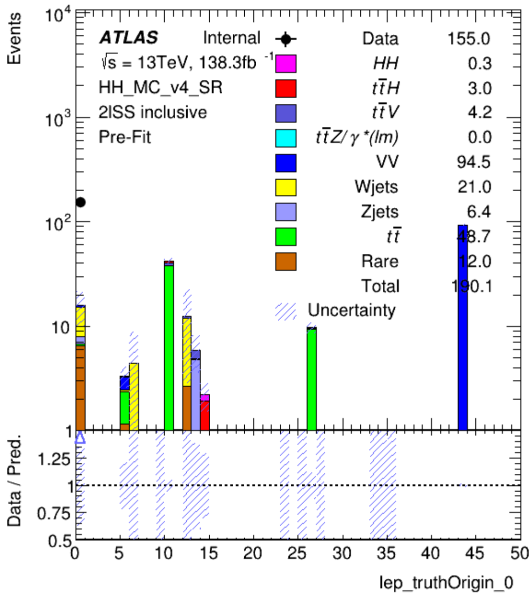

(a) Origin of the fakes for the leading lepton in signal region with combined flavours selection.

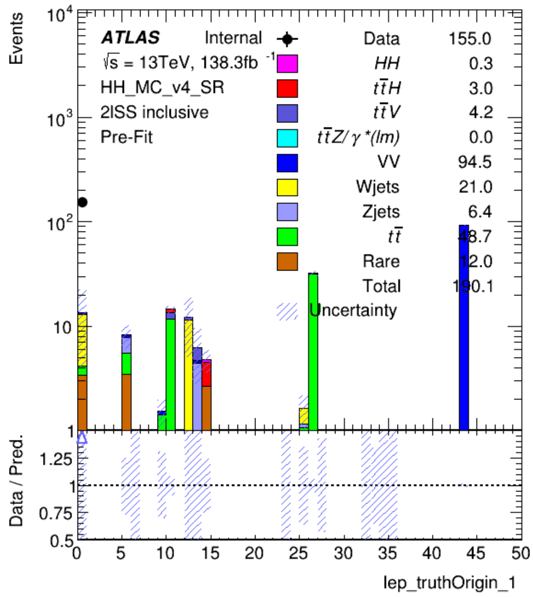

(b) Origin of the fakes for the sub-leading lepton in signal region with combined flavours selection.

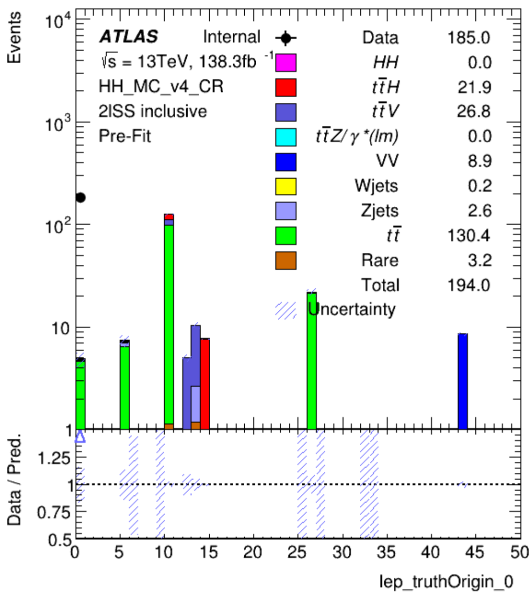

(c) Origin of the fakes for the leading lepton in control region with combined flavours selection.

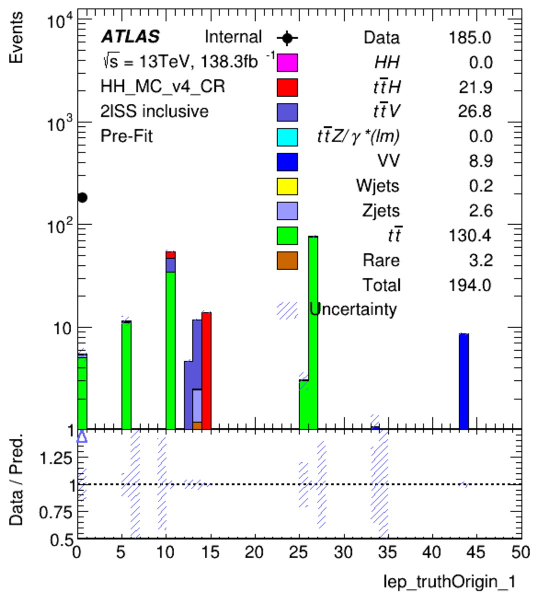

(d) Origin of the fakes for the sub-leading lepton in control region with combined flavours selection.

Figure 75: Origins of the fakes for the leading lepton and sub-leading lepton in both signal and control region with combined flavours selection.

Real and Fake Efficiencies For the efficiency generation, bin ranges of transverse momenta {7, 12, 20, 35, 50, 1000} GeV are used in order to have sufficient statistics in each bin.

The real efficiency is defined as the ratio of the number of events with real leptons passing the tight selection over the number of events with real leptons passing the loose selection. The fake efficiency is defined as the ratio of the number of events with fake leptons passing the tight selection over the number of events with fake leptons passing the loose selection.

For the recorded data, real and fake are not defined by the truth information, thus the following approach is used. For the real efficiency, a high-statistics $Z \to \ell\ell$ sample is used and the real efficiency is determined by the tag-and-probe method. One lepton is required to pass the tight selection, and the second lepton passing the loose selection is used as probe. The efficiency is defined as the ratio of the probe lepton passing the tight selection to all events in the $Z \to \ell\ell$ sample with one tagged lepton.

For the fake efficiency determination, the CR sample is used. In this case the tagged lepton is the leading lepton fulfilling the tight selection and the probe lepton is the subleading lepton. The efficiency is defined as the ratio of the probe lepton passing the tight selection to all events in the CR with one tagged lepton.

Electrons for $t\bar{t}$ Monte-Carlo Figures 76 to 78 show the fake and real electron efficiencies for mcA, mcD and mcE. The same structure within the uncertainties is noted for the three simulation time periods.

Muons for $t\bar{t}$ Monte-Carlo Figures 79 to 81 show the fake and real muon efficiencies for mcA, mcD and mcE. The same structure within the uncertainties is noted for the three simulation time periods.

Electrons and muons for data without background subtraction For the efficiency determination from recorded CR data, only the combined fake efficiencies are shown (Figures 82a and 83a) as the statistics of the individual years is small (Table 46). The real efficiencies are shown for 2016 data (Figures 82b and 83b) as the data statistics is large.

	Electron		Muon	
	Loose [CR]	Tight [CR]	Loose [CR]	Tight [CR]
2015	2	1	1	0
2016	40	22	23	18
2017	42	30	31	14
2018	66	36	37	23

Table 46: Number of events for the determination of electron and muon efficiencies for each of the data sets 2015-2018 for the CR selection.

Electrons and muons for data with background subtraction For the efficiency determination from recorded CR data, only the combined fake efficiencies are shown (Figures 84a and 85a) as the statistics of the individual years is small. The real efficiencies are also shown for combined data (Figures 84b and 85b). Background is from simulated ttW, ttZ and ttH events. These reactions are chosen because they lead to

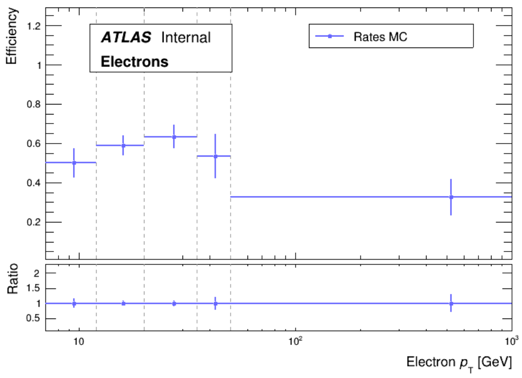

(a) Fake electron mcA efficiency.

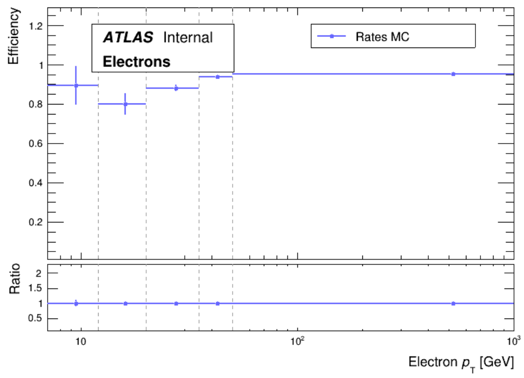

(b) Real electron mcA efficiency.

Figure 76: Fake and real efficiencies for electrons for $t\bar{t}$ mcA files.

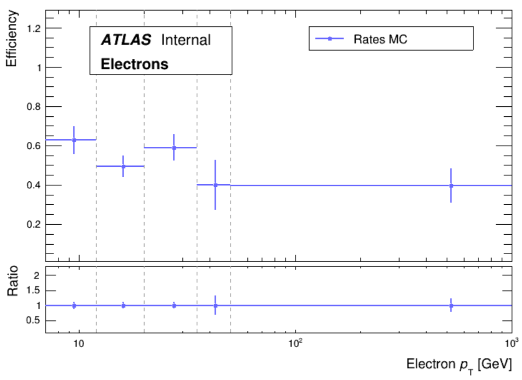

(a) Fake electron mcD efficiency.

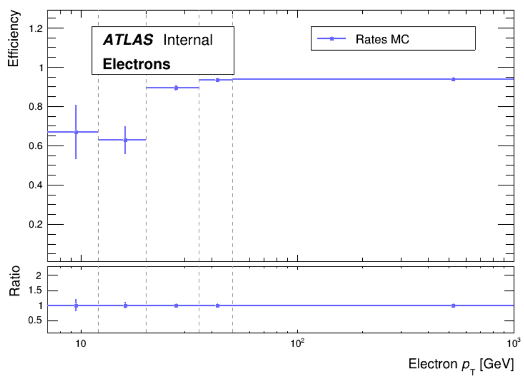

(b) Real electron mcD efficiency.

Figure 77: Fake and real efficiencies for electrons for $t\bar{t}$ mcD files.

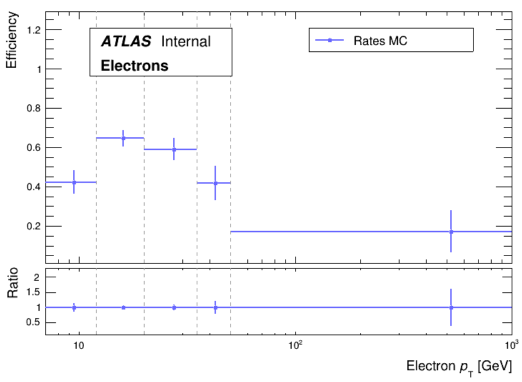

(a) Fake electron mcE efficiency.

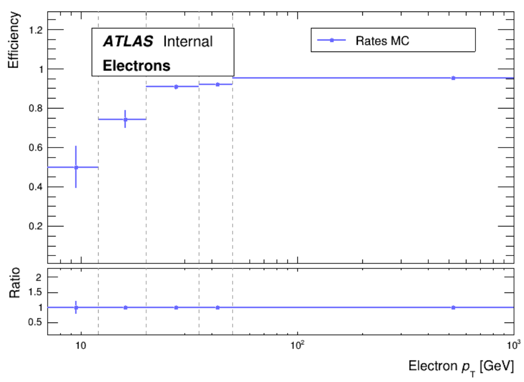

(b) Real electron $t\bar{t}$ mcE efficiency.

Figure 78: Fake and real efficiencies for electrons for mcE files.

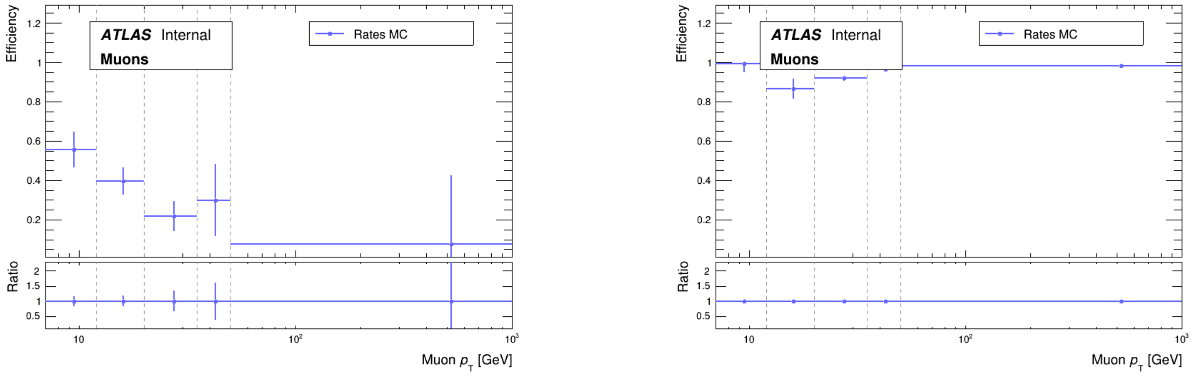

(a) Fake muon mcA efficiency. (b) Real muon mcA efficiency.

Figure 79: Fake and real efficiencies for muons for $t\bar{t}$ mcA files.

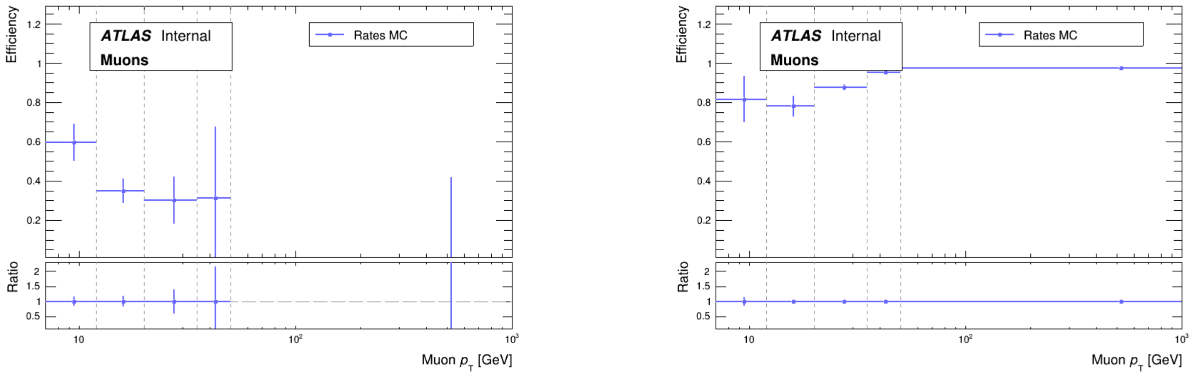

(a) Fake muon mcD efficiency. (b) Real muon mcD efficiency.

Figure 80: Fake and real efficiencies for muons for $t\bar{t}$ mcD files.

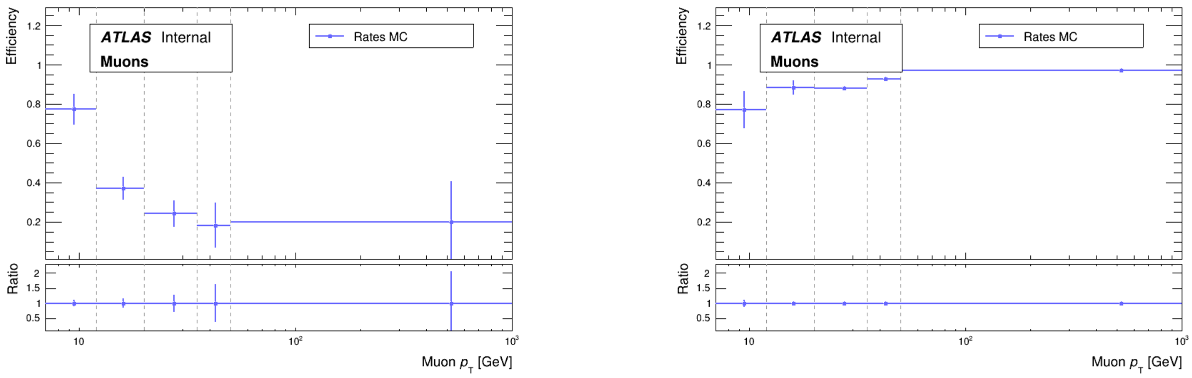

(a) Fake muons mcE efficiency. (b) Real muons mcE efficiency.

Figure 81: Fake and real efficiencies for muons for $t\bar{t}$ mcE files.

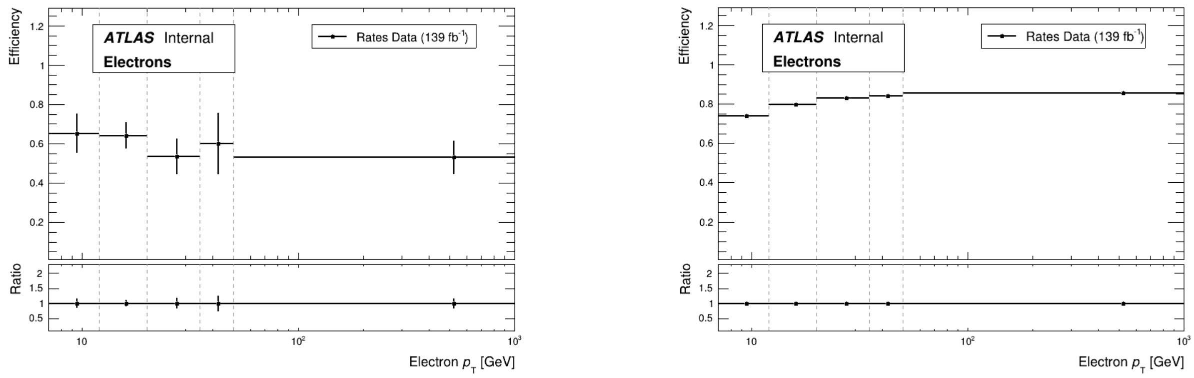

(a) Fake electron efficiency for combined 2015-2018 data.

(b) Real electron efficiency for combined 2015-2018 data.

Figure 82: Fake and real efficiencies for electrons from CR data without background subtraction.

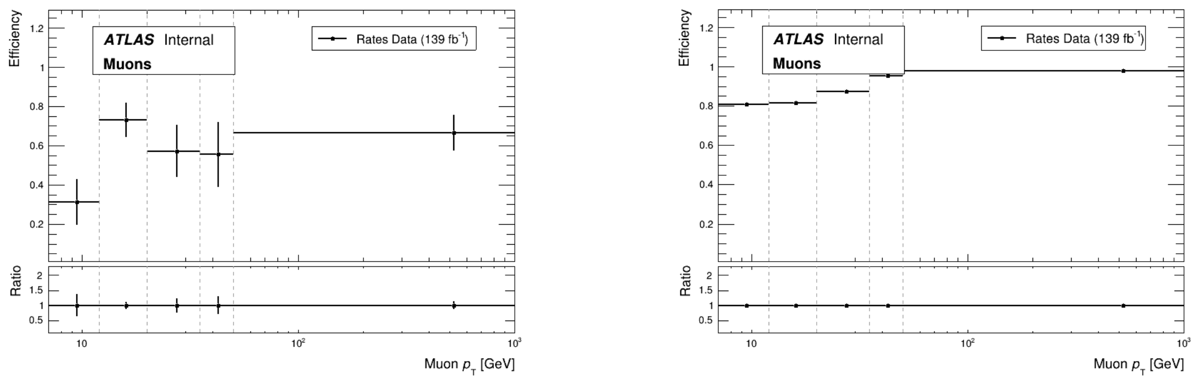

(a) Fake muon efficiency for combined 2015-2018 data.

(b) Real muon efficiency for combined 2015-2018 data.

Figure 83: Fake and real efficiencies for muons from CR data without background subtraction.

similar final states, but have only prompt leptons, which contaminate the fake lepton distributions. The expected number of these events are subtracted from the data distributions before the distributions are used to determine the real and fake efficiencies. The ratio pad in the figures can be ignored.

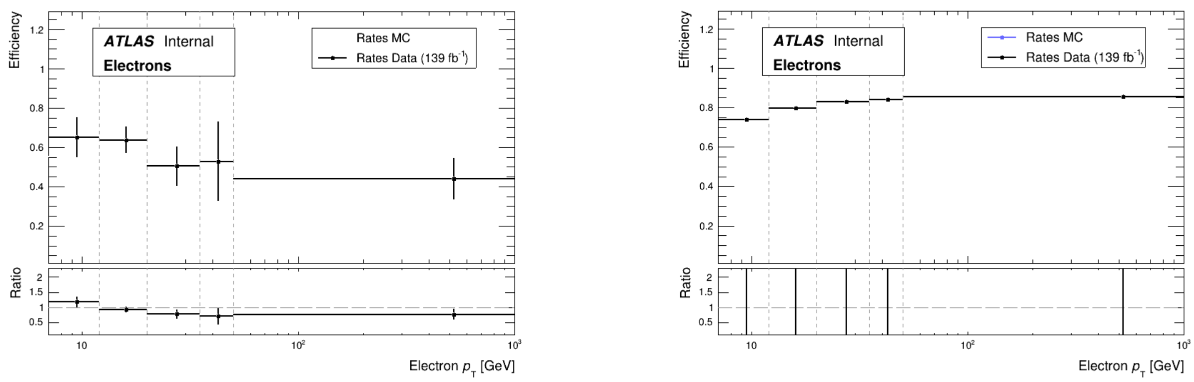

(a) Fake electron efficiency for combined 2015-2018 data.

(b) Real electron efficiency for combined 2015-2018 data.

Figure 84: Fake and real efficiencies for electrons from CR data with background subtraction.

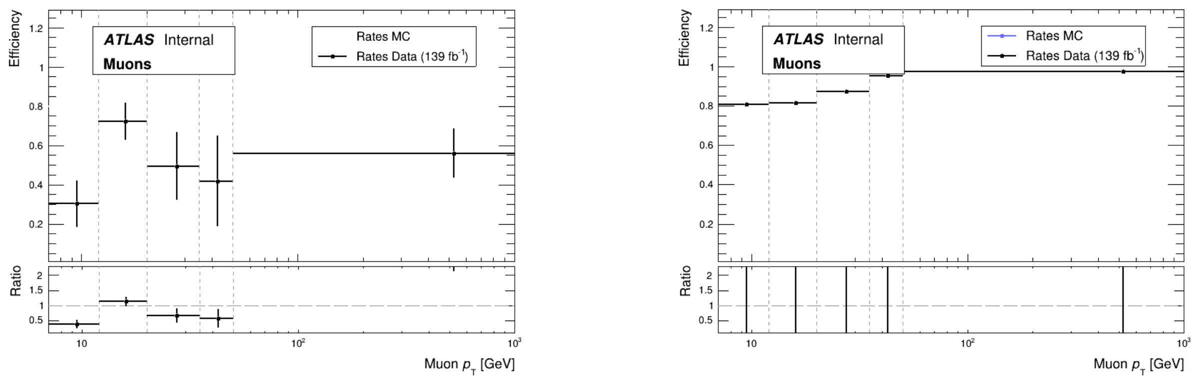

(a) Fake muon efficiency for combined 2015-2018 data.

(b) Real muon efficiency for combined 2015-2018 data.

Figure 85: Fake and real efficiencies for muons from CR data with background subtraction.

There is no significant difference between the mcA, mcD and mcE distributions. The efficiency distributions are the input for the Matrix Method.

Closure Tests

ee Leading lepton transverse momentum distributions for Monte-Carlo simulation and Matrix Method for ee selection are shown in Figure 86 for signal region and Figure 87 for control region.

The closure test for signal and control regions with ee selection are shown in Table 47.

ee selection	SR [$t\bar{t}$ events]	CR [$t\bar{t}$ events]
MC $t\bar{t}$	19.2 ± 1.7	50.8 ± 2.7
MM $t\bar{t}$	19.0 ± 2.4	48.7 ± 4.1
Ratio	1.01 ± 0.16	1.04 ± 0.10

Table 47: Closure test for signal and control region with ee selection. Statistical uncertainties are given.

The systematic uncertainty is assigned to be 16%, as the statistical uncertainty is larger than the deviation from unity of the ratio mean value.

μμ Leading lepton transverse momentum distributions for Monte-Carlo simulation and Matrix Method for $\mu\mu$ selection are shown in Figure 88 for signal region and Figure 89 for control region.

The closure test for signal and control regions with $\mu\mu$ selection are shown in Table 48.

$\mu\mu$ selection	SR [$t\bar{t}$ events]	CR [$t\bar{t}$ events]
MC $t\bar{t}$	4.68 ± 1.08	11.9 ± 1.3
MM $t\bar{t}$	7.95 ± 0.71	17.1 ± 1.0
Ratio	0.59 ± 0.15	0.70 ± 0.09

Table 48: Closure test for signal and control region with $\mu\mu$ selection. Statistical uncertainties are given.

The systematic uncertainty is assigned to be 41%, as the statistical uncertainty is small than the deviation from unity of the ratio mean value.

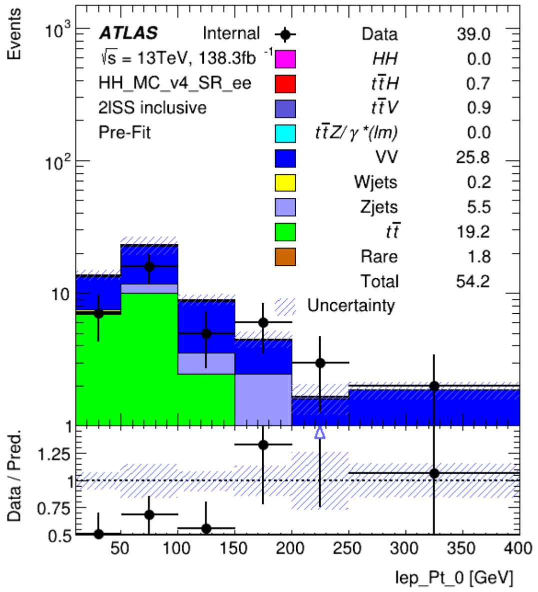

(a) Distribution of events for full Monte-Carlo simulation in signal region.

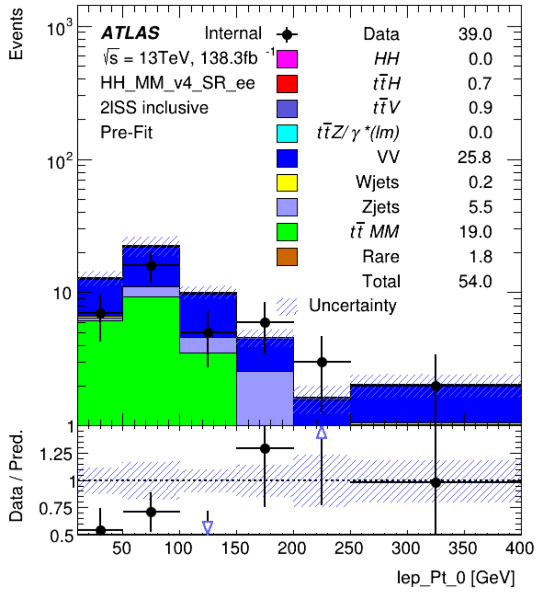

(b) Distribution of events for Matrix Method $t\bar{t}$ in signal region.

Figure 86: Distributions of events for Monte-Carlo simulation and Matrix Method in signal region for ee selection.

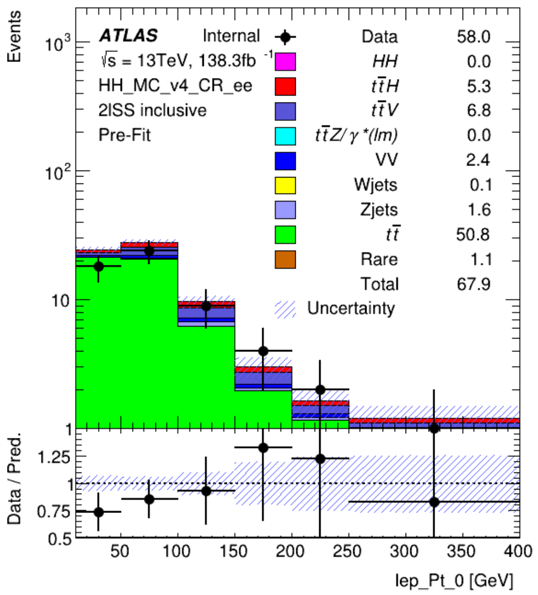

(a) Distribution of events for full Monte-Carlo simulation in control region.

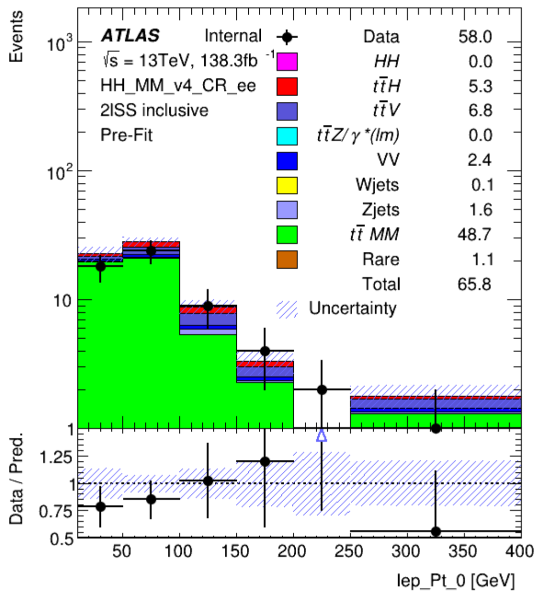

(b) Distribution of events for Matrix Method $t\bar{t}$ in control region.

Figure 87: Distributions of events for Monte-Carlo simulation and Matrix Method in control region for ee selection.

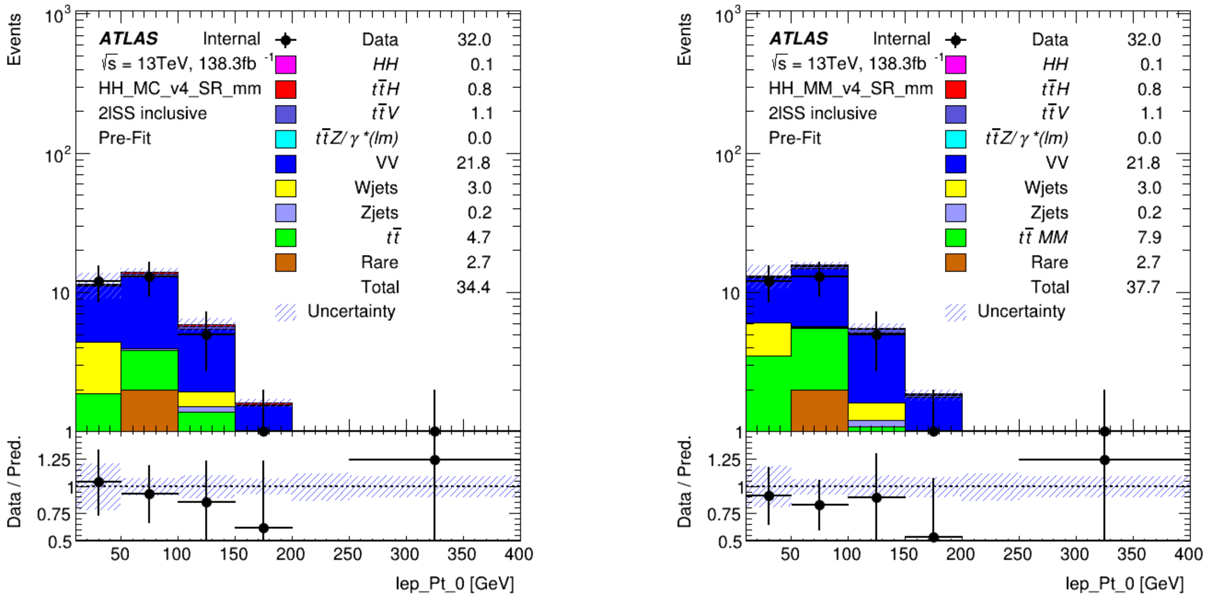

(a) Distribution of events for full Monte-Carlo simulation in signal region.

(b) Distribution of events for Matrix Method $t\bar{t}$ in signal region.

Figure 88: Distributions of events for Monte-Carlo simulation and Matrix Method in signal region for $\mu\mu$ selection.

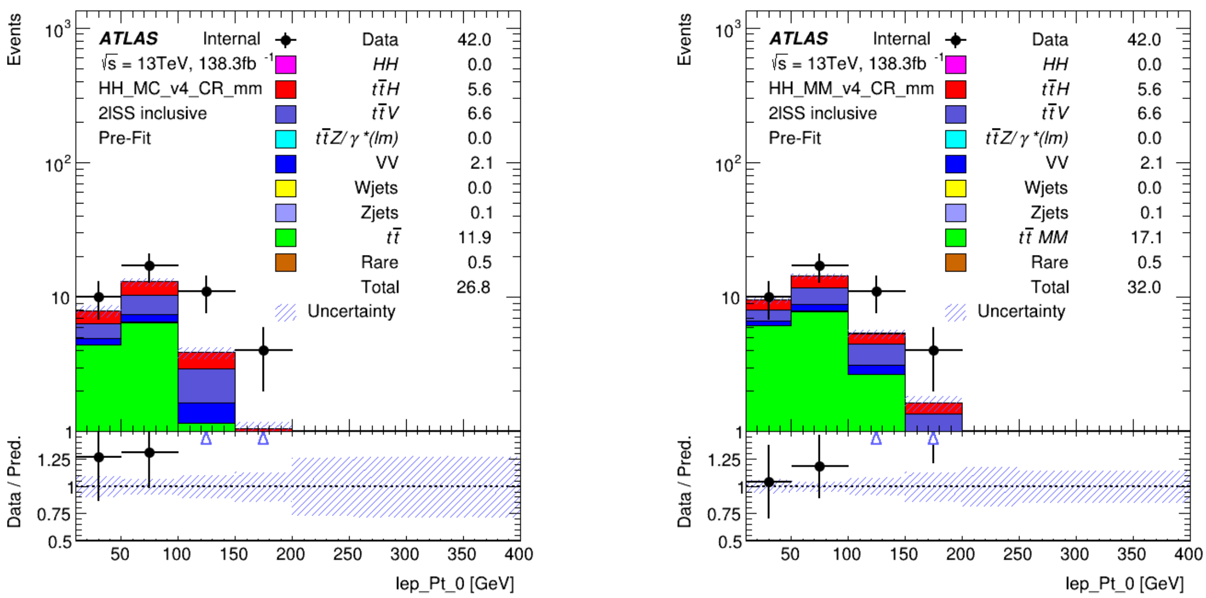

(a) Distribution of events for full Monte-Carlo simulation in control region.

(b) Distribution of events for Matrix Method $t\bar{t}$ in control region.

Figure 89: Distributions of events for Monte-Carlo simulation and Matrix Method in control region for $\mu\mu$ selection.

eμ Leading lepton transverse momentum distributions for Monte-Carlo simulation and Matrix Method for $e\mu$ selection are shown in Figure 90 for signal region and Figure 91 for control region.

The closure test for signal and control regions with eμ selection are shown in Table 49.

eμ selection	SR [$t\bar{t}$ events]	CR [$t\bar{t}$ events]
MC $t\bar{t}$	24.9 ± 1.9	61.1 ± 3.7
MM $t\bar{t}$	24.3 ± 2.3	67.6 ± 3.0
Ratio	1.02 ± 0.12	0.90 ± 0.07

Table 49: Closure test for signal and control region with $e\mu$ selection. Statistical uncertainties are given.

The systematic uncertainty is assigned to be 12%, as the statistical uncertainty is larger than the deviation from unity of the ratio mean value.

Combined flavours Distributions of events for Monte-Carlo simulation and Matrix Method for combined flavour selection can be seen from Figure 92 for signal region and Figure 93 for closure region.

The closure test for signal and control region with combined flavour selection can be seen from Table 50.

Combined flavours	SR [$t\bar{t}$ events]	CR [$t\bar{t}$ events]
MC $t\bar{t}$	48.7 ± 2.6	130.4 ± 4.2
MM $t\bar{t}$	51.2 ± 3.4	126.9 ± 5.6
Ratio	0.95 ± 0.08	1.03 ± 0.06

Table 50: Closure test for signal and control region with combined flavour selection. Statistical uncertainties are given.

The systematic uncertainty is assigned to be 8%, as the statistical uncertainty is larger than the deviation from unity of the ratio mean value.

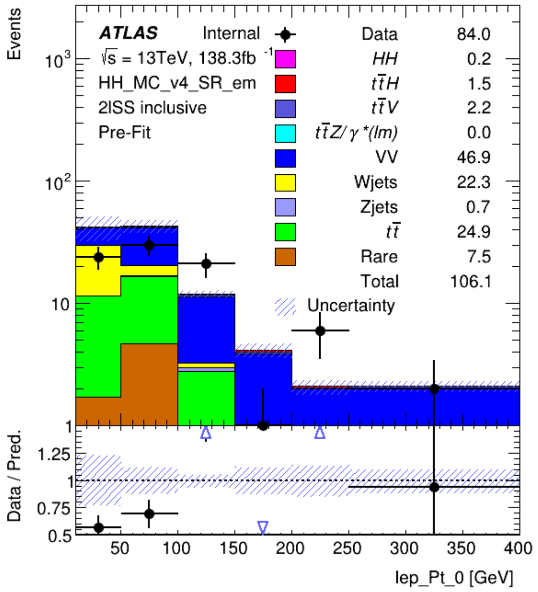

(a) Distribution of events for full Monte-Carlo simulation in signal region.

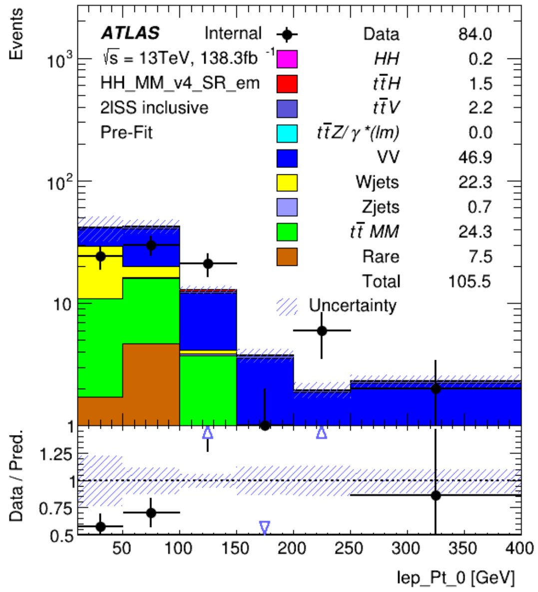

(b) Distribution of events for Matrix Method $t\bar{t}$ in signal region.

Figure 90: Distributions of events for Monte-Carlo simulation and Matrix Method in signal region for eμ selection.

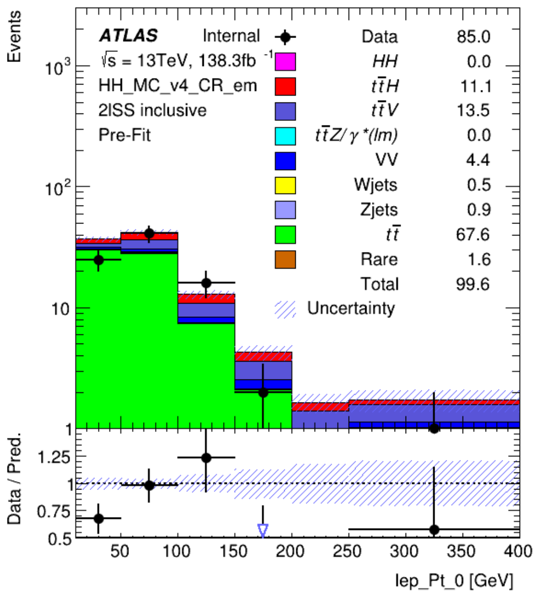

(a) Distribution of events for full Monte-Carlo simulation in control region.

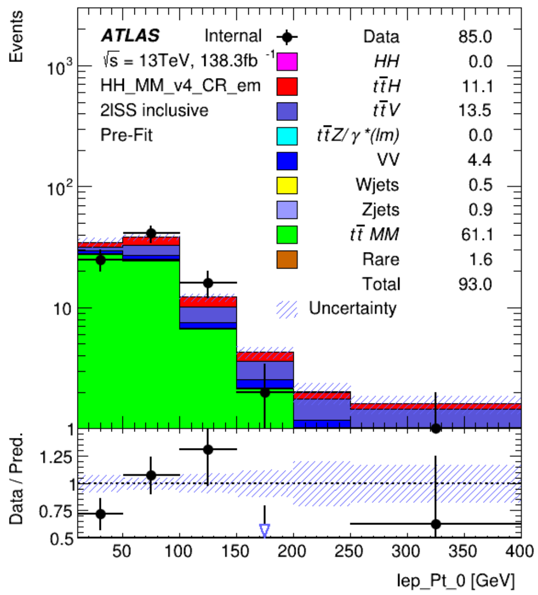

(b) Distribution of events for Matrix Method $t\bar{t}$ in control region.

Figure 91: Distributions of events for Monte-Carlo simulation and Matrix Method in control region for eμ selection.

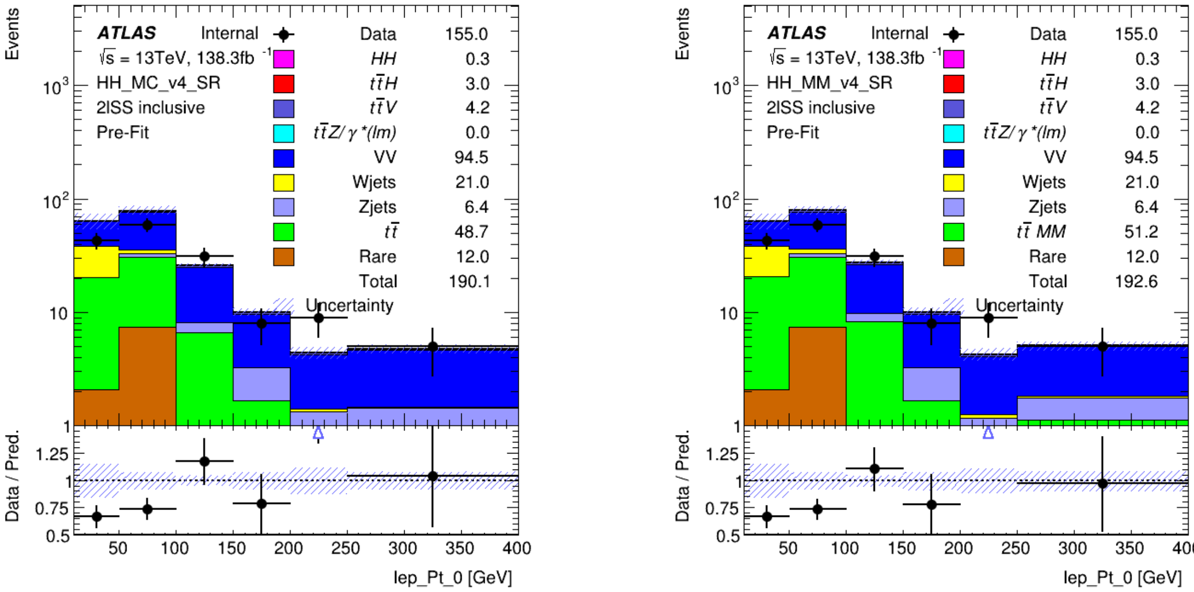

(a) Distribution of events for full Monte-Carlo simulation in signal region.

(b) Distribution of events for Matrix Method $t\bar{t}$ in signal region.

Figure 92: Distributions of events for Monte-Carlo simulation and Matrix Method in signal region for combined flavour selection.

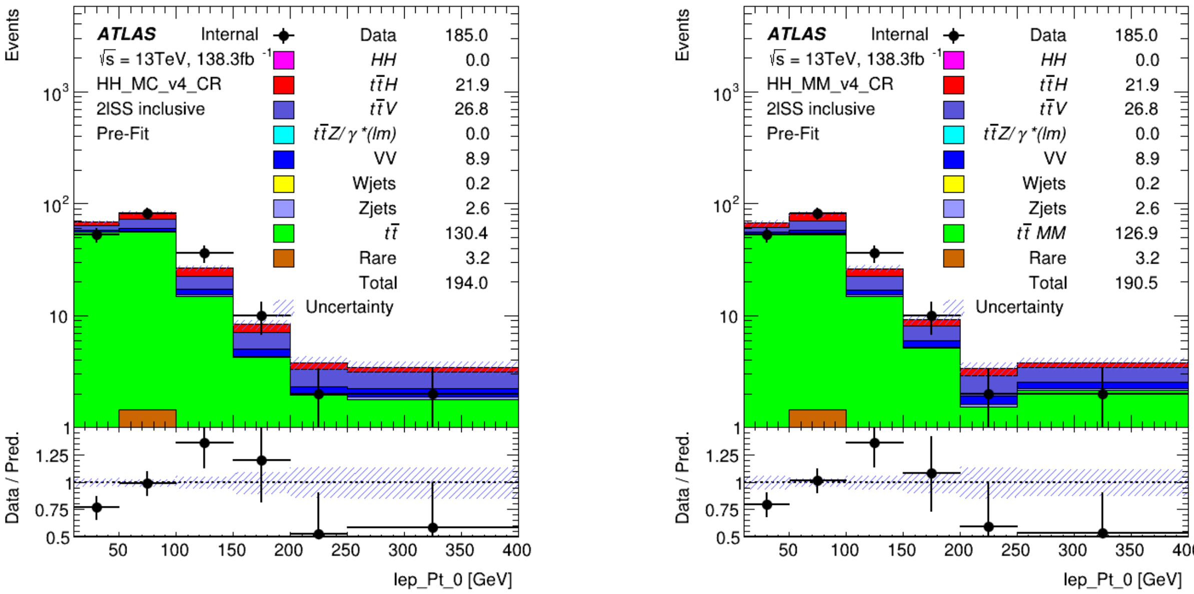

(a) Distribution of events for full Monte-Carlo simulation in control region.

(b) Distribution of events for Matrix Method $t\bar{t}$ in control region.

Figure 93: Distributions of events for Monte-Carlo simulation and Matrix Method in control region for combined flavour selection.

2010 Fake rate test in CR

2011 **Without efficiency background subtraction** The Matrix Method fake rate result, determined from fake
2012 and real efficiencies for electrons and muons based on recorded CR data, is validated in the CR. Figure 94
2013 show the distribution of the Matrix Method $t\bar{t}$ events. Comparing the data-driven MM result Figure 94a
2014 with the MC-only distribution Figure 93a, the number of $t\bar{t}$ events increases from 130.4 events (MC-only)
2015 to 170.1 events (data-driven MM). The separations for ee, $e\mu$ and $\mu\mu$ are shown in Figures 95 to 97.

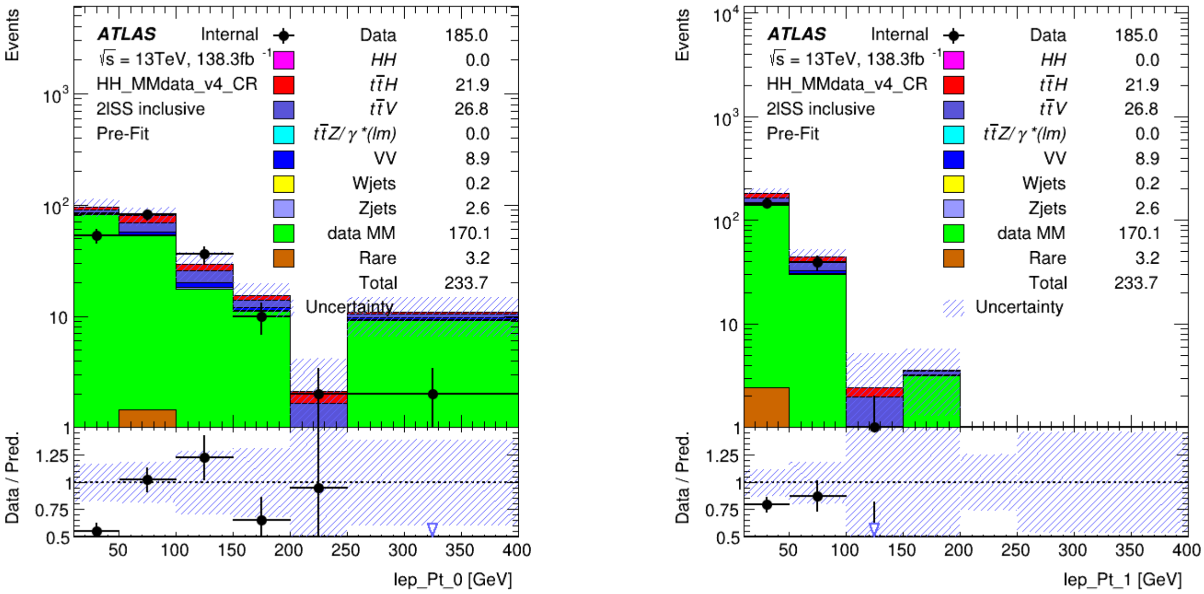

(a) Leading lepton. (b) Sub-leading lepton.

Figure 94: Distributions of events for Monte-Carlo simulation and Matrix Method (efficiencies from data) in control region for combined flavour selection. "data MM" replaces the MC $t\bar{t}$.

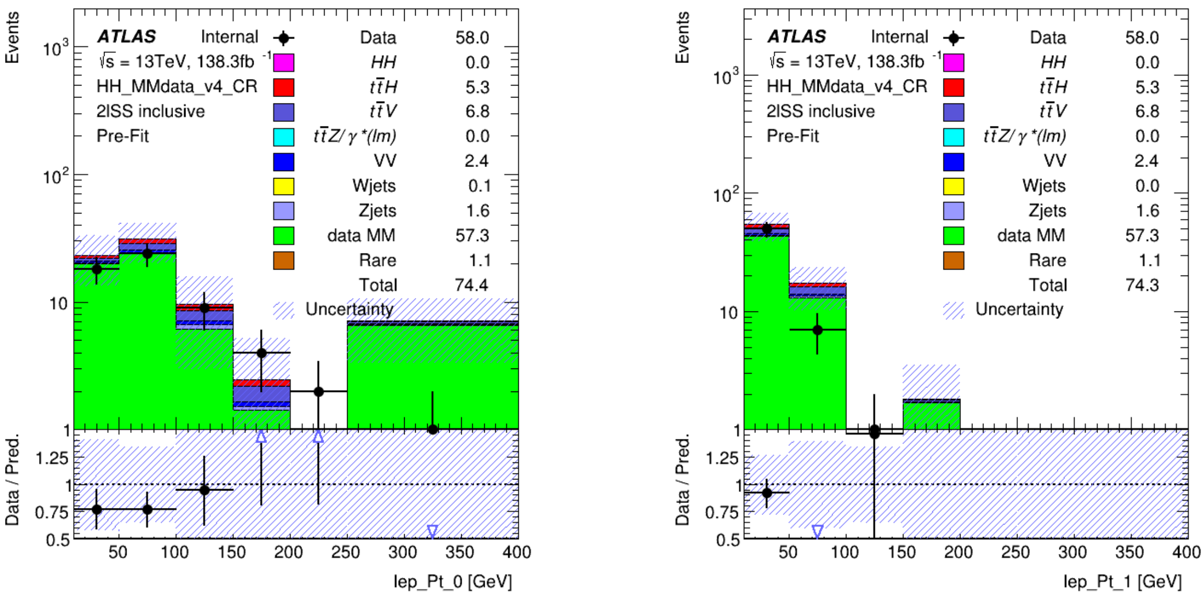

(a) Leading lepton. (b) Sub-leading lepton.

Figure 95: Distributions of events for Monte-Carlo simulation and Matrix Method (efficiencies from data) in control region for di-electron selection. "data MM" replaces the MC $t\bar{t}$.

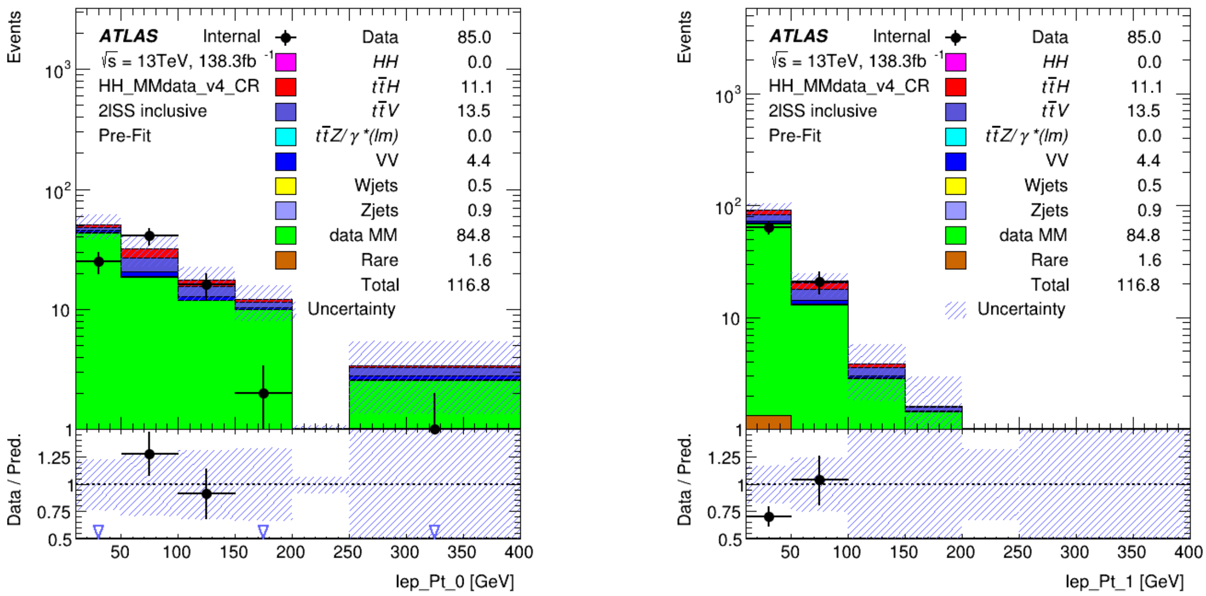

(a) Leading lepton.

(b) Sub-leading lepton.

Figure 96: Distributions of events for Monte-Carlo simulation and Matrix Method (efficiencies from data) in control region for electron-muon selection. "data MM" replaces the MC $t\bar{t}$.

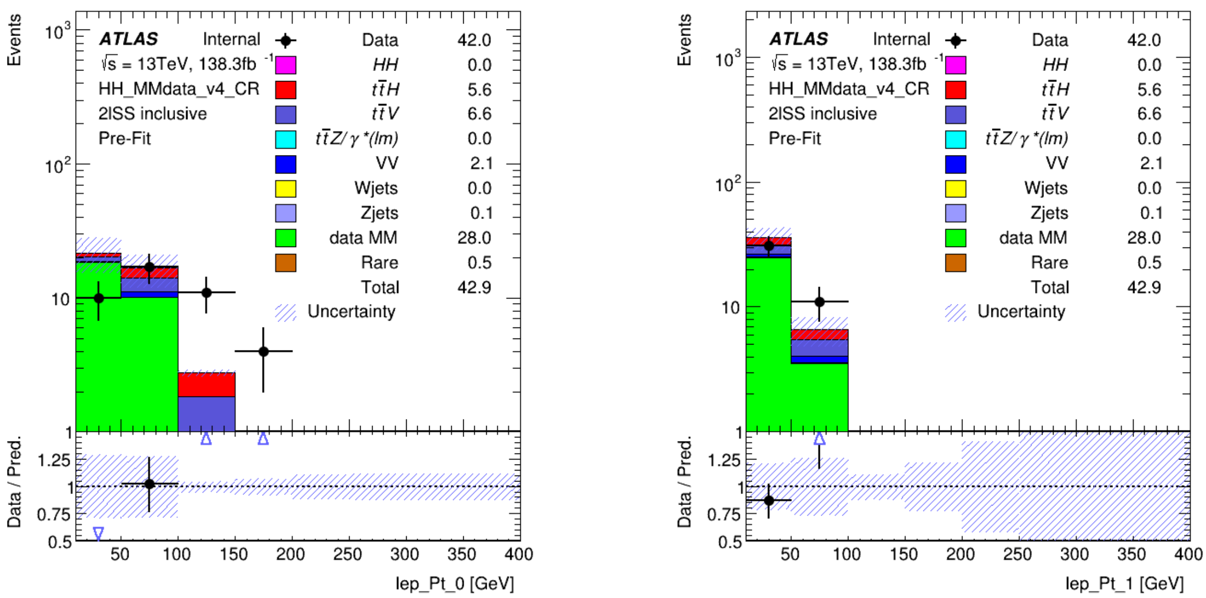

(a) Leading lepton.

(b) Sub-leading lepton.

Figure 97: Distributions of events for Monte-Carlo simulation and Matrix Method (efficiencies from data) in control region for di-muon selection. "data MM" replaces the MC $t\bar{t}$.

2016 **With efficiency background subtraction** The Matrix Method fake rate result, determined from fake
2017 and real efficiencies for electrons and muons based on recorded CR data, is validated in the CR.

2018 For the real and fake efficiency determination, the simulated background from ttH, ttW and ttZ is
2019 subtracted.

2020 Figure 98 show the distribution of the Matrix Method $t\bar{t}$ events. Comparing the data-driven MM result
2021 Figure 98a with the MC-only distribution Figure 93a, the number of $t\bar{t}$ events increases from 130.4 events
2022 (MC-only) to 153.3 events (data-driven MM). The separations for ee, $e\mu$ and $\mu\mu$ are shown in Figures 99
2023 to 101.

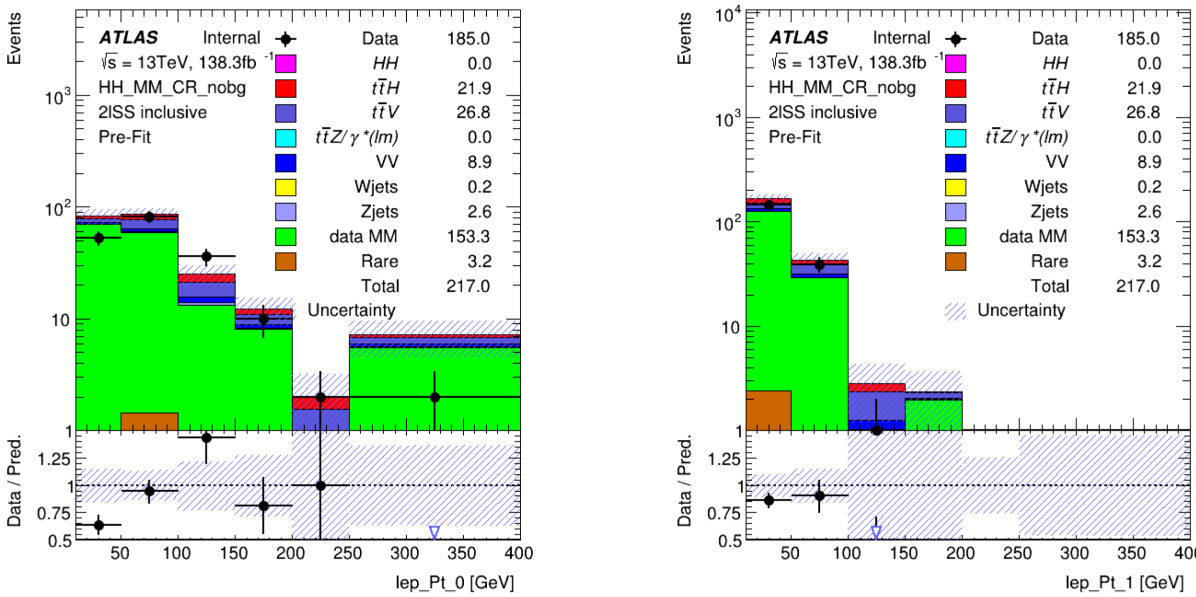

(a) Leading lepton.

(b) Sub-leading lepton.

Figure 98: Distributions of events for Monte-Carlo simulation and Matrix Method (efficiencies from data) in control region for combined flavour selection. "data MM" replaces the MC $t\bar{t}$.

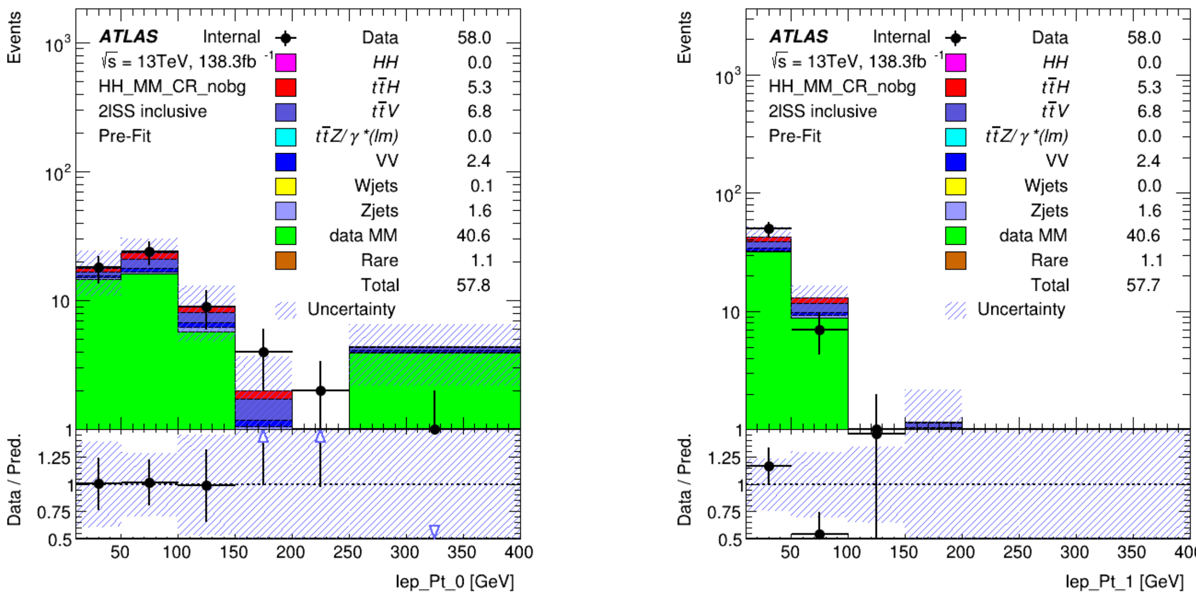

(a) Leading lepton.

(b) Sub-leading lepton.

Figure 99: Distributions of events for Monte-Carlo simulation and Matrix Method (efficiencies from data) in control region for di-electron selection. "data MM" replaces the MC $t\bar{t}$.

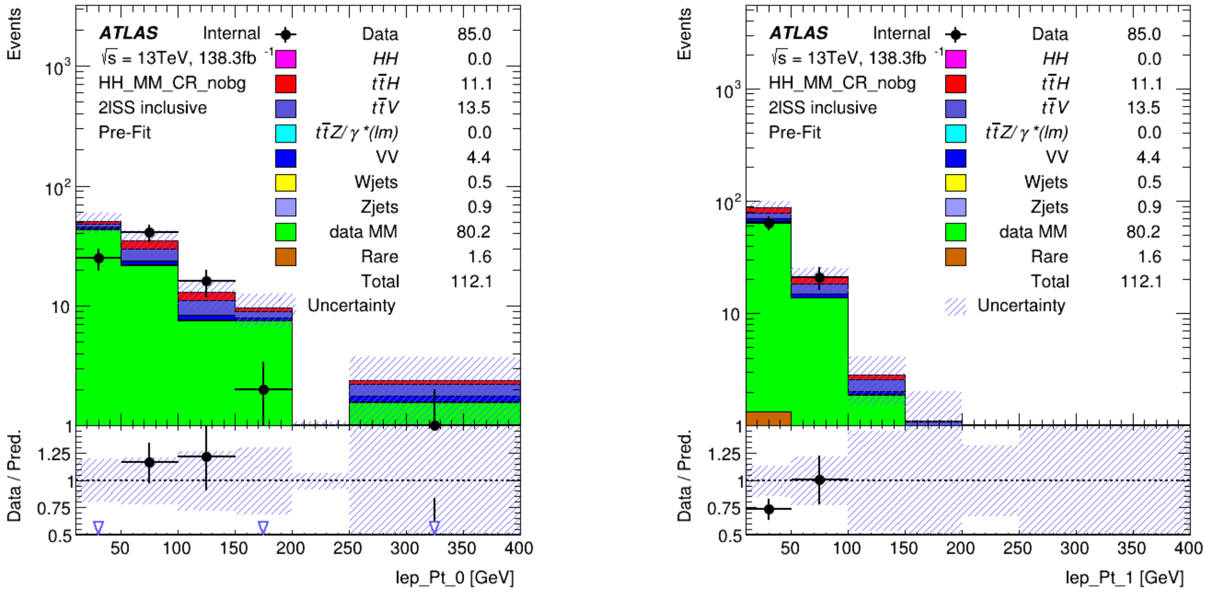

(a) Leading lepton. (b) Sub-leading lepton.

Figure 100: Distributions of events for Monte-Carlo simulation and Matrix Method (efficiencies from data) in control region for electron-muon selection. "data MM" replaces the MC $t\bar{t}$.

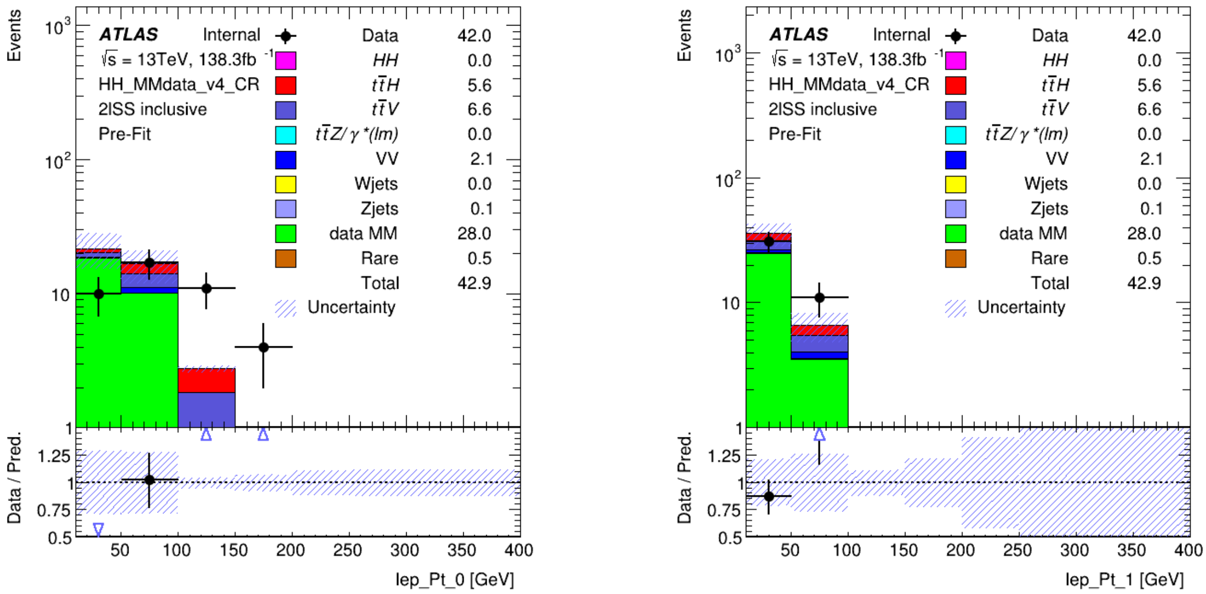

(a) Leading lepton. (b) Sub-leading lepton.

Figure 101: Distributions of events for Monte-Carlo simulation and Matrix Method (efficiencies from data) in control region for di-muon selection. "data MM" replaces the MC $t\bar{t}$.

Fake rate determination in SR

Without efficiency background subtraction Figure 102 shows the distribution of the Matrix Method $t\bar{t}$ events. Comparing the data-driven MM result Figure 102a with the MC-only distribution Figure 92a, the number of $t\bar{t}$ events increases from 48.7 events (MC-only) to 108.9 events (data-driven MM). The application of the Matrix Method results in the SR are shown in Figure 102. The separations for ee, $e\mu$ and $\mu\mu$ are shown in Figures 103 to 105.

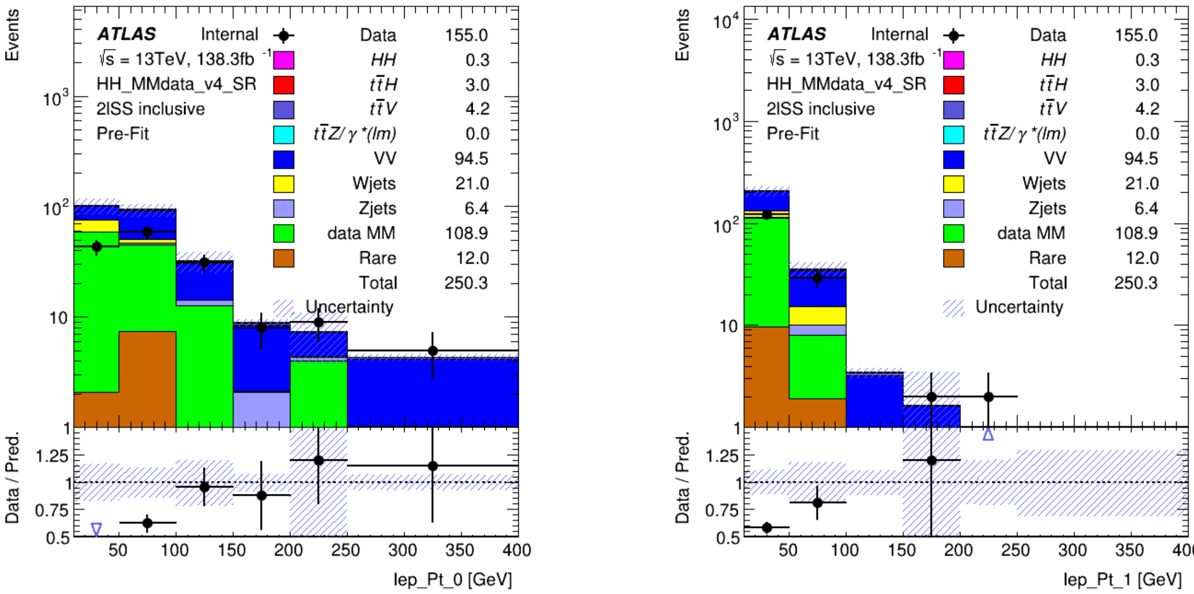

(a) Leading lepton.

(b) Sub-leading lepton.

Figure 102: Distributions of events for Monte-Carlo simulation and Matrix Method (efficiencies from data) in control region for combined flavour selection. "data MM" replaces the MC $t\bar{t}$.

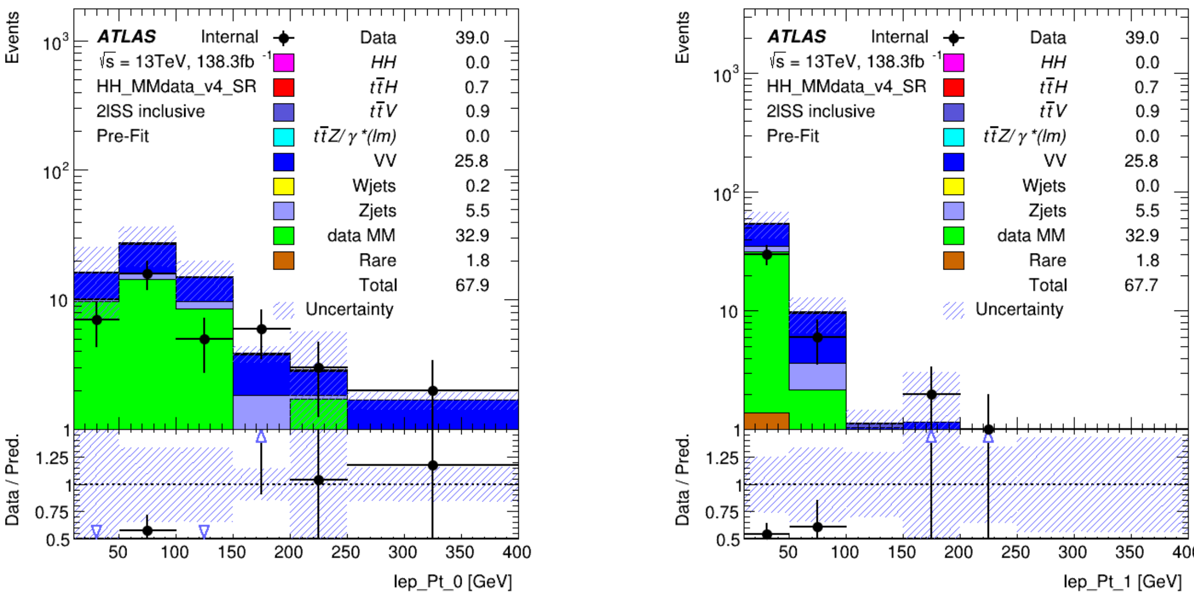

(a) Leading lepton.

(b) Sub-leading lepton.

Figure 103: Distributions of events for Monte-Carlo simulation and Matrix Method (efficiencies from data) in control region for di-electron selection. "data MM" replaces the MC $t\bar{t}$.

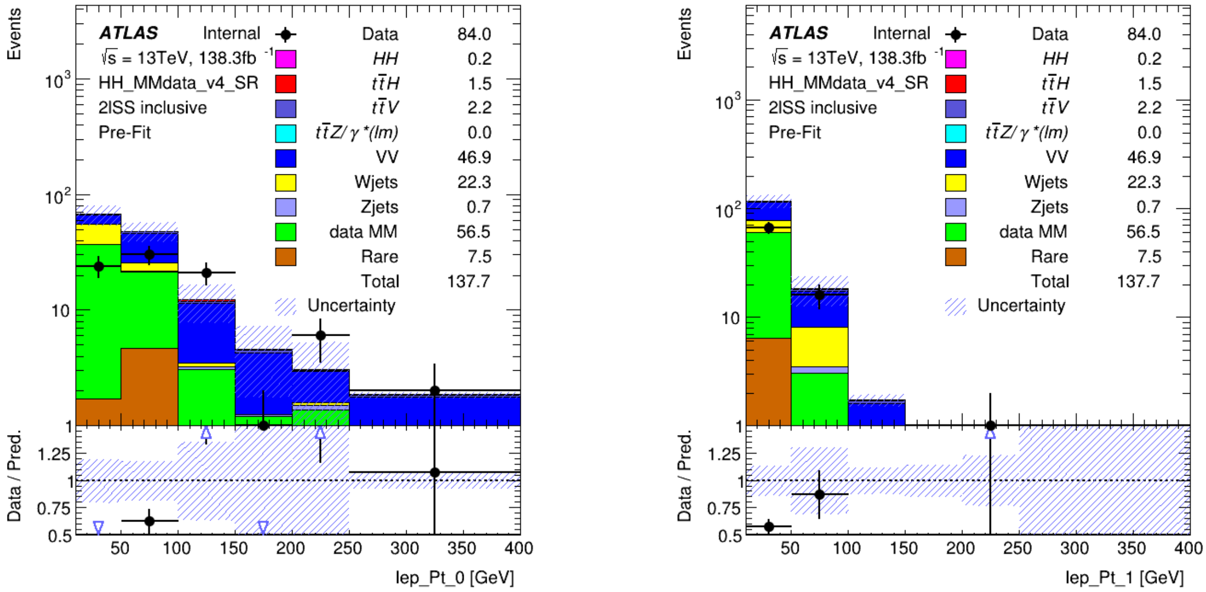

(a) Leading lepton.

(b) Sub-leading lepton.

Figure 104: Distributions of events for Monte-Carlo simulation and Matrix Method (efficiencies from data) in control region for electron-muon selection. "data MM" replaces the MC $t\bar{t}$.

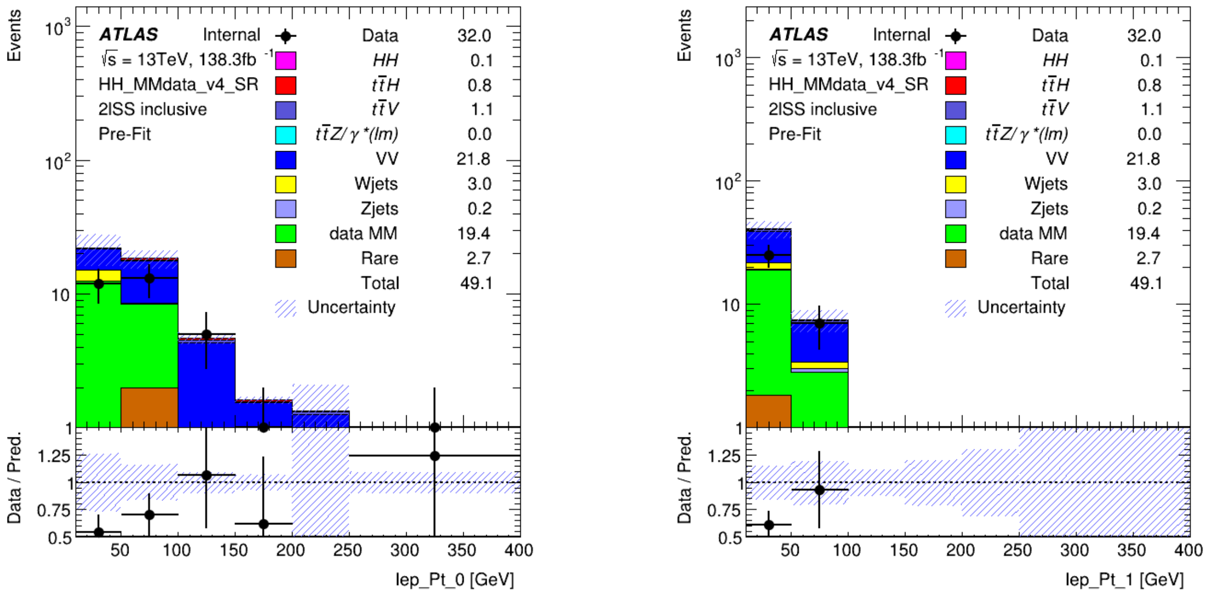

(a) Leading lepton.

(b) Sub-leading lepton.

Figure 105: Distributions of events for Monte-Carlo simulation and Matrix Method (efficiencies from data) in control region for di-muon selection. "data MM" replaces the MC $t\bar{t}$.

With efficiency background subtraction Figure 106 shows the distribution of the Matrix Method $t\bar{t}$ events. Comparing the data-driven MM result Figure 106a with the MC-only distribution Figure 92a, the number of $t\bar{t}$ events increases from 48.7 events (MC-only) to 104.2 events (data-driven MM). The application of the Matrix Method results in the SR are shown in Figure 106. The separations for ee, $e\mu$ and $\mu\mu$ are shown in Figures 107 to 109.

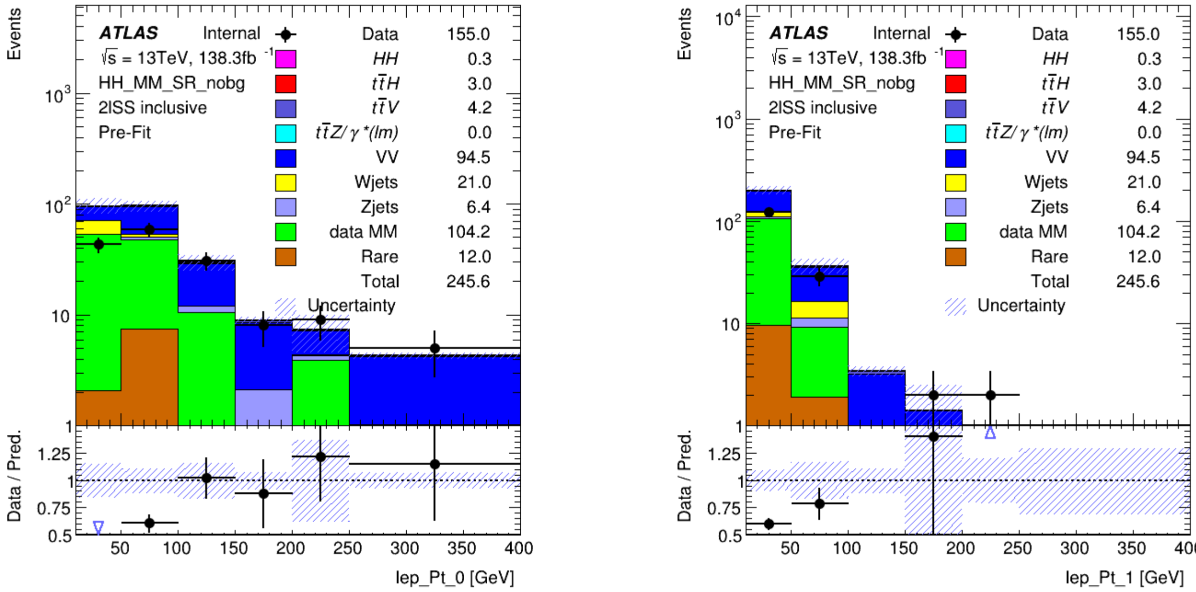

(a) Leading lepton.

(b) Sub-leading lepton.

Figure 106: Distributions of events for Monte-Carlo simulation and Matrix Method (efficiencies from data) in control region for combined flavour selection. "data MM" replaces the MC $t\bar{t}$.

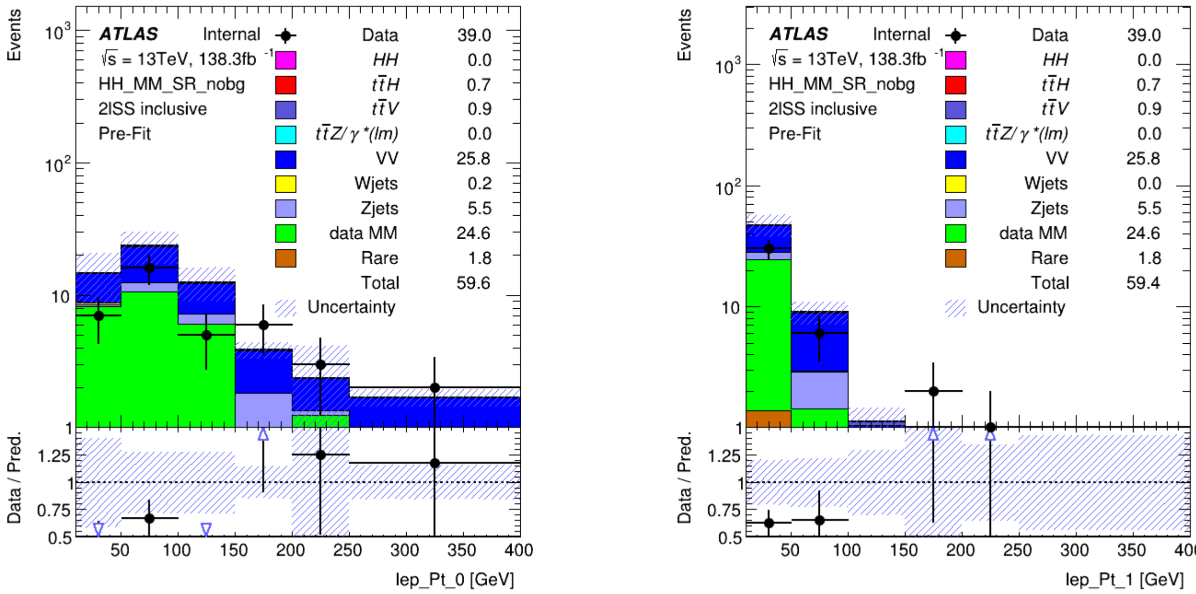

(a) Leading lepton.

(b) Sub-leading lepton.

Figure 107: Distributions of events for Monte-Carlo simulation and Matrix Method (efficiencies from data) in control region for di-electron selection. "data MM" replaces the MC $t\bar{t}$.

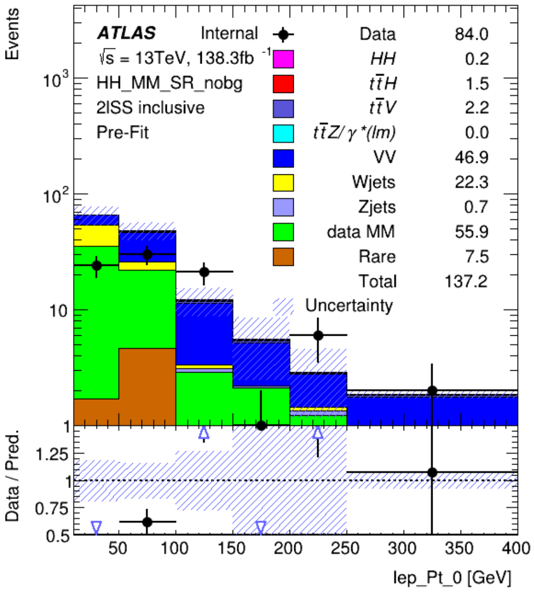

(a) Leading lepton.

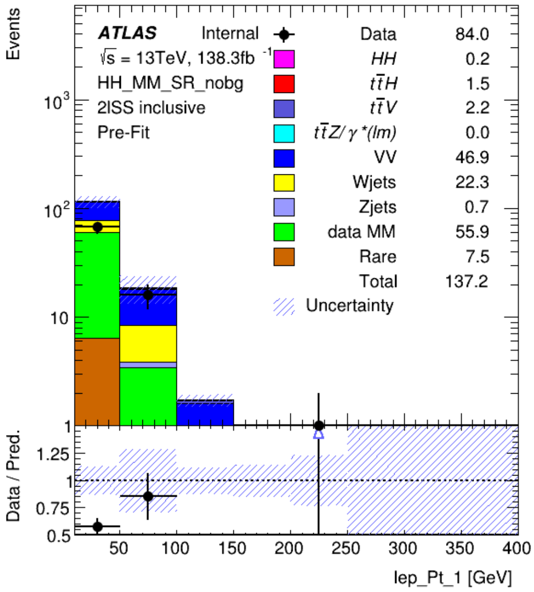

(b) Sub-leading lepton.

Figure 108: Distributions of events for Monte-Carlo simulation and Matrix Method (efficiencies from data) in control region for electron-muon selection. "data MM" replaces the MC $t\bar{t}$.

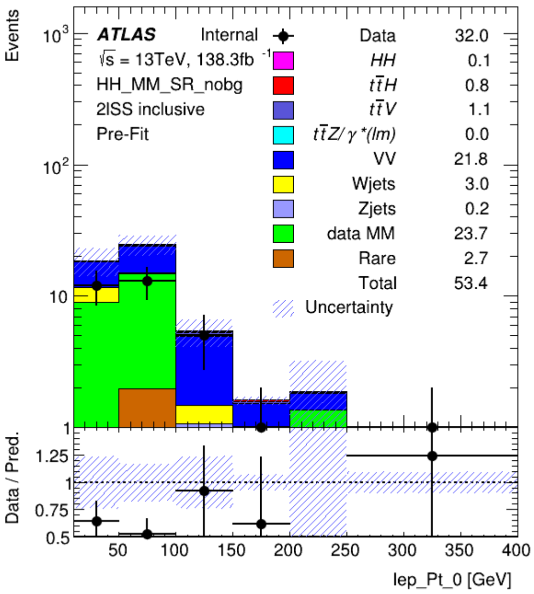

(a) Leading lepton.

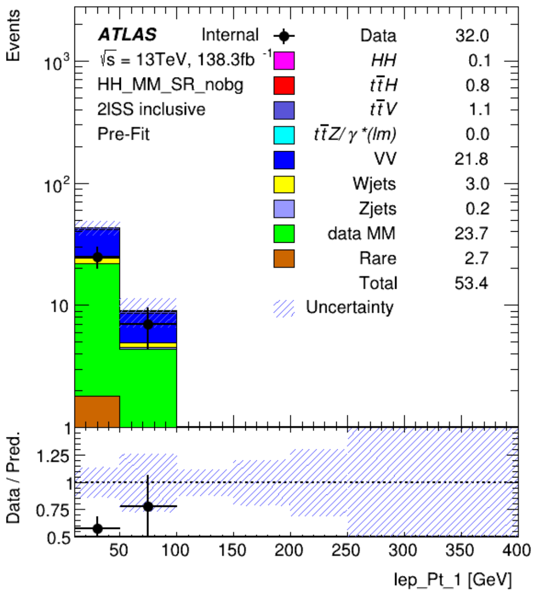

(b) Sub-leading lepton.

Figure 109: Distributions of events for Monte-Carlo simulation and Matrix Method (efficiencies from data) in control region for di-muon selection. "data MM" replaces the MC $t\bar{t}$.

Results The main results of this study are:

- The IFF tools recommended by the ATLAS physics analysis coordination are used to determine the fake rate from $t\bar{t}$ production in the 2lSS1tau channel.
- The type and origin of true fakes are determined from simulated events and the $t\bar{t}$ rates are dominant for the 2lSS1tau analysis.
- Good similarity of type and origin are observed in the SR and CR.
- The real electron and muon efficiencies are determined with a tag-and-probe method using the IFF tools for mcA (2015, 2016), mcD (2017) and mcE (2018) detector simulations.
- The fake electron and muon efficiencies are determined with a tag-and-probe method using the IFF tools, where the efficiency is defined as ratio between Loose and Tight objects.
- Using the real and fake efficiencies, the Matrix Method is applied. As input standard group analysis ntuples are used and these ntuples have been extended by a variable of MM weights for each event.
- These extended ntuples then serve as input for the TRexFitter tool to illustrate the event distributions in a standard format.
- Closure tests were performed for di-electron, di-muon, and electron-muon selections of events with same electric charge. The closure tests completed with an agreement within 1 standard deviation for the di-electon selection, within 3-4 standard deviations for the di-muon selection, and within 1-2 standard deviations for the electron-muon selection, both for the SR and CR.
- For the combined closure test of three di-lepton channels, the agreement between MC and MM predictions is within standard deviation, and the uncertainty is 8%.
- The real and fake efficiencies were also determined for the recorded CR data. Owing to the low statistics in each year of data-taking for the fake efficiency determination, the data of each year were combined, and thus no differences in the efficiencies for individual years were assumed. For the real efficiency determination, high statistics were available and the data recorded in 2016 were used.
- The Matrix Method was applied in the CR as validation, using the efficiencies determined in the CR.
- The Matrix Method was applied in the SR, using the efficiencies determined in the CR. Thus, the MC $t\bar{t}$ background expectation is replaced by the data-driven estimate from the Matrix Method.
- Some excess of MM events plus simulated background events compared to the data are noted in the validation.
- The comparison between data and prediction was improved by applying a background subtraction of ttH, ttW and ttZ events for the data-driven efficiency determinations.
- Using the real and fake efficiencies determined from the CR, the MM is applied in the SR and the simulated $t\bar{t}$ events are replaced by the MM expectation.
- Technical details on the implementation are given in the note [76].

Summary of Matrix Method in the 2lSS1tau Channel The specific analysis channel contains two same-sign electrically charged light leptons and one hadronically decaying tau. Two selections of events were used, one Signal Region with the requirement of no b-tagged jet, and one Control Region with the requirement of at least one b-tagged jet. For both signal and control regions, the type and origin of expected real and fake light leptons was studied and found to be similar. A Matrix Method was used to determine the number of expected events with fake leptons for different cases. The analysis was performed for a di-electron, di-muon, electron-muon and a combined di-lepton selection. In order to test the Matrix Method fake rate determination, closure tests were performed for the leading $t\bar{t}$ background. The method proved to meet the expectations, and an uncertainty of 8% was determined by taking the maximum between the deviation of the Matrix Method result and the simulation expectation, and the statistical uncertainty on the comparison. A test in the CR was performed using the real and fake efficiencies determined from the control region data. Using the same efficiencies, the Matrix Method was applied on recorded signal region data for a data-driven determination of the $t\bar{t}$ background expectation. Background subtraction in the data-driven efficiency determination improved the agreement in the control region, and the agreement between data and simulation in the signal region. As a follow-up, a validation region orthogonal to the control region used for the efficiency determination will be defined.

A.1.7 QmisID background estimation

Electron charge flip background study The following paragraphs present the measurement of the background, introduced to final states with two same-sign light leptons ($e^\pm e^\pm$, $e^\pm\mu^\pm$) due to electron charge misidentification (QMisID).[5] There are two main mechanisms contributing to QMisID:

- Hard Bremsstrahlung ($e^\pm \to e^\pm\gamma^* \to e^\pm e^+ e^-$). In this case, QMisID occurs when the EM cluster is coupled to the track of the opposite-sign electron in the trident. Since the probability of this process depends on the traversed detector material, dependence of the QMisID rate on $|\eta|$ is expected.
- Mismeasurement of the electron track-curvature. This effect is more important in the high p_T range (smaller curvature), therefore dependence of the rate on p_T is also expected.

The misidentification of the muon charge-sign is not considered in this study. It may occur by mismeasurement of the track curvature, however, due to the long lever arm in the muon system and the fact that the charge is measured both in the inner detector and the muon spectrometer, the QMisID rate is marginal.

The estimation of the QMisID background is based on the electron QMisID rates $\vec{\epsilon}$. The latter are derived from the data, in three-dimensional (3D) bins according to $|\eta|$, p_T and the region to which the electron belongs with respect to photon conversions, i.e. it designated as internal- or external-conversion candidate or as prompt lepton (as defined in the same-sign signal region).

Background estimation strategy Final states with an opposite-sign lepton pair (mainly $Z \to e^+e^-$ followed by $t\bar{t} \to b\bar{b}W^+W^- \to b\bar{b}e^+e^-\nu\bar{\nu}$) contaminate the signal region, defined by two same-sign leptons, when the charge of exactly one lepton is misidentified. In the case of e^-e^+, the fraction of events that are reconstructed as same-sign (e^-e^- or e^+e^+) is:

$$\epsilon_i(1-\epsilon_j) + \epsilon_j(1-\epsilon_i) = \epsilon_i + \epsilon_j - 2\epsilon_i\epsilon_j, \quad (28)$$

[5] Unless specified otherwise, positrons and electrons are both called electrons.

where ϵ_i and ϵ_j are the QMisID rates for each of the two electrons. For $e^{\pm}\mu^{\mp}$ events, on the other hand, the respective fraction is equal to the QMisID rate ϵ_i of the electron. By knowing the QMisID rates it is thereby possible to compute the expected number of misidentified same-sign events $\bar{N}_{\mathrm{SS}}$ from the observed number of opposite-sign events N_{OS}, using the expressions:

$$\bar{N}_{\mathrm{SS}} = \frac{\epsilon_i + \epsilon_j - 2\epsilon_i\epsilon_j}{1 - (\epsilon_i + \epsilon_j - 2\epsilon_i\epsilon_j)} N_{\mathrm{OS}} \quad \text{and} \quad \bar{N}_{\mathrm{SS}} = \frac{\epsilon_i}{1 - \epsilon_i} N_{\mathrm{OS}} \tag{29}$$

for the ee and $e\mu$ channel, respectively.

Estimation of the charge mis-identification rates with the likelihood method The QMisID rates are derived from the data, based on the fraction of $Z \to ee$ decays that are reconstructed as a same-sign electron pair. For this measurement, events in the m_{ee} region around the reconstructed Z-boson peak m_Z are used. For N^{ij} electron pairs falling in the bin combination i, j (where each of i, j uniquely represents a 3D bin as defined above) the expected number of same-sign events is:

$$\bar{N}^{ij}_{\mathrm{SS}}(\epsilon_i, \epsilon_j) = N^{ij} \cdot (\epsilon_i + \epsilon_j - 2\epsilon_i\epsilon_j). \tag{30}$$

Asumming that all of the observed same-sign events, N^{ij}_{SS}, in the m_Z window are products of electron charge mis-identification, they follow a Poisson distribution around the expectation value:

$$f(N^{ij}_{\mathrm{SS}} | \bar{N}_{\mathrm{SS}}(\epsilon_i, \epsilon_j)) = \frac{[\bar{N}^{ij}_{\mathrm{SS}}]^{N^{ij}_{\mathrm{SS}}} e^{-\bar{N}^{ij}_{\mathrm{SS}}}}{N^{ij}_{\mathrm{SS}}!}. \tag{31}$$

which is integrated into a likelihood:

$$L(\vec{\epsilon} | N_{\mathrm{SS}}) = \prod_{i,j} f(N^{ij}_{\mathrm{SS}} | \bar{N}_{\mathrm{SS}}(\epsilon_i, \epsilon_j)). \tag{32}$$

that can be maximized (minimization of $-2 \ln L$) to obtain the rates that best describe the data.

As mentioned above, this method relies on the assumption that ee events in the m_Z window are products of Z-boson decays. Therefore, any contribution from other processes (e.g. fake electrons) to N^{ij}_{SS} must be subtracted. As long as these processes do not exhibit a resonant-like behaviour of the m_{ee} distribution, this background can be estimated from the sidebands of the m_Z window, for each bin combination i, j, separately for same-sign ($N^{ij}_{\mathrm{SS,BG}}$) and opposite-sign ($N^{ij}_{\mathrm{OS,BG}}$) events. For this, upper and lower sidebands are defined with width equal to the m_Z window so that the introduced background can be obtained from the average yield. The background estimate is then used to correct the expectation (equation 30) to:

$$\bar{N}^{ij}_{\mathrm{SS}} = N^{ij}_{\mathrm{SS,BG}} + (N^{ij} - N^{ij}_{\mathrm{SS,BG}} - N^{ij}_{\mathrm{OS,BG}}) \cdot (\epsilon_i + \epsilon_j - 2\epsilon_i\epsilon_j). \tag{33}$$

The minimisation of $-2 \ln L$ is finally performed by MIGRAD, while HESSE is called to evaluate the uncertainty on the rate estimates.

Data and Monte Carlo samples The QMisID rate and background estimation is performed using the full dataset, with an integrated luminosity of 139 fb^{-1}. For the validation of the method and many of the tests that follow, simulated $Z \to ee$ (Sherpa), $t\bar{t}$ (Powheg-BOX) and $t\bar{t}\gamma$ (MG5_aMC) samples are also used.

No additional criteria are applied to electrons for the QMisID rate estimation. In order to increase the size of the tight electron sample, anti-tight electrons are also exploited. The latter are defined as those electrons that fail the tight identification criteria but yet pass the overlap removal. Although such electrons are not used in the analysis, by using a looser set of electrons and classifying them as tight and anti-tight (on top of the 3D classification described above), introduces events with one tight and one anti-tight electron in the rate estimation, and therefore improves the statistical precision of the tight-electron rates with the likelihood method.

M_{ee} sidebands for $Z \to ee$ background estimation The likelihood method uses $Z \to ee$ decays with both same-sign and opposite-sign electrons in the final state. As shown in figure 110, the m_{ee} distribution of same-sign electrons is shifted towards lower values with respect to that of opposite-sign electrons, due to the loss of electron momentum in tridents. To account for this shift, a different m_Z window is defined for each case. The m_Z window is determined by gaussian fit around the peak (using all loose electrons) and defined as $\pm 4\sigma$ around the mean (4σ has been found to provide the best results in terms of closure). The side-bands are defined with equal width to the m_Z window, i.e. 8σ each. The region definitions are summarised in table 51. The variation of the rates with the definition of the m_Z window ($\pm 1\sigma$) is considered as a systematic uncertainty.

Sample	lower SB	m_Z window	upper SB
Same-sign	[51.7,76.5]	[76.5,101.3]	[101.3,126.0]
Opposite-sign	[54.7,78.5]	[78.5,102.3]	[102.3,126.0]

Table 51: Definition of the m_Z window and side-bands (SB) used in the likelihood method.

Data-driven rates estimates with p_{T} continuous rates The binning in $|\eta|$ and p_{T} must be optimized to best describe the dependence of the rates on each quantity while maintains statistical precision.

The binning scheme distinguishes four bins in $|\eta|$ (one of which just isolates the crack region) and four bins in p_{T}, for each region w.r.t. to photon conversions. To mitigate the statistical uncertainties introduced by the size of the available dataset in the case of tight-electrons, p_{T} bins are merged in the case of the internal conversion control region (merging is implemented by assigning the same rate in the likelihood). The data-driven QMisID rates, derived with the above binning configuration, are presented in figure 112.

Figure 111(a) shows the expected p_{T} distribution in the data, using reweighted opposite-sign events, compared to the observation. Significant non closures are observed at the edges of the p_{T} bins. These non-closures are covered by the non-closure systematic uncertainties in average only. The local non-closures exceed significantly the systematic uncertainties. They can of 200% in the 60-80 GeV range, and higher than 200% in the 150-200 GeV ranges.

In order to control this effect, p_{T} continuous modeling of the rates is used. The effective rate at a given p_{T} is obtained by the weighted sum of the rates from the adjacent p_{T} bins. The weighting is based on p_{T} only and accounts for the p_{T} distribution shape.

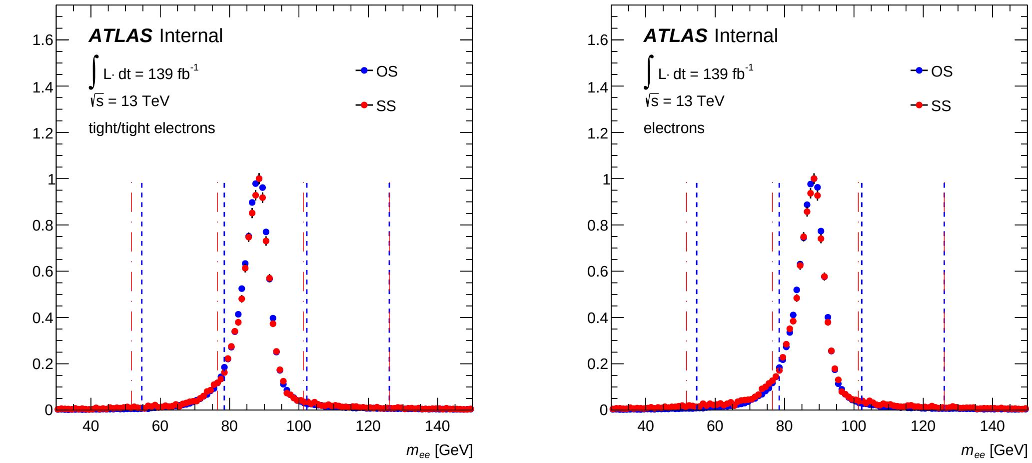

Figure 110: Comparison of the m_{ee} distribution between same-sign and opposite-sign data events for pairs of (a) tight and (b) loose electrons. The distributions are normalized by the maximum value. The peak for same-sign electrons is shifted with respect to opposite-sign electrons due to the loss of electron momentum in tridents.

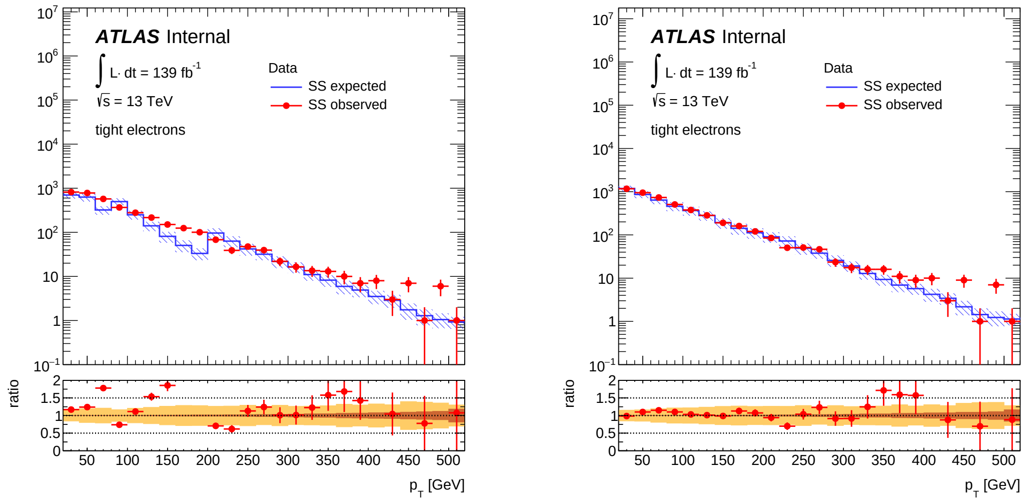

Figure 111: Comparison between the expected and observed p_{T} distribution of same-sign electrons. The dashed bands represent the total (statistical + systematic) uncertainty of the estimation. The comparison is shown for data events. The rates used to compute the predicted distribution are binned in p_{T} (left) or continuous in p_{T} (right).

Validation of the likelihood method (truth-closure) To validate the likelihood method the QMisID rates are derived from simulated Z+jets events and compared to the rates based on the MC truth information (truth-matching). The comparison is shown in figure 113 as a function of $|\eta|$ and parameterized in p_{T}. To mitigate the large statistical uncertainties introduced due to the size of the MC sample, the $|\eta|$-bins are merged. Furthermore, for the internal conversion region, p_{T} bins are also merged. The results show no significant disagreement between the two approaches. Any difference is considered as a systematic uncertainty to the rates (see section A.1.7). Finally, the same comparison is presented for the case of anti-tight electrons in order to verity the agreement of the two approaches with higher statistics.

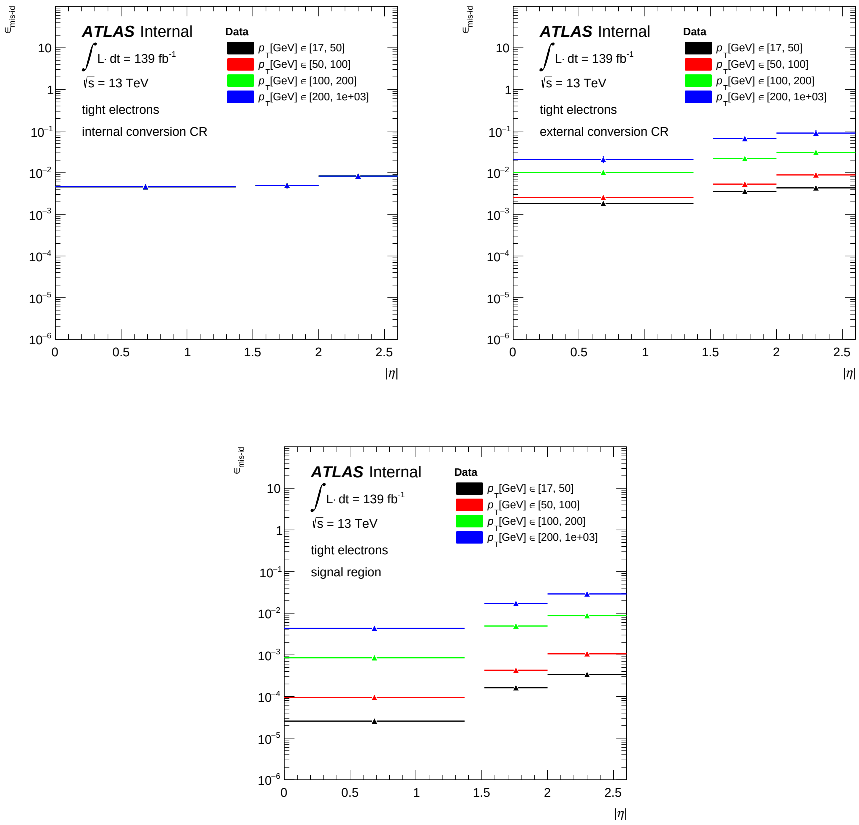

Figure 112: QMisID rates derived from the data with the likelihood method for tight electrons. The rates are presented as a function of $|\eta|$ and parameterised in p_{T} for the photon-conversion CRs and the signal region. Due to lack of statistics, the the bins in p_{T} are merged for the internal-conversion CR.

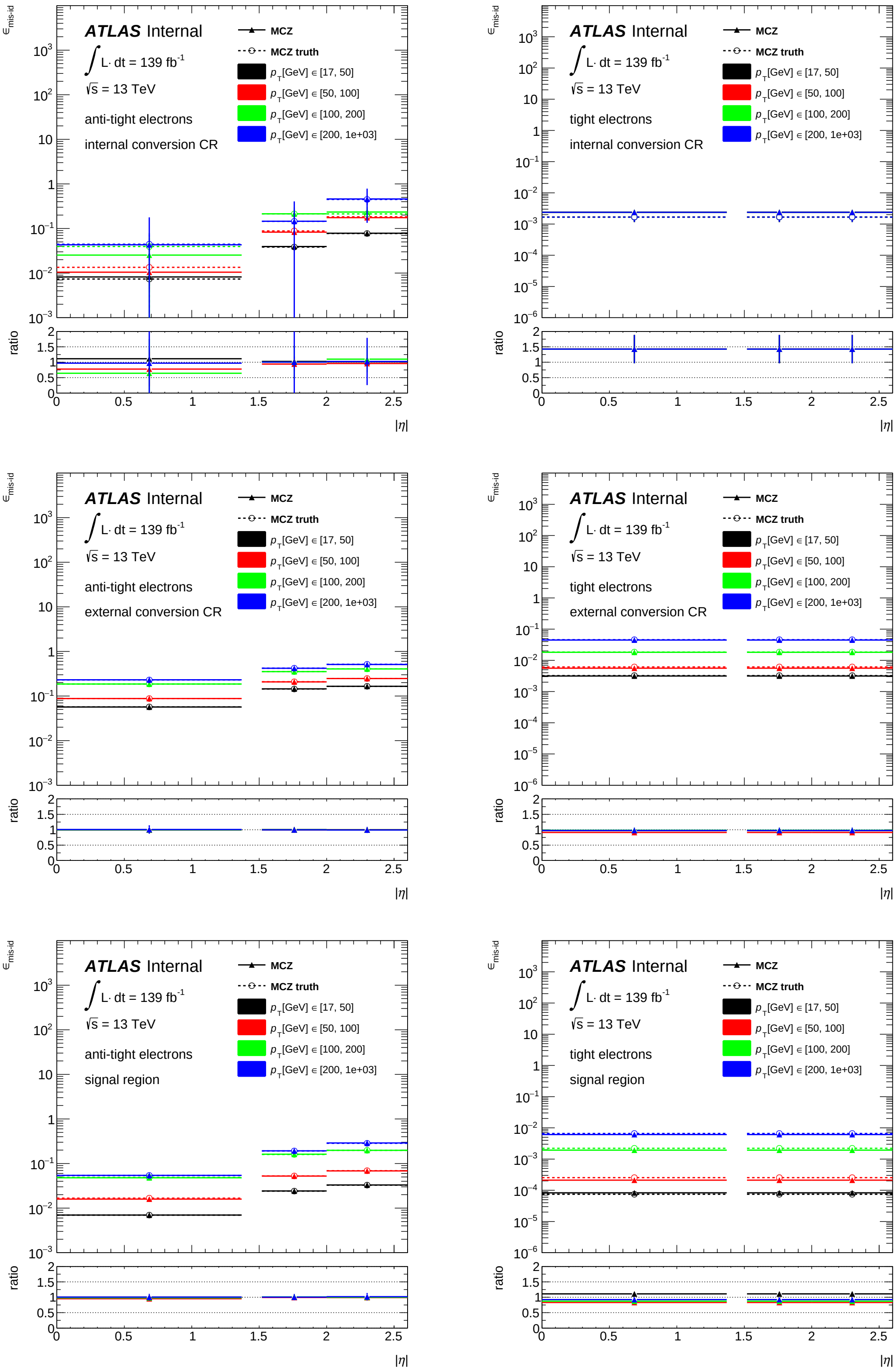

Figure 113: QMisID rates derived from $Z \to ee$ simulated events with the likelihood method, compared to truth-based rates for anti-tight (left) and tight (right) electrons. The rates are presented as a function of $|\eta|$, parameterized in p_{T} for the photon-conversion CRs and the signal region. Due to lack of statistics, in the case of tight electrons, the bins in $|\eta|$ are merged. For the internal-conversion CR, the bins in p_{T} are also merged.

Systematic uncertainties Four sources of systematic uncertainties are assigned to the QMisiD rates:

- the error estimates from the likelihood maximization (figure 114) which depend on the statistical size of the control region of the data in which the rates are estimated;
- the difference between the rates measured with the likelihood method and those obtained by truth-matching with simulated $Z \to ee$ events (figure 114);
- the variation of the rates with the m_Z window (figure 115);
- low m_{ee} mis-modelings observed on simulated $t\bar{t}$ samples and that can be relevant to some control regions.

The total uncertainty is defined as the quadratic sum of the above contributions (figure 115).

Closure test The rates are validated by comparing the estimated number of same-sign ee events (using the QMisID rates on opposite-sign events) to the measured number of same-sign events. In order to increase the statistical precision, this test is performed without any requirement regarding the number of jets. Figure 116, shows the expected distribution of m_{ee} in the data, compared to the observation (the latter also contains contributions from non-prompt electrons). After subtracting the non-prompt electron background using the sidebands, the measured number of same-sign events in the m_Z window is found to be 6474 (1076) for events with at least 1 jet (3 jets) while the expectation is 6951 ± 1024 (1156 ± 95). The p_{T} distribution (within the m_Z window) is also presented in figure 116, showing agreement between the measurement and the prediction, which however begins to deteriorate in the very high p_{T} region, due to the fact that the region above 200 GeV is described by an inclusive QmisID rate.

The respective comparison with Z+jets MC (in which the non-prompt contribution is removed using the truth information) is shown in figure 117.

A.2 Fake τ_{had} estimation

Most processes with irreducible background (real taus) are modelled using MC simulation. The reducible backgrounds with jets misidentified as tau candidates, referred to as fakes, are estimated using data-driven method. Backgrounds with non-prompt light leptons (ℓ = electron or muon) are small and estimated using MC. The events with one light lepton, two same-sign τ_{had} , and two or more jets, are also selected, providing a validation region (VR) for the background estimation.

The contribution of fake taus is estimated using the data-driven fake factor method [77] since such background is difficult to simulate in MC. The fake factor method uses an extrapolation from a dedicated fake dominated control region (CR) to estimate the number of fakes in the signal regions (SR). The CR selection requirements are analogous to those used to define SR, except that one or both of taus are required to fail the medium tau identification, but still pass a very loose tau requirement, referred to as anti-medium tau. The contribution of fakes in SRs can then be calculated by rescaling the templates of anti-medium taus in the CR with fake factors (FF). The templates are produced by substracting the real tau contributions from MC. The fake factor (FF) is a transfer factor estimated as a ratio of misidentified τ_{had} candidates that pass or fail the medium tau ID selection.

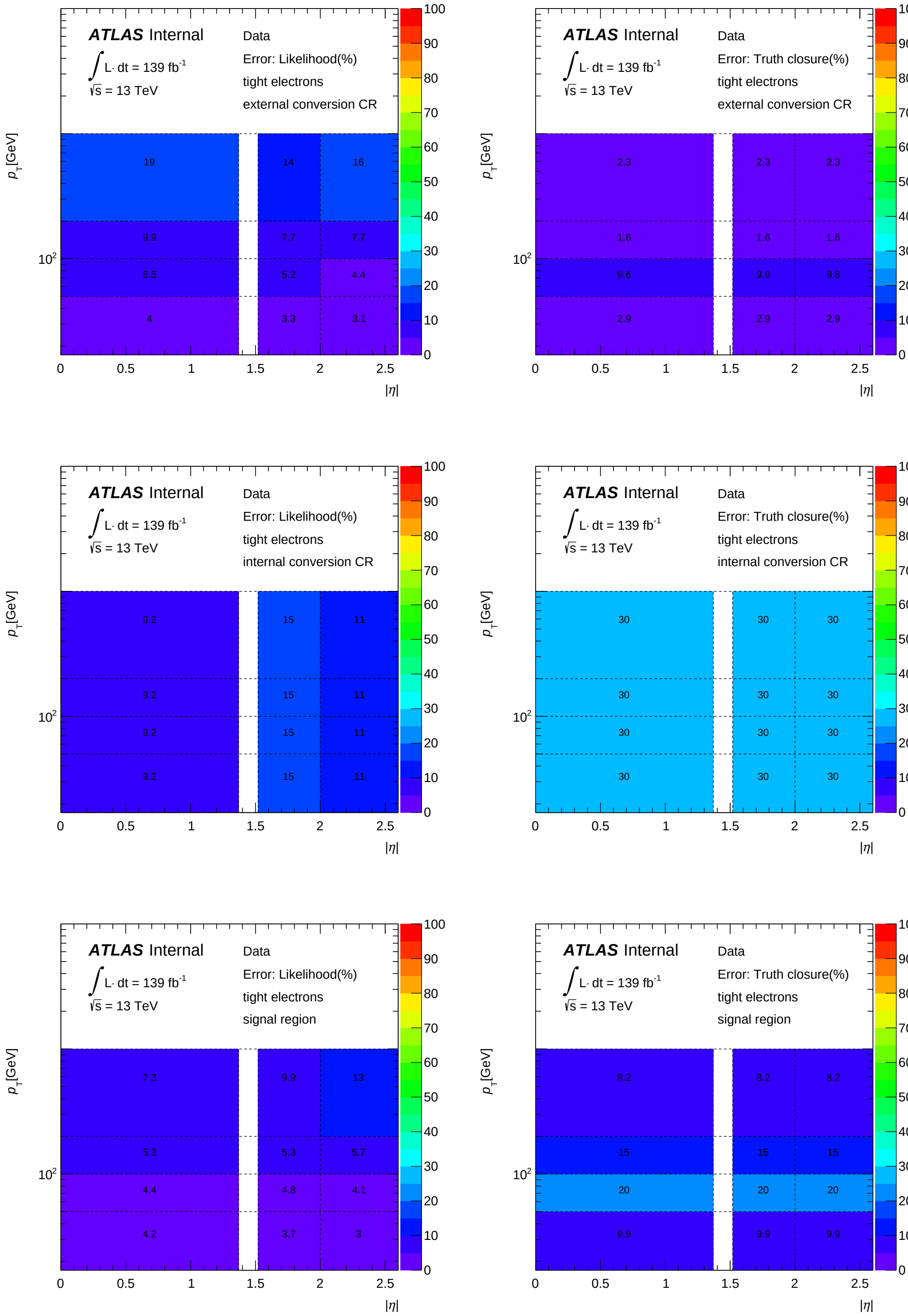

Figure 114: Left: systematic uncertainty (%), introduced from the statistical size of the control region of the data that is used in the likelihood method, in bins of $|\eta|$ and p_{T}. Right: systematic uncertainty (%), introduced from the comparison of rates obtained from simulated $Z \to ee$ events with the likelihood method to truth-based rates.

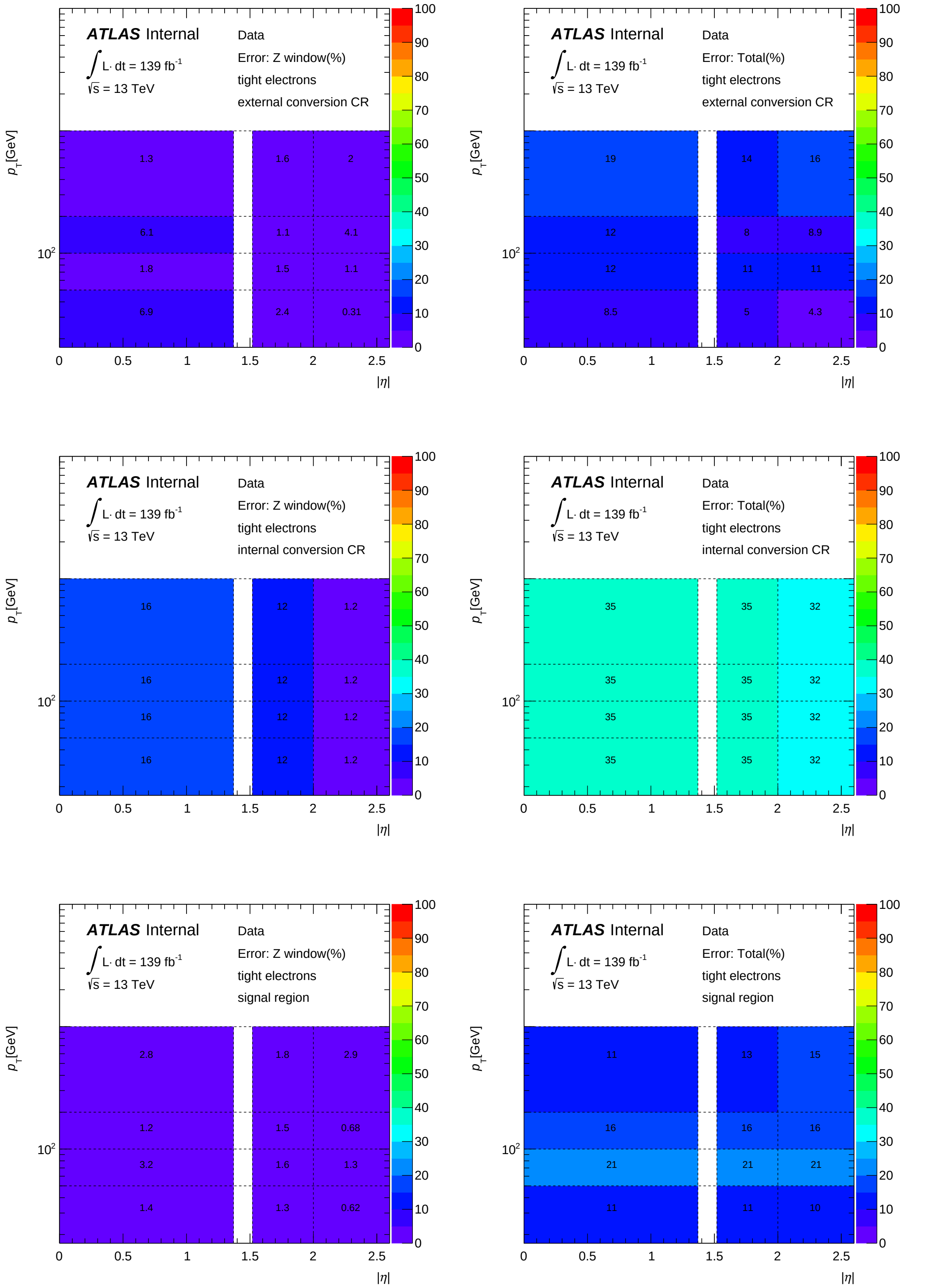

Figure 115: Left: systematic uncertainty (%), introduced from the variation of the m_Z window (and its sidebands) that is used to obtain the rates, in bins of $|\eta|$ and p_{T}. Right: Total systematic uncertainty (%).

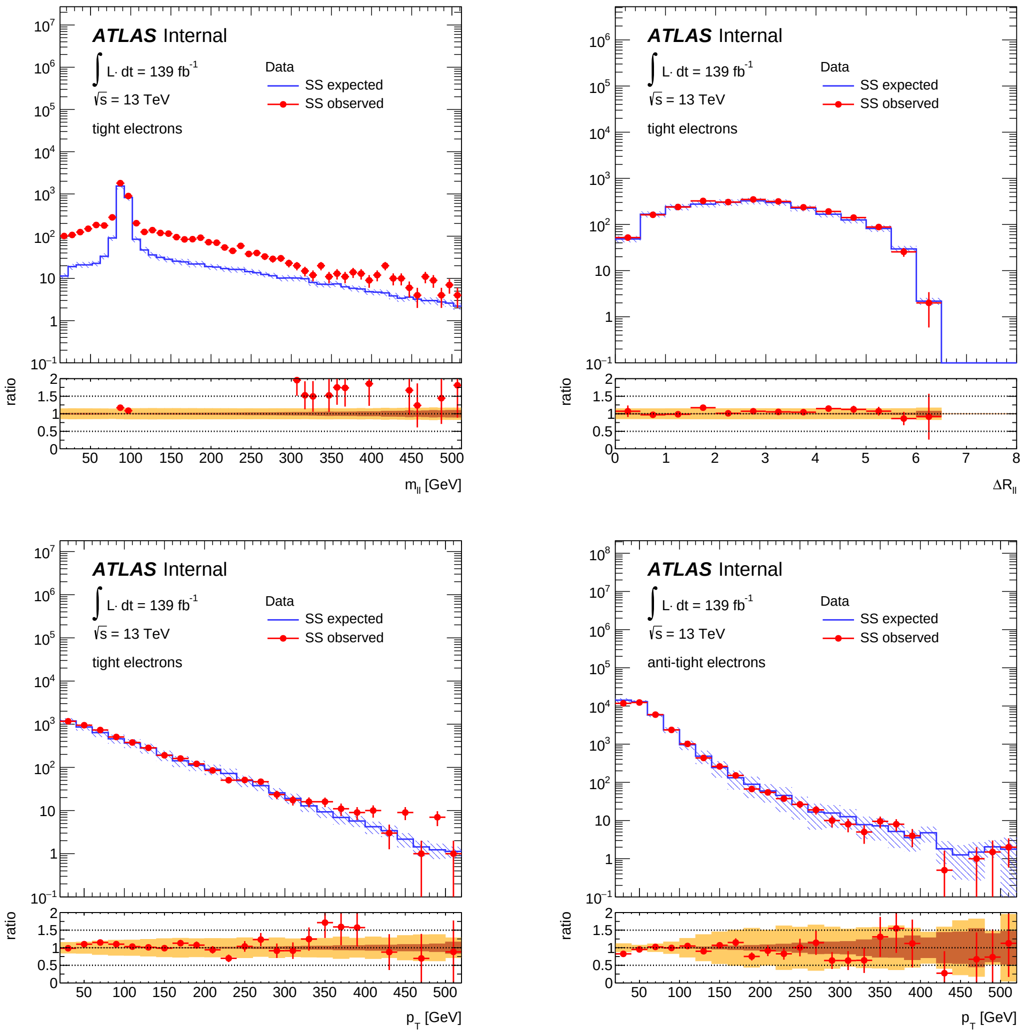

Figure 116: Comparison between the expected and observed m_{ee}, ΔR_{ee}, pT (tight) and p_{T} (anti-tight) of same-sign electrons. The dashed bands represent the total (statistical + systematic) uncertainty of the estimation. The comparison is shown for data events. The observed m_{ee} distribution includes the contribution of fake electrons, which are later subtracted by using the sidebands.

There are two τ_{had} candidates selected in SRs, either of which can be fake. The number of fakes can be calculated as:

$$N_{fakes} = N_{M0} \cdot N_{L1} \cdot FF_1 + N_{L0} \cdot FF_0 \cdot N_{M1} - \mathcal{K} \cdot N_{L0} \cdot FF_0 \cdot N_{L1} \cdot FF_1$$

where N_{Mi}, N_{Li}, FF_i are the number of medium taus, anti-medium taus, and FF for i=0,1 for leading and sub-leading τ_{had} candidates in data after subtracting the real tau MC contributions. The $\mathcal{K}$ is a correcting factor for the addition loose tau requirement imposed in the HIGG8D1 derivation for the ℓ + tau final states. By comparing the faction of events containing at least one loose taus out of two anti-medium taus in $Z(\ell\ell)$+jets and ℓ+jets events, the $\mathcal{K}$ is found to be 1.5 in order to compensate the reduction of double fakes in SR due to the addition cut in the derivation.

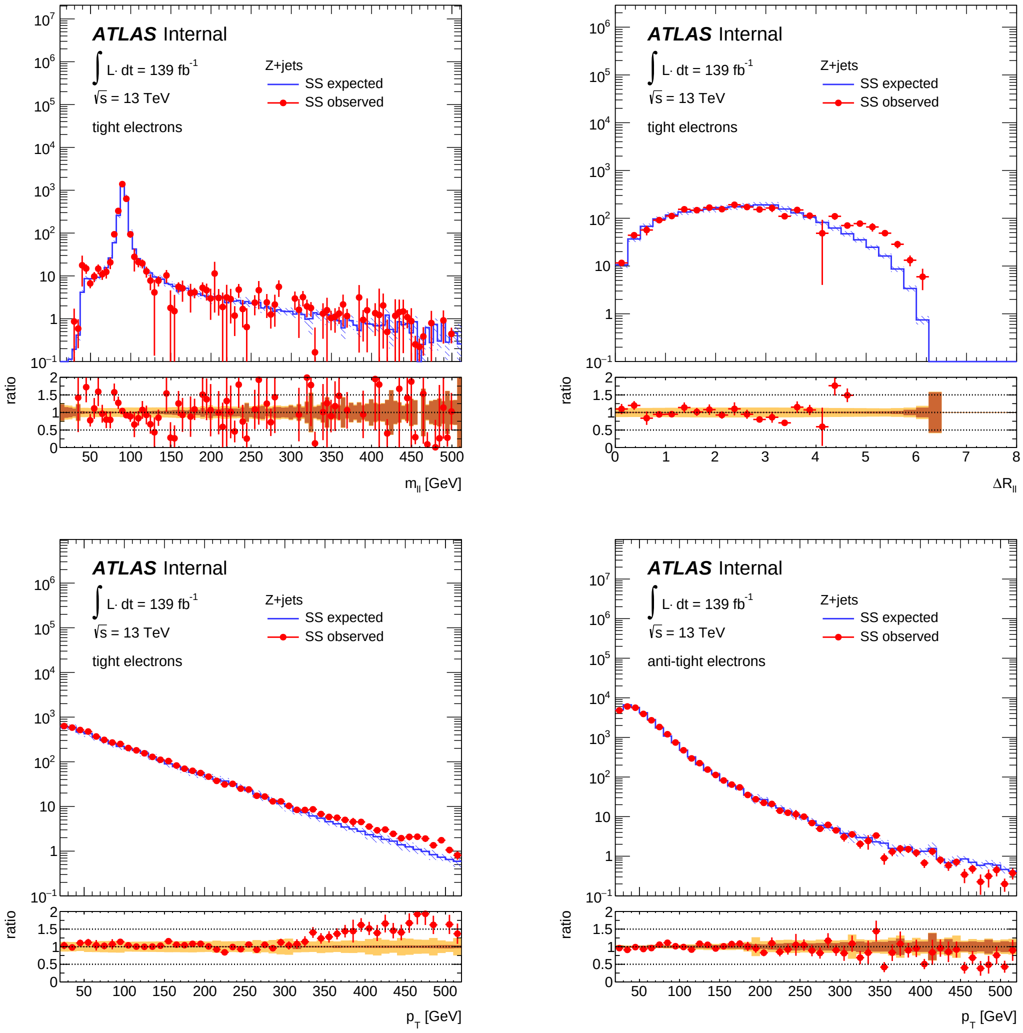

Figure 117: Comparison between the expected and observed m_{ee}, ΔR_{ee}, p_{T} (tight) and p_{T} (anti-tight) of same-sign electrons. The dashed bands represent the total (statistical + systematic) uncertainty of the estimation. The comparison is shown for Z+jets events. Fake electrons are removed from the sample by using the truth information.

A.3 Fake photon estimation

B Appendix of the Analysis of 2LOS Channel

Add appendix of the text for 2LOS channel

C Appendix of the analysis of two Same Signed Lepton

C.1 Event selection

C.1.1 Plots at preselection level

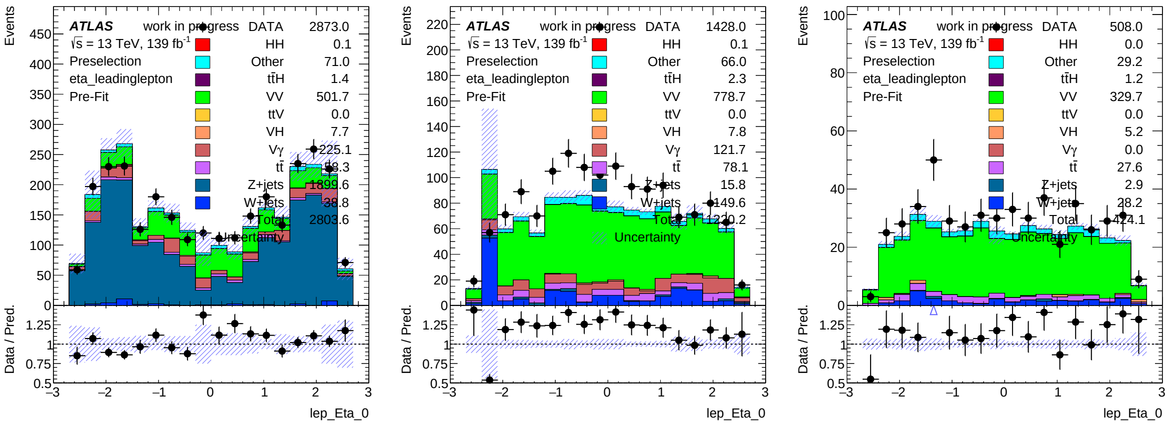

Figure 118: Leading lepton η in $e^{\pm}e^{\pm}$, $e^{\pm}\mu^{\pm}$, $\mu^{\pm}\mu^{\pm}$ channel.

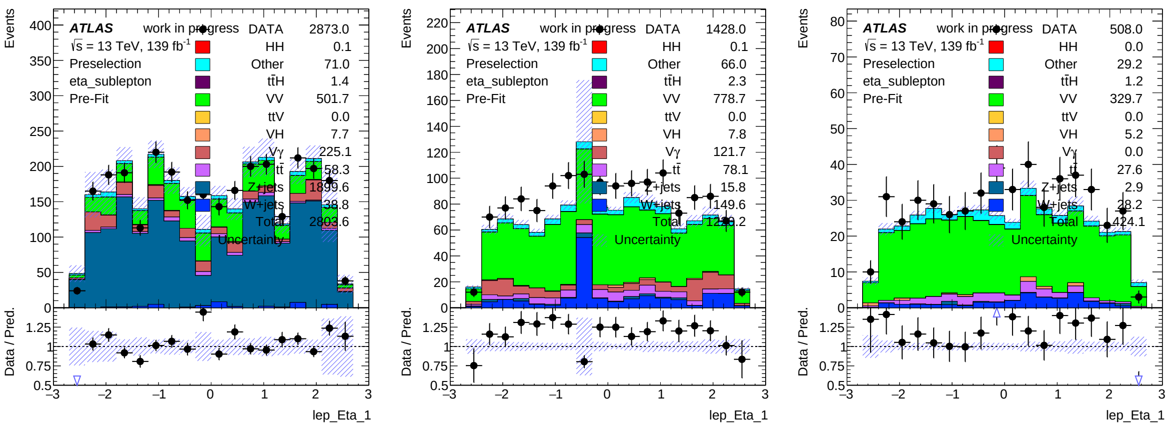

Figure 119: Sub-Leading lepton η in $e^{\pm}e^{\pm}$, $e^{\pm}\mu^{\pm}$, $\mu^{\pm}\mu^{\pm}$ channel.

C.1.2 Cutflow of preselection

C.1.3 Lepton truth origin after preselection

Two leptons origination obtained from MCTruth Classifier in the preselection region are presented in Figure.

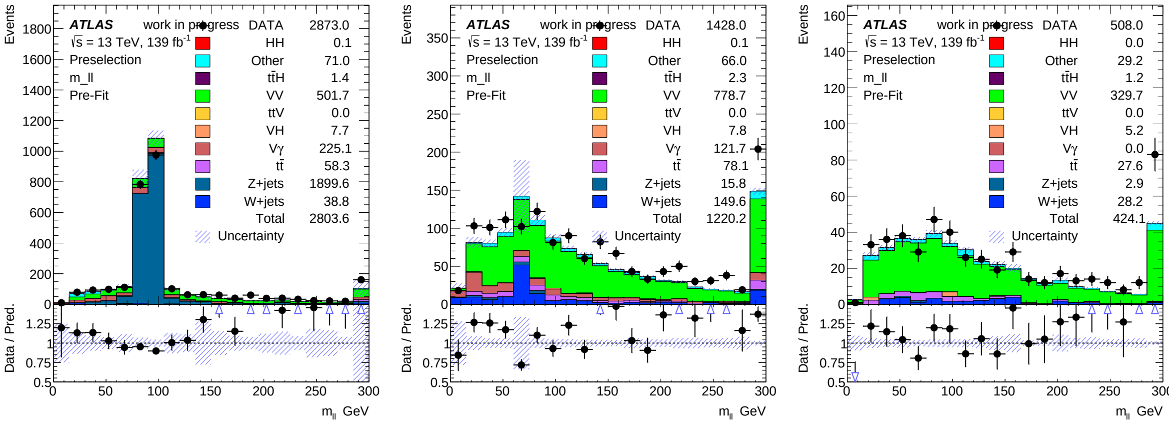

Figure 120: m_{ll} in $e^{\pm}e^{\pm}$, $e^{\pm}\mu^{\pm}$, $\mu^{\pm}\mu^{\pm}$ channel.

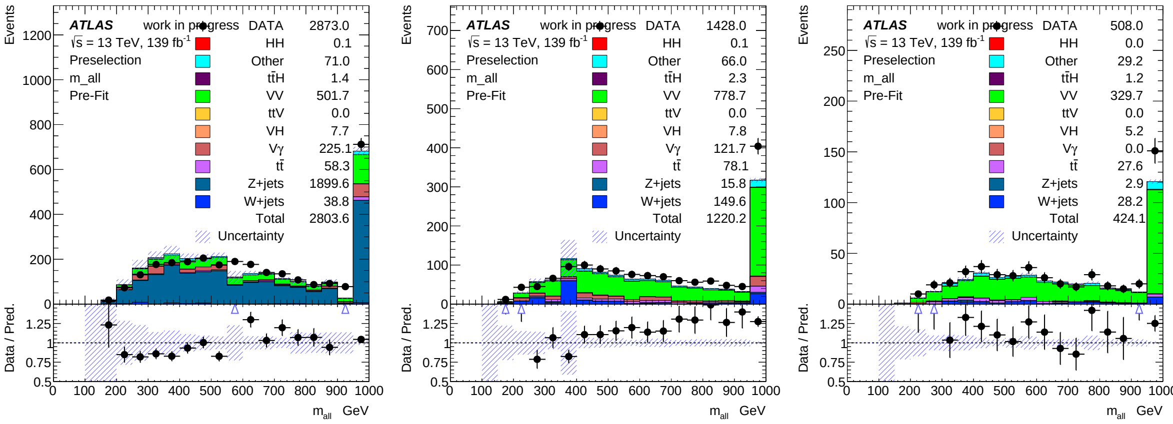

Figure 121: m_{all} in $e^{\pm}e^{\pm}$, $e^{\pm}\mu^{\pm}$, $\mu^{\pm}\mu^{\pm}$ channel.

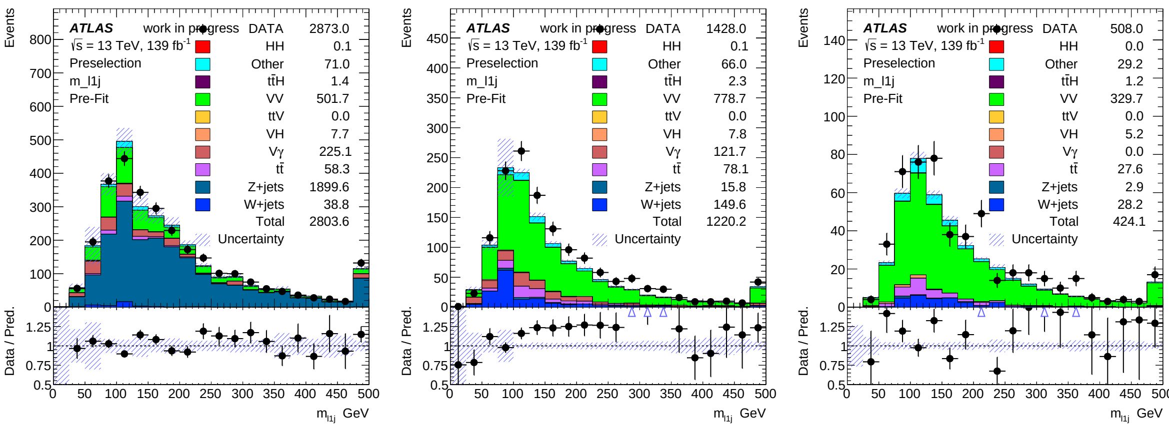

Figure 122: m_{l0j} in $e^{\pm}e^{\pm}$, $e^{\pm}\mu^{\pm}$, $\mu^{\pm}\mu^{\pm}$ channel.

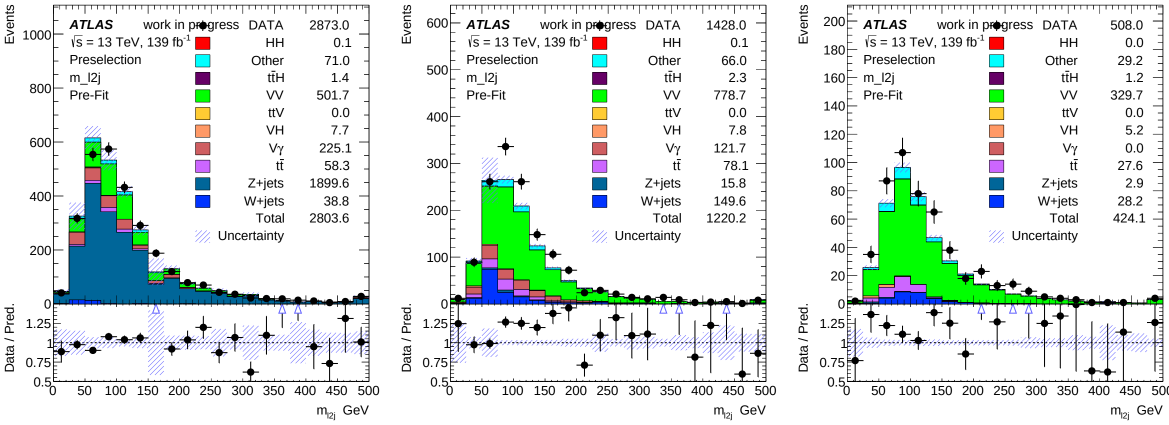

Figure 123: m_{l1j} in $e^{\pm}e^{\pm}$, $e^{\pm}\mu^{\pm}$, $\mu^{\pm}\mu^{\pm}$ channel.

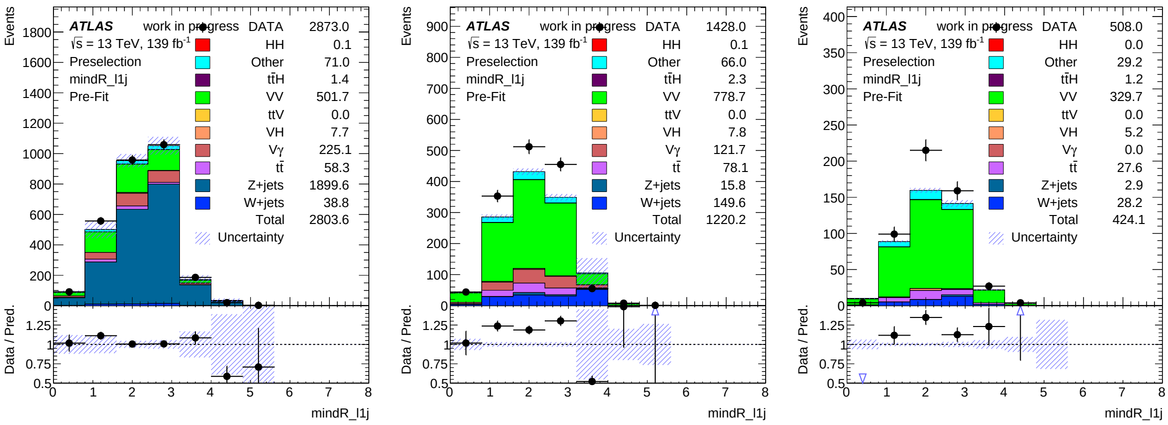

Figure 124: $mindR_{l0j}$ in $e^{\pm}e^{\pm}$, $e^{\pm}\mu^{\pm}$, $\mu^{\pm}\mu^{\pm}$ channel.

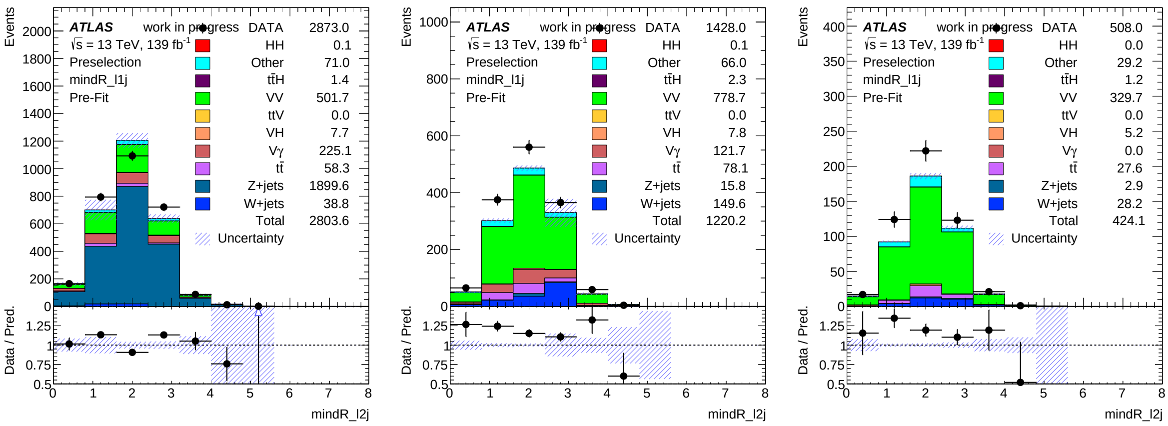

Figure 125: $mindR_{l1j}$ in $e^{\pm}e^{\pm}$, $e^{\pm}\mu^{\pm}$, $\mu^{\pm}\mu^{\pm}$ channel.

2223 ## C.2 Charge mis-identified background - IHEP

2224 For the 2ℓSS channel, prompt background events from Z+jets and $t\bar{t}$ with two opposite-charge same flavour
2225 leptons can pass tight selection due to charge flip. The misidentification of the muon charge-sign is not

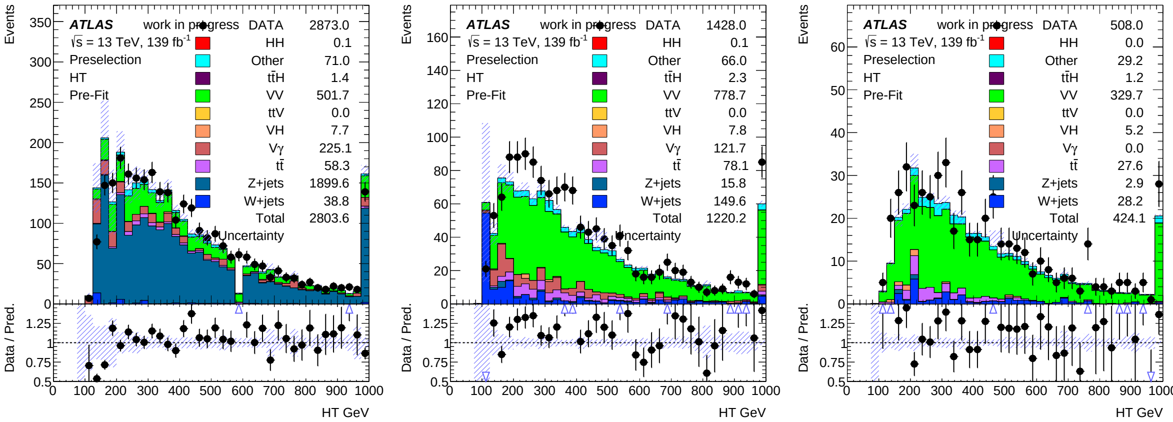

Figure 126: HT in $e^{\pm}e^{\pm}$, $e^{\pm}\mu^{\pm}$, $\mu^{\pm}\mu^{\pm}$ channel.

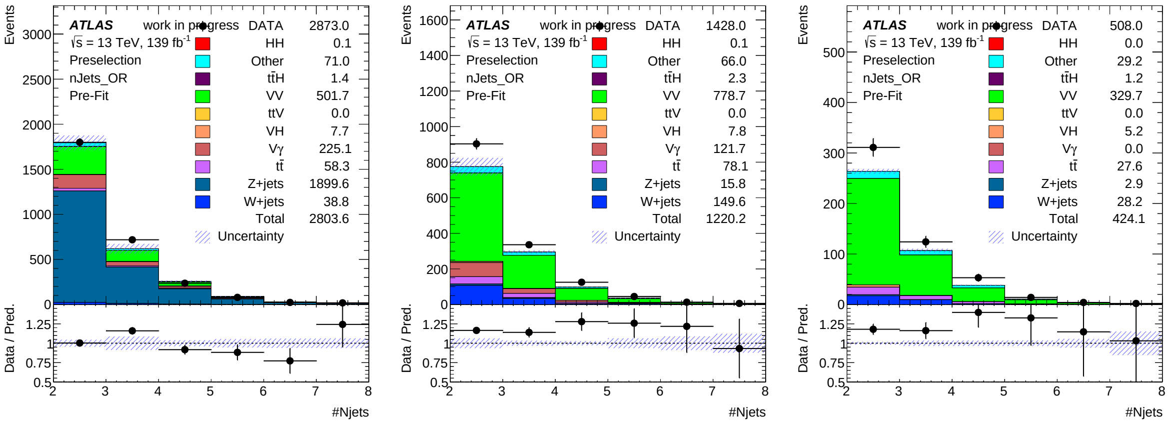

Figure 127: N_{jets} in $e^{\pm}e^{\pm}$, $e^{\pm}\mu^{\pm}$, $\mu^{\pm}\mu^{\pm}$ channel.

Analyzers	Shuiting	Océane	Shuiting	Océane	Shuting	Océane	Shuiting	Océane	Shuiting	Océane
Cuts	HH		VV		W+jets		Z+jets		$t\bar{t}$	
Loose Leptons	110784	/		/	1421471	/	2023483	/	2865073	/
Tight Leptons	51323	51323	2845293	2845293	33930	33930	90247	90247	50720	50720
B-veto	44544	44544	2699362	2699362	27889	27889	73501	73601	14980	14980
$p_T^{\ell 0}, p_T^{\ell 1} \geq 20$ GeV	35458	35458	1849770	1849770	2817	2817	59190	59190	4772	4772
MET > 10 GeV	35000	35000	1786628	1786628	2742	2742	53893	53893	4683	4683
M_{ll} > 15 GeV	34974	34974	1771602	1771602	2695	2695	53879	53879	4634	4634
Z-veto	34312	34312	1717587	1717587	2621	2621	10640	10640	4510	4510
$N_{jets} \geq 3$	19229	19229	452277	452277	634	634	3060	3060	1952	1952

Table 52: Cutflow of preselection for signal and VV , W+jets , Z+jets , $t\bar{t}$ background, raw event number are shown from two analyzers.

considered in this study, because the track curvature are measured with the help of muon spectrometer resulting in negligible muon QmisID rate, generally below 10^{-5}.

There are two sources contributing to electron QmisID. The most likely mechanism of electron QmisID is hard Bremsstrahlung process ($e^{\pm} \rightarrow e^{\pm}\gamma^{s}* \rightarrow e^{\pm}e^{+}e^{-}$). When an electron emits bremsssstrahlung, then the radiated photon converts into $e^{+}e^{-}$ pair because of interactions with detector material. The energy deposits in the calorimeters may be reconstructed by matching the track of the opposite-sign electron.

Analyzers	Shuiting	Océane	Shuiting	Océane	Shuting	Océane	Shuiting	Océane	Shuiting	Océane
Cuts	HH		VV		W+jets		Z+jets		$t\bar{t}$	
Loose Leptons	35.5743	/	46838.9023	/	/	/		/	418938.1083	/
Tight Leptons	4.02	4.02	15,579.10	15,612.80	19,372.60	19,372.56	18,427.30	18,428.43	6,668.99	6,669.00
B-veto	3.56	3.56	14,996.20	15,028.04	18,474.60	18,474.58	17,732.40	17,732.35	2,011.92	2,011.91
$p_T^{\ell 0}, p_T^{\ell 1} \geq 20$	2.74	2.74	9,816.13	9,823.63	1,181.81	1,181.81	14,943.50	14,943.48	649.56	649.56
MET > 10 GeV	2.69	2.69	9,501.24	9,508.65	1,082.08	1,082.08	12,608.50	12,608.45	637.45	637.45
M_{ll} > 15 GeV	2.69	2.69	9,412.60	9,420.00	1,100.89	1,100.88	12,597.00	12,596.88	630.96	630.96
Z-veto	2.61	2.61	9,071.88	9,079.14	1,168.84	1,168.84	3,154.67	3,154.67	614.81	614.81
$N_{jets} \geq 3$	1.32	1.32	1,300.73	1,300.76	118.11	118.11	97.94	97.94	266.19	266.20

Table 53: Cutflow of preselection for signal and VV , W+jets , Z+jets , $t\bar{t}$ background,weighted event number are shown from two analyzers.

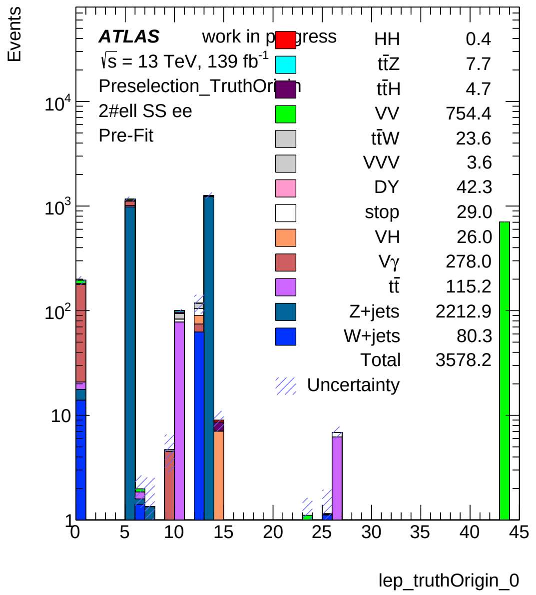

(a) Origin of the fakes for the leading lepton in preselection region with $e^{\pm}e^{\pm}$ selection.

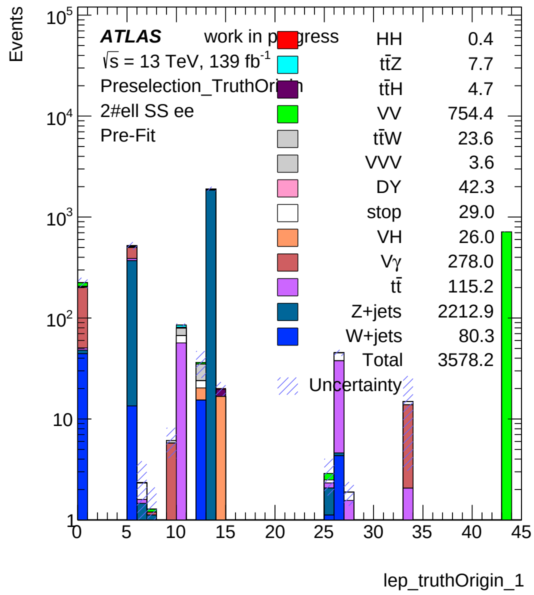

(b) Origin of the fakes for the sub-leading lepton in preselection region with $e^{\pm}e^{\pm}$ selection.

Figure 128: Origins of the fakes for the leading lepton and sub-leading lepton with $e^{\pm}e^{\pm}$ selection.

Since the Bremsstrahlung process depends on the amount of traversed detector material, the $|\eta|$ dependence on the QmisID rate would be considered. Charge flipped events could also arise from measurement error of the electron track curvature. This effect is more significant for electrons with high momenta or at large pesudorapidites, thus the p_T dependence would also be considered.

The MC simulation on QmisID process are not fully reliable due to the complicated processes with detector materials. The QmisID rates are estimated using a data-driven method based on a maximum likelihood technique. The likelihood fit is done on $Z- > ee$ data sample, events around Z peak are categorized into same-sign electron pair (SS) or opposite-sign pair (OS). The contribution from other small background are subtracted from the side-band data. To define such Z-mass window and to determine the background contributions in N_{SS} and N_{OS} a background + signal fit is performed on the distributions of invariant mass of the electron pairs, where the signal shape is a gaussian convolute a Breit-Wigner function, and the background pdf is a 3th order polynomial function. The fit results are shown in Figure 131 for inclusive

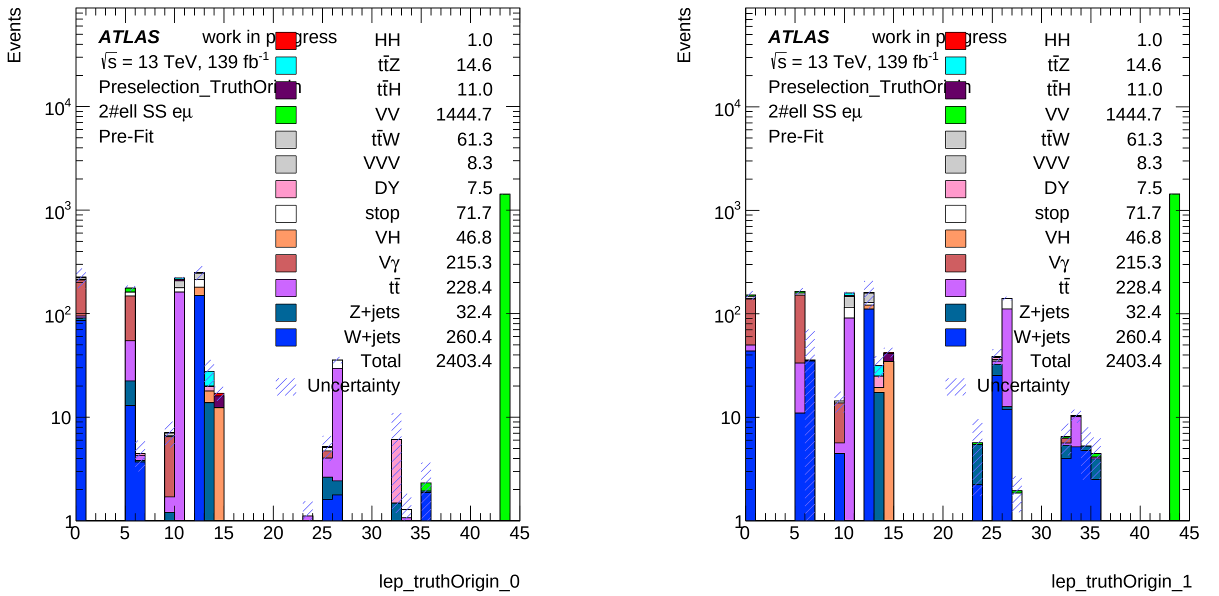

(a) Origin of the fakes for the leading lepton in preselection region with $e^{\pm}\mu^{\pm}$ selection.

(b) Origin of the fakes for the sub-leading lepton in preselection region with $e^{\pm}\mu^{\pm}$ selection.

Figure 129: Origins of the fakes for the leading lepton and sub-leading lepton with $e^{\pm}\mu^{\pm}$ selection.

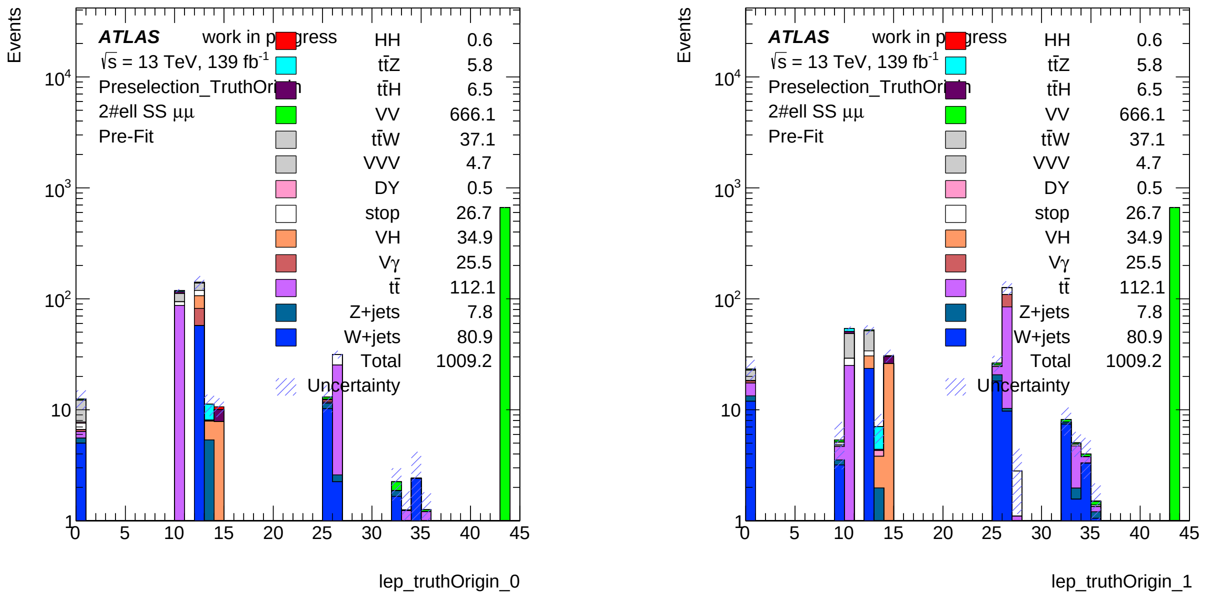

(a) Origin of the fakes for the leading lepton in preselection region with $\mu^{\pm}\mu^{\pm}$ selection.

(b) Origin of the fakes for the sub-leading lepton in preselection region with $\mu^{\pm}\mu^{\pm}$ selection.

Figure 130: Origins of the fakes for the leading lepton and sub-leading lepton with $\mu^{\pm}\mu^{\pm}$ selection.

Loose and Tight electron pairs accounting for OS and SS, respectively, for both $Z- > ee$ and data, as the invariant mass spectra of two same-sign electrons is shifted comparing with opposite-sign electrons.

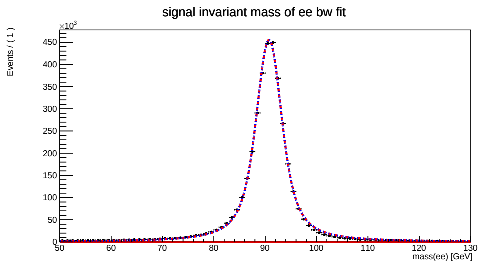

(a) opposite-sign electron pairs, MC.

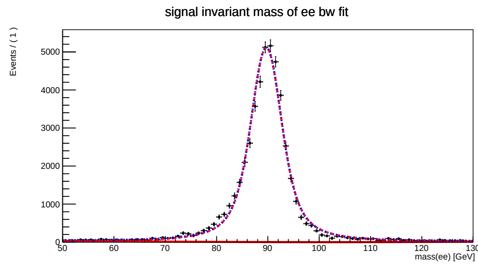

(b) same-sign electron pairs, MC.

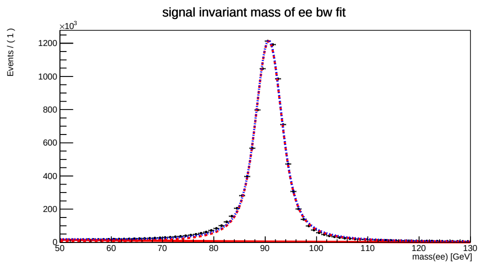

(c) opposite-sign electron pairs, data.

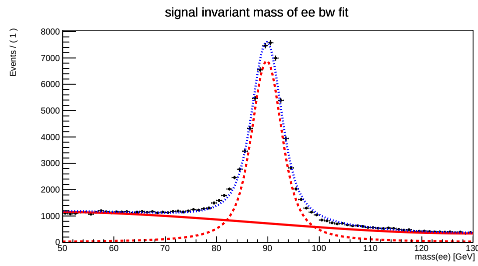

(d) same-sign electron pairs, data.

Figure 131: Invariant mass of electron pairs of 2ℓSS channel. (a) and (b) are for $Z- > ee$ MC and (c) and (d) are for full run2 data. The dashed red peak shows the fitted signal shape and the solid red line is the background distribution, the black dots show the data.

The number of same-sign electron pair (N_{SS}) and number of opposite-sign electron pair(N_{OS}) are the input of this fit. The probability to observe same-sign pairs follows a Passion statistic, write as

$$f\left(N_{\mathrm{SS}}^{ij}; \hat{N}_{\mathrm{SS}}^{ij}\left(\varepsilon_i, \varepsilon_j\right)\right) = \frac{\lambda^{N_{\mathrm{SS}}^{ij}} \mathrm{e}^{-\hat{N}_{\mathrm{SS}}^{ij}\left(\varepsilon_i, \varepsilon_j\right)}}{N_{\mathrm{SS}}^{ij}!} \tag{34}$$

Where ε_i and ε_j represent the QmisID rates for each of two electrons in bin(i, j), $N_S C^{ij}$ is the number of same-sign pairs,$\hat{N}_{\mathrm{SS}}^{ij}\left(\varepsilon_i, \varepsilon_j\right) = N^{ij}(\varepsilon_i(1-\varepsilon_j) + \varepsilon_j(1-\varepsilon_i))$ is the expected number of same-sign events. The expected number of QmisID events $\hat{N}_{\mathrm{SS}}^{ij}\left(\varepsilon_i, \varepsilon_j\right)$ therefor can be computed by measuring the number of opposite-sign events N_{OS} and QmisID rates in $e^{\pm}e^{\pm}$ and $e^{\pm}\mu^{\pm}$ channels,

$$\hat{N}_{\mathrm{SS}} = \frac{\varepsilon_i + \varepsilon_j - 2\varepsilon_i\varepsilon_j}{1 - \left(\varepsilon_i + \varepsilon_j - 2\varepsilon_i\varepsilon_j\right)} N_{\mathrm{OS}} \quad \text{and} \quad \hat{N}_{\mathrm{SS}} = \frac{\varepsilon_i}{1-\varepsilon_i} N_{\mathrm{OS}} \tag{35}$$

The negative log likelihood used to determine the QmisID rates is constructed as

$$-\ln L\left(\varepsilon \mid N_{SS}, N\right) = \sum_{i,j} \ln\left[N^{ij}\left(\varepsilon_i(1-\varepsilon_j) + \varepsilon_j(1-\varepsilon_i)\right)\right] N_{SS}^{ij} - N^{ij}\left(\varepsilon_i(1-\varepsilon_j) + \varepsilon_j(1-\varepsilon_i)\right) \tag{36}$$

The QmiID rate are parameterized as a function of electron p_T and $|\eta|$. The binning scheme are designed as [20,50],[50,100],[100,200],[200,1000] in electron p_T and [0,0.6],[0.6,1.1],[1.1,1.37][1.52,1.7],[1.7,2],[2,2.5]. The Z-peak is obtained by a signal + background fit introduced before, then $\pm 4\sigma$ around the mean value is defined as the m_Z window. In terms of background subtraction the side-bands region are defined by $\pm 4\sigma$

processes	lower Side-band	m_Z window	upper Side-band
Same-sign	[53.7,74.4]	[74.4,106.6]	[106.6,124.5]
Opposite-sign	[61.4,75.8]	[75.8,104.8]	[104.8,119.4]

Table 54: Definition of the m_Z window and side-bands

width for each side of m_Z window. To increse the statistic of the tight-electrons, anti-tight electrons are tested in this estimation. As shown in Figure **??**, no significant difference is found for different combination of tight and an-tight electron pairs. The definitions of the m_Z window are listed in Table 54.

The QMisID rates estimated by data-driven approach, corresponding to $139 fb^{-1}$ data in p_t and $|\eta|$ 2D kinematic space, separately for tight and an-tight electrons are presented in figure 132, where events in **??** are classified into Tight-Tight pairs, Tight-AntiTight pairs to increase the statistical for the likelihood fit. It is found that QMidID BDT suppress the QMisID probabilities by a factor of 10.

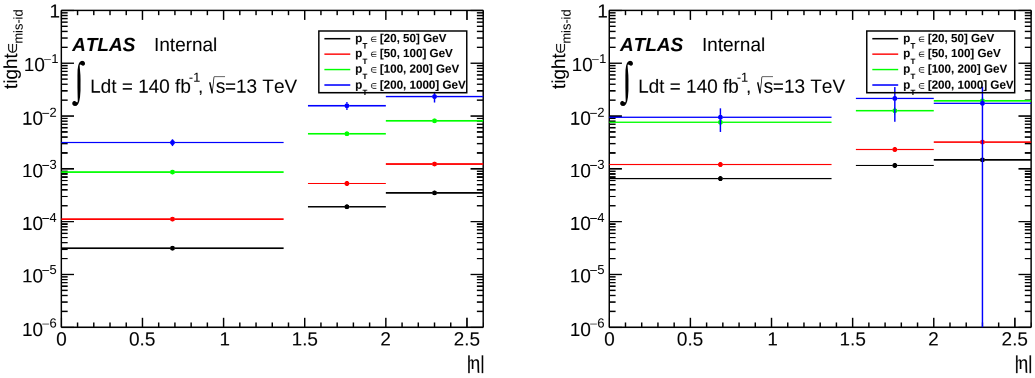

(a) QMisID rates for Tight leptons

(b) QMisID rates for AntiTight leptons

Figure 132: QMisID rates estimated by data-driven approach.

To validate the likelihood method used to determine QmisID rates, a closure test is done by comparing the QmisID rates derived from Z+jets simulation with the rates using truth information. There is no big disagreement between the two approaches, as the comparison plots shown in figure 133. The $|\eta|$ bins are merged to have enough events in each of the p_t bins.

C.3 Investigation of BDT training

The kinematics of training variables are crucial to fit a BDT model. Comparison of some training variables with different MC process are presented in Figure 134

The figure of merit of BDTG optimization is to maximise the area under the ROC. The values of hyperparameters are choosen from a grid search, as shown in Table **??**. A five fold cross-validation method is performed to evaluate the performance. The set of hyperparameters giving the highest AUC is finally selected. The results are shown in Table 56 for 4 BDTs.

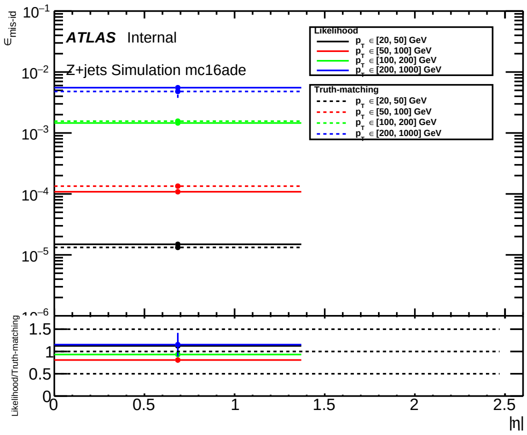

Figure 133: QMisID rates validation.

After determing the value of hyperparameters, two MVAs are trained on the even / odd-numbered events, then the MVA trained with even-numbered events is applied to odd-numbered events, so that the cross-use of events in training and application is avoided.

Table 55: Search grid of hyperparameters for MVA optimization in 2ℓSS channel.

Parameter	Values
NTrees	200, 400, 800, 1000, 1200, 1500, 2000
MinNodeSize	0.01%, 0.1%, 1%, 2.5%
BaggedSampleFraction	0.3, 0.5, 0.8
Shrinkage	0.01, 0.02, 0.05, 0.1, 0.2
nCuts	15, 20, 25, 30
MaxDepth	1, 2, 3, 4

Table 56: Derived hyperparameters values for MVA optimization in 2ℓSS channel, including BDT_{VV} ,$BDT_{t\bar{t}}$,BDT_{Z+jets} and BDT_{Combined}

Parameter	VV BDT	Zjets BDT	ttbar BDT	Combined BDT
NTrees	1000	400	1200	2000
MinNodeSize	2.5%	2.5%	2.5%	2.5%
BaggedSampleFraction	0.5	0.5	0.5	0.5
Shrinkage	0.1	0.02	0.02	0.1
nCuts	30	30	25	25
MaxDepth	3	2	2	3

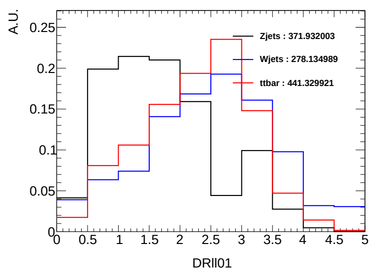

(a) ΔR of two lepton.

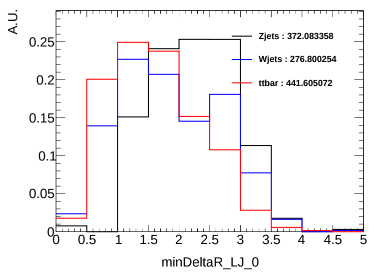

(b) $\Delta_{min}R$ of leading lepton and jet.

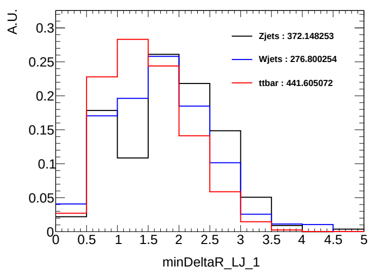

(c) $\Delta_{min}R$ of leading lepton and jet.

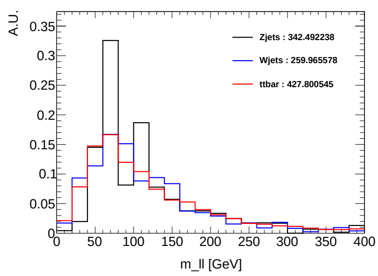

(d) $m_{\ell\ell}$ of two lepton.

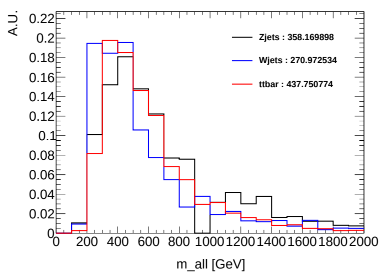

(e) Mass of all objects.

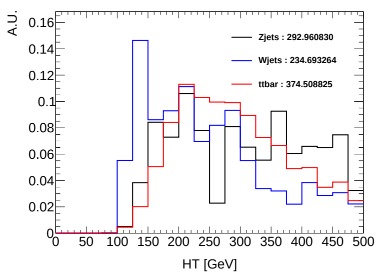

(f) HT.

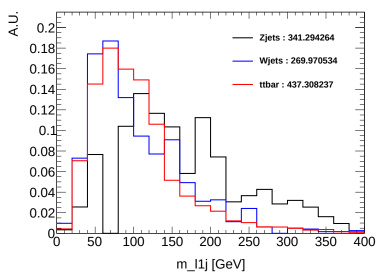

(g) Invariant mass of leading lepton and closest jet.

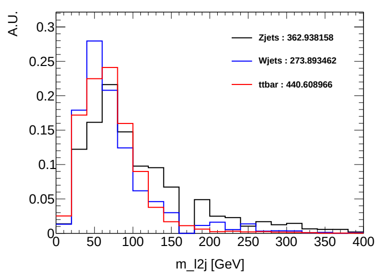

(h) Invariant mass of sub-leading lepton and closest jet.

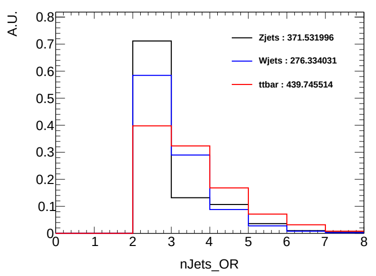

(i) Number of jets.

Figure 134: Some inputs variables distribution of $t\bar{t}$, Z+jets , W+jets for BDT training.

C.4 Studies on the diboson modeling in the 2ℓ SS channel

Diboson background (VV) combine all processes consisting of two vector bosons V (V=W,Z). W and Z bosons can either decay leptonically or hadronically, therefore, their final state is very diverse and can contain 0-4 charged leptons, missing energy from neutrinos and hadronic jets. Diboson processes can enter therefore in several ways in the signal region of the 2ℓ same-sign channel:

- Through fake leptons: This is the case for final states containing $\leq$ 1 lepton.
- Charge mis-identification: if the final state contains == 2ℓ, but which are of opposite sign (for instance: $W^{\pm}W^{\mp}$ or $W(\rightarrow qq)Z(\rightarrow \ell\ell)$)
- Irreducible background: VV processes enter the SR as they contain 2ℓ which are same sign or $\geq$ 3 leptons where one or more leptons fall out of the detector acceptance.

The first two items listed above, fake leptons and leptons whose charge is misidentified, are part of the reducible background which are estimated using dedicated studies. The contribution of reducible diboson

2ℓ VV enriched CR	
$HH2\ell$ SS Preselection	
BDTG$_{All1}$	< -0.4
BDTG$_{VV}$	> -0.8
m_{ll} [GeV]	< 80 OR > 100

Table 57: Selection cuts to create a region enriched in VV events. The $HH2\ell$ SS Preselection refers to the selection defined in Section 4.2.1.

background is however low, in total smaller than 0.5% in the signal region. Diboson processes with ≥ 3 leptons or == 2 leptons of the same charge, however, make up the dominant irreducible background in the signal region ($\approx 50\%$). Confidence in their modeling is therefore important for the analysis.

Background from fully leptonically decaying $WZ \rightarrow \ell\nu\ell\ell$ is the largest background in the signal region, among the diboson processes and also in overall. It contributes to the signal region to about 35%. It passes the signal selection if one lepton drops out of the detector acceptance, either due to the limited phase space coverage of the detector or due to object selection, like p_T cuts or lepton selection efficiencies < 1. Other irreducible diboson background comes from ZZ, where two leptons are not identified by the detector, which is a contribution of 3.5%. An important contribution is background from $VVjj$ processes, electroweak production of diboson events, either $WZjj$ or $W^{\pm}W^{\pm}jj$, which contribute with 12.5% to the signal region. The differential cross section measurement of WZ events as a function of the jet multiplicity N_{jets}, showed that the `Sherpa 2.2.1` MC overestimates the data for $N_{jets} \geq 2$ [78]. This overestimation of the simulation has been also observed in the dedicated WZ control region ($N_{jets} \geq 2$) of the $3\ell0\tau$ channel, where a normalization factor of 0.84 ± 0.02 has been derived. In a VV enriched control region in the 2ℓ SS analysis, defined in Table 57, however, it is observed that the data overshoots the MC. This is demonstrated in Figure 135.

As both, the 2ℓ SS and the $3\ell0\tau$ channel enter in the combined fit, it is important to resolve that tension.

Measurements on VBS processes (e.g. [79, 80]) showed that the MC simulation underestimates the cross section in data. Especially $W^{\pm}W^{\pm}jj$ [80] is expected to enter the signal region due to the same particles in the final state (≥2 jets and 2 same-sign leptons). Therefore, studies on a separate treatment/correction of these two components, the fully leptonically decaying WZ and $VVjj$ events, are performed.

Two normalization factors are derived for WZ in a 3ℓ WZ control region and in a 2ℓ SS VV control region enriched in VV_{jj} events. For first studies, normalization factors for WZ (μ_{WZ}) and of VV_{jj} (μ_{VVjj}) are derived in a simultaneous binned fit to a WZ-enriched 3ℓ CR and a $VVjj$-enriched 2ℓ SS CR. Then, post-fit data-MC agreements are checked in that region and the compatibility of the μ_{WZ} and μ_{VVjj} with earlier studies is checked. Finally, the data-MC agreement in the larger, more inclusive, low-BDT score validation region is checked after applying μ_{WZ} and μ_{VVjj}.

As a first step, a VV CR enriched in VV_{jj} is constructed. Typically, the invariant mass of the two jets leading in p_T (m_{jj}) and H_T are discriminating between VV and $VVjj$. Further, both of these variables discriminate between the fakes and the prompt background, cutting on those variables therefore reduces as well the mismodelled fake lepton background contribution and reduces the potential bias introduced by those events. Based on the VV-enriched CR defined in Table 57, a VV_{jj}-enriched 2ℓ SS region is created. Studies showed, that cutting on m_{jj} manages to enrich better a region in VV_{jj}: A cut on $m_{jj} > 300$ GeV

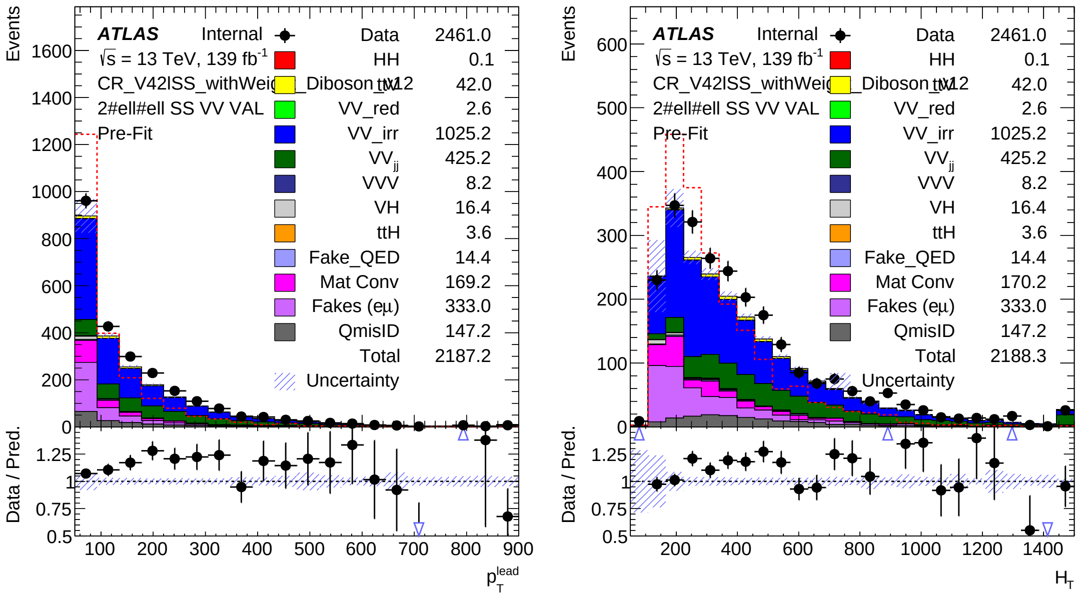

Figure 135: Control plots of the VV-enriched CR defined in Table 57. The p_T of the leading jet in p_T is shown on the left, of the event H_T on the right. Systematics contain statistical and preliminary systematics on the data-driven fake lepton estimation.

would enrich the region in VV_{jj} to about 40% while keeping about 30% of the total events and 60% of VV_{jj} events. A cut on H_T with the same performance w.r.t VV_{jj} purity, however, would require to cut at about $H_T > 800$ GeV which would retain about 10% of the total region statistics and 20% of the VV_{jj} events. Figure 136 shows the p_T^{lead} (p_T of the leading jet) and H_T distributions in the VV_{jj}-enriched region after applying a cut of $m_{jj} > 300$ GeV in addition to the selection presented in Table 57. It can clearly be seen that the data overshoots the prediction.

In a second step, the 3ℓ WZ CR is created, based on the WZ CR by the $3\ell0\tau$ channel, extending the selection of the 2ℓ SS channel. The selection is shown in Table 58 and compared to the $3\ell0\tau$ and 2ℓ SS preselection.

Figure 137 shows the N_{jets} distribution in that WZ CR. Note that the fake lepton background is modeled using MC simulation, the semi-data-driven fake lepton background estimation is not applied yet.

A combined fit is performed in these two regions, with μ_{WZ} and μ_{VVjj} normalization factors floating freely. Note that for the following studies, the fake lepton and charge mis-ID background is modeled using MC simulation. The cut on m_{jj} reduces already this background. A 50% systematic uncertainty is applied to the fake lepton and lepton charge mis-ID background, following the order of magnitude of the fake background normalization factors found in the auxiliary control regions. Systematics on the prompt background are applied according to PMG modeling studies and recommendations: on ZZ events, an uncertainty of 6% is applied [81], on ttZ events, an uncertainty of 11% [82], on the ttH background, an uncertainty of 10% [82], on VH of 5% according to internal recommendations, and on ttW background 3% and on triboson background of 30% [81]. In order to discriminate between WZ and VV_{jj}, the H_T distribution is fitted in the 2ℓ SS VV_{jj}-enriched CR. Fits to m_{jj} and with different binnings in H_T were also studied. As the WZ CR is rather pure in WZ events, a one-bin fit is performed in the WZ CR. Studies

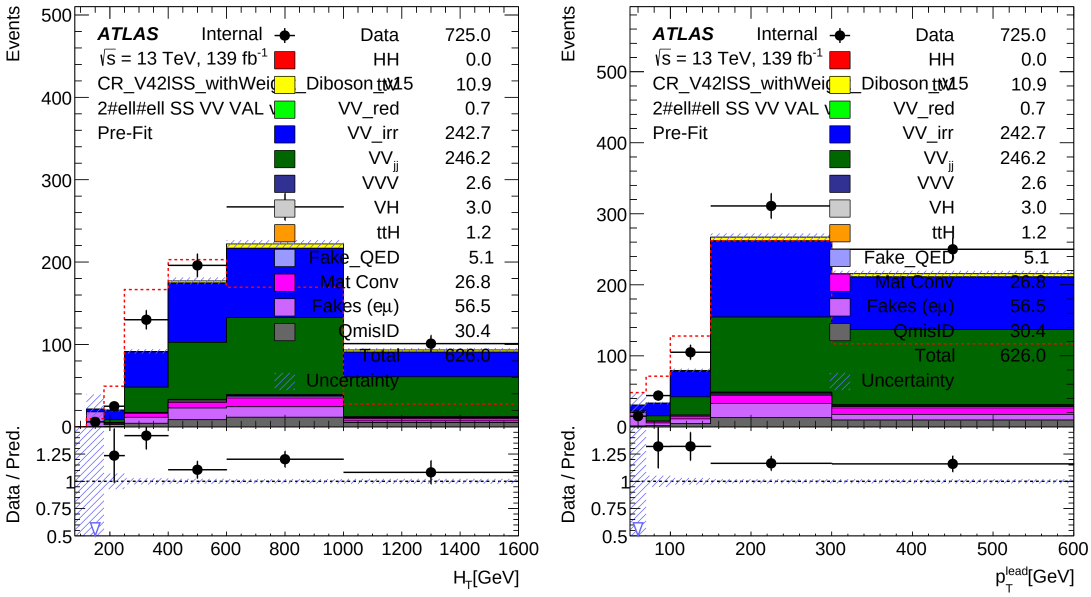

Figure 136: p_T^{lead} and H_T in a VV_{jj}-enriched control region.

Selection cut	2ℓSS	3ℓ	3ℓ WZ CR for 2ℓ SS
Trigger	SL OR DL	SL OR DL	SL OR DL
TrigMatch	Tight e or μ	✓	✓
N_ℓ	==2	==3	==3 (2ℓ SS +1 type Loose)
Total charge	+ 1	±1	±1
Lepton selection	T	ℓ_1: L, $\ell_{2,3}$: T	ℓ_0: L, $\ell_{1,2}$: T
low di-lepton mass veto	$m(\ell^\pm\ell^\pm) > 12$ GeV	$m(\ell^+\ell^-) > 12$ GeV	$m(\ell_i\ell_j) > 12$ GeV ($i, j \in \{0, 1, 2\}$)
p_T^ℓ	> 20 GeV	ℓ_1 :> 10 GeV, $\ell_{2,3}$:> 15 GeV	ℓ_0 :> 10 GeV, $\ell_{1,2}$:> 20 GeV
τ-veto	✓	✓	✓
b-veto	✓	✓	✓
N_{jets}	≥ 2	≥ 2	≥ 2
Z-veto	-	$\lvert m_{SFOS} - 91.2\rvert > 10$ GeV	-
$Z - \gamma$-veto	-	$\lvert m_{lll} - 91.2\rvert > 10$ GeV	$\lvert m_{lll} - 91.2\rvert > 10$ GeV
$\ell\ell$-pair	-	-	≥ 1 OSSF pair
Z+jets selection	-	-	$\lvert m_{SFOS} - 91.2\rvert < 10$ GeV
E_T^{miss}	-	-	> 30 GeV

Table 58: 3ℓ WZ CR for the 2ℓ SS analysis, compared to the 3ℓ and 2ℓ SS pre-selection.

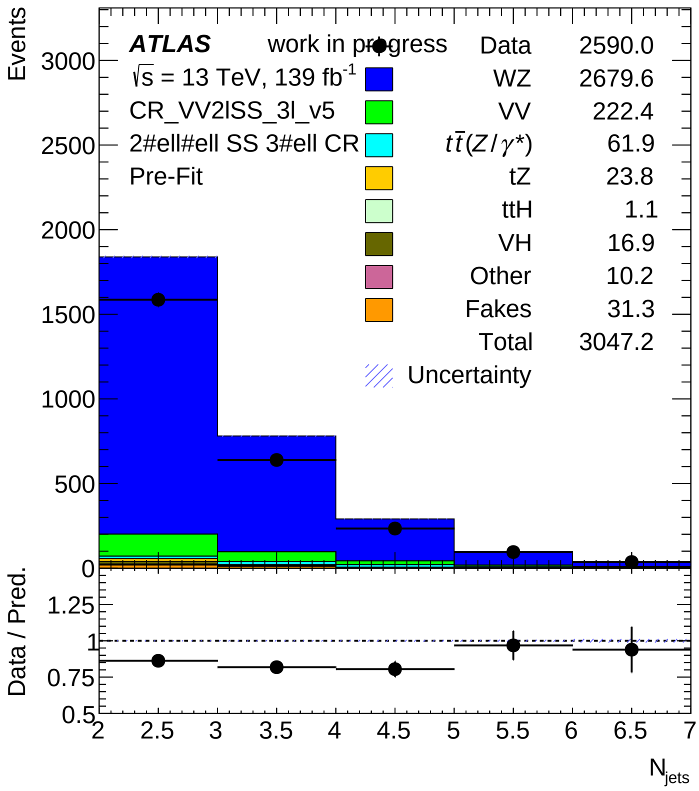

Figure 137: N_{jets} distribution in the WZ CR of the 2ℓ SS channel, based on the CR by the $3\ell 0\tau$ channel.

showed that a binned fit in the WZ CR does not bring any benefits. The results of μ_{WZ} and μ_{VVjj} for various fit configurations are shown in Table 59.

The factor μ_{WZ} is stable for different fit configuration and is compatible with the WZ normalization factor found by the $3\ell 0\tau$ analysis (0.84 ± 0.02). A signal strength of electroweakly produced $W^{\pm}W^{\pm}jj$ of $1.44^{+0.26}_{-0.24}(\text{stat.})^{+0.28}_{-0.22}(\text{syst.})$ has been extracted in Ref. [80]. This is in agreement with the μ_{VVjj} extracted in the combined fit. A finer or optimized binning in H_T in the 2ℓ SS CR has shown to reduce the correlation between μ_{VVjj} and the fake lepton background nuisance parameter from -75% to -60%. This background shows in addition and upwards pull of $\geq 1\ \sigma$, except for the configurations "H_T binning 2(3)" where the pull is reduced to about 0.5 σ. It has been observed that the simulation mismodels and underestimates the fake lepton background, a pull upwards is therefore not surprising. An anti-correlation of the normalization factors with the largest background nuisance parameter is expected as well. It is desirable, however, to reduce the correlation with the parameters of interest to have more confidence in the final normalization factor and to keep the bias low: options with larger anti-correlations show larger pulls of the fake lepton nuisance parameters and lower μ_{VVjj}. The configurations "H_T binning 2(3)" are therefore the best options. The extracted normalization factors do not differ between these two options. In general, the normalization factors have a low spread w.r.t their uncertainties and are all compatible with each other. The post-fit plots of the fit with the configuration "H_T binning 2" is shown in Figure 138. A good post-fit data-MC agreement is observed in the VV control regions.

For the moment, factors of $\mu_{WZ} = 0.80 \pm 0.02$ and $\mu_{VVjj} = 1.72 \pm 0.15$ are assumed. For the final normalization factors, it is considered to include one or both of these regions in the combined fit. These

Configuration	μ_{WZ}	μ_{VVjj}
Nominal (H_T)	0.80±0.02	1.61±0.18
H_T binning 2	0.80±0.02	1.72±0.15
H_T binning 3	0.80±0.02	1.72±0.14
m_{jj}	0.80±0.02	1.56±0.17
E_T^{miss} in WZ CR	0.80±0.02	1.58±0.18

Table 59: Results for the normalization factors extracted from the combined fit to the 2ℓ SS VV_{jj}-enriched CR and to a WZ 3ℓ CR. The nominal configuration corresponds to 4 bins in H_T in the 2ℓ SS CR and a 1-bin fit in the WZ CR. The configuration "H_T binning 2" corresponds to a slightly reshuffled binning in H_T where the first and the last bins have been modified to better discriminate between fakes, WZ and VV_{jj}. A finer binning in H_T has been chosen for "H_T binning 3" (6 bins). "m_{jj}" means that a fit to m_{jj} instead of H_T has been performed and the configuration "E_T^{miss} in WZ CR" corresponds to the nominal configuration in line 1 but with the WZ CR split in bins in E_T^{miss}.

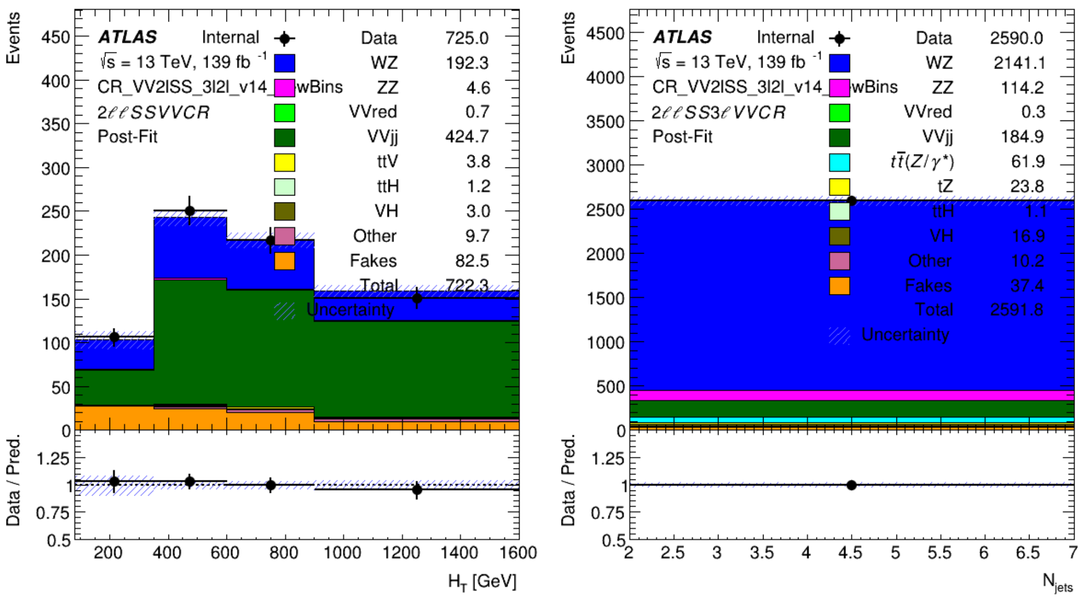

Figure 138: Post-fit data-MC agreement in the 2ℓ SS VV_{jj}-enriched CR (left) and the 3ℓ WZ CR.

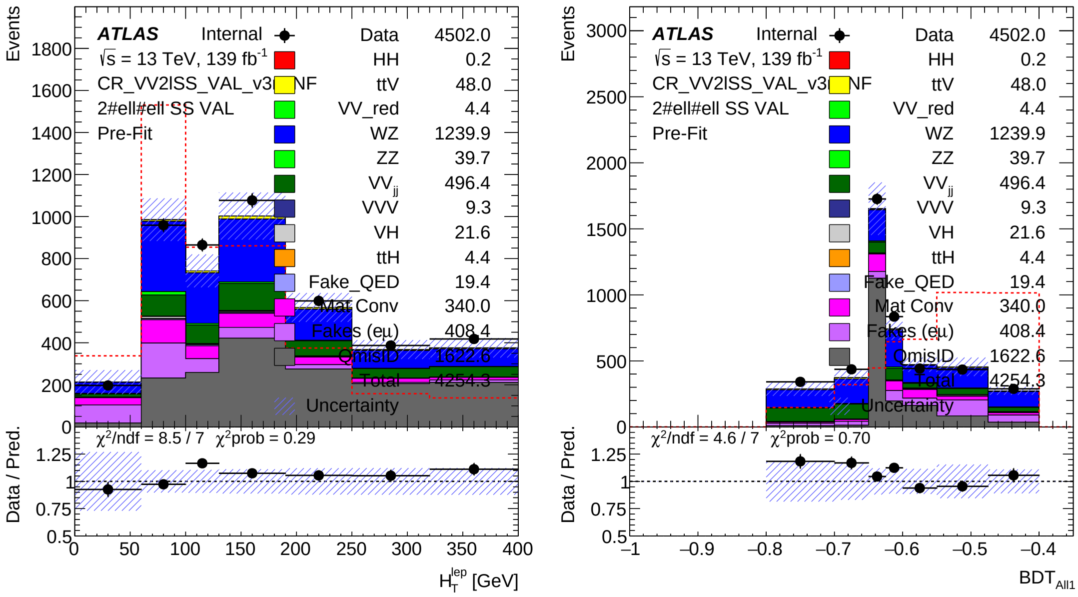

Figure 139: Plots of the lepton H_T (sum of the lepton p_Ts) and the combined BDT score at low values (< 0.4). The fake lepton background has been estimated using semi-data-driven methods. No normalization factor but additional uncertainties have been applied to the irreducible diboson backgrounds considering disagreements between ATLAS Standard Model measurements at large jet multiplicities [80, 81] (WZ: 20% , VV_{jj}: 45%).

studies have to be repeated in any case however, with the data-driven fake lepton background estimation.

In order to check the feasibility of this approach, these normalization factors ($\mu_{WZ} = 0.80 \pm 0.02$ and $\mu_{VVjj} = 1.72 \pm 0.15$) are applied to the low-score validation region of the combined BDT (Pre-selection+$BDT_{All1} < -0.4$) of the 2ℓ SS channel and the data-MC agreement of kinematic plots is verified. This region consists of 30% of WZ and 12% of VV_{jj} events, the most dominant contribution come from events with charge-misidentified leptons which is estimated using a semi-data-driven method. Figure 139 shows the data-MC agreement before applying the diboson normalization found in these studies and Figure 140 shows the data-MC agreement after applying the diboson normalization factors for WZ and $VVjj$. The data-MC agreements improves after applying the diboson normalization factors, statistically, the agreement slightly worsens, however, note that the uncertainties are larger on the diboson contributions in the case without normalization factors applied.

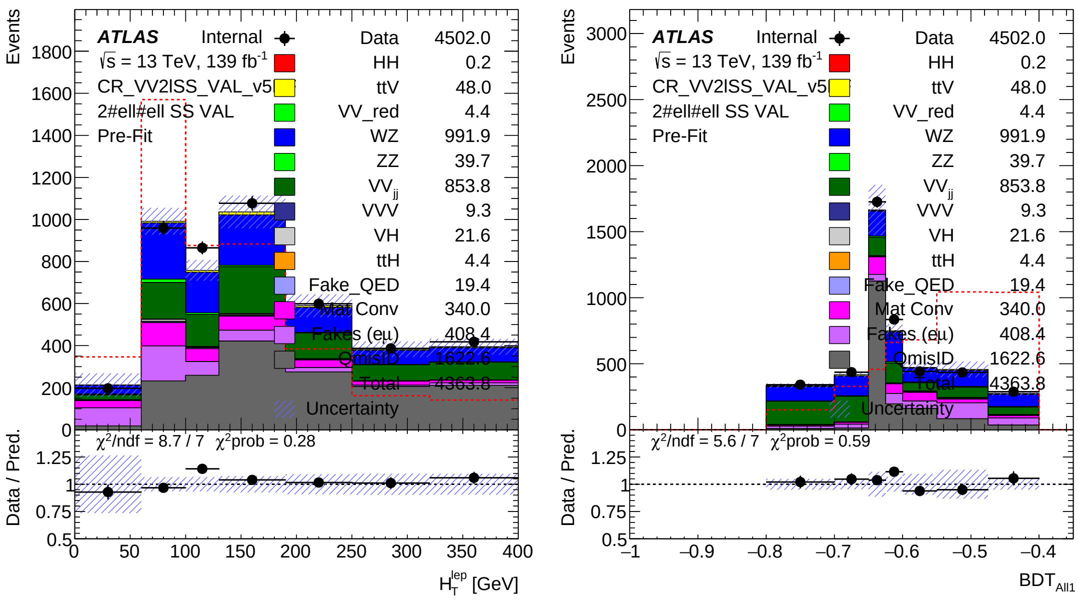

Figure 140: Plots of the lepton H_T (sum of the lepton p_T s) and the combined BDT score at low values (< 0.4). The fake lepton background has been estimated using semi-data-driven methods. Normalization factors to WZ and VV_{jj} backgrounds (μ_{WZ} = 0.80 ± 0.02 and μ_{VVjj} = 1.72 ± 0.15) have been applied.

D The Appendix of the Analysis of 3 Lepton Channel

Add the appendix of the text for 3L

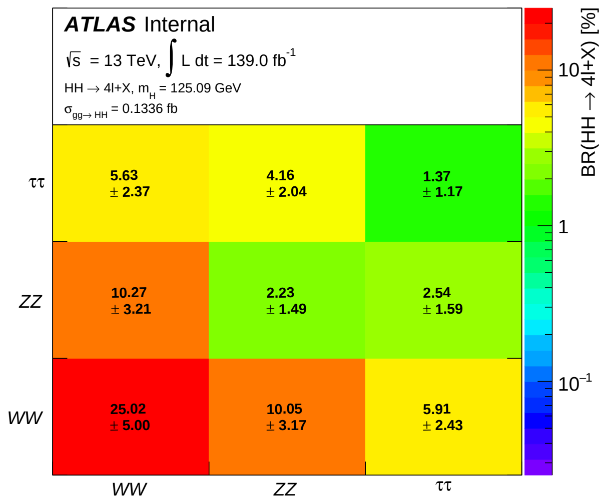

Figure 141: Di-Higgs decay modes and the calculated branching fraction of Di-Higgs to four leptons and X at the reconstruction level. The assumed Higss mass is 125.09 GeV and the Higgs pair production cross-section in gluon-fusion is 0.1336 fb.

E Appendix of the Analysis of 4 Lepton Channel

In this channel, the non-resonant Di-Higgs decays to $4\ell(\ell = e,$ or $\mu)$ is analysed. Any of the Higgs decays to $2W$, $2Z$ or 2τ, leading to $4\ell + X$, where X could either be missing transverse energy or jets. The combination of the Higgs decay products is shown in Figure 141 with their branching fractions. There are nine possible permutations, namely— $4W$, $4Z$, 4τ, $2W2Z$, $2Z2W$, $2W2\tau$, $2\tau2W$, $2Z2\tau$ and $2\tau2Z$. About 25% of the HH events are expected to come from the $HH \to 4W$, 20% from $HH \to 2Z2W$, and 11% from $HH \to 2W2\tau$. Other HH events such as $HH \to 4Z$, $HH \to 4\tau$, and $HH \to 2Z2\tau$ are expected to be less than 10%.

E.1 Event selection

Electrons must be within the inner tracking detector system ($|\eta| < 2.47$ excluding the $1.37 < |\eta| < 1.52$ region) and have transverse energy $E_T > 7$ GeV. Muons are required to be inside $|\eta| < 2.7$ scope of the muon spectrometer, and have transverse momentum $p_T > 5$ GeV. Events are selected if they only contain exactly four leptons with $p_T^\ell > 10$ GeV, and a total charge sum equal to zero. Events are required to pass single- and di-lepton trigger, and at least one of the lepton candidate need to be matched to the trigger. After choosing four isolated leptons, events are classified further according to the number of lepton pairs. Events must have two same-flavour and opposite charges (2-SFOS) lepton pairs such as $4e$, 4μ and $\mu2e$. In addition to events with one or zero same-flavour opposite charges pairs (1-SFOS or 0-SFOS), for instance, $e\mu\mu\mu$ and $e\mu e\mu$. The 0-SFOS events are combined with 1-SFOS (0/1-SFOS) due to the low statistics. In each quadruplet, the p_T of the leading lepton has to be higher than the succeeding one. The quadruplets are selected based on matching the invariant mass of the second lepton pairs m_{Z_2} to be closest to the Z boson mass, and the first lepton pair were taken as m_{Z_1}. Events carrying one or more b-jets are vetoed to

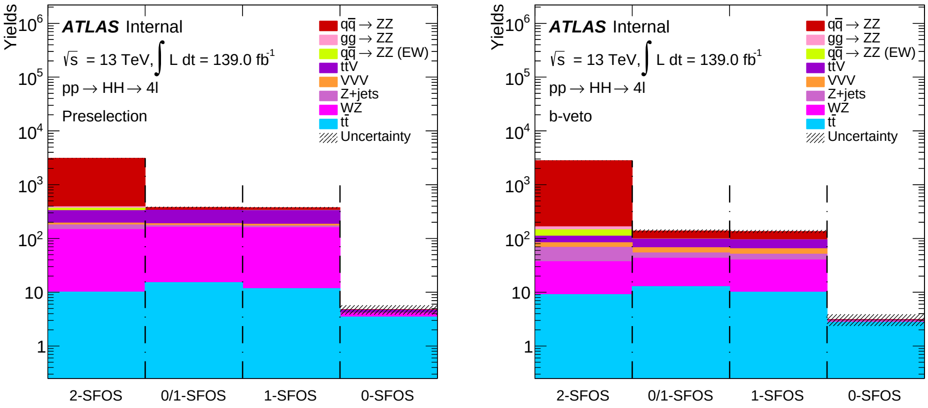

(a) (b)

Figure 142: The expected background yields for MC simulation after the a preselection and b b-veto for the 2-SFOS, 1-SFOS, 0/1-SFOS and 0-SFOS categories.

suppress top related backgrounds further. Figure 142 shows the yield for each background component with and without the b-jet veto for 2-SFOS, 1-SFOS, 0-SFOS, and 0/1-SFOS categories.

E.2 Analysis strategy

After selecting four isolated leptons with zero total charge, preselection events are categorized further according to the number of the lepton pairs. Events containing $4e$, 4μ and $\mu 2e$ are organized as two same-flavour and opposite sign lepton pairs (2-SFOS). Events including only one same-flavoured and opposite sign lepton pairs (1-SFOS) such as $e\mu\mu\mu$. The rest of the events where there are no same-flavour opposite sign leptons (0-SFOS) like $e\mu e\mu$. The last category is combined with the 1-SFOS lepton category due to low statistics. The composition of background components from different sources for each category is shown in Figure 142. This categorisation is the same as the previous round of the analysis in Ref. [83].

In each quadruplet, the p_{T} of the leading lepton has to be higher than the succeeding one. The quadruplets are selected based on matching the invariant mass of the second lepton pairs m_{Z_2} to be closest to the Z boson mass, and the first lepton pair were taken as m_{Z_1}.

The b tagged jets (b-jets) play an essential role in suppressing the top related backgrounds, as shown in Figure 143 for 2-SFOS and 0/1-SFOS categories. Where for more than one b-jets, $t\bar{t}V$ and $t\bar{t}$ backgrounds become aggressive. Figure 142b shows that the employment of b-veto decreases the $t\bar{t}V$ background by more than 80% and the $t\bar{t}$ background by about 10%. Also, the effect of b-vetoing is illustrated in Figure 143 using the number of jets multiplicity. In this analysis, two techniques are considered to optimize the signal region selection—cut-based and multivariate analyses.

Table 60: The expected yields for non-resonant di-Higgs boson signal and the total background calculated from the state-of-the-art MC simulation with an integrated luminosity of 139 fb^{-1}. The uncertainties included on the table are statistical uncertainty.

	Non-Res	$qq \to ZZ^*$	$gg \to ZZ^*$	$qq \to ZZ^*(EW)$	$t\bar{t}V$	VVV	Z+jets	WZ	$t\bar{t}$	Total background
4ℓ	0.63±0.02	5767.04±10.35	35.41±0.07	107.34±31.42	514.39±3.07	42.27±0.26	6653.27±550.68	110.18±1.79	2651.21±20.57	15881.11±618.22
Trigger	0.53±0.02	4394.75±8.54	27.13±0.06	90.71±31.42	433.12±2.85	37.15±0.25	3805.91±324.02	83.28±1.49	1852.13±16.99	10724.18±385.62
Trigger Match	0.53±0.02	4394.61±8.54	27.12±0.06	90.71±31.42	433.06±2.85	37.14±0.25	3805.53±324.02	83.24±1.49	1851.97±16.99	10723.40±385.61
$p_{\mathrm{T}}^{\ell} > 10$ GeV	0.49±0.02	4069.61±8.20	25.94±0.05	86.80±31.42	408.85±2.76	36.13±0.25	2437.94±237.66	66.94±1.34	1419.96±14.87	8552.17±296.54
$\|\eta\|$ requirement	0.45±0.01	3756.47±7.69	24.19±0.05	83.02±31.42	383.66±2.67	33.50±0.24	2264.25±226.40	59.42±1.26	1277.64±14.11	7882.15±283.84
Loose ID	0.45±0.01	3756.47±7.69	24.19±0.05	83.02±31.42	383.66±2.67	33.50±0.24	2264.25±226.40	59.42±1.26	1277.64±14.11	7882.15±283.84
Loose Iso	0.34±0.01	3177.79±6.89	21.78±0.05	39.80±0.29	289.48±2.28	30.63±0.23	54.26±14.82	14.57±0.62	41.16±2.52	3669.47±27.71
$m_{\ell^+\ell^-}$ (SFOS) > 12	0.33±0.01	2875.99±6.69	21.28±0.05	37.66±0.28	281.82±2.26	30.42±0.23	44.95±14.13	13.83±0.61	26.71±2.05	3332.65±26.30

E.2.1 The cut-based analysis

A simple signal optimisation depending on shape comparison between signal and backgrounds is used.

$$Z_{\mathrm{Sig}_1} = \sqrt{2 \cdot \left((s + b) \cdot \ln \left(1 + \frac{s}{b} \right) - s \right)}, \quad \& \quad Z_{\mathrm{Sig}_2} = \frac{s}{\sqrt{s + b}}, \tag{37}$$

where s and b are the signal and background yields, respectively.

E.2.2 The Multivariate analysis

A boosted decision tree (BDT) based on the Multivariate analysis package (TMVA) is used to separate the $hh \to 4\ell + X$ signal from the background. Events are divided equally into two sets; the first half is used for training the BDT algorithm. And the other half is employed to test the performance of the method. Table 61 shows the unweighted events of the signal and backgrounds for 0/1-SFOS and 2-SFOS categories after the b-veto.

Table 61: Unweighted events for the signal and backgrounds component in each category used in the training and testing. Events are shown after vetoing the b-jets.

	0/1-SFOS	2-SFOS
$q\bar{q} \to ZZ$	21675	1528977
$q\bar{q} \to ZZ$ (EW)	375	28806
$gg \to ZZ$	2966	256910
$t\bar{t}V$	11031	10105
VVV	18467	57908
Z+jets	69	116
WZ	328	276
$t\bar{t}V$	92	68
$hh \to 4\ell + X$	4340	3781

Table 62: Input features used for the training and their ranking and separation power for 2-SFOS and 0/1-SFOS category. The higher the percentage value of the separation power, the better the ranking—the best-ranking start from 1 to the worst-ranked 16.

Input variable	Description	0/1-SFOS		2-SFOS	
		Rank	Separation	Rank	Separation
$E_{\mathrm{T}}^{\mathrm{miss}}$	Missing transverse energy	11	4.56%	2	37.82%
m_{Z_1}	Invariant mass of the first lepton pair	16	2.16%	1	52.44%
m_{Z_2}	Invariant mass of the second lepton pair	1	26.31%	4	30.88%
$m_{4\ell}$	Four-lepton invariant mass	4	6.10%	5	16.93%
$\Delta\phi_{Z_1}$	The azimuthal angle between the first lepton pair	2	11.52%	7	15.75%
$\Delta\phi_{Z_2}$	The azimuthal angle between the second lepton pair	6	5.73%	9	9.99%
$p_{\mathrm{T}}^{\ell_1}$	p_{T} of the first lepton	3	7.35%	12	5.36%
$p_{\mathrm{T}}^{\ell_2}$	p_{T} of the second lepton	8	5.16%	13	5.25%
$p_{\mathrm{T}}^{\ell_3}$	p_{T} of the third lepton	13	3.82%	15	3.74%
$p_{\mathrm{T}}^{\ell_4}$	p_{T} of fourth lepton	14	2.58%	10	6.17%
$p_{\mathrm{T}}^{4\ell}$	p_{T} of the four-lepton system	7	5.49%	3	31.66%
$p_{\mathrm{T}}^{Z_1}$	p_{T} of the first lepton pair	12	4.29%	16	3.02%
$p_{\mathrm{T}}^{Z_2}$	p_{T} of the second lepton pair	15	2.29%	11	6.11%
N_{jets}	Number of the jets	10	4.61%	8	15.05%
H_{T}^{ℓ}	Scalar sum of the leptons p_{T}	5	5.95%	14	4.41%
$H_{\mathrm{T}}^{\mathrm{jets}}$	Scalar sum of the jets p_{T}	9	2.16%	6	16.92%

Sixteen variables are used as inputs to the BDT, including the four leptons invariant mass. The correlation between features is shown in Figure 146. Some of the variables have a high correlation; for instance, the first lepton momentum is correlated with the scalar sum of leptons. Table 62 summarises the description of each variable, its ranking and the separation power. The best- and worst-ranked variable are labelled 1 and 16, respectively. The invariant mass of the second lepton pair has the best ranking in 0/1-SFOS, while the invariant mass of the first lepton pair is the best in 2-SFOS. A comparison between BDT and other MVA methods is illustrated in Figure 147a for 2-SFOS. It shows that the Receiver operating characteristic (ROC) curve for the BDT is better. Figure 147b shows the ROC curve for the 0/1-SFOS and 2-SFOS categories.

The area under the curve (AUC) is found to be 95.9% (87.4%) for 2-SFOS (0/1-SFOS). Finally, the classification of the BDT output is shown for 0/1-SFOS and 2-SFOS signal regions in Figures 147c and 147d, respectively.

E.3 Control region study

E.4 Systematic uncertainties

A global uncertainty of ±1.7% on the total integrated luminosity of the data reported between 2015 and 2018 is considered. In addition, theoretical uncertainties on the signal's cross section are considered. For examples, ±2.1% uncertainty on the PDF and α_S, and $^{+2.2\%}_{-5.0\%}$ from the QCD scale. Other experimental systematic uncertainties are not included in the analysis, like the lepton energy scale and resolution, etc.

E.5 Results

Statistical analysis is performed using the profile-likelihood-ratio test statistic [72]. A simultaneous fit on the 0/1-SFOS and 2-SFOS signal regions using background only Asimov data is carried. Since the invariant mass of the 4-lepton is included during the training, the classification BDT output is utilised as a discriminant. A bin transformation method was used to avoid bins with low statistics. Figure 151 shows the post-fit result after the background only Asimov data fit. The $q\bar{q} \to ZZ$ and $gg \to ZZ$ backgrounds normalisation is set to free during the fit. The CL_s approach is used to set-up an upper limit on the cross-section times the branching ratio of the Higgs pair production. The upper limit is found to be as follows:

$$L = 61.22$$

E.6 Summary

A search for the non-resonant SM Higgs pair production via gluon fusion in the four-lepton channel is performed. The data used in the analysis is coming from MC simulation with an integrated luminosity equivalent to 139 fb^{-1}. The expected upper limit at 95% CL_s on cross-section times the non-resonant Higgs pair branching ratio is found to be 61.22 times the SM prediction.

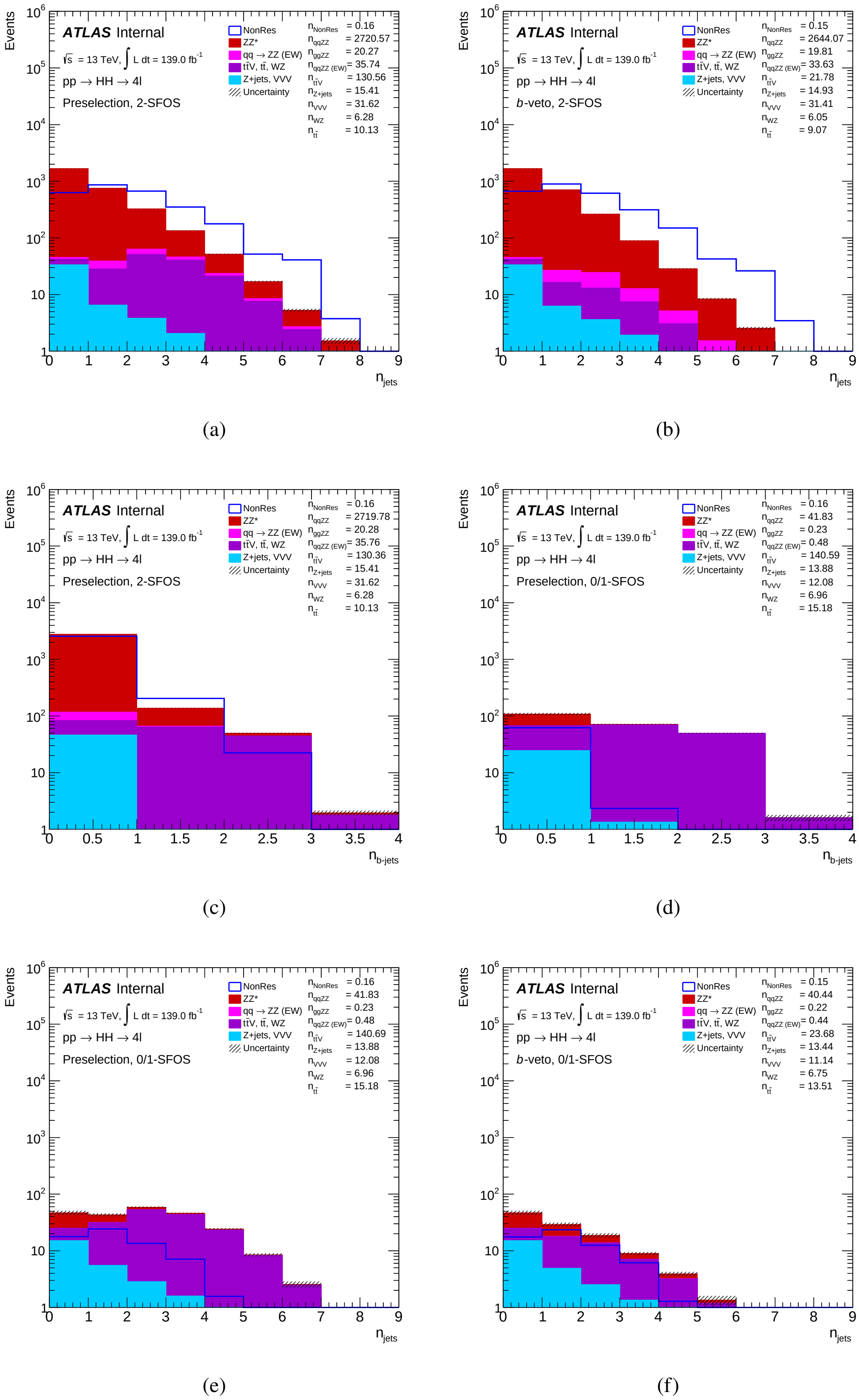

Figure 143: Kinematic distributions of the number of jets multiplicity after the preselection a 2-SFOS and e 0/1-SFOS and r c 2-SFOS and d 0/1-SFOS categories. And after the b-jet veto b 2-SFOS and f 0/1-SFOS. The non-resonant di-Higgs signal is normalised to the total number of background in each category.

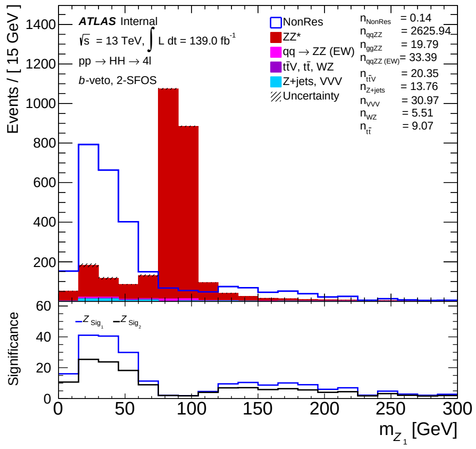

(a)

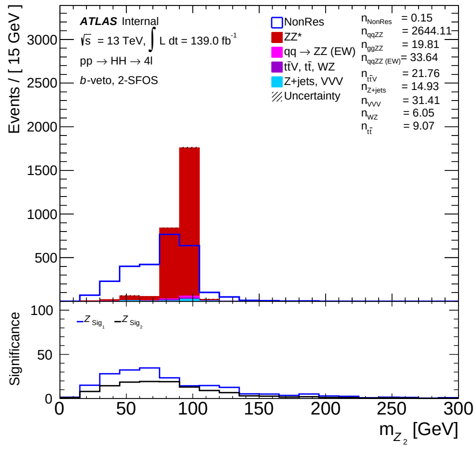

(b)

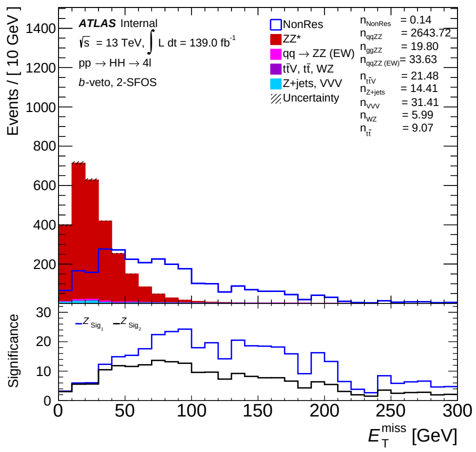

(c)

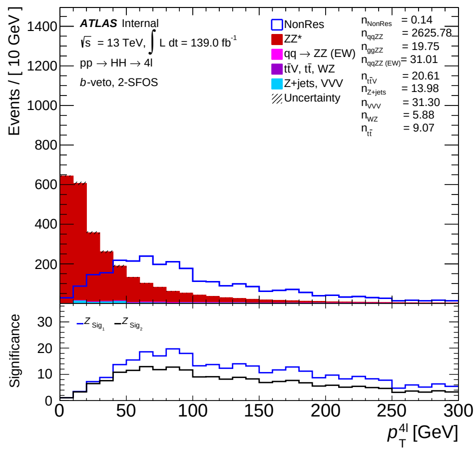

(d)

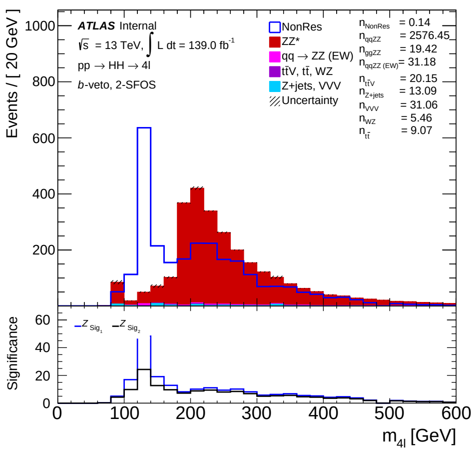

(e)

Figure 144: Kinematic distributions for the 2-SFOS category of the a m_{Z_1}, b m_{Z_2}, b $E_{\mathrm{T}}^{\mathrm{miss}}$, d $p_{\mathrm{T}}^{4\ell}$, and e $m_{4\ell}$.

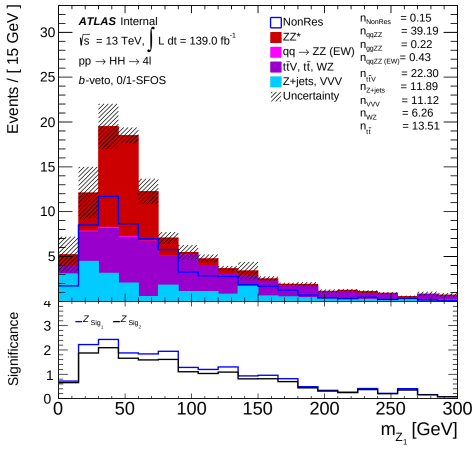

(a)

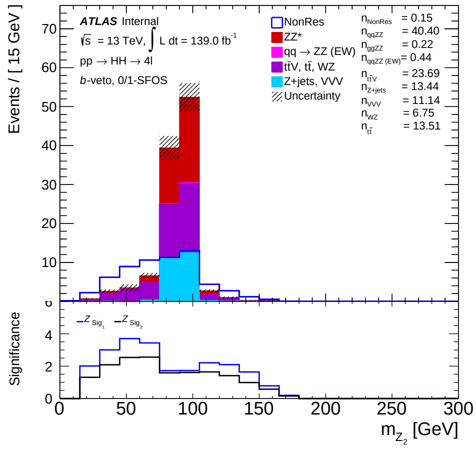

(b)

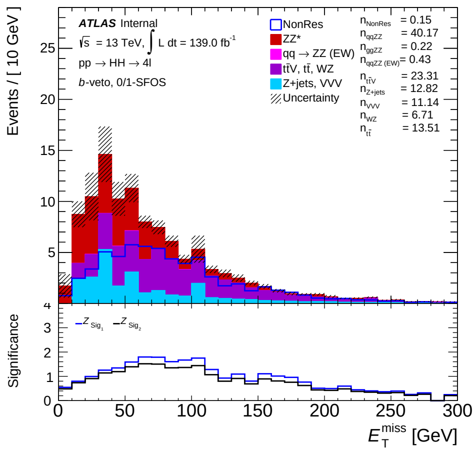

(c)

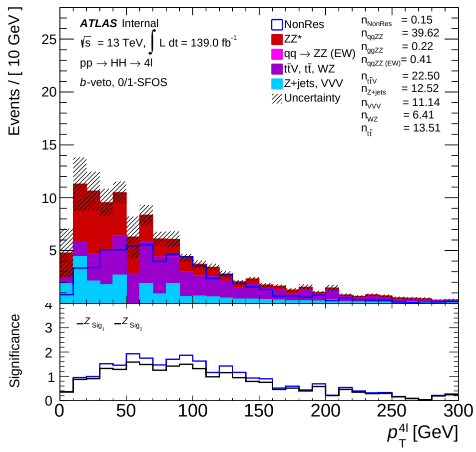

(d)

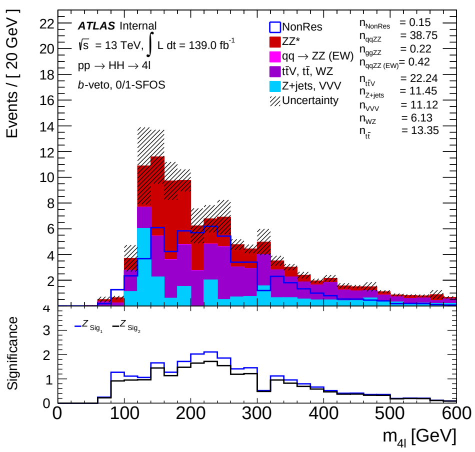

(e)

Figure 145: Kinematic distributions for the 0/1-SFOS category of the a m_{Z_1}, b m_{Z_2}, b $E_{\mathrm{T}}^{\mathrm{miss}}$, d $p_{\mathrm{T}}^{4\ell}$, and e $m_{4\ell}$.

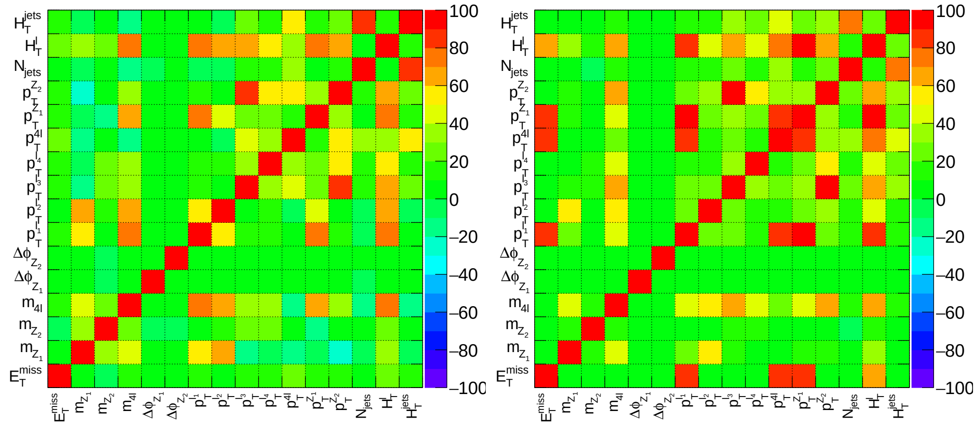

(a) Signal (b) Backgrounds

Figure 146: The correlation between input features for signal and background of the 2-SFOS category.

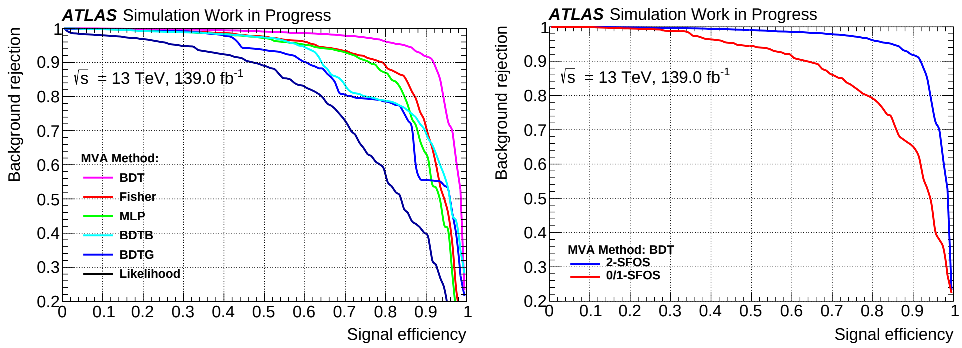

(a) (b)

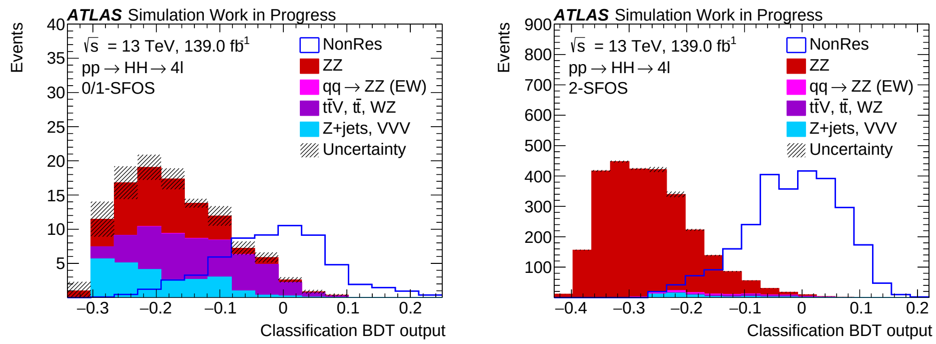

(c) 0/1-SFOS (d) 2-SFOS

Figure 147: The BDT classification output of the signal and background captured after the training and the resulting weight application. The Receiver operating characteristic (ROC) curve showing the background rejection as a function of the signal efficiency for a different MVA algorithms and b the BDT for both 2-SFOS and 0/1-SFOS categories.

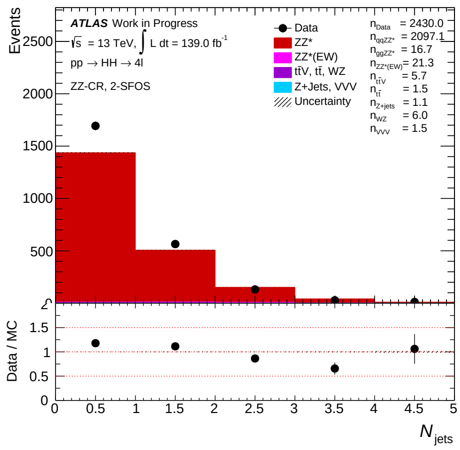

(a)

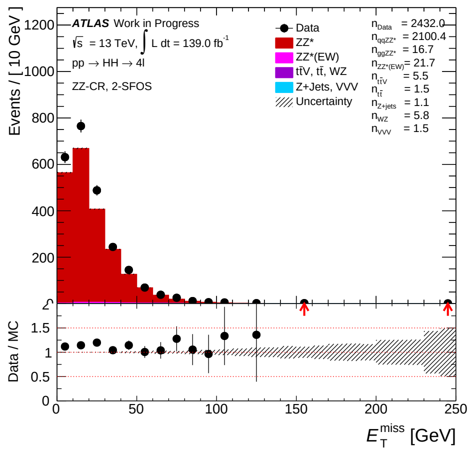

(b)

Figure 148: Kinematic distributions of the a number of jets and b missing transverse energy.

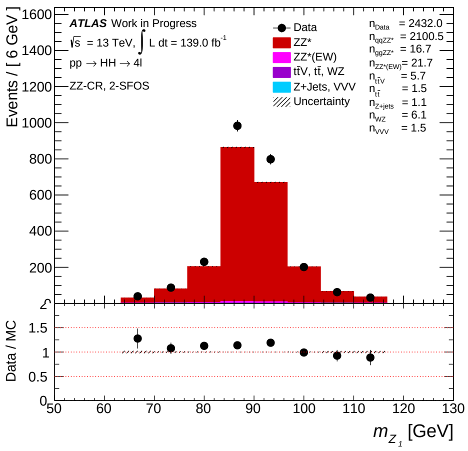

(a)

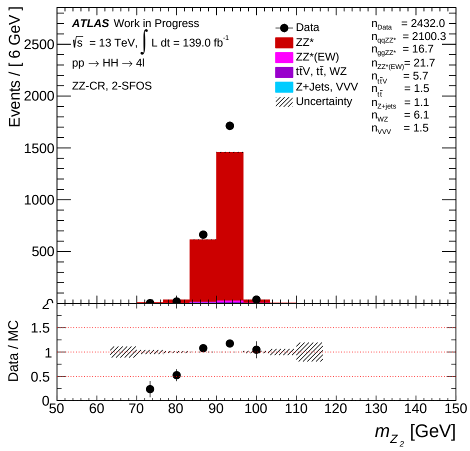

(b)

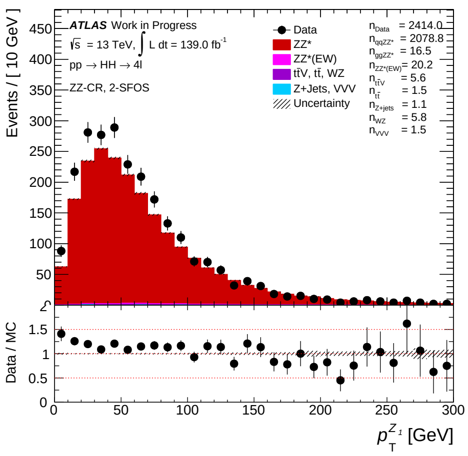

(c)

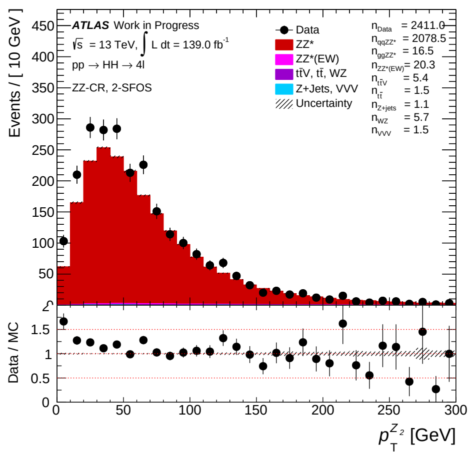

(d)

Figure 149: Kinematic distributions of the a four leptons invariant mass, b four leptons transverse momentum, c rapidity of the four leptons system, d four leptons pseudorapidity.

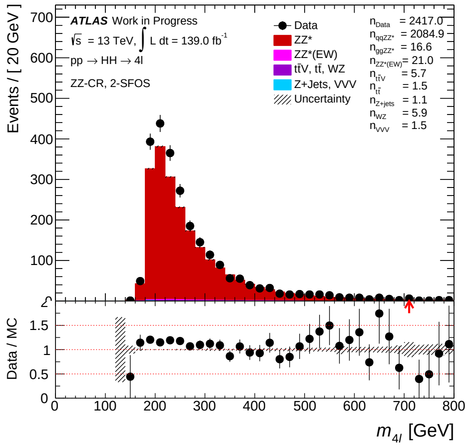

(a)

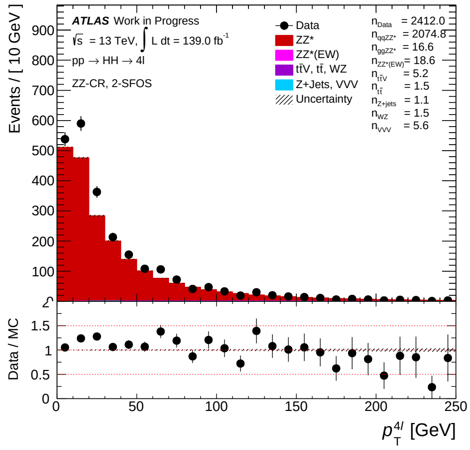

(b)

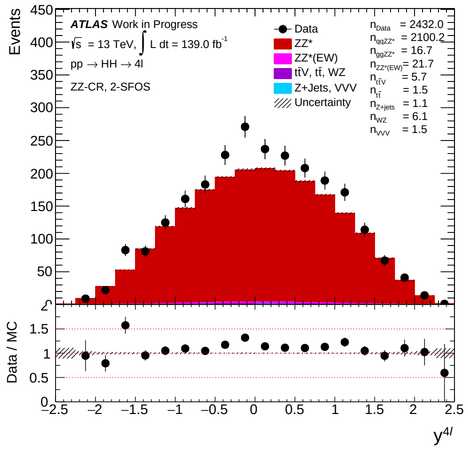

(c)

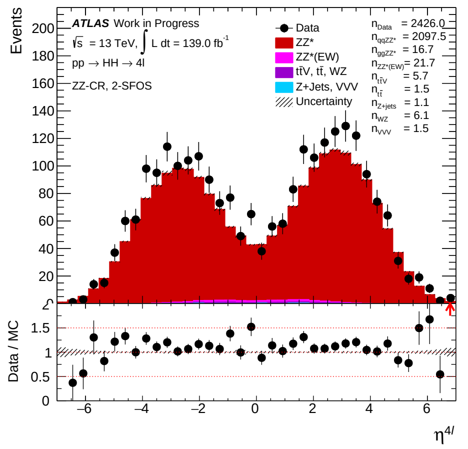

(d)

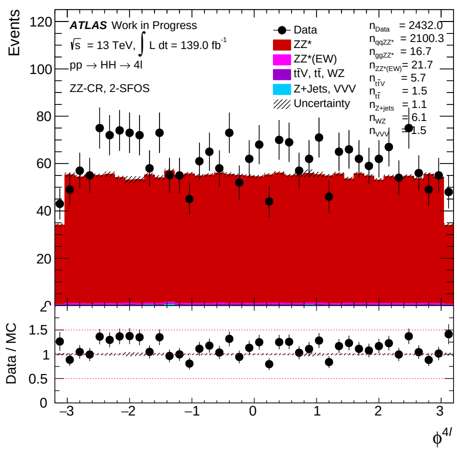

(e)

Figure 150: Kinematic distributions of the a four leptons invariant mass, a four leptons transverse momentum, c rapidity of the four leptons system, d four leptons pseudorapidity and e azimuthal angle of the four leptons system.

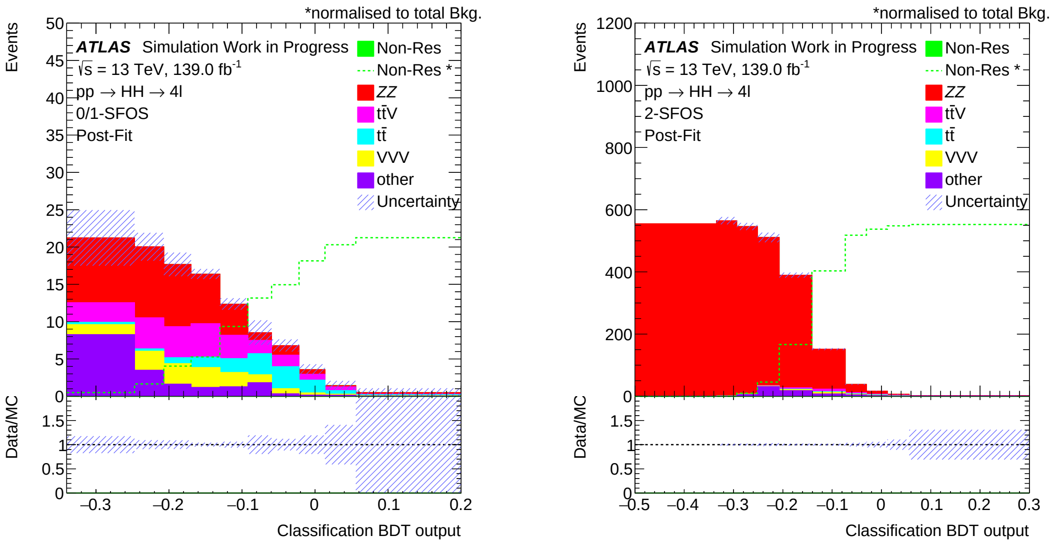

Figure 151: The classification BDT output fitted to background only Asimov data for 0/1-SFOS (left) and 2-SFOS (right) signal regions.

F Appendix of the Analysis of $\gamma\gamma$+Lepton Channel

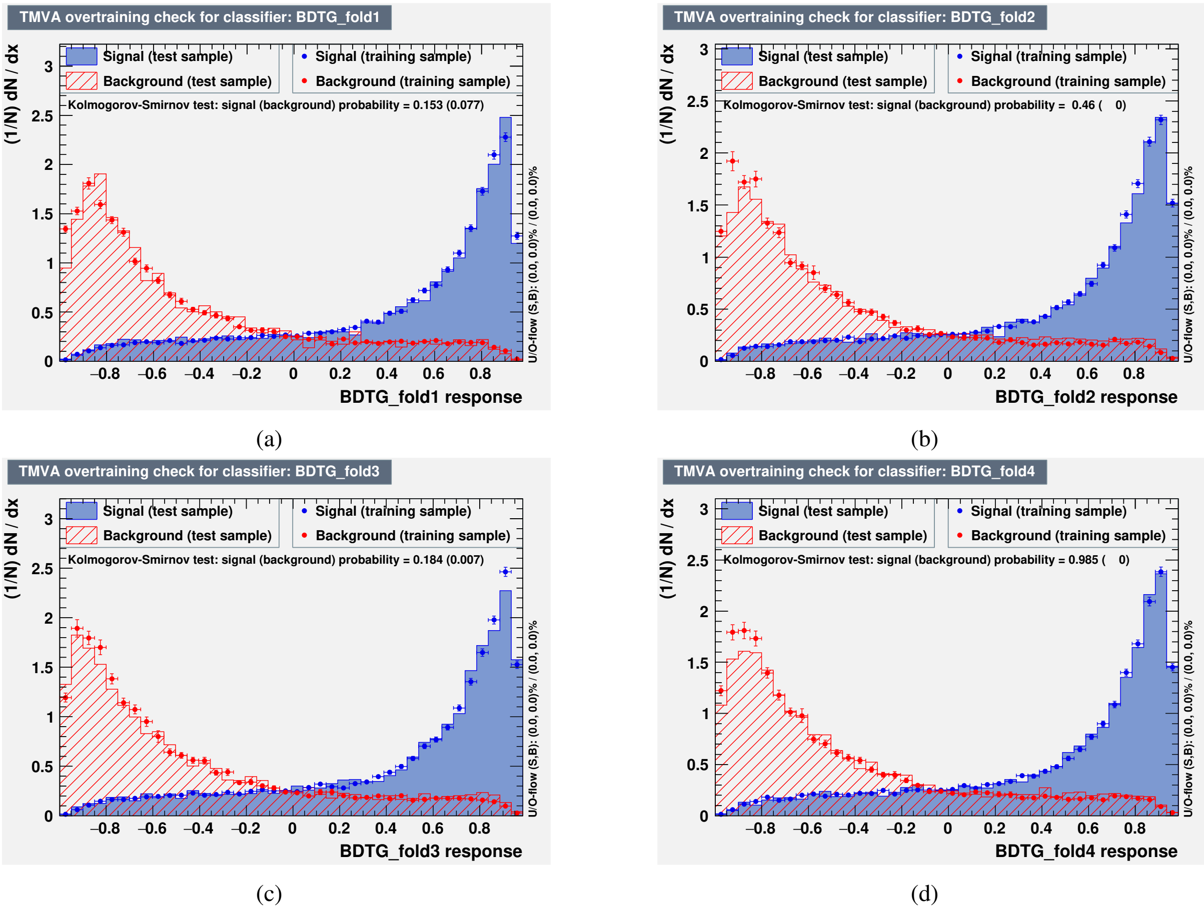

Figure 152: The overtraining plots with ks test values for 4 individual folds in 1ℓ + jets channel.

F.1 Appendix of the analysis $\gamma\gamma$+2τ_{had} channel

This section describes the analysis of $\gamma\gamma$+2τ_{had} channel.

F.1.1 Event selection

Events are selected for this channel if there are at least two photons and at least two oppositely charged τ_{had} , which satisfy the criteria outlined in Section. The diphoton invariant mass is initially required to fall within a broad mass window of 105 GeV < $m_{\gamma\gamma}$ < 160 GeV. In order to remain orthogonal to the ATLAS search for $HH \rightarrow \gamma\gamma b\bar{b}$, any event with b-jet using the 70% efficient working point is rejected.

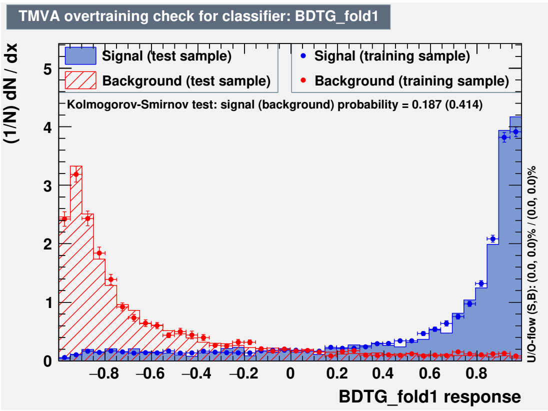

(a)

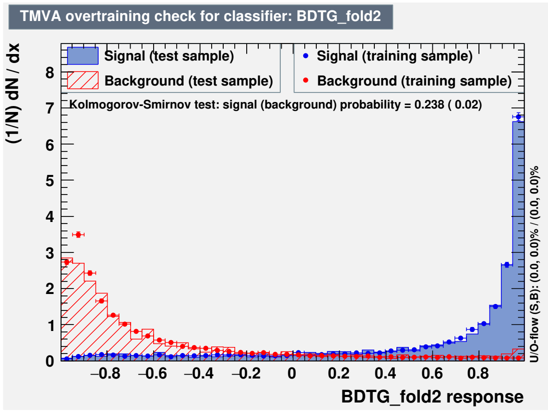

(b)

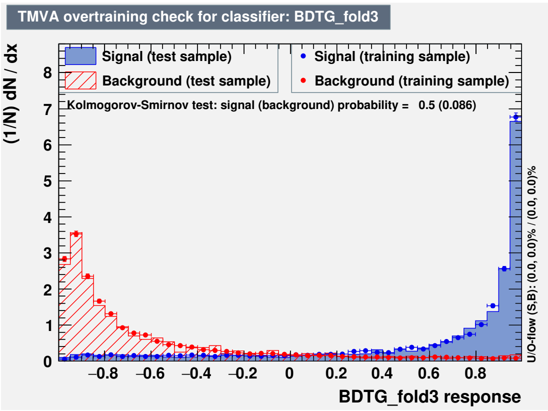

(c)

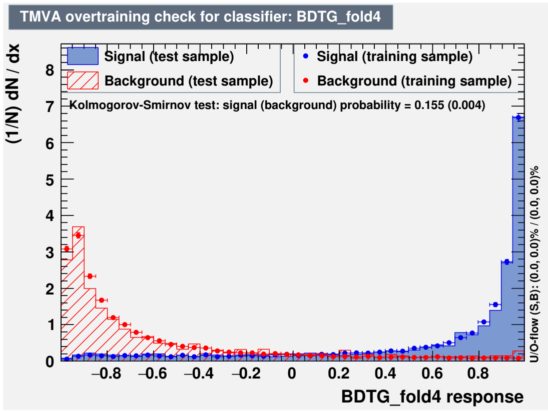

(d)

Figure 153: The overtraining plots with ks test values for 4 individual folds in 1τ + jets channel.

F.1.2 Background composition

This analysis is affected both by backgrounds from single-Higgs-boson production and by non-resonant backgrounds with continuum $m_{\gamma\gamma}$ spectra. The major single Higgs boson production contributing to the background are associated production with a Z boson (ZH), associated production with a top quark pair ($t\bar{t}H$). As for continuum backgrounds, the major contributions are vector boson production associated with photons ($V\gamma\gamma$) and multi-jet processes associated with photons ($\gamma\gamma$+jets).

Simulated samples are used to model single-Higgs-production and vector boson production associated with photons ($V\gamma\gamma$), while processes with fake-τ_{had} are estimated using data-driven techniques, as discussed below. In $\gamma\gamma$+2τ_{had} channel, the fake-τ_{had} backgrounds are from multi-jet processes in the sense that some of QCD jets can be mis-identified as hadronically decay τ jets. A data-driven fake-factor method is used to estimate the multi-jet processes as described in Section .

Events with electrons and muons that are misidentified as τ_{had} objects, dominantly coming from the $V\gamma\gamma$ production ($V \rightarrow l^+l^-$), represent a minor background in the analysis and they are estimated from simulation.

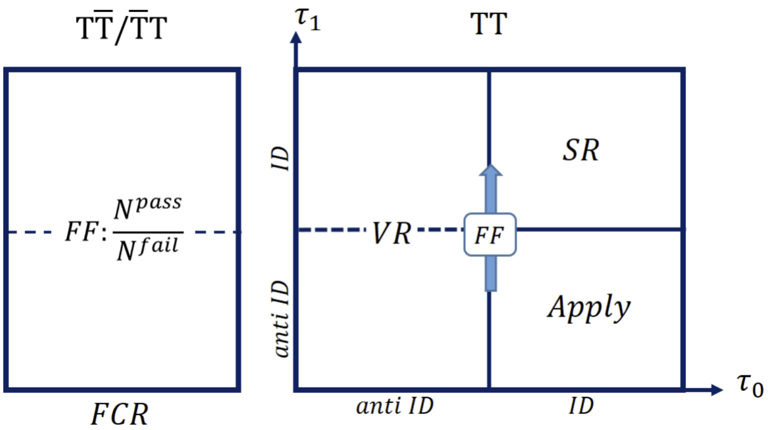

Figure 154: schematic depiction of the application of the fake factor mehthod used to estimate the $\gamma\gamma$+jets background in the di-Higgs $\gamma\gamma$+2τ_{had} channel. Left: Fake factors are calculated in the FCR with tight/anit-tight ($T\bar{T}/\bar{T}T$) identification on the two photons candidates. Right: Fake factors are then applied to the "Apply" region with two tight photons, loose leading τ_{had} and anti-loose subleading τ_{had} to estimate $\gamma\gamma$+2τ_{had} contribution in signal region (SR). A validation region (VR) is also defined as event with two tight photons and anti-loose leading τ_{had} .

F.1.3 $\gamma\gamma$+jets with fake-τ_{had} in the $\gamma\gamma$+2τ_{had} channel

To estimate the $\gamma\gamma$+jets background contribution we employ a fake factor method. This method is schematically depicted in Fig.154.

A fake-τ_{had} control region (FCR) is designed to derive the fake factors with the same definition as the signal region, except that the tight photon-ID requirement on one of the two photon candidates is inverted ($T\bar{T}/\bar{T}T$). To have as large statistic as possible, no tau-ID requirement is applied to the leading τ_{had} candidate and no oppositely-charged requirement is applied to the two τ_{had} candidates. The tau-ID fake factors, f_{τ_1-ID}, are then defined as the number of events with two τ_{had} candidates passing loose tau-ID, divided by the number of events with leading τ_{had} candidate passing loose tau-ID while sub-leading τ_{had} candidate failing loose tau-ID.

$$f_{\tau_1-ID}(p_{T\,\tau_1}, N_{trks}) = \frac{N_{data}^{pass\ \tau_1-ID,\ FCR}(p_{T\,\tau_1}, N_{trks}) - N_{other\ MCs}^{pass\ \tau_1-ID,\ FCR}(p_{T\,\tau_1}, N_{trks})}{N_{data}^{fail\ \tau_1-ID,\ FCR}(p_{T\,\tau_1}, N_{trks}) - N_{other\ MCs}^{fail\ \tau_1-ID,\ FCR}(p_{T\,\tau_1}, N_{trks})} \quad (38)$$

where τ_1 denotes the subleading τ_{had} candidate and N_{trks} is the number of associated tracks of the subleading τ_{had} candidate. The tau-ID fake factors are determined as a function of transverse momentum of subleading τ_{had} and measured separately depending on the number of associated tracks of the subleading τ_{had} candidate. All other significant backgrounds () are subtracted in fake-τ_{had} control region before computing the fake factors to give a very pure multi-jets region and avoid possible biased due to differences in normalization and shape of the other backgrounds between the individual regions.

The FFs are applied to a control region with the same definition as the signal region, except that the loose tau-ID requirement on the subleading τ_{had} candidate is inverted (fail-ID region). This gives both the shape and normalization of the $\gamma\gamma$+jets contribution. The $\gamma\gamma$+jets contribution in the signal region, $N_{\gamma\gamma+jets}$ is then predicted by weighting the events from the fail-ID region by their fake factors:

$$N_{\gamma\gamma+jets}(p_{T\,\tau_1}, N_{trks}) = f_{\tau_1-ID}(p_{T\,\tau_1}, N_{trks}) \times (N_{data}^{fail\ \tau_1-ID}(p_{T\,\tau_1}, N_{trks}) - N_{other\ MCs}^{fail\ \tau_1-ID}(p_{T\,\tau_1}, N_{trks})) \quad (39)$$

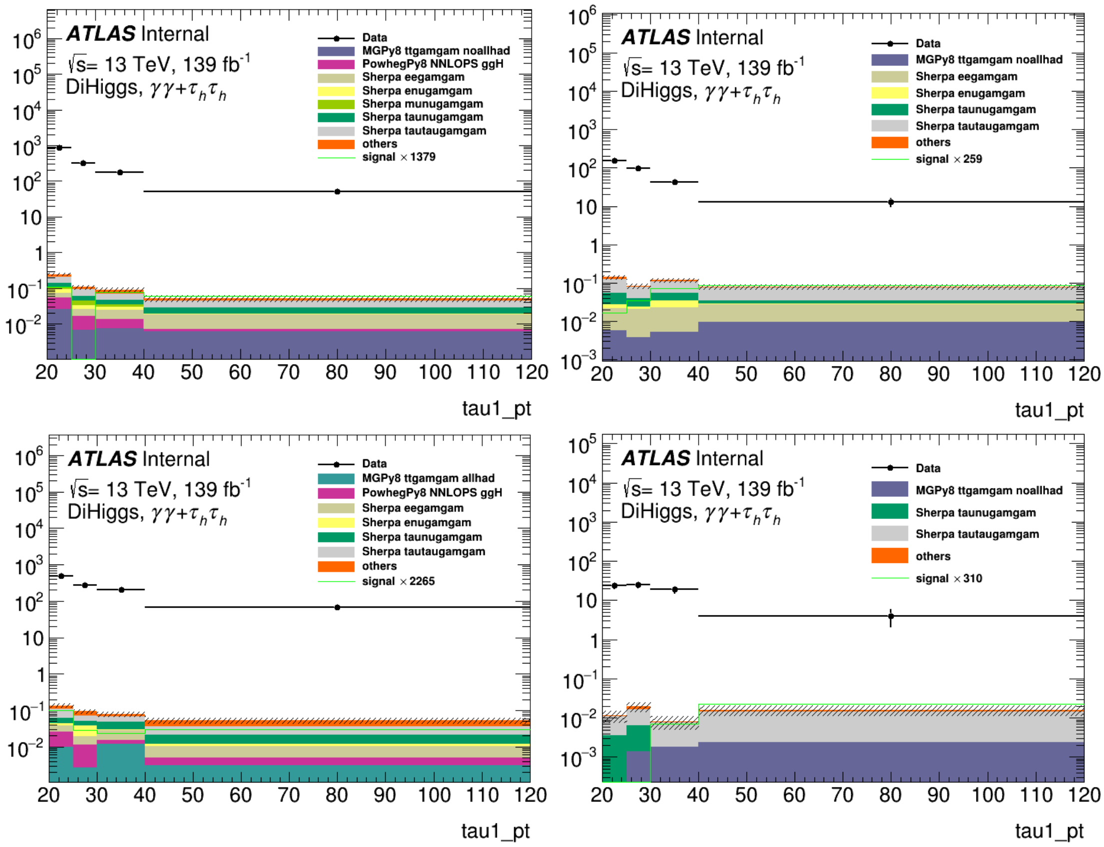

Figure 155: p_T distributions in FCR for 1-prong (top) and 3-prong (bottom) subleading τ_{had} candidate failing (left) / passing (right) loose tau-ID.

Again, all other significant backgrounds are subtracted in fail-ID region before applying the fake factors.

The subleading τ_{had} candidate p_T distributions in the FCR are shown in Fig.155, separately for 1- and 3-prong τ_{had} . The measured fake factors are shown in Fig.156 and only statistical uncertainty is plotted. A closure test is performed to show that the derived fake factors can yield distribution consistent with data with regard to other observables by applying the fake factor back to the FCR, As shown in Fig.157.

To validate the fake factor method, a validation region should be as close as possible to the signal region, meanwhile, should be better have adequate statistic. A first thought is to do the validation in the sideband, [105, 120]&[130, 160]GeV, of $m_{\gamma\gamma}$ distribution (signal region is [120, 130]GeV), which fails the statistic requirement. Therefore, the validation region is finally defined requiring events containing two tight photons and two oppositely charged τ_{had} candidates, among which the leading τ_{had} candidate fails loose tau-ID. As shown in Fig.158, the fake factor method estimation is compared to observed data in VR with regard to $m_{\gamma\gamma}$. more validation plots to be added for MVA input variables...

F.1.4 MVA method

BDT is trained to discriminate between the $\gamma\gamma$+2τ_{had} signal and major backgrounds including $\gamma\gamma$+jets (normalized to fake factor estimation), ZH, $V\gamma\gamma$ ($\tau\tau\gamma\gamma$, $\tau\nu_\tau\gamma\gamma$). Kinematic variables used in BDT training can be categorized as follows:

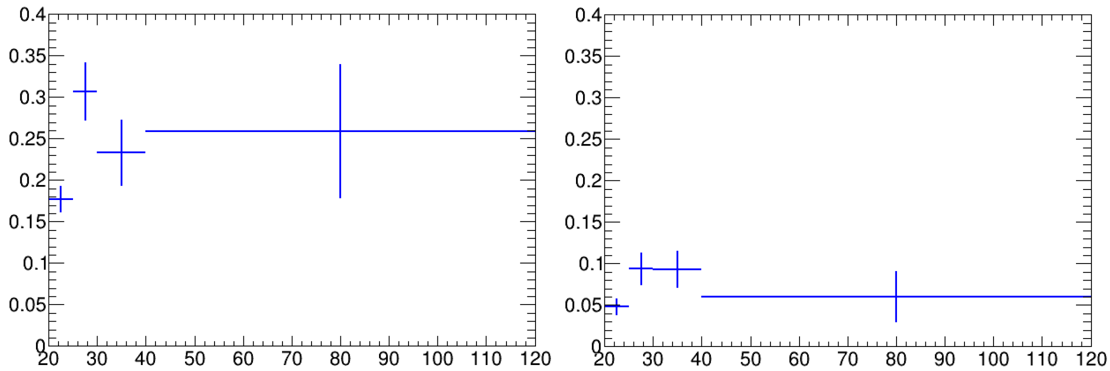

Figure 156: Fake factors depend on subleading τ_{had} p_T for 1-prong (left) and 3-prong (right) τ_{had} . Error bars show statistically only uncertainty.

Properties of the Higgs boson: the visible mass and transverse momentum of the di-τ system, $m^{vis}_{\tau\tau}$,$p_T{}^{vis}_{\tau\tau}$, the transverse momentum and pseudorapidity of the di-γ system, $p_{T\,\gamma\gamma}$, $\eta_{\gamma\gamma}$.

Properties of resonant di-τ and di-γ decays: the angular distances $\Delta R_{\tau\tau}$ and $\Delta R_{\gamma\gamma}$

Visible transverse momentum of leading τ_{had} candidate $p_{T\,\tau_0}$, missing transverse momentum E_T^{miss} and scalar sum of E_T

The most important variables in the training are $\Delta R_{\gamma\gamma}$ and $p_{T\,\gamma\gamma}$. The resulting BDT score distribution is shown in Fig.159 for event pass the preselection and show the ability of the BDT to separate the signal process from background processes. The BDT score is used as observable in the final fit.

2-folds cross validation...

F.1.5 Results

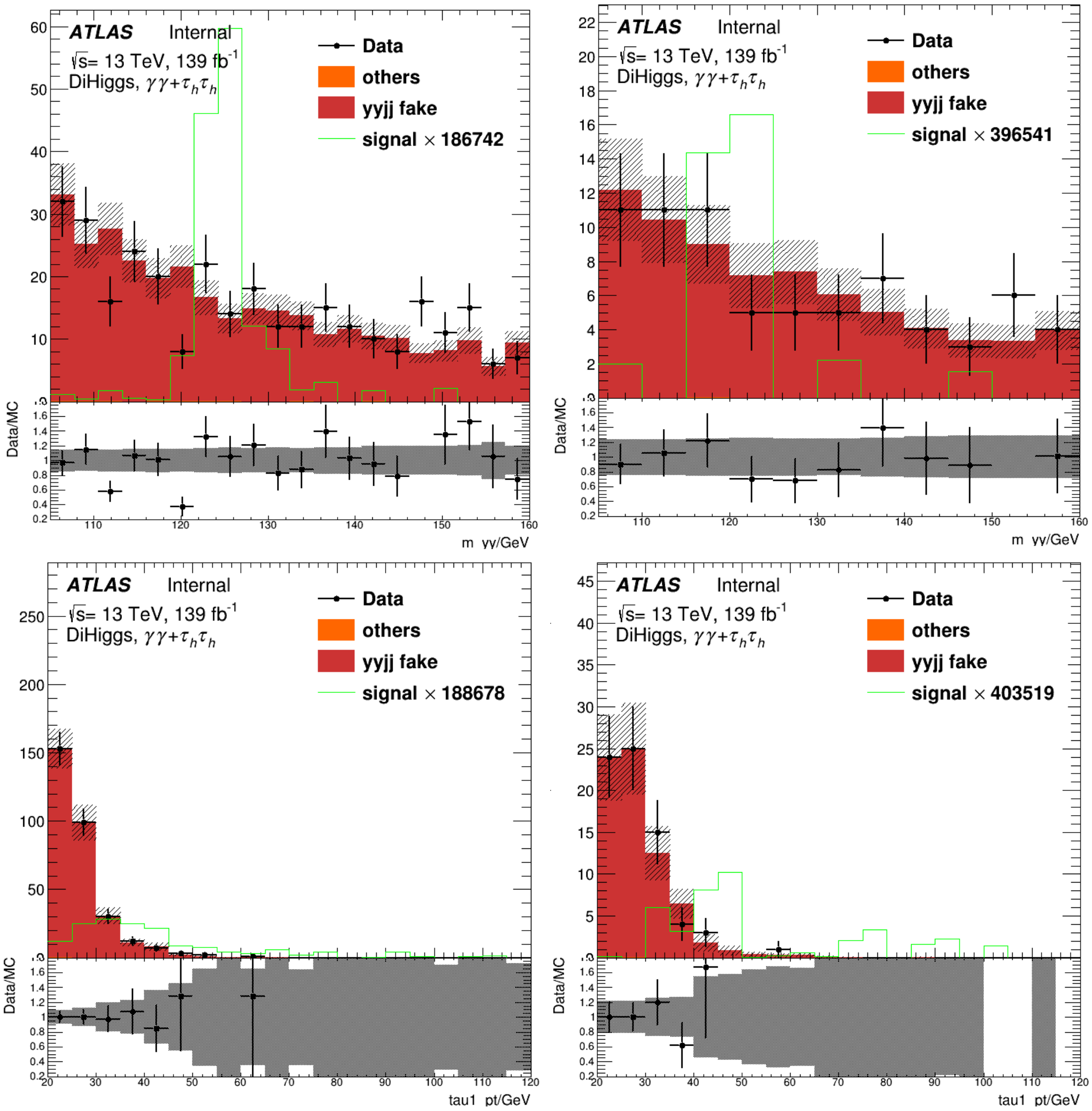

Figure 157: Closure test performed with regard to $m_{\gamma\gamma}$ (upper) and $p_{T\,\tau_1}$ (bottom) for 1-prong (left) and 3-prong (right) τ_{had} in. Event numbers of pass-ID region of FCR are estimated by applying fake factors back to event numbers of fail-ID region of FCR.

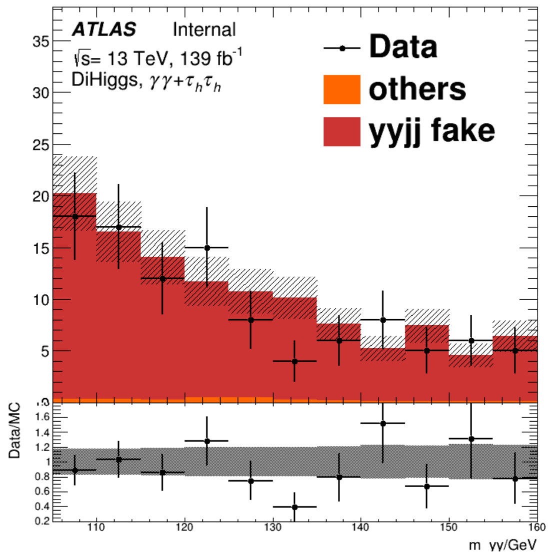

Figure 158: $m_{\gamma\gamma}$ distribution in the validation region

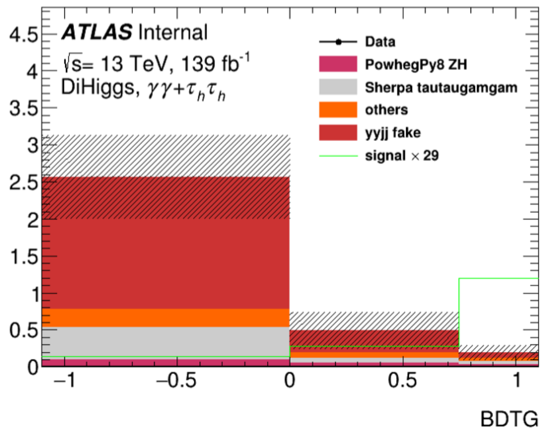

Figure 159: BDT_{score} distribution after the preselection

G Appendix of the Analysis of τ Channels

G.1 1ℓ+$2\tau_{\mathrm{had}}$ channel

In this section, the signal region optimization study is described in detail.

G.1.1 Optimizing event selection

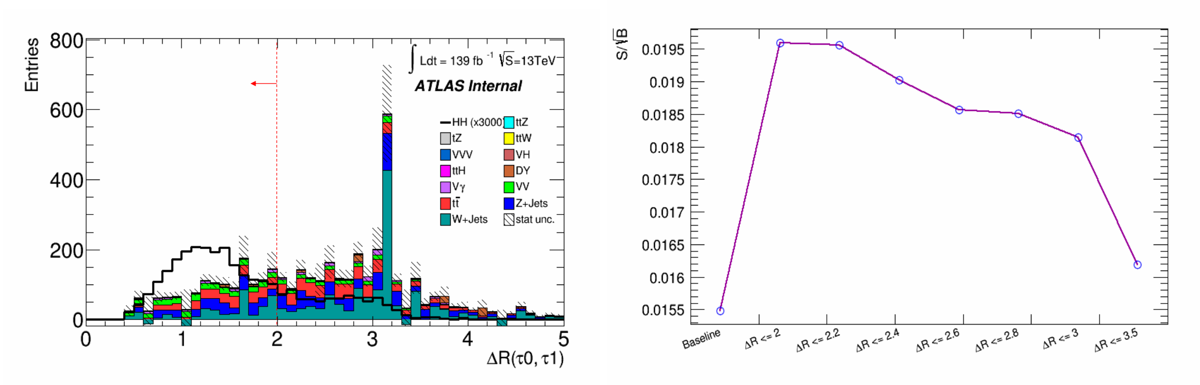

Figure 160: ...

G.1.2 Optimizing lepton identification and isolation working point

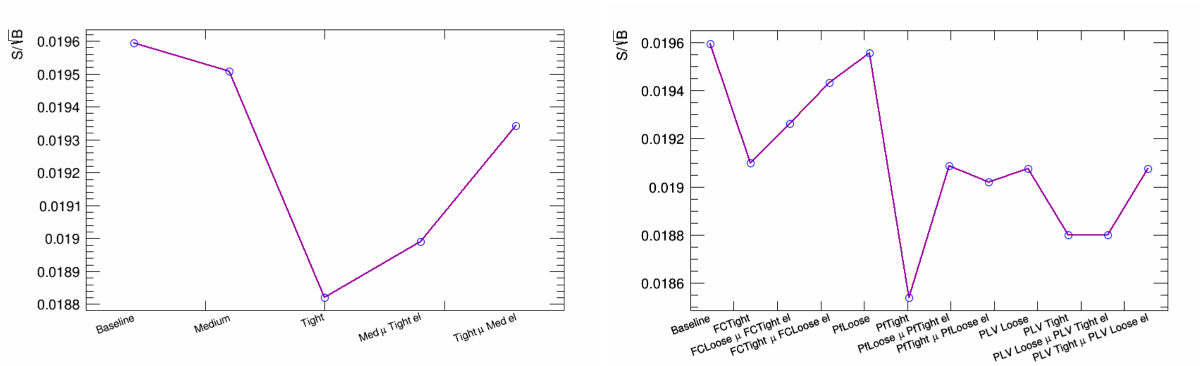

Figure 161: ...

G.1.3 Optimizing hadronic tau candidates

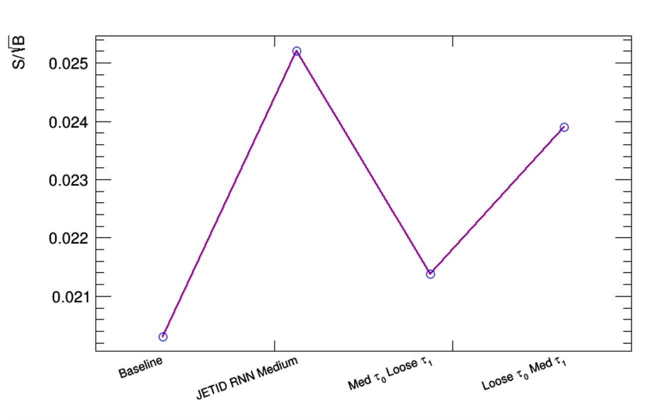

Figure 162: ...

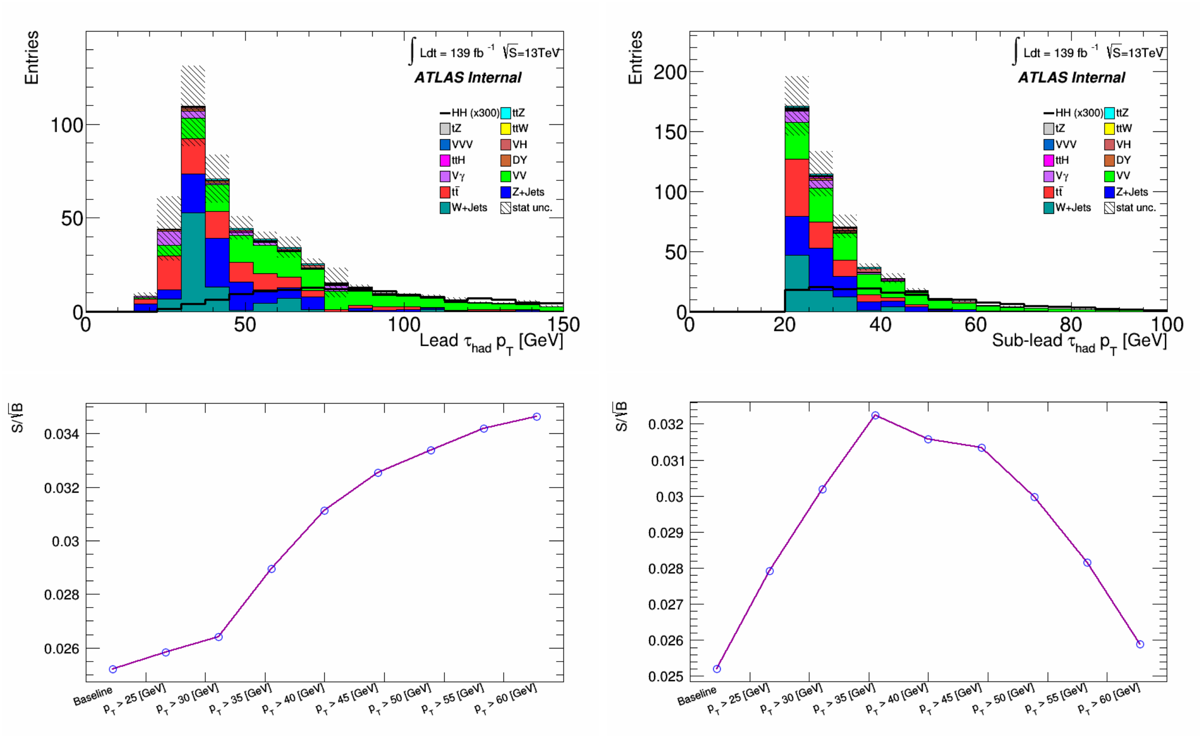

Figure 163: ...

H Appendix of the Analysis of bb + 4l Channels

H.1 Isolation strategy

For the $4l + bb$ channel, two different strategies of lepton isolation are tested. One requires all the four leptons contained in the selected events passing the isolation, which is denoted as Tight Isolation. The Tight Isolation is the standard isolation strategy to reject most of the non-prompt background, like $t\bar{t}$ and Z+jets process which contain only two real leptons in the final state, but in the meantime it would also hurt a lot on the signal efficiency and decrease the sensitivity. In this case an alternative isolation strategy is applied with only the third or fourth lepton passing the isolation, which is denoted as Loose Isolation.

Table 63 shows the event yields from MC prediction with two different isolation strategies. Expect the lepton isolation, the other selection is the same as the SR. The BDT training is also performed after the event selection. The training and testing results are shown in Figure 164 and there is some overtraining observed due to the low statistics for Tight Isolation.

	Event Yields	
	Loose Isolation	Tight Isolation
$t\bar{t}$	19.02±0.87	1.40±0.25
$t\bar{t}Z$	4.45±0.17	1.78±0.10
VV	4.84±0.13	2.80±0.10
Higgs	4.62±0.81	3.07±0.81
Z+jets	5.00±1.83	0.44±0.21
ggF HH	0.16±0.00	0.10±0.00
VBF HH	0.007±0.000	0.005±0.000

Table 63: The expected yields of the SM background in SR with two isolation strategies.

.

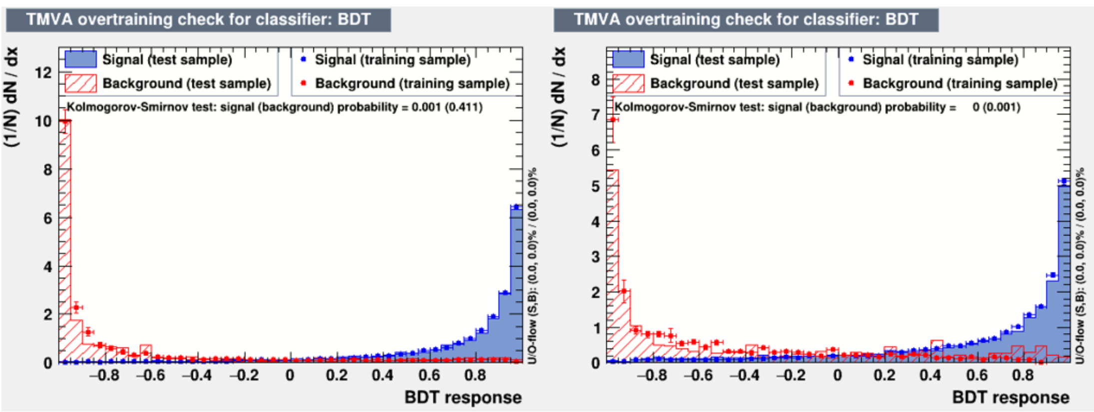

(a) Loose Isolation

(b) Tight Isolation

Figure 164: Overtraining results.

There are two BDT classifiers extracted with two different isolation strategies. They are also applied to the corresponding samples respectively to get the BDTG output. The distributions of BDTG are shown in

Figure 165. The expected limits are extracted with the SR only fitting to compare the sensitivity between two strategies and shown in Table 64. Although the non-prompt background gets some increasing with Loose Isolation, the BDT training can still achieve good separation between signal with background so that the expected limit gets better with Loose Isolation than Tight Isolation.

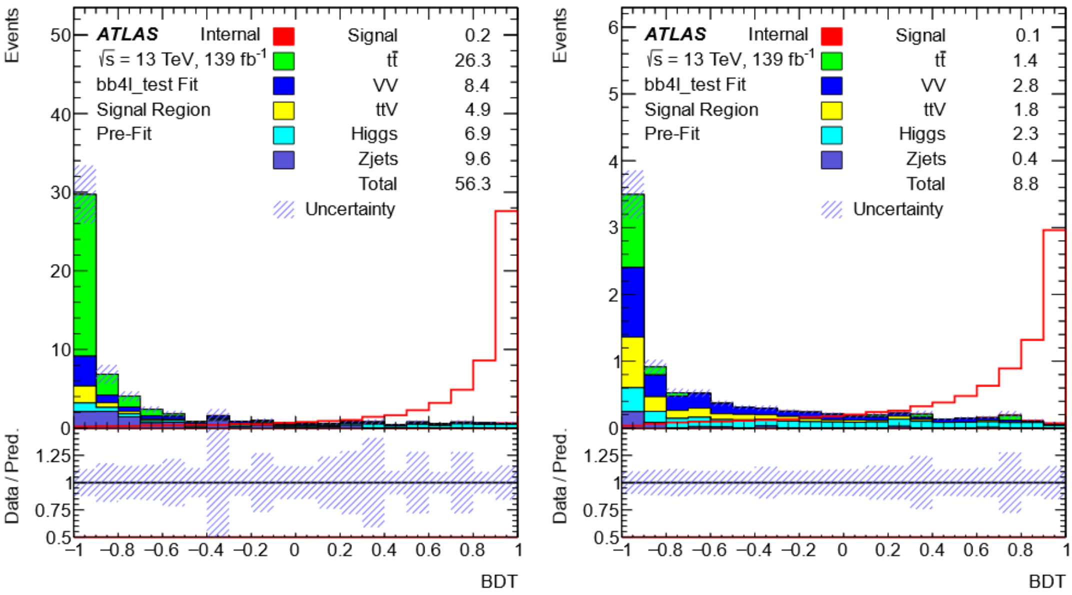

(a) Loose Isolation (b) Tight Isolation

Figure 165: BDTG distributions in SR. Dashed line represents signal normalized to total background

	-2σ	-1σ	Expected	$+1\sigma$	$+2\sigma$	Observed
Loose Isolation	15.19	20.39	28.29	42.93	67.81	blinded
Tight Isolation	18.74	25.16	34.92	54.44	101.05	blinded

Table 64: Observed and expected upper limits on the SM non-resonant HH production cross-section at 95% CL and their ratios to the SM prediction. The $\pm 1\sigma$ and $\pm 2\sigma$ variations about the expected limit are also shown. Only statistical uncertainties are included.

To make the further validation on the Loose Isolation, p_T distributions of the four leptons are checked in the VR after the CRs only fitting. Figure 166 shows good agreement between the data and SM prediction so it means the background is well controlled with Loose Isolation.

H.2 Contamination of $HH \rightarrow bbll$ process in SR

The MC samples shown in Table 65 are used for the $bbll$ process study. The events of the $bbll$ process are required to pass the same event selection described in Section and the raw event number is shown in Table 66. The efficiency is about 0.014% and the yields normalized to 139 fb^{-1} is about 0.00008, so the contamination is quite negligible.

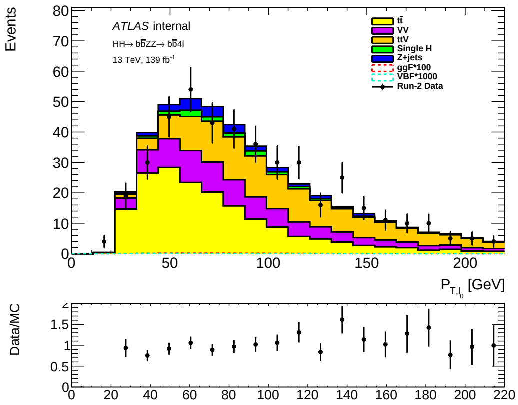

(a)

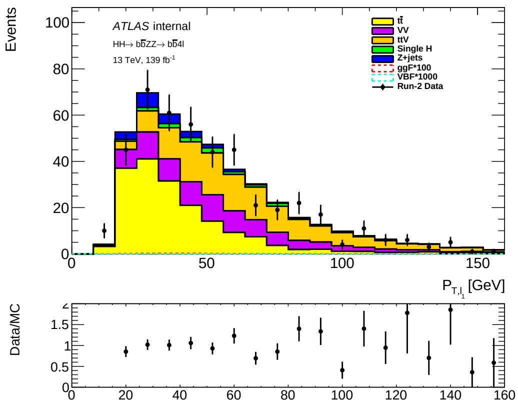

(b)

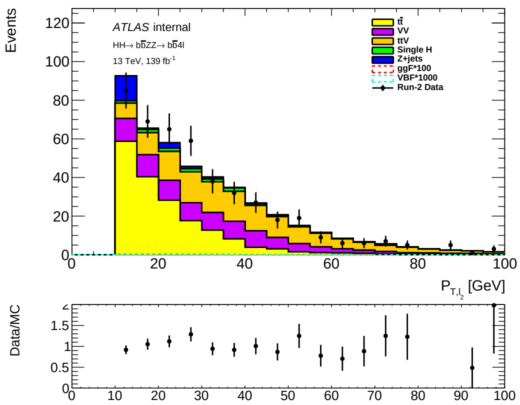

(c)

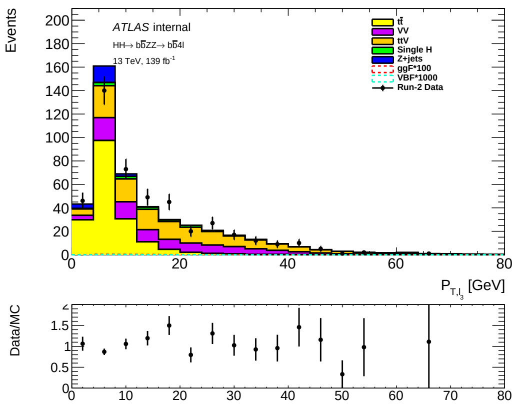

(d)

Figure 166: p_T distributions of the four leptons in the VR.

mc16_13TeV.600469.PhPy8EG_PDF4LHC15_HHbbZZ2l_cHHH01d0.recon.AOD.e8222_s3126_r9364
mc16_13TeV.600469.PhPy8EG_PDF4LHC15_HHbbZZ2l_cHHH01d0.recon.AOD.e8222_s3126_r10201
mc16_13TeV.600469.PhPy8EG_PDF4LHC15_HHbbZZ2l_cHHH01d0.recon.AOD.e8222_s3126_r10724

Table 65: $bbll\nu\nu$ sample list.

Event selection	Raw event number
Events in DADO	488044
Exactly 4 leptons	3906
Pre-selection	7

Table 66: Raw event number of $bbll\nu\nu$ yields.

I Appendix of the Analysis of 2L+bb+2j Channels

Add appendix of the text for 2Lbb2j channels

J Appendix of the Combination

J.1 Preliminary stats-only results

As the statistical procedure described in 11.3, each channel share a common $\mu = \frac{\sigma_{HH}}{\sigma^{SM}_{HH}}$. In the first version of stats-only workspace, the signal samples in which the parton is showered by Herweig7 were used, and only MC statistical uncertainties are considered in the fitting. The data driven background is not included in this workspace, QmisID and fake events are estimated by $t\bar{t}$ and V+jets MC.

A hybrid Asimov dataset is built in bb4L channel in order to preform a CR + SR simultaneous fit. The data sets are used in 5 specific control regions and blinded in the signal region. The fitted normalization factors and μ are summarized in Figure 167.

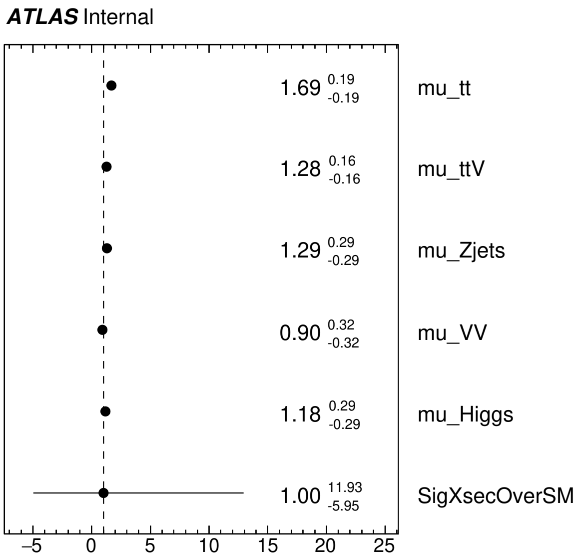

Figure 167: Fitted normalization factors and μ for the CR + SR fit in the bb4L channel. The normalization factors for the ttbar, VV, Zjets, single higgs are free floating.

The results derived from older version of nominal samples is shown in table 67. The combination of all channels in this analysis results in the expected upper limits equals to 8.06 times Stand Model di-Higgs production cross section.

In an ATLAS note, use the appendices to include all the technical details of your work that are relevant for the ATLAS Collaboration only (e.g. dataset details, software release used). This information should be printed after the Bibliography.

Table 67: Upper limits on the signal strength.

Channels	$+2\sigma$	$+\sigma$	Median	$-\sigma$	-2σ
$2LSS0\tau$	61.54	46.07	29.20	21.04	15.67
$3L0\tau$	64.39	48.30	26.54	19.13	14.25
$2LSS1\tau$	81.41	61.00	33.54	24.17	18.00
$1L2\tau$	72.28	51.54	28.88	20.82	14.90
$\gamma\gamma + 2L$	71.90	45.45	29.90	21.55	16.05
$\gamma\gamma + LepJet$	53.21	38.09	21.63	15.59	11.61
$\gamma\gamma + TauJet$	101.85	70.18	43.96	31.68	23.60
$\gamma\gamma + OL$	94.06	67.95	47.9	34.51	25.71
bb4L	67.91	43.30	27.76	20.00	14.90
Combined	16.33	11.56	8.06	5.81	4.32